Transport and microrheology of active colloids

Thesis by
Zhiwei Peng

In Partial Fulfillment of the Requirements for the
Degree of
Doctor of Philosophy

Caltech

CALIFORNIA INSTITUTE OF TECHNOLOGY
Pasadena, California

2022
Defended April 26, 2022

ACKNOWLEDGEMENTS

First and foremost, I would like to thank my advisor, Professor John Brady. I consider myself very lucky to have had the opportunity to work with him. I thank Professor Brady for his guidance throughout the journey of my research at Caltech. I am most grateful for his encouragement, support, and open-mindedness which allowed me the freedom to explore various research problems in the field. His great mentoring style, unparalleled physical insight, and mathematical prowess have fundamentally shaped my development as a researcher. In addition, my sincere thanks go to my thesis committee: Professor Zhen-Gang Wang, Professor Mikhail Shapiro, and Professor Tim Colonius.

I have been very fortunate to be surrounded by wonderful and talented colleagues, from whom I learned a lot both academically and personally. I would like to thank Eric Burkholder, Ahmad Omar, Austin Dulaney, Camilla Kjeldbjerg, Karol Makuch, Stewart Mallory, Hyeongjoo Row, Alec Glisman, and Edmond Zhou. I would also like to thank my former advisor Gwynn Elfring at the University of British Columbia for his constant encouragement and genuine advice.

Finally, I would like to thank my partner Jingru Shi. Her love and support keep me moving forward, especially during times of adversity. I dedicate this thesis to her.

ABSTRACT

Active colloids are micron-sized particles that self-propel through viscous fluids by converting energy extracted from their environment into mechanical motion. The origin or mechanism of their locomotion can be either biological or synthetic ranging from motile bacteria to artificial phoretic particles. Owing to their ability to self-propel, active colloids are out of thermodynamic equilibrium and exhibit interesting macroscopic or collective dynamics. In particular, active colloids exhibit accumulation at confining boundaries, upstream swimming in Poiseuille flow, and a reduced or *negative* apparent shear viscosity. My work has been focused on a theoretical and computational understanding of the dynamics of active colloids under the influence of confinement and external fluid flows, which are ubiquitous in biological processes. I consider the transport of active colloids in channel flows, the microrheology of active colloids, and lastly I propose and study a vesicle propulsion system based on the learned principles.

A generalized Taylor dispersion theory is developed to study the transport of active colloids in channel flows. I show that the often-observed upstream swimming can be explained by the biased upstream reorientation due to the flow vorticity. The longitudinal dispersion of active colloids includes the classical shear-enhanced dispersion and an active swim diffusivity. Their coupling results in a non-monotonic variation of the dispersivity as a function of the flow speed. To understand the effect of particle shape on the transport of active colloids, a simulation algorithm is developed that is able to faithfully resolve the inelastic collision between an ellipsoidal particle and the channel walls. I show that the collision-induced rotation for active ellipsoids can suppress upstream swimming. I then investigate the particle-tracking microrheology of active colloids. I show that active colloids exhibit a swim-thinning microrheology and a negative microviscosity can be observed when certain hydrodynamic effects are considered. I show that the traditional constant-velocity probe model is not suitable for the quantification of fluctuations in the suspension. To resolve this difficulty, a generalized microrheology model that closely mimicks the experimental setup is developed. I conclude by proposing a microscale propulsion system in which active colloids are encapsulated in a vesicle with a semi-permeable membrane that allows water to pass through. By maintaining an asymmetric number density distribution, I show that the vesicle can self-propel through the surrounding viscous fluid.

PUBLISHED CONTENT AND CONTRIBUTIONS

Zhiwei Peng and John F. Brady. Upstream swimming and Taylor dispersion of active Brownian particles. *Phys. Rev. Fluids*, 5:073102, Jul 2020. doi: 10.1103/PhysRevFluids.5.073102. Z. Peng participated in the conception of the project, performed the numerical calculations and analysis, performed the simulations, analyzed the data, and participated in the writing of the manuscript.

Zhiwei Peng, Tingtao Zhou, and John F Brady. Activity-induced propulsion of a vesicle. *arXiv preprint arXiv:2112.05904*, 2021. Z. Peng participated in the conception of the project, performed the analysis and simulations, and participated in the writing of the manuscript.

Tingtao Zhou, Zhiwei Peng, Mamikon Gulian, and John F Brady. Distribution and pressure of active Lévy swimmers under confinement. *J. Phys. A: Math. Theor.*, 54(27):275002, jun 2021. doi: 10.1088/1751-8121/ac0509. Z. Peng participated in the conception of the project, developed the simulation software, performed the simulations, analyzed the data and participated in the writing of the manuscript. This paper introduces a new active matter model different from the active Brownian particle model considered in the thesis and thus is not included as part of the thesis.

TABLE OF CONTENTS

LIST OF ILLUSTRATIONS

LIST OF TABLES

Chapter 1

INTRODUCTION

1.1 Swimming at low Reynolds number

Self-propulsion is a core feature of many living organisms. That is, they are able to exhibit locomotion without being driven by external forces—they are active ‘particles’. Animals exhibit various modes of locomotion such as running, jumping, swimming, and flying. The ability to move is essential for the survival of living organisms because it allows them to search for food, find a suitable habitat, and escape predators.

Net motion of a motile organism originates from physical interaction between the organism and its surrounding medium. First, the organism typically has to deform its body or appendages periodically, which constitutes the ‘gait’ of locomotion. An equally important aspect of locomotion is the surrounding medium. For example, human walking involves having at least one foot in contact with the ground at all times (Bianchi et al. 1998; Donelan et al. 2002), the body undulations of fish interact with the surrounding water to generate propulsive thrust (Blake 1983; Lauder and Tytell 2005; Lauder et al. 2007; Lauder 2015), and the flapping flight of birds results from aerodynamics of the surrounding air (DeLaurier 1993; Platzer et al. 2008; Shyy et al. 2010; Chin and Lentink 2016). As walkers move on a substrate or swimmers move through a fluid, they inevitably exert forces on the environment and in turn experience reactive forces due to the environment.

The mechanics of locomotion through fluids at the microscale such as the swimming of microorganisms has received substantial attention in recent decades (Lighthill 1976; Brennen and Winet 1977; Lauga and Powers 2009; Elgeti et al. 2015; Pak et al. 2015; Lauga 2016). The physics governing swimming at the microscale is different from that of swimming/flying of large animals or the terrestrial locomotion of walkers and crawlers. For a typical microorganism such as *E. coli*, which has a characteristic body length $L \sim 10\mu\text{m}$ and a swim speed $U \sim 30\mu\text{m/s}$, the Reynolds number,

$$Re = \frac{\rho U L}{\eta}, \tag{1.1}$$

in water (density $\rho \approx 10^3\text{kg/m}^3$ and shear viscosity $\eta \sim 10^{-3}\text{Pa}\cdot\text{s}$) is on the order of

3×10^{-4}. In this low Re regime, viscous damping is paramount and inertia effects play no role in the locomotion of microswimmers. Swimming or flying strategies adopted by animals in the high Reynolds number regime such as fish and birds are ineffective at the small scale. Any attempt to impart momentum to the surrounding fluid, as is familiar to humans, will be countered by viscous damping at low Re.

In the absence of inertia, the fluid mechanics is governed by the Stokes equations:

$$-\nabla p + \eta \nabla^2 \boldsymbol{u} = \boldsymbol{0}, \tag{1.2}$$

$$\nabla \cdot \boldsymbol{u} = 0, \tag{1.3}$$

where p is the pressure and $\boldsymbol{u}$ is the flow field. Equivalently, the momentum balance (1.2) can be written as $\nabla \cdot \boldsymbol{\sigma} = \boldsymbol{0}$, where $\boldsymbol{\sigma} = -p\boldsymbol{I} + \eta \left[\nabla \boldsymbol{u} + (\nabla \boldsymbol{u})^{\intercal}\right]$ is the Newtonian stress tensor. Equation (1.3) is the incompressibility condition. The linearity and time-independence of the Stokes equations (1.2) and (1.3) lead to kinematic reversibility, which is a fundamental constraint associated with the motion of bodies at zero Reynolds number. Consider the rigid body translation of an arbitrary object with a prescribed velocity $\boldsymbol{U}$ in an otherwise quiescent viscous fluid. If we double the translational velocity $\boldsymbol{U} \rightarrow 2\boldsymbol{U}$, then due to linearity the entire flow and pressure fields are doubled: $\boldsymbol{u} \rightarrow 2\boldsymbol{u}$ and $p \rightarrow 2p$. Similarly, if the translational velocity is reversed, $\boldsymbol{U} \rightarrow -\boldsymbol{U}$, the streamlines of the flow field is identical except that the direction of flow is reversed: $\boldsymbol{u} \rightarrow -\boldsymbol{u}$.

An important consequence of the linearity and time-independence of the Stokes equations is Purcell's "scallop theorem", which states that a reciprocal motion (a deformation exhibiting time-reversal symmetry) cannot generate any net propulsive thrust (Purcell 1977). To bypass the constraint of time-reversibility, microorganisms in nature adopt a variety of propulsion mechanisms including passing planar deformation waves along the flagellum, rotating a helical flagellum, and beating arrays of cilia (short flagella) covering their body surface (Taylor 1951; 1952; Lighthill 1952; Gray and Hancock 1955; Chwang and Wu 1971; Blake 1971; Lighthill 1976; Brennen and Winet 1977; Higdon 1979; Purcell 1997; Rodenborn et al. 2013). Meanwhile, recent advances in micro-fabrication technologies have enabled the development of microscale robots such as synthetic flexible filaments or Janus particles that are capable of swimming at speeds comparable to microorganisms (Dreyfus et al. 2005; Howse et al. 2007; Pak et al. 2011; Williams et al. 2014; Yadav et al. 2015; Maier et al. 2016). These motile microrobots, either synthetic or biohybrid, have been used for the delivery of medical cargo into single cells for the purpose of imaging, diagnostics and therapeutics (Medina-Sánchez et al. 2018; Erkoc et al. 2019; Singh et al. 2019; Bunea and Taboryski 2020).

To illustrate the swimming mechanics of a single microswimmer, we consider the squirmer model first studied by Lighthill (1952) and Blake (1971), which was originally intended to mimic the locomotion of organisms possessing dense arrays of cilia such as *Paramecium*. The squirmer model consists of a body that has a prescribed surface actuation described by the velocity field $\boldsymbol{u}^s(t)$—the swimming gait. The *instantaneous* velocity on the body surface S_B is given by

$$\boldsymbol{u}(\boldsymbol{x} \in S_B) = \boldsymbol{U} + \boldsymbol{\Omega} \times \boldsymbol{x} + \boldsymbol{u}^s, \tag{1.4}$$

which serves as a boundary condition for the Stokes equations (1.2) and (1.3). Here, the angular velocity and the actuation is measured in a reference frame that is attached to an arbitrary point in the squirmer body. The swimming problem is to determine the instantaneous linear and angular velocities $\boldsymbol{U}(t)$ and $\boldsymbol{\Omega}(t)$ for a given $\boldsymbol{u}^s$. To do this, we require the hydrodynamic force ($\boldsymbol{F}^H$) and torque ($\boldsymbol{L}^H$) to vanish because self-propulsion is force- and torque-free. In a viscous fluid as we consider here, the hydrodynamic force and torque are, respectively, given by

$$\boldsymbol{F}^H = \int_{S_B} \boldsymbol{\sigma} \cdot \boldsymbol{n} dS, \tag{1.5}$$

$$\boldsymbol{L}^H = \int_{S_B} \boldsymbol{x} \times (\boldsymbol{\sigma} \cdot \boldsymbol{n})\, dS, \tag{1.6}$$

where $\boldsymbol{n}$ is the unit normal vector of S_B pointing into the fluid. After specifying a far-field condition, which typically is given by $\boldsymbol{u} \to \boldsymbol{0}, p \to 0$, the equations governing the fluid mechanics of swimming is complete.

To satisfy the force- and torque-free condition, one may be tempted to first solve the Stokes equations to obtain the stress tensor $\boldsymbol{\sigma}$ and then carry out the integrals in (1.5) and (1.6). However, an immediate difficulty arises because the boundary condition (1.4) is still unknown and has to be determined as part of the solution. This difficulty can be bypassed using the reciprocal theorem (Stone and Samuel 1996) provided that one can solve the resistance/mobility problem for the swimmer shape. In particular, for a spherical squirmer of radius R, we have

$$\boldsymbol{U} = -\frac{1}{4\pi R^2} \int_{S_B} \boldsymbol{u}^s dS, \tag{1.7}$$

$$\boldsymbol{\Omega} = -\frac{3}{8\pi R^3} \int_{S_B} \boldsymbol{n} \times \boldsymbol{u}^s dS. \tag{1.8}$$

A detailed pedagogical introduction to the reciprocal theorem can be found in Masoud and Stone (2019). We note that, however, the reciprocal theorem does not produce the flow or pressure field outside the squirmer. If the flow field is of interest, one must solve the Stokes equations directly.

Making use of linearity, we can decompose the swimming problem into a thrust problem and a drag problem. In the thrust problem, the swimmer body is held fixed while undergoing surface actuation $\boldsymbol{u}^s$ thus generating thrust (The thrust is also called the 'swim' force.). In the drag problem, the swimmer undergoes rigid body translation with velocity $\boldsymbol{U}$ which induces hydrodynamic drag. The balance of the thrust and the drag constitutes the original swimming problem. Taking the spherical squirmer undergoing tangential surface actuation as an example, the hydrodynamic drag of translation is simply the Stokes drag, $\boldsymbol{F}^D = -6\pi\eta R\boldsymbol{U}$, while the thrust problem gives the swim force

$$\boldsymbol{F}^S = -\frac{3}{2}\frac{\eta}{R}\int_{S_B}\boldsymbol{u}^s dS. \tag{1.9}$$

One can see that the balance

$$\boldsymbol{F}^S + \boldsymbol{F}^D = \boldsymbol{0} \tag{1.10}$$

recovers equation (1.7).

1.2 Active colloids

So far we have outlined the fundamentals of swimming of a *single* organism in the low Re regime. More recently, the focus has been on the macroscopic or collective behavior of swimming microorganisms or active particles. While the concept of 'activity' comes most naturally from living microorganisms, it can be easily extended to non-living objects. Self-propulsion of synthetic swimmers can be achieved using a multitude of mechanisms including electrophoresis (Paxton et al. 2006), self-diffusiophoresis (Theurkauff et al. 2012; Würger 2015), thermophoresis (Baraban et al. 2013), flexible nanowire motors (Pak et al. 2011), bubble propulsion (Gibbs and Zhao 2009; Wang and Wu 2014), and so on. In most cases, these synthetic swimmers mimic the size (μm) and swim speeds (μm/s) of living microorganisms.

Owing to their ability to self-propel, active particles (whether living or synthetic) are out of thermal equilibrium; they exhibit a cascade of interesting behaviors including accumulation at confining boundaries (Wensink and Löwen 2008; Li and Tang 2009; Elgeti and Gompper 2013; Yan and Brady 2015b), Casimir effect

(Ray et al. 2014; Kjeldbjerg and Brady 2021), self-assembly (Mallory et al. 2018), upstream swimming in pressure-driven channel flows (Hill et al. 2007; Kaya and Koser 2012; Zöttl and Stark 2013; Peng and Brady 2020), motility-induced phase separation (Cates and Tailleur 2015; Takatori and Brady 2015), and the existence of a steady-state spontaneous flow in the absence of any external forces (Lushi et al. 2012; Guo et al. 2018). Most of these phenomena are universal to active particles; these behaviors do not rely on the underlying propulsion mechanism (e.g., chemical self-propulsion versus biological self-propulsion) but result from physical interactions among active particles and/or with the environment (e.g., the solvent or boundaries, *et cetera*.) This important observation allows us to probe the physics behind such behaviors using a minimal model—the active Brownian particle (ABP) model (Romanczuk et al. 2012).

In the context of this thesis, we consider the dynamics of viscous suspensions of active Brownian particles. In essence, ABPs are active colloidal particles and we refer to the viscous suspension of ABPs as active colloidal suspensions (or colloidal active matter).

1.2.1 The active Brownian particle model

Suppose that the surface actuation of a spherical squirmer is axisymmetric with the axis of symmetry denoted by $\boldsymbol{q}(t)$ ($|\boldsymbol{q}| = 1$) and consider an expansion of the slip velocity in the irreducible spherical tensor harmonics given by

$$\boldsymbol{u}^s(\boldsymbol{x} \in S_B) = A_1\boldsymbol{q} + A_2\boldsymbol{q}\times\boldsymbol{n} + A_3\left(\boldsymbol{q}\boldsymbol{q} - \frac{1}{3}\boldsymbol{I}\right)\cdot\boldsymbol{n} + A_4\boldsymbol{q}\cdot\left(\boldsymbol{n}\boldsymbol{n} - \frac{1}{3}\boldsymbol{I}\right) + \cdots, \tag{1.11}$$

where A_i ($i = 1, 2...$) are numerical coefficients having dimensions of velocity. Using (1.9), we obtain the thrust as $\boldsymbol{F}^S = -\zeta R A_1 \boldsymbol{q}$, where $\zeta = 6\pi\eta R$ is the Stokes drag coefficient of a sphere. Setting $A_1 = -U_s$, equation (1.10) becomes

$$\zeta U_s \boldsymbol{q} - \zeta \boldsymbol{U} = \boldsymbol{0}. \tag{1.12}$$

In other words, the instantaneous velocity $\boldsymbol{U} = U_s\boldsymbol{q}$: U_s is the swim speed and $\boldsymbol{q}$ is a unit vector in the direction of swimming. The above analysis is performed under the assumption that the expansion (1.11) is allowed and that an isolated squirmer is considered. We note that the swim force for general swimmers or in the presence of other swimmers/particles is more involved and we refer the reader to the work of Yan and Brady (2015a) and Burkholder and Brady (2018).

The above analysis reveals the first ingredient of the ABP model—the self-propulsion characterized by a constant swim speed U_s. Because the ABPs are at the colloidal scale, they experience random fluctuations from the solvent. Furthermore, motile bacteria such as *E. coli* do not swim in straight lines but instead has discrete tumbling events in which the direction of swimming changes abruptly [1]. To take into account either thermal or biological fluctuations, we assume that the ABPs undergo translational and rotational Brownian motion—which are the second ingredient of the ABP model.

The inclusion of Brownian motion renders the system stochastic and thus a statistical mechanical approach is adopted. To this end, we consider the probability density $P(\boldsymbol{x}, \boldsymbol{q}, t)$ of finding the ABP at position $\boldsymbol{x}$, orientation $\boldsymbol{q}$ at time t. Because the probability is conserved, P is governed by the Smoluchowski equation, which reads

$$\frac{\partial P}{\partial t} + \nabla \cdot \boldsymbol{j}_T + \nabla_R \cdot \boldsymbol{j}_R = 0, \tag{1.13}$$

where the translational and rotational fluxes are, respectively,[2]

$$\boldsymbol{j}_T = U_s \boldsymbol{q} P - D_T \nabla P, \tag{1.14}$$

$$\boldsymbol{j}_R = -D_R \nabla_R P. \tag{1.15}$$

Here, D_T is the translational diffusivity and D_R is the rotational diffusivity. An important length scale for ABPs is the run or persistence length, $\ell = U_s \tau_R$, where $\tau_R = 1/D_R$ is the reorientation time.

The global conservation condition reads

$$\int_V d\boldsymbol{x} \int_{|\boldsymbol{q}|=1} P d\boldsymbol{q} = 1, \tag{1.16}$$

where V is the physical domain ($\boldsymbol{x} \in V$).

In contrast to passive Brownian particles, the self-propulsion of active particles introduces a coupling between their rotational and translational dynamics via the swimming motion. That is, even for an isolated active Brownian sphere (which is geometrically isotropic), one must track both its orientation and position. One manifestation of such a coupling is the enhanced long-time self-diffusivity beyond the translational diffusivity D_T, which for an ABP with constant properties in free space is $D^{\text{eff}} = D_T + D^{\text{swim}}$, where $D^{\text{swim}} = U_s^2 \tau_R / 6$ (in 3D) is the swim diffusivity.

---

[1] There is a run-and-tumble particle (RTP) model that intends to mimic the behavior of bacteria motion more closely. For many situations, its dynamics is equivalent to that of the ABPs (Cates and Tailleur 2013; Solon et al. 2015).

[2] See appendix A for a discussion of the Smoluchowski equation and its moments.

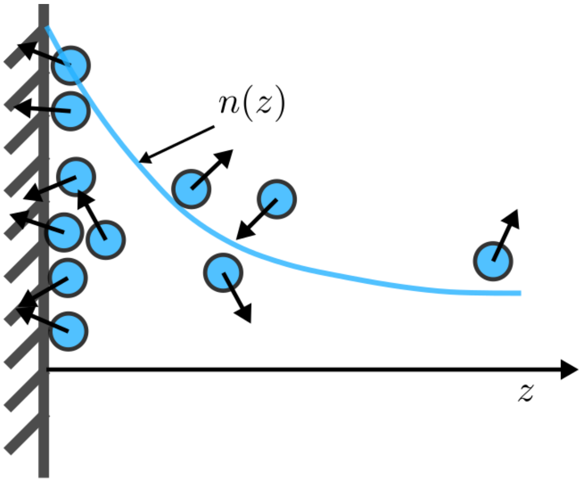

Figure 1.1: Schematic of ABPs on one side of an infinite planar wall ($z = 0$) and the number density distribution.

1.2.2 Pressure in active colloids

Consider a body immersed in a *dilute* suspension of active colloids. The net force the active colloids exert on the body is given by (Brady 1993; Squires and Brady 2005)

$$\boldsymbol{F} = -k_B T \int_{S_B} n(\boldsymbol{x}, t)\boldsymbol{n} dS, \tag{1.17}$$

where S_B is the surface of the body, $\boldsymbol{n}$ is the unit normal vector of S_B that is pointing into the suspension, and

$$n(\boldsymbol{x}, t) = \int_{|\boldsymbol{q}|=1} P d\boldsymbol{q} \tag{1.18}$$

is the number density of active colloids. To understand the force on an immersed body, we consider an infinite flat plate with normal in z-direction (See figure 1.1 for a schematic.), which has been solved by Yan and Brady (2015b).

From (1.17), the force per unit area or pressure on the wall is just the osmotic pressure, $\Pi^w_{\text{osmo}} = n^w k_B T$, where n^w is the number density on the wall. Yan and Brady (2015b) showed that

$$\frac{n^w}{n^\infty} = 1 + \frac{k_s T_s}{k_B T} > 1, \tag{1.19}$$

where $k_B T = \zeta D_T$ is the thermal energy, $k_s T_s = \zeta D^{\text{swim}}$ is the 'activity' (Takatori et al. 2014), and n^∞ is the bulk ($z \to \infty$) number density. As shown in figure 1.1, active colloids accumulate at the wall (a no-flux boundary) and the number density decays from n^w to n^∞ as one moves away from the wall. Using equation (1.19), we can relate the pressure at the wall to that at infinity:

$$\Pi^w_{\text{osmo}} = n^w k_B T = n^\infty k_B T + n^\infty k_s T_s = \Pi^\infty_{\text{osmo}} + \Pi^\infty_{\text{swim}}, \tag{1.20}$$

where $\Pi^\infty_{\text{swim}} = n^\infty k_s T_s$ is the so-called swim pressure (Takatori et al. 2014). Therefore, the osmotic pressure on the wall is the sum of the osmotic pressure and the swim pressure far away in the bulk. We note that the activity of active colloids does not introduce a new mechanism for pressure generation beyond that of the osmotic pressure. The swim pressure appears when one wishes to isolate the value of the osmotic pressure at a wall Π^w_{osmo} and relate it to quantities far away.

For many colloidal active matter systems, $k_s T_s / k_B T \gg 1$. In this high activity or athermal limit, we have

$$\Pi^w_{\text{osmo}} = \Pi^\infty_{\text{swim}}. \tag{1.21}$$

In other words, the osmotic pressure at the wall is given by the swim pressure far away. For an arbitrary immersed object, the above equation can be generalized to include the effect of the boundary curvature (Yan and Brady 2015b; 2018; Peng et al. 2021). We note that the total pressure (osmotic plus the fluid pressure p_f), $P = p_f + n k_B T$, does not contain the swim pressure.

1.3 Thesis outline

In this thesis, I investigate the transport and microrheology of active colloids. As shown in the previous section, active colloids under confinement exhibit wall accumulation. Here, I consider how external flow (or forcing) in addition to confinement affect the dynamics of active colloids. This is particularly useful because many biological active processes happen in the presence of fluid flows and under confinement.

1.3.1 Transport of active colloids

Locomotion of active particles such as motile bacteria or phoretic swimmers often takes place in the presence of applied flows and confining boundaries. Interactions of these active swimmers with the flow environment are important for the understanding of many biological processes, including infection by motile bacteria (Siitonen and Nurminen 1992; Kao et al. 2014) and the formation of biofilms (Rusconi et al. 2010; Kim et al. 2014). Recent experimental and theoretical work have shown that active particles in a Poiseuille flow exhibit interesting dynamics including accumulation at the wall and upstream swimming (Bechinger et al. 2016).

In Chapter 2, I develop a generalized Taylor dispersion theory to study the effective transport (average drift and effective longitudinal dispersion) of active colloids in a pressure-driven channel flow. In this problem, the active colloids experience both channel confinement and the background Poiseuille flow, the interplay of which gives rise to interesting behaviors such as upstream swimming (i.e., rheotaxis) and non-monotonic dispersion as a function of the flow speed. In our model, the active colloids are considered as point-like particles.

Many biological microswimmers are non-spherical. For example, the motile bacteria *E. coli* can be better represented by ellipsoidal particles than spherical ones. In Chapter 3, the dynamics and transport of ellipsoidal active particles in channel flows are studied. One difficulty in this effort is the boundary interaction. For spherical particles, one can just use the no-flux boundary condition at the wall; in this case the wall simply exerts a force to keep the particle from penetrating the wall. When the particle is non-spherical, however, the collision between it and a planar wall can induce a torque on the particle. As a result, when an ellipsoid approaches the wall at an oblique angle, the wall torque tends to rotate the particle and align it with the wall. It is shown that the inelastic collision between an ellipsoid and a planar wall can be formulated as a complementarity problem. Coupling this collision-resolution method with Brownian dynamics simulations, the dynamics and transport of active ellipsoids can be studied.

1.3.2 Microrheology of active colloids

The macroscopic (bulk) rheological response of active colloidal suspensions is distinct from that of passive colloids. In particular, experiments (López et al. 2015; Chui et al. 2021) and theoretical studies (Hatwalne et al. 2004; Haines et al. 2009; Saintillan 2010; Ryan et al. 2011; Loisy et al. 2018) have shown that the low-Pe shear (weak shear) viscosity of dilute active suspensions consisting of anisotropic and pusher (tail-actuated) microswimmers can be zero—or even *negative*. This apparent negative viscosity has been attributed to the interaction between the hydrodynamic stresslet induced by the force dipoles of an active particle and the applied simple shear flow.

In the context of biological active matter such as cellular environments, the active ‘particles’ are often subjected to spatially localized cues and biochemical signals rather than to bulk flow or body forces. These localized behaviors lead to an inherently heterogeneous intracellular environment with differing material properties such as spatial variations in viscosity and elasticity. In addition, classical bulk rheology equipment cannot be used to probe the microenvironment inside individual living cells without disrupting their mechanical structure. To address such challenges, microrheological techniques have been developed. In microrheology, the local rheological properties such as viscoelasticity of a complex fluid are inferred from the free (thermal) or forced motion of ‘probe’ particles. The probes can be either embedded colloidal particles or tagged organelles and molecules existing in the biological material. The study of the deformation or flow of biological materials at small length scales has been termed bio-microrheology and deemed a frontier in microrheology (Weihs et al. 2006). Indeed, particle-tracking microrheology has been widely used in experimental measurements to characterize the rheological properties inside living cells.

Theoretical machinery developed for forced-probe microrheology of colloidal suspensions focused on either constant-force (CF) or constant-velocity (CV) probes while in experiments neither the force nor the kinematics of the probe is fixed. More importantly, the constraint of CF or CV introduces a difficulty in the meaningful quantification of the fluctuations of the probe due to a thermodynamic uncertainty relation. It is known that for a Brownian particle trapped in a harmonic potential well, the product of the standard deviations of the trap force and the particle position is dk_BT in d dimensions with k_BT being the thermal energy. As a result, if the force (position) is not allowed to fluctuate, the position (force) fluctuation becomes infinite. To allow the measurement of fluctuations, in Chapter 4 I consider a microrheology model in which the embedded probe is dragged along by a moving harmonic potential so that both its position and the trap force are allowed to fluctuate. A theoretical framework is developed using the Smoluchowski equation governing the dynamics of an active colloidal suspension. It is shown that this model can be reduced to several important problems such as tracer diffusion, the CV/CF microrheology, and pair-correlation when appropriate limits are taken.

Compared to bulk rheology, study of the microrheology of active colloids are very recent and many questions remain to be answered. In particular, is there a microrheological analogue of the negative bulk shear viscosity? If a negative microviscosity exists, what is the mechanism for such a behavior?

In Chapter 5, I study the microrheology of active colloids by driving a constant-velocity (CV) probe through a bath of active colloids. The external force required to maintain the steady probe motion compared to the Stokes drag law defines a microviscosity. It is shown that the microviscosity of active colloids is reduced in the low probe speed regime in the absence of hydrodynamic interactions. If the probe speed is large, the swimming motion of the active colloids is obscured and one recovers the microviscosity of *passive* colloids. Though active colloids exhibit a swim-thinning behavior, the microviscosity is always positive.

It is then shown that hydrodynamic interactions are important in order to obtain a negative microviscosity. To this end, two mechanisms that can lead to a negative microviscosity are studied. First, the dipolar disturbance flow induced by a puller particle in front of the probe acts to pull the probe forward, which facilitate the probe motion. Second, the disturbance flow of the translating probe can induce negative microviscosity by transporting active colloids to the back of the probe; once the active colloids are in the back, they can help 'push' the probe forward.

To probe the viscoelastic behavior of active colloids, in Chapter 6 an oscillatory probe motion is considered. For small-amplitude oscillations, the microviscoelasticity of active colloids is computed.

1.3.3 Activity-induced propulsion

In the microrheology problem, a probe particle is immersed in an active colloidal suspension and the force on the probe is measured. The advection of the probe introduces front-back asymmetry in the suspension microstructure, which leads to a net force on the probe.

To exploit this notion of asymmetry, in Chapter 7 I propose a novel osmotic propeller in which active colloids are confined inside a vesicle with a semi-permeable membrane. The vesicle is immersed in water and the membrane only allows water to pass through while the active colloids cannot escape the vesicle. If an asymmetric osmotic pressure on the interior wall of the membrane can be generated, the vesicle is able to exhibit net motion. A theoretical framework is developed and analyzed to show that indeed propulsion is possible.

The key ingredient in this model is the generation of an asymmetric number density (the osmotic pressure is nk_BT) distribution inside a spherical vesicle. Previous works have shown that a spatial variation in the swim speed leads to a spatial variation in the number density of active particles (Schnitzer 1993; Tailleur and Cates 2008; Row and Brady 2020). By tuning the swim speed distribution of ABPs confined inside the vesicle, a spherically asymmetric density distribution can emerge and lead to net motion of the vesicle. The second approach considered is an external orienting field in which the orientational dynamics of active colloids is biased.

Chapter 2

UPSTREAM SWIMMING AND TAYLOR DISPERSION

Locomotion of self-propelled particles such as motile bacteria or phoretic swimmers often takes place in the presence of applied flows and confining boundaries. Interactions of these active swimmers with the flow environment are important for the understanding of many biological processes, including infection by motile bacteria and the formation of biofilms. Recent experimental and theoretical work have shown that active particles in a Poiseuille flow exhibit interesting dynamics including accumulation at the wall and upstream swimming. Compared to the well-studied Taylor dispersion of passive Brownian particles, a theoretical understanding of the transport of active Brownian particles (ABPs) in a pressure-driven flow is relatively less developed. In this Chapter, employing a small wavenumber expansion of the Smoluchowski equation describing the particle distribution, we explicitly derive an effective advection-diffusion equation for the cross-sectional average of the particle number density in Fourier space. We characterize the average drift (specifically upstream swimming) and effective longitudinal dispersion coefficient of active particles in relation to the flow speed, the intrinsic swimming speed of the active particles, their Brownian diffusion and the degree of confinement. In contrast to passive Brownian particles, both the average drift and the longitudinal dispersivity of ABPs exhibit a non-monotonic variation as a function of the flow speed. In particular, the dispersion of ABPs includes the classical shear-enhanced (Taylor) dispersion and an active contribution called the swim diffusivity. In the absence of translational diffusion, the classical Taylor dispersion is absent and we observe a giant longitudinal dispersion in the strong flow limit. Our continuum theory is corroborated by a direct Brownian dynamics simulation of the Langevin equations governing the motion of each ABP.

This Chapter includes content from our previously published article:

- Zhiwei Peng and John F. Brady. Upstream swimming and Taylor dispersion of active Brownian particles. Phys. Rev. Fluids, 5:073102, Jul 2020. doi: 10.1103/PhysRevFluids.5.073102

2.1 Introduction

Transport and mixing within suspensions of swimming micro-organisms are important for the understanding of many biological and industrial processes, such as infection by motile bacteria (Siitonen and Nurminen 1992; Kao et al. 2014) or the formation of biofilms (Rusconi et al. 2010; Kim et al. 2014). Different from passive particles, the ability of active swimmers to self-propel gives rise to interesting dynamics including accumulation at confining boundaries and upstream swimming in the presence of a pressure-driven flow (Bechinger et al. 2016).

The transport of passive matter (e.g., diffusing solute) that experiences molecular diffusion and fluid advection in a Poiseuille flow has been extensively studied since the seminal work of Taylor (Taylor 1953; 1954a;b), who demonstrated that the effective dispersion coefficient in the direction of flow is enhanced compared to the bare molecular diffusivity. Shortly after, Aris (1956) underpinned Taylor's analysis with a theoretical framework based on longitudinal moments of the solute distribution function. This phenomenon of enhanced longitudinal spreading, often referred to as Taylor (or Taylor-Aris) dispersion, results from the coupling of molecular diffusion in the transverse direction and advection in the longitudinal direction. To understand the interaction between these two separate mechanisms for solute transport, it is helpful to first consider advection alone, and then to include the effect of molecular diffusion. In the absence of molecular diffusion, a point-sized particle introduced into the flow simply moves downstream along the streamline at that location. The presence of molecular diffusion, on the other hand, enables the particle to migrate across streamlines and then immediately be advected downstream with different velocities. This process represents a random walk and leads to an advective contribution to the longitudinal dispersion in addition to the molecular diffusivity. In a random walk process, the diffusivity scales as l^2/τ, where l is the step size and τ is the decorrelation time. Consider a Brownian solute with diffusivity D_T in a pressure-driven channel flow with characteristic width H and centerline speed U_f. The decorrelation time is purely Brownian and given by $\tau \sim H^2/D_T$ while the step size is due to advection in this time: $l \sim U_f \tau$. As a result, we have $(D^{\text{eff}} - D_T)/D_T \sim Pe^2$, where D^{eff} is the effective longitudinal dispersivity and $Pe = U_f H/D_T$ is the Péclet number.

One can also rationalize the classical Taylor dispersion from a macroscopic point of view. Suppose that initially a diffusing solute is introduced at a small segment of the channel flow with a uniform concentration (see figure 2.1 for a schematic). At

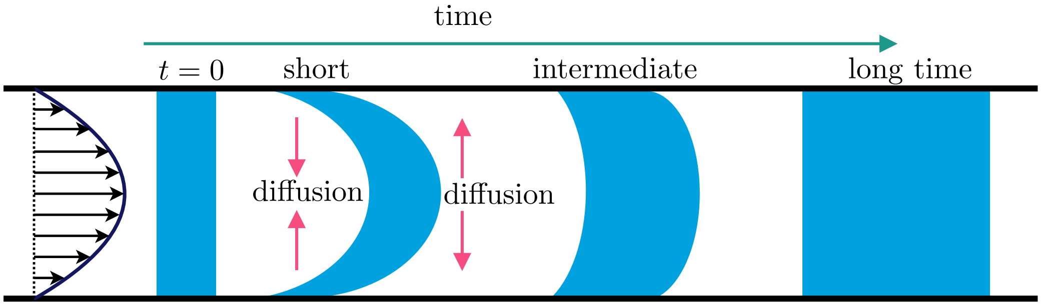

Figure 2.1: Schematic of the Taylor dispersion process of passive matter in a pressure driven flow.

times shorter than the diffusive time scale H^2/D_T, the non-uniform fluid advection generates a concentration gradient across the channel, which induces a diffusive flux of the material transverse to the direction of flow. At long times, the concentration in the transverse direction becomes uniform again due to molecular diffusion. In this long-time asymptotic limit, the cross-sectional average concentration is governed by an effective one-dimensional advection-diffusion equation. The drift velocity in this equation is simply the cross-sectional average fluid velocity, while the effective Taylor dispersivity is greater than the molecular diffusivity.

During the past half century, the original analysis by Taylor and Aris has been extended to accommodate a wide class of dispersion problems including complex geometries (Brenner 1980; Dorfman and Brenner 2002) and chemical reactions (Shapiro and Brenner 1986; 1987). In particular, a generalized Taylor dispersion theory (GTDT) has been developed (Frankel and Brenner 1989). GTDT provides a systematic scheme to derive the coarse-grained transport equation starting from the probability density function describing the motion of a Brownian tracer in its phase space. A detailed discussion on the application of GTDT to material dispersion can be found in the book by Brenner and Edwards (2013).

In contrast to passive tracers, the study of the transport of active microswimmers that self-propel is more recent and their dynamics is less well understood. To capture the essential physics of a microswimmer on a coarse-grained level, the active Brownian particle (ABP) model is often used. An ABP self-propels with a fixed intrinsic speed U_s and undergoes translational and rotational Brownian motion with diffusivities D_T and D_R. We note that in modeling the locomotion of swimming microorganisms the diffusivities are typically biological rather than thermal in origin. The rotary diffusion describes the random reorientation of microorganisms such as tumbling. The translational diffusivity can be interpreted as a simple model representing the fluctuation of the center-of-mass position during the flagellar bundling or unbundling process. In other words, D_T and D_R are independent quantities and not constrained by the fluctuation-dissipation theorem. Due to rotary Brownian motion, the swimming direction of an ABP relaxes over the reorientation time scale $\tau_R = 1/D_R$. One can define a run length $\ell = U_s \tau_R$ that characterizes the persistence of swimming in a given direction. The directed swimming persists at short time ($t \ll \tau_R$) and one observes ballistic motion. At times much larger than τ_R, the swimming motion becomes a random walk due to Brownian reorientation. This active random walk can be characterized by an effective diffusivity $D^{\text{swim}} \sim \ell^2/\tau_R \sim U_s^2 \tau_R$ called the swim diffusivity. A detailed calculation gives $D^{\text{swim}} = U_s^2 \tau_R/2$ in two-dimensional unbounded space (Berg 1993). This implies that the long-time dispersion coefficient of ABPs is enhanced, $D^{\text{eff}} = D_T + D^{\text{swim}}$ (Takatori et al. 2014; Takatori and Brady 2014). The swim-enhanced dispersion originates from the coupling of diffusion in orientational space to the translational via self-propulsion, which is a unique signature of active matter systems.

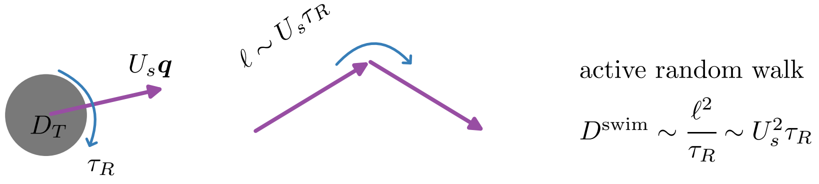

Figure 2.2: Schematic of an ABP in an unbounded domain with no background flow and its long-time ($t \gg \tau_R$) active random walk process. The swimming direction is denoted by a unit vector $\boldsymbol{q}$.

When placed under confinement, such as in a channel, ABPs tend to accumulate at the wall. Unlike non-interacting Brownian particles in thermal equilibrium that exhibits a uniform density distribution, ABPs can spontaneously generate regions of higher density under geometric confinement. This boundary accumulation is another distinct feature of active matter, which is ubiquitous in biological processes involving motile bacteria or swimming spermatozoa. Exploiting this behavior, Sokolov et al. (2010) showed that a motile bacteria suspension can power microscopic gears with asymmetric teeth. Interestingly, this boundary accumulation phenomenon was first observed decades ago by Rothschild (1963), who measured a non-uniform concentration of swimming bull spermatozoa in a glass chamber. More recently, experiments by Berke et al. (2008) reported the same accumulation phenomenon with swimming *Escherichia coli* (*E. coli*) confined between two glass plates. Rothschild postulated that wall accumulation might originate from hydrodynamic interaction of swimmers with the wall. Berke et al. pursued this idea and provided a theoretical model to explain their experimental results. On the other hand, studies neglecting hydrodynamic interaction between swimmers and boundary also observed wall accumulation (Li and Tang 2009; Li et al. 2011; Costanzo et al. 2012; Elgeti and Gompper 2013; Yan and Brady 2015a; 2018). These studies suggest that wall accumulation can be understood from a purely kinematic perspective while hydrodynamic interaction only modifies this behavior quantitatively. That is, owing to persistent self-propulsion, a swimmer hitting the boundary maintains its orientation for a finite time τ_R until it rotates away via Brownian reorientation. Conversely, swimmers pointing away from the boundary simply swim into the bulk. As a result, there is an accumulation of swimmers near the boundary with a net orientation or polar order pointing into the boundary.

To gain a quantitative understanding, consider ABPs confined between two parallel plates separated by a distance H. Before considering the number density and polar order distribution, it is helpful to recognize the three length scales in this problem: the run length ℓ, a microscopic length $\delta = \sqrt{D_T \tau_R}$ that characterizes the distance an ABP travels by diffusion within the reorientation time, and the channel width H. Two dimensionless groups, ℓ/H and ℓ/δ, can thus be defined. The dimensionless quantity ℓ/δ compares the distance traveled by swimming to translational diffusion in τ_R, and thus characterizes the activity level of ABPs. The second parameter ℓ/H quantifies the strength of confinement. In the limit $\ell/H \ll 1$, an ABP can travel its full run length without colliding with the wall. If $\ell/H \gg 1$, the swimming trajectories of ABPs are frequently disrupted by the wall. We use orientational moments, in particular number density (n^0) and polar order in the transverse direction (m_y^0) as a function of the transverse coordinate y, to quantify the effect of confinement. The polar order m_y^0 characterizes the amount of particles pointing in the $\pm y$ direction (See section2.2 for the mathematical definition and formulation). Using a vanishing nematic order closure to the Smoluchowski equation, Yan and Brady (2015b) obtained the number density and polar order distribution of ABPs in several confinement geometries. For ABPs between two parallel plates in 2D, it is shown that

$$\frac{n^0(y)}{\overline{n}} = 1 + \frac{1}{2}\left(\frac{\ell}{\delta}\right)^2 \frac{\cosh(\lambda y)}{\cosh(\lambda H/2)}, \tag{2.1}$$

$$\frac{m_y^0(y)}{\overline{n}} = \frac{1}{2}\lambda\ell\frac{\sinh(\lambda y)}{\cosh(\lambda H/2)}. \tag{2.2}$$

Here, $y \in [-H/2, H/2]$ is the transverse coordinate, n^0 is the number density, m_y^0 is the polar order in the transverse direction and $\lambda = \sqrt{1 + \frac{1}{2}(\ell/\delta)^2}/\delta$ is the inverse screening length. To be consistent with notation in this Chapter, the average concentration $\overline{n}$ is obtained such that $(1/H)\int_{-H/2}^{H/2} n^0 dy = 1$. To prevent ABPs from penetrating the wall, the swimming flux into the wall ($U_s m_y^0$) is balanced by a diffusive flux ($-D_T dn^0/dy$) away from the wall (See equation (2.51) in the appendix.). This balance dictates that the screen length λ^{-1} is proportional to the microscopic length δ and depends on the activity ℓ/δ. For a given confinement strength (ℓ/H), the accumulation boundary layer becomes thinner as activity (ℓ/δ) increases. Since $\delta/H = \ell/H(\ell/\delta)^{-1}$, the boundary layers becomes thinner as confinement ℓ/H decreases for a fixed ℓ/δ. Therefore, we observe a sharp accumulation boundary layer for $\ell/H \ll 1$. As ℓ/H increases, the two boundary layers at the top and bottom walls merge and a more uniform number density profile is observed. The variation of the number density profile as a function of ℓ/H is shown in figure 2.3(a). Strong accumulation of ABPs at the wall is accompanied by a net polar order as seen in figure 2.3(b) for $\ell/H = 0.1$. The case of passive Brownian particles, which has a uniform number density, can be obtained by setting $\ell = 0$.

Due to the linear geometry of the channel, we can obtain the effective longitudinal dispersion coefficient by a simple physical argument. Because the Brownian kicks in each direction are independent, the confinement in the transverse direction does not affect motion in the longitudinal direction. We expect the effective longitudinal dispersion to be identical to that in free space, $D^{\text{eff}}/D_T = 1 + \frac{1}{2}(\ell/\delta)^2$. In figure 2.3(c), we show D^{eff}/D_T as a function of ℓ/δ obtained from both finite element simulations (circles) and moment equations (blue solid line). These results agree well with the free space dispersivity given by the red dashed line. We remark that confinement can have an effect on longitudinal dispersion if the channel width is non-uniform.

The application of an external flow in the channel further complicates the transport process of ABPs. First, ABPs are now advected by the flow in addition to its self-advection. Second, the orientational dynamics of ABPs are coupled to the local

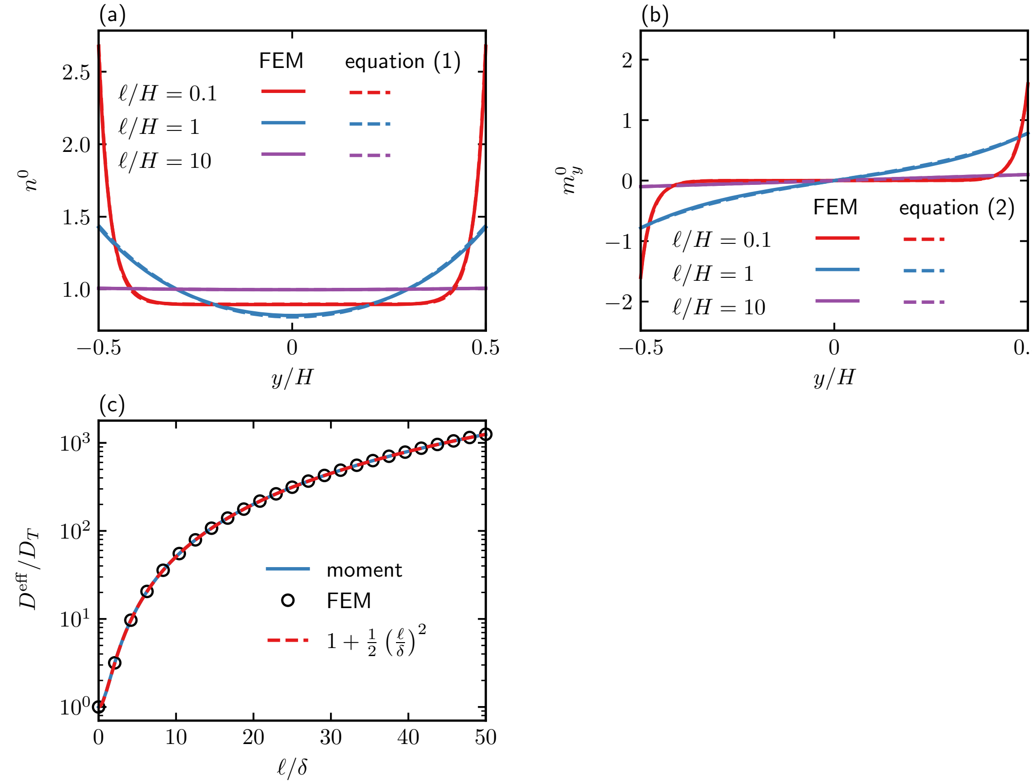

Figure 2.3: (a) Number density n^0 as a function of the transverse coordinate y for $\ell/\delta = U_s\tau_R/\sqrt{D_T\tau_R} = 2$ and different confinement strengths: $\ell/H = U_s\tau_R/H = \{0.1, 1, 10\}$. (b) Polar order in the transverse direction m_y^0 as a function of the transverse coordinate y for $\ell/\delta = 2$ and different confinement strengths. (c) Effective longitudinal dispersion coefficient D^{eff}/D_T as a function of activity ℓ/δ. Circles are results from finite element simulations and the solid line is the solution from moment equations. The free space effective dispersivity of ABPs is denoted by the dashed line. In all three panels, the flow is absent. Refer to section 2.2 for details on FEM and moment equations.

fluid shear, which varies spatially in a quadratic flow. One manifestation of such a coupling effect is the upstream swimming of motile particles in a pressure-driven flow. Here, we are speaking in terms of upstream swimming in a laboratory-fixed frame rather than that relative to the downstream flow. Put differently, a swimmer can overcome the downstream advection with some excess speed to move upstream. Koser and coworkers (Hill et al. 2007; Kaya and Koser 2009) observed upstream swimming with *E. coli* in a microfluidic channel flow and proposed a mechanism for upstream motility involving chirality of the flagella and hydrodynamic interaction with the wall. A later study by Kaya and Koser (2012) systematically measured the swim speed of *E. coli* and reported a transition between upstream and downstream motion. Below a critical but nonzero flow speed, *E. coli* were found to swim upstream. For strong flow, the swimming motion is dominated by fluid advection and net downstream motion is observed. In a recent work by Kantsler et al. (2014), mammalian sperm cells are also found to exhibit upstream motility.

Various theoretical models have been proposed to explain the swimming dynamics of microorganisms in flow, many of which include the effect of fluid shear, body shape asymmetry, flagellar chirality, steric and/or hydrodynamic interaction with the wall, and so forth (Nash et al. 2010; Zöttl and Stark 2012; Costanzo et al. 2012; Kantsler et al. 2014; Uspal et al. 2015; Ezhilan and Saintillan 2015; Junot et al. 2019; Mathijssen et al. 2019). These models are able to produce, at least qualitatively, upstream motion similar to those observed in experiments. On the other hand, Ezhilan and Saintillan (2015) implemented a simpler model, which consists of non-interacting slender ABPs, to investigate the effect of flow on transport of microswimmers. Using numerical and asymptotic solutions to the Smoluchowski equation governing particle conservation, they investigated the distribution of ABPs across the channel systematically and predicted net upstream swimming. In their study, the focus is on mildly active ABPs that are moderately confined: $\ell/\delta = \sqrt{6}$ (≈ 2.45) and $\ell/H \leq 2$.

Previous work on the dispersion of active particles in flow has examined suspensions of gyrotactic micro-organisms (Pedley and Kessler 1990; Hill and Bees 2002; Manela and Frankel 2003; Bees and Croze 2010; Croze et al. 2013; Bearon et al. 2011) and chemotactic run-and-tumble bacteria (Bearon 2003). Due to asymmetry in mass distribution, gyrotactic swimmers experience a gravitational torque in addition to the viscous torque from the local fluid vorticity. The balance between viscous and gravitational torques leads to a preferred orientation of the particles and thus a non-uniform particle distribution across the channel. More recently, Chilukuri et al. (2015) investigated the dispersion of flagellated swimming micro-organisms in planar Poiseuille flow using Brownian dynamics (BD) simulation. In their work, a flagellated swimmer is represented by two beads connected by a stiff spring. They focused on the effect of flow speed on the dispersion of very active particles under moderate to strong confinement with $\ell/\delta = 80$ and $\ell/H = \{2.5, 4, 10\}$. It is shown that the longitudinal dispersivity exhibits a non-monotonic variation as a function of the flow speed with a minimum obtained when the flow speed is comparable to the self-propulsion speed. Intuitive physical scaling arguments were used to qualitatively explain the dispersion behavior in the weak and strong flow limits. Interestingly, a similar non-monotonic dispersion behavior is predicted by Alonso-

Matilla et al. (2019) in the context of ABPs in external flow through periodic porous media. Dehkharghani et al. (2019) studied the dispersion of swimming bacteria in flow through a microfluidic lattice consists of a periodic array of circular pillars using both experiments and computer simulation. They showed that the external flow hinders transverse dispersion and enhances longitudinal dispersion of active particles with no translational diffusion beyond the Taylor dispersion of passive Brownian particles. Using the same ellipsoidal ABP model as Ezhilan and Saintillan (2015), Jiang and Chen (2019) studied the dispersion of active particles in confined unidirectional flows. The longitudinal dispersion of ABPs are related to the physical space moments of the probability density function of an ABP based on the GTDT. In this work, they solved the resulting equations numerically and presented the dispersivity for $\ell/\delta = \sqrt{6}$ and $\ell/H = 1$.

In view of the above discussion, it is clear that upstream swimming is almost certainly universal to active particles and transcends some of the details of the specific mathematical model or microorganism used. This suggests an underlying mechanism shared among different models that is fundamental and responsible for upstream swimming, while additional details represent only a correction for the quantitative behavior. Though the dispersion of active particles in flow has been studied much less compared to upstream swimming, the same argument should apply. Indeed, as an example, Chilukuri et al. (2015) showed that hydrodynamic interaction with the wall does not qualitatively alter the longitudinal dispersion of their beads-spring swimmers. Therefore, we believe that there is value in studying the dynamics of active particles in flow with a model that is simple yet able to capture the interesting advective-diffusive behavior discussed above. To this end, we consider spherical ABPs suspended in a Poiseuille flow between two parallel plates in 2D. Our study ignores hydrodynamic interaction with the wall. In appendix 2.8, we discuss the effect of non-spherical shape that might be relevant to microorganisms such as *E. coli*. We also assume that the particle suspension is dilute so that the background flow is not affected by the suspended ABPs and excluded-volume interaction between particles is irrelevant.

In this work, we show that both upstream swimming and non-monotonic dispersion as a function of the flow speed are recovered using the spherical ABP model. Upstream swimming can be understood as a result of channel confinement and rotation by the flow alone. Particles at the wall are rotated towards the upstream direction owing to the fluid vorticity that reaches its maximum at the wall. Once aligned against the flow, self-propelled particles are able to swim upstream because the fluid velocity vanishes at the wall. Furthermore, ABPs accumulate at the wall when the flow is weak compared to self-propulsion. In the weak flow regime, strong upstream swimming is observed. As the flow speed increases, the intrinsic swim speed becomes sub-dominant and the number density of ABPs becomes more uniform across the channel. This leads to a transition from net upstream motion to downstream motion as the flow speed increases. The net speed of ABPs in the longitudinal direction approaches that of passive Brownian particles in the strong flow limit.

As predicted by previous work, the long-time longitudinal dispersion coefficient of ABPs is a non-monotonic function of the flow speed. In addition to translational diffusion enjoyed by both active and passive Brownian particles, ABPs can also sample different flow speeds using self-propulsion coupled to a reorientation mechanism. For ABPs in flow, there are two mechanisms for reorientation: random rotary diffusion and deterministic rotation by the fluid vorticity. The longitudinal dispersion of ABPs consists of the translational diffusivity, the swim diffusivity and the classical Taylor dispersivity. The swim diffusivity of ABPs is altered by the pressure-driven flow and the classical Taylor dispersivity of ABPs is different from that of passive Brownian particles because activity modifies the number density distribution. In the limit of weak flow, where ABPs explore the physical space dominantly via self-propulsion and random Brownian reorientation, the dispersion coefficient approaches that in the absence of flow. In the limit of strong flow, the dispersion coefficient converges to that of passive Brownian particles because ABPs lose their persistence due to the rapid rotation by the fluid vorticity.

We formulate the problem from a continuum perspective using the Smoluchowski equation governing the position and orientation of an ABP in the channel. We consider a dilute suspension and neglect particle-particle and particle-wall hydrodynamic interactions. From the Smoluchowski equation we derive an effective advection-diffusion equation for the cross-sectional average number density in Fourier space and calculate both the average drift and the effective dispersion coefficient in the flow direction in the long-time limit. In addition to the continuum model, the equivalent particle-based Langevin equations are considered. After the derivation of the governing equations, we elucidate the origin of upstream swimming by considering the case of deterministic particle dynamics without diffusion ($D_T = 0$ and $D_R = 0$). We then characterize the drift velocity of active particles without translational diffusion

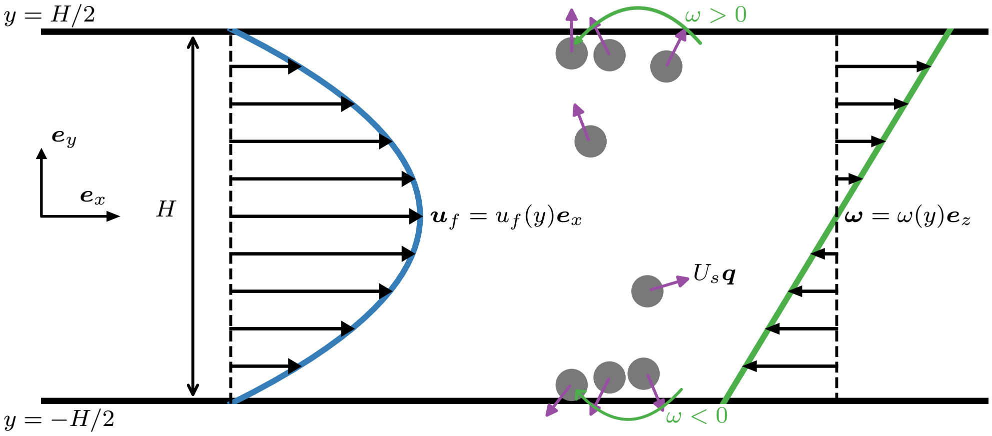

Figure 2.4: Schematic of active Brownian particles suspended in a planar Poiseuille flow between two parallel plates. The ABPs reorient on a time scale of $\tau_R = 1/D_R$, where D_R is the rotary diffusivity. The blue solid line is the Poiseuille flow and the green solid line is the scalar vorticity. The arrows represent the magnitude and sign of the fluid speed or vorticity. The vorticity is an odd function of the transverse coordinate y.

($D_T = 0$), followed by the general case of finite translational and rotational diffusion. Next, in Section 2.4 we consider the dispersive behavior of active particles before concluding the Chapter in Section 2.5.

2.2 Problem formulation

We consider a dilute suspension of spherical ABPs in a planar Poiseuille flow between two parallel plates separated by a distance H as illustrated in figure 2.4. We assume that the radius of the ABPs is negligible compared to the width of the channel. The background flow is given by $\boldsymbol{u}_f = u_f(y)\boldsymbol{e}_x$, where

$$u_f = U_f\left(1 - 4\frac{y^2}{H^2}\right), \quad -\frac{H}{2} \leq y \leq \frac{H}{2}, \tag{2.3}$$

with the maximum velocity U_f at the centerline of the channel ($y = 0$).

Following previous work on active suspensions (Saintillan and Shelley 2015), we define a probability density function $P(\boldsymbol{x}, \boldsymbol{q}, t)$ of finding an ABP at position $\boldsymbol{x}$ with orientation $\boldsymbol{q}$ ($|\boldsymbol{q}| = 1$) at time t. The evolution of P satisfies the Smoluchowski equation,

$$\frac{\partial P}{\partial t} + \nabla \cdot \boldsymbol{j}^T + \nabla_R \cdot \boldsymbol{j}^R = 0, \tag{2.4}$$

where ∇ and $\nabla_R = \boldsymbol{q} \times \frac{\partial}{\partial \boldsymbol{q}}$ are gradient operators in physical and orientation space, respectively. The translational and rotational fluxes are given by, respectively,

$$\boldsymbol{j}^T = \boldsymbol{u}_f P + U_s \boldsymbol{q} P - D_T \nabla P, \tag{2.5}$$

$$\boldsymbol{j}^R = \frac{1}{2}\boldsymbol{\omega} P - D_R \nabla_R P, \tag{2.6}$$

where $\boldsymbol{\omega} = \nabla \times \boldsymbol{u}_f$ is the vorticity vector of the background flow. The flux normal to a boundary surface must vanish, $\boldsymbol{e}_y \cdot \boldsymbol{j}^T = 0$ at $y = \pm H/2$. Integrating the Smoluchowski equation in orientation space gives a conservation equation for the number density,

$$\frac{\partial n}{\partial t} + \nabla \cdot \left(\boldsymbol{u}_f n + U_s \boldsymbol{m} - D_T \nabla n\right) = 0, \tag{2.7}$$

where $n(\boldsymbol{x}, t) = \int P d\boldsymbol{q}$ is the number density and $\boldsymbol{m}(\boldsymbol{x}, t) = \int \boldsymbol{q} P d\boldsymbol{q}$ is the polar order field.

The unboundedness in the flow direction makes it convenient to work in Fourier space. To this end, we introduce a Fourier transform with respect to x given by $\hat{f}(k) = \int \exp(-ikx) f(x) dx$. In Fourier space, the governing equation for number density becomes

$$\frac{\partial \hat{n}}{\partial t} + ik\left(u\hat{n} + U_s \hat{m}_x\right) - D_T (ik)^2 \hat{n} + \frac{\partial}{\partial y}\left(U_s \hat{m}_y - D_T \frac{\partial \hat{n}}{\partial y}\right) = 0. \tag{2.8}$$

Averaging over the width of the channel, we obtain

$$\frac{\partial \overline{n}}{\partial t} + k^2 D_T \overline{n} + ik\left(\overline{u(y)\hat{n}} + U_s \overline{\hat{m}}_x\right) = 0, \tag{2.9}$$

where the boundary terms vanish due to the zero normal flux condition and an overhead bar denotes cross-sectional average, $\overline{n}(k, t) = (1/H) \int_{-H/2}^{H/2} \hat{n}(k, y, t) dy$. It is convenient to relate $\hat{P}$ to $\overline{n}$ via the definition of a structure function $\hat{g}$ such that

$$\hat{P}(k, y, \boldsymbol{q}, t) = \overline{n}(k, t)\hat{g}(k, y, \boldsymbol{q}, t). \tag{2.10}$$

By construction, we have the normalization condition

$$\frac{1}{H}\int dy \int \hat{g} d\boldsymbol{q} = 1. \tag{2.11}$$

On the other hand, taking the Fourier transform of the Smoluchowski equation (2.4) yields

$$\frac{\partial \hat{P}}{\partial t} + ik\hat{j}_x^T + \frac{\partial \hat{j}_y^T}{\partial y} + \nabla_R \cdot \hat{\boldsymbol{j}}^R = 0. \tag{2.12}$$

Using the definition of $\hat{P}$ given in equation (2.10), we multiply equation (2.9) by $\hat{g}$ and subtract it from equation (2.12) to obtain

$$\begin{aligned}\frac{\partial \hat{g}}{\partial t} + \frac{\partial}{\partial y}\left(U_s q_y \hat{g} - D_T \frac{\partial \hat{g}}{\partial y}\right) - D_R\, \nabla_R^2 \hat{g} + \nabla_R \cdot \left(\frac{1}{2}\boldsymbol{\omega}\hat{g}\right) \\ - ik\left(U_s \overline{\tilde{m}_x}\frac{\hat{g}}{\overline{n}} + \overline{u\tilde{n}}\,\frac{\hat{g}}{\overline{n}} - U_s q_x \hat{g} - u\hat{g}\right) = 0. \qquad (2.13)\end{aligned}$$

Consider a small wavenumber expansion, $\hat{g} = g_0(y, \boldsymbol{q}, t) + ikd_0(y, \boldsymbol{q}, t) + O(k^2)$, corresponding to a slow variation over a large length scale (weak gradient) (Zia and Brady 2010; Takatori and Brady 2014). Substituting this expansion into equation (2.9), we obtain an effective advection-diffusion equation for the average number density in Fourier space,

$$\frac{\partial \overline{n}}{\partial t} + ikU^{\text{eff}}\,\overline{n} + k^2 D^{\text{eff}}\,\overline{n} = 0, \qquad (2.14)$$

where the average drift and the effective longitudinal dispersion coefficient are

$$U^{\text{eff}} = U_s\overline{m_x^0} + \overline{u(y)n^0}\,, \qquad (2.15)$$

$$D^{\text{eff}} = D_T - U_s\overline{\tilde{m}_x} - \overline{u(y)\tilde{n}}\,. \qquad (2.16)$$

Here, the average and fluctuating field variables are defined as the orientational moments of g_0 and d_0:

$$n^0 = \int g_0 d\boldsymbol{q}, \quad \boldsymbol{m}^0 = \int \boldsymbol{q} g_0 d\boldsymbol{q}, \quad \tilde{n} = \int d_0 d\boldsymbol{q}, \quad \tilde{\boldsymbol{m}} = \int \boldsymbol{q} d_0 d\boldsymbol{q}. \qquad (2.17)$$

The average drift of ABPs consists of the average of the flow speed weighted by the number density, $\overline{u(y)n^0}$, and the average streamwise swimming velocity $U_s\overline{m_x^0}$. Similarly, the effective longitudinal dispersion coefficient includes the translational diffusion D_T, the fluctuation in the self-propulsive velocity, $-U_s\overline{\tilde{m}_x}$, and the fluctuation in the particle number density weighted by the flow, $-\overline{u(y)\tilde{n}}$.

The classical Taylor dispersion of passive Brownian particles can be readily recovered by setting $U_s = 0$. Without self-propulsion, the rotary diffusion is decoupled from the translational motion (and therefore is irrelevant) and the number density becomes uniform $n^0 \equiv 1$. As a result, we obtain $U^{\text{eff}} = \overline{u} = 2U_f/3$ and $D^{\text{eff}} = D_T - \overline{u\tilde{n}}$ for passive particles. In contrast, the ability of ABPs to self-propel alters the number density distribution and introduces additional terms in the expressions for the average drift and the effective dispersion coefficient.

Substituting the small wavenumber expansion into equation (2.13), we obtain at leading order

$$\frac{\partial g_0}{\partial t} + \frac{\partial}{\partial y}\left(U_s q_y g_0 - D_T \frac{\partial g_0}{\partial y}\right) - D_R \nabla_R^2 g_0 + \nabla_R \cdot (\frac{1}{2}\boldsymbol{\omega} g_0) = 0. \tag{2.18}$$

At order ik, we obtain the governing equation for the fluctuating field d_0,

$$\frac{\partial d_0}{\partial t} + \frac{\partial}{\partial y}\left(U_s q_y d_0 - D_T \frac{\partial d_0}{\partial y}\right) - D_R \nabla_R^2 d_0 + \nabla_R \cdot (\frac{1}{2}\boldsymbol{\omega} d_0) = \left(U^{\text{eff}} - u - U_s q_x\right) g_0. \tag{2.19}$$

The no-flux boundary conditions for g_0 and d_0 at $y = \pm H/2$ are given by

$$U_s q_y g_0 - D_T \frac{\partial g_0}{\partial y} = 0 \text{ and } U_s q_y d_0 - D_T \frac{\partial d_0}{\partial y} = 0. \tag{2.20}$$

The normalization condition translates into

$$\frac{1}{H}\int dy \int g_0 d\boldsymbol{q} = 1 \text{ and } \frac{1}{H}\int dy \int d_0 d\boldsymbol{q} = 0. \tag{2.21}$$

At this point, the continuum formulation is complete. The governing equations are characterized by three dimensionless groups: the strength of confinement $\ell/H = U_s\tau_R/H$, the activity level $\ell/\delta = U_s\tau_R/\sqrt{D_T\tau_R}$ and the Péclet number $Pe = U_f H/D_T$. The Péclet number characterizes the relative importance of advection by flow and translational diffusion. To quantify the effect of flow speed U_f on the drift and dispersion, one can vary Pe while keeping ℓ/H and ℓ/δ fixed. However, it is cumbersome to characterize the effect of U_s, τ_R or D_T separately because all of them appear in two dimensionless parameters. We therefore introduce two alternate dimensionless groups,

$$\beta = \frac{U_s}{U_f} \quad \text{and} \quad Pe_{\dot{\gamma}} = \bar{\dot{\gamma}}\tau_R = \frac{2U_f\tau_R}{H}, \tag{2.22}$$

where $\bar{\dot{\gamma}} = \overline{|du/dy|} = 2U_f/H$ is the average shear rate across the channel. The first parameter β is a direct comparison of the swim speed of the ABPs and the flow speed at the centerline of the channel. The second parameter $Pe_{\dot{\gamma}}$ is a Péclet number that compares the two time scales of reorientation: rotational Brownian motion on the scale of τ_R and rotation from fluid shear with a time scale $1/\bar{\dot{\gamma}}$. Using β, Pe and $Pe_{\dot{\gamma}}$ as independent dimensionless parameters, we can conveniently probe the effect of U_s, D_T and τ_R separately. For example, variation of the swim speed U_s is fully

Fixed	Varying	Physical parameter
$\ell/H,\ \ell/\delta$	Pe	flow speed (U_f)
$\ell/H,\ \ell/\delta = \infty\ (D_T = 0)$	$Pe_{\dot{\gamma}}$	flow speed
$\ell/H,\ Pe_{\dot{\gamma}}$	ℓ/δ	translational diffusivity (D_T)
$\beta,\ D_T = 0$	$Pe_{\dot{\gamma}}$	reorientation time (τ_R)
$Pe_{\dot{\gamma}},\ Pe = \infty\ (D_T = 0)$	β	swim speed (U_s)
$Pe_{\dot{\gamma}},\ Pe$	β	swim speed
$\beta,\ Pe_{\dot{\gamma}}$	Pe	translational diffusivity
$\beta,\ Pe$	$Pe_{\dot{\gamma}}$	reorientation time

Table 2.1: Variation of different dimensionless parameters and the corresponding physical parameter that is varied.

characterized by variation of β while both Pe and $Pe_{\dot{\gamma}}$ are fixed. Similarly, variation of τ_R is represented by variation of $Pe_{\dot{\gamma}}$ while β and Pe are fixed. To measure the effect of D_T, we can vary Pe and fix both $Pe_{\dot{\gamma}}$ and β. The two dimensionless parameters ℓ/H and ℓ/δ can be expressed in terms of β, Pe and $Pe_{\dot{\gamma}}$ via the relations $\ell/H = \beta Pe_{\dot{\gamma}}/2$, $\ell/\delta = \beta\sqrt{PePe_{\dot{\gamma}}/2}$. Conversely, we have $\beta = (\ell/\delta)^2(\ell/H)^{-1}Pe^{-1}$ and $Pe_{\dot{\gamma}} = 2Pe(\ell/H)^2(\ell/\delta)^{-2}$. In Table 2.1, we summarize the different schemes of varying dimensionless groups and their corresponding physical situation in terms of dimensional parameters. In experiments, some variation schemes are easier than others. For example, one could easily vary the flow speed and quantify the transport of active particles as a function of Pe for a given ℓ/δ and ℓ/H.

Henceforth, we consider ABPs in 2D where the orientation vector $\boldsymbol{q}$ is in the velocity-gradient plane. As a result, one can parameterize $\boldsymbol{q}$ in terms of a single orientation angle $\theta \in [0, 2\pi)$ where $\boldsymbol{q} = \cos\theta\boldsymbol{e}_x + \sin\theta\boldsymbol{e}_y$. We note that the qualitative behavior of the average drift and longitudinal dispersion does not depend on the dimensionality of the orientation space. We shall discuss three separate methods to solve (2.15) – (2.21): truncated orientational moment expansion, solution of (2.18) and (2.19) using the finite element method (FEM) and Brownian dynamics (BD) simulation. For the first two methods, we determine g_0 from (2.18) and the average drift U^{eff} from (2.15). With solution to g_0 and U^{eff}, we then determine d_0 from (2.19) and D^{eff} from (2.16).

As a first approach, we approximate the average and fluctuating field in terms of their truncated orientational moments (Saintillan and Shelley 2013; Theillard et al.

2017)

$$
\begin{aligned}
g_0 &\approx \frac{1}{2\pi}\left(n^0 + 2\boldsymbol{q}\cdot\mathbf{m}^0 + 4\boldsymbol{qq} : \boldsymbol{Q}^0\right), \\
d_0 &\approx \frac{1}{2\pi}\left(\tilde{n} + 2\boldsymbol{q}\cdot\tilde{\mathbf{m}} + 4\boldsymbol{qq} : \tilde{\boldsymbol{Q}}\right),
\end{aligned} \tag{2.23}
$$

where $\boldsymbol{Q}^0 = \int(\boldsymbol{qq} - \boldsymbol{I}/2)g_0 d\boldsymbol{q}$ is the average nematic field and $\tilde{\boldsymbol{Q}} = \int(\boldsymbol{qq} - \boldsymbol{I}/2)d_0 d\boldsymbol{q}$ is the fluctuating nematic field. Substituting these expressions for g_0 and d_0 and taking orientational moments of appropriate order yield a set of closed ordinary differential equations at steady state for the average and fluctuating number density, polar and nematic fields (refer to Appendix 2.6 for details). Mathematically, this approximation can be interpreted as a severely truncated Fourier series expansion of g_0 and d_0 in the orientation angle. The moment expansion converges rapidly only when the probability distributions are near isotropy.

For the problem of this Chapter, the distribution can be very anisotropic in the presence of a Poiseuille flow. It is then beneficial to solve the governing equations for g_0 and d_0 directly and then take the needed orientational moments to obtain the average drift and effective dispersion coefficient. To this end, we solve (2.18) and (2.19) directly with a finite element method implemented using `FreeFem++` (Hecht 2012) with adaptive mesh refinement. In the FEM formulation, periodic boundary condition in θ is enforced, $g_0(y, \theta = 0, t) = g_0(y, \theta = 2\pi, t)$ and $d_0(y, \theta = 0, t) = d_0(y, \theta = 2\pi, t)$. After the system reaches steady state, the orientional moments of g_0 and d_0 are calculated according to (2.17) and then the drift and effective dispersion coefficient are obtained using (2.15) and (2.16).

From a particle-level perspective, the evolution of the configuration of ABPs can be described by the overdamped Langevin equations. For each ABP, this force and torque balance is given by

$$
\mathbf{0} = -\zeta\left(\frac{d\boldsymbol{x}}{dt} - \boldsymbol{u}_f\right) + \boldsymbol{F}^B + \boldsymbol{F}^S, \tag{2.24}
$$

$$
\mathbf{0} = -\zeta_R\left(\frac{d\boldsymbol{q}}{dt} - \frac{1}{2}\boldsymbol{\omega}\times\boldsymbol{q}\right) + \boldsymbol{L}^B \times \boldsymbol{q}. \tag{2.25}
$$

Here, $\boldsymbol{F}^S = \zeta U_s \boldsymbol{q}$ is the swim force (Takatori et al. 2014), $\boldsymbol{F}^B$ ($\boldsymbol{L}^B$) is the Brownian force (torque). ζ and ζ_R are the translational and rotational hydrodynamic drag coefficients, respectively. The Brownian force and torque satisfy white-noise statistics

$$\langle \boldsymbol{F}^B \rangle = 0, \quad \langle \boldsymbol{F}^B(0)\boldsymbol{F}^B(t) \rangle = 2D_T\zeta^2\delta(t)\boldsymbol{I}, \tag{2.26}$$

$$\langle \boldsymbol{L}^B \rangle = 0, \quad \langle \boldsymbol{L}^B(0)\boldsymbol{L}^B(t) \rangle = \frac{2}{\tau_R}\zeta_R^2\delta(t)\boldsymbol{I}, \tag{2.27}$$

where $\delta(t)$ is the delta function and the angle brackets denote ensemble average over Brownian fluctuations. We emphasize that the translational and rotational diffusion coefficients represent biological noises and their variation can be independent.

We evolve the Langevin equation with a typical Brownian dynamics algorithm (Bechinger et al. 2016) for approximately 10^5 non-interacting particles to ensure good statistics. The duration of the BD simulation was chosen to be longer than the slowest time scale in the problem so that the long-time behavior is captured. The domain of simulation is a square box of side length H with periodic boundary condition in the flow direction and hard walls at $y = \pm H/2$. The hard-wall boundary condition is implemented using the potential-free algorithm (Heyes and Melrose 1993) that ensures that the particle does not cross the wall. The interaction of the particle with the wall does not change the particle orientation. The absolute position of each ABP is recorded to calculate the effective drift and diffusivity. Further details of the BD simulation are presented in Appendix 2.7.

2.3 Upstream swimming

The drift U^{eff} quantifies the average motion of ABPs along the channel due to the combined effects of advection by the ambient flow and self-propulsion. In the absence of flow ($U_f \equiv 0$), the notion of upstream or downstream is lost and the longitudinal polarization m_x^0 vanishes by symmetry. As a result, the drift U^{eff} is zero if the flow is not present. The introduction of an ambient flow breaks the left-right symmetry in the longitudinal direction, which enables non-zero polarization ($m_x^0 \neq 0$). This symmetry-breaking ultimately leads to the tendency of ABPs to swim upstream in a pressure-driven flow, which has been investigated experimentally (Hill et al. 2007; Kaya and Koser 2012; Kantsler et al. 2014) and theoretically (Ezhilan and Saintillan 2015). A number of mechanisms for the upstream swimming of micro-organisms have been proposed including chirality of flagellar bundles and hydrodynamic interactions (Marcos et al. 2012; Shen et al. 2012; Kantsler et al. 2014; Tung et al. 2015; Omori and Ishikawa 2016). However, even for the simplest case of spherical particles without fluid-mediated or particle-particle interactions as we consider here, upstream swimming is still present. In the following section, by considering the case of non-Brownian particles, we show that this peculiar upstream swimming behavior can be explained with simple physical arguments: a self-propelling particle reaching the wall points into the wall. The body-fixed swimming director $\boldsymbol{q}$ is then rotated towards the upstream direction owing to the strong fluid vorticity at the wall. As a result, the particle moves upstream.

Though the moment equations are not analytically tractable, a number of symmetry properties can be obtained. First, solution to the Smoluchowski equation (2.18) along with the boundary condition (2.20) satisfies the symmetry property that $g_0(y, \theta, t) = g_0(-y, 2\pi - \theta, t)$. Integrating over the orientation, we have $n^0(y) = n^0(-y)$, i.e., the number density is an even function of y. Similarly, one can show that $m_y^0(-y) = -m_y^0(y)$ (and therefore, $\overline{m_y^0} \equiv 0$) and $m_x^0(-y) = m_x^0(y)$. Taking the cross-sectional average of the steady-state moment equation (2.31), we can further obtain $\overline{m_x^0} = -\frac{1}{2}\tau_R \overline{\omega m_y^0}$. This expression shows that the vorticity induces a coupling between the polar order in the flow direction and that in the transverse direction.

2.3.1 Non-Brownian active particles

We first consider non-Brownian particles with $D_T = 0$ and $D_R = 0$ (or $\tau_R = \infty$). In this case, the active particle has an infinite run length $\ell = U_s \tau_R = \infty$. Without translational and rotational Brownian motion, an active particle follows a deterministic trajectory. Zöttl and Stark (2012) examined the nonlinear dynamics of non-Brownian microswimmers in Poiseuille flow in a cylindrical tube. Both upstream and downstream trajectories are observed depending on the flow speed. When the flow speed is small, the microswimmer that comes into contact with the wall is turned upstream and performs a swinging motion between the walls while swimming upstream. Here, we examine this interesting behavior in more detail and quantify the transition between upstream and downstream motion in the absence of Brownian motion. The equations of motion given by equations (2.24) and (2.25) reduce to $dx/dt = u + U_s \cos\theta$, $dy/dt = U_s \sin\theta$, $d\theta/dt = \frac{1}{2}\omega$, where $\omega = 8U_f y/H^2$ is the scalar vorticity. The unit orientation vector is written in a parametric form, $\boldsymbol{q} = \cos\theta \boldsymbol{e}_x + \sin\theta \boldsymbol{e}_y$. We note that a second order equation for the orientation angle can be obtained: $d^2\theta/dt^2 = 4U_f U_s \sin\theta/H^2$. In general, the particle trajectory depends on its initial position and orientation. If the particle is located on the centerline ($y_0 = 0$) and aligned with the flow ($\theta_0 = 0$) initially, the equations of motion can be solved exactly to obtain $\theta \equiv 0$, $y \equiv 0$ and $x(t) = x_0 + (U_f + U_s)t$. Because the torque due to shear vanishes on the centerline, the particle will not rotate, and thus stays on the centerline for all time. Starting from this initial condition, the

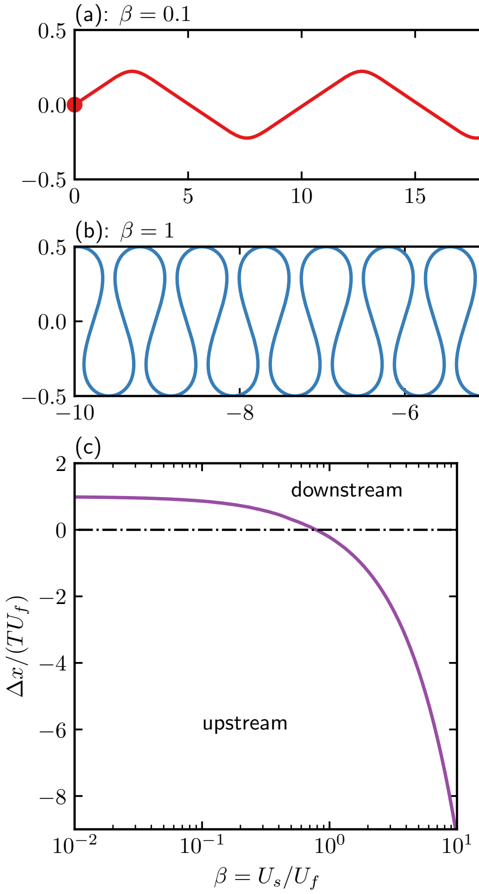

Figure 2.5: (a)-(b) Trajectories of a non-Brownian active particle for different speed ratios $\beta = U_s/U_f$. The initial positions are marked by dots. (c) Average speed in the longitudinal direction as a function of β. Initial conditions for all three panels are identical: $x_0 = 0$, $y_0 = 0$, $\theta_0 = \pi/2$.

particle will always move downstream. On the other hand, if the particle is located on the centerline but aligned against the flow ($\theta = \pi$) at $t = 0$, the solution becomes $x(t) = x_0 + (U_f - U_s)t$. Depending on the relative magnitude of self-propulsion and fluid advection ($\beta = U_s/U_f$), the particle can move upstream ($\beta > 1$) or downstream ($\beta < 1$). The upstream-downstream transition occurs at $\beta = 1$, where the particle will be stationary for all time. We note that the upstream motion of a non-Brownian active particle with initial condition $y_0 = 0$ and $\theta_0 = \pi$ is a stable fixed point while the downstream motion with $y_0 = 0$ and $\theta_0 = 0$ is an unstable fixed point. In general, the swimming behavior is different from this special case and the fluid vorticity plays a major role in the orientation dynamics of the active particle.

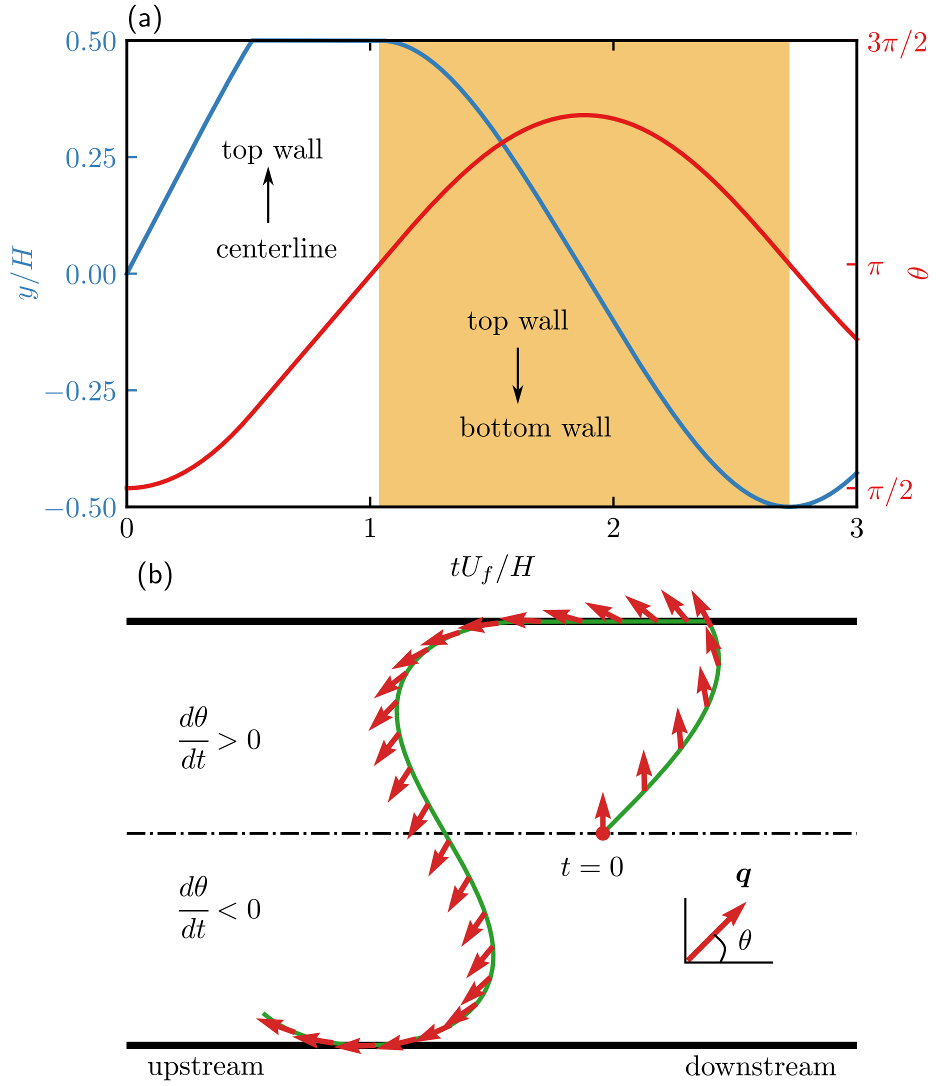

Figure 2.6: (a) Initial trajectory y/H (blue, left axis) and orientation angle θ (red, right axis) as a function of the dimensionless time tU_f/H for a non-Brownian active particle. The shaded region represents the time period in which the particle moves from the top wall to the bottom wall. (b) Initial trajectory (solid, green line) and orientation vector (red, arrows) of the active particle in the channel. Particles rotate counterclockwise ($d\theta/dt > 0$) in the upper half of the channel and clockwise ($d\theta/dt < 0$) in the lower half of the channel. Parameters: $y_0 = 0$, $\theta_0 = \pi/2$ and $\beta = 1$.

For arbitrary initial conditions, we solve the equations of motion numerically using the explicit Runge-Kutta method (RK4). Interaction of the particle with the channel wall is treated using the potential-free algorithm (Heyes and Melrose 1993) as discussed earlier. We reiterate that the interaction of the particle with the wall specified by the potential-free algorithm does not change the particle orientation. If the swim speed is small compared to the flow speed ($\beta \ll 1$), the active particle will always move downstream. In the small β limit, due to its slow swimming speed, the active particle cannot reach the wall before its direction changes significantly due to the fluid shear. A typical particle trajectory in this advection-dominated regime is presented in figure 2.5(a).

For large β, the active particle located on the channel centerline can travel to the wall if it is not aligned in the longitudinal direction. Due to the large fluid vorticity at the wall, the particle will be reorientated upstream. The continuing reorientation and swimming results in periodic movement between the walls and net upstream motion. A particle trajectory in this regime is shown in figure 2.5(b). Similar trajectories to figure 2.5(a-b) are found in Zöttl and Stark (2012). To quantify the net motion of a particle, we present the net speed in the longitudinal direction scaled by the flow speed as a function of β in figure 2.5(c). The net speed is given by $\Delta x/T$, where Δx is the distance traveled in the longitudinal direction within a period (T) of its motion. The period T is obtained using autocorrelation of the orientation angle θ. As expected, the particle moves downstream at small β and upstream at large β.

It is instructive to examine this upstream-swimming trajectory in more detail. In figure 2.6(a) we show the y-coordinate and orientation angle θ of the active particle as a function of the scaled time tU_f/H. To better visualize the swimming behavior, the same particle trajectory in $x-y$ plane (green line) with red arrows denoting the orientation vector is shown in figure 2.6(b). Initially, the particle is located on the centerline and pointed towards the top wall. As time starts, the particle moves to the top wall while being rotated counterclockwise by the fluid vorticity and advected downstream. If the swim speed U_s is large enough compared to U_f, the particle is able to arrive at the top wall where the fluid vorticity is the greatest. Because the particle cannot penetrate through the hard wall, it remains at the wall until the vorticity rotates it towards the upstream so that it can finally escape into the bulk. As the particle escapes into the bulk, it now points towards the bottom wall and starts to swim towards it. Once the particle reaches the lower half of the channel, the fluid vorticity reverses sign and the particle is again rotated towards the upstream direction. It will then approach the bottom wall if its speed U_s permits. Once the particle reaches the bottom wall, the above process repeats itself and we observe a periodic upstream trajectory confined between the two walls at later times.

In this section, we considered the transport of a self-propelled non-Brownian particle in a pressure-driven flow. Specifically, we studied the swimming behavior of non-Brownian active particles that start on the centerline. We note that a particle starting from a location other than the centerline exhibits similar behavior to those shown in figure 2.6. With a sufficiently large speed of self-propulsion, an active particle is able to swim upstream rather than being advected downstream by the flow. The interplay of biased rotation due to the fluid vorticity and confinement gives rise to this interesting upstream swimming behavior.

2.3.2 No translational diffusion

We now consider the case in which the ABPs have no translational diffusion ($D_T = 0$) but finite rotational diffusion ($D_R \neq 0$). In the Smoluchowski perspective, the absence of translational diffusion is singular. A diffusive flux at the wall is required to balance the flux due to self-propulsion. In the limit of vanishing D_T, a boundary layer develops at the walls (Yan and Brady 2015b). Starting from the Smoluchowski equation, one can reformulate the problem in a singular perturbation approach and obtain equations inside the boundary layer and out in the bulk. In the presence of flow, the resulting equations are not analytically tractable. Instead, we make use of the BD simulation introduced earlier to probe this regime of zero translational diffusion.

For $D_T = 0$, we have $\ell/\delta = \infty$ and $Pe = \infty$ given that all other dimensional parameters are nonzero and finite. In this case, $\beta = U_s/U_f$ and $Pe_{\dot{\gamma}} = 2U_f\tau_R/H$ are used as the two independent dimensionless groups. Recall the relation $\ell/H = \beta Pe_{\dot{\gamma}}/2$. In figure 2.7(a), we show the average drift $U^{\text{eff}}/\overline{u}$ as a function of $Pe_{\dot{\gamma}}$ for different values of the confinement strength ℓ/H. For a fixed ℓ/H, the variation of $Pe_{\dot{\gamma}}$ is better interpreted as a variation of the flow speed at the centerline U_f while other dimensional parameters are fixed. If the flow speed $U_f \equiv 0$, the average drift U^{eff} vanishes by symmetry. We note that, however, $U^{\text{eff}}/\overline{U_f}$ does not vanish in the limit $U_f \to 0$ as shown in figure 2.7(a). When the flow is weak ($Pe_{\dot{\gamma}} \ll 1$), active particles accumulate and swim upstream at the wall, which makes the average drift less than the average flow speed ($U^{\text{eff}} < \overline{u}$). We emphasize that the causes for this reduction of drift is twofold: first, the number density is higher at the wall than at the

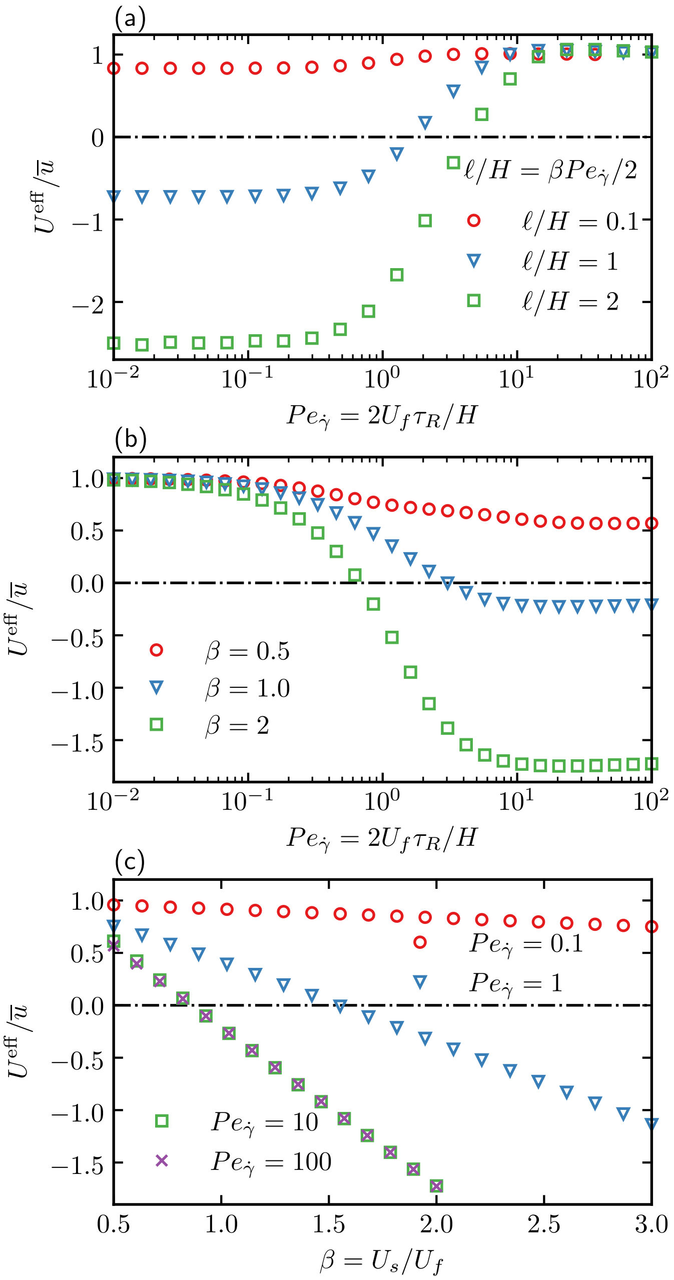

Figure 2.7: Variation of the average drift $U^{\mathrm{eff}}/\overline{u}$ in the absence of translational diffusion ($D_T = 0$) as a function of the flow speed U_f, the reorientation time τ_R and the swim speed U_s are shown in (a), (b) and (c) respectively. (a) Drift $U^{\mathrm{eff}}/\overline{u}$ as a function of $Pe_{\dot\gamma} = 2U_f\tau_R/H$ for $\ell/H = \{0.1, 1, 2\}$. (b) Drift $U^{\mathrm{eff}}/\overline{u}$ as a function of $Pe_{\dot\gamma}$ for $\beta = U_s/U_f = \{0.5, 1, 2\}$. (c) Drift $U^{\mathrm{eff}}/\overline{u}$ as a function of β for $Pe_{\dot\gamma} = \{0.1, 1, 10, 100\}$. The horizontal dash-dotted lines denote the transition between downstream and upstream drift.

centerline, which implies that $\overline{un^0} < \overline{u}$ because the flow speed is zero at the wall and is the greatest at the centerline; second, a negative polar order in the flow direction develops, which means that $U_s\overline{m_x^0} < 0$. For small ℓ/H, the swimming speed is not strong enough to overcome the downstream advection, i.e., $|U_s m_x^0| < \overline{un^0}$, and we obtain a downstream drift. For larger ℓ/H, upstream swimming is dominant and an upstream drift is achieved as shown in figure 2.7(a) for $\ell/H = \{1, 2\}$.

For $Pe_{\dot{\gamma}} \gg 1$ with ℓ/H fixed, the flow speed U_f is much faster than the swim speed U_s. From (2.15), we have $U^{\text{eff}}/\overline{u} = 3\beta\overline{m_x^0}/2 + \overline{un^0}/\overline{u} \to \overline{un^0}/\overline{u}$ since $\beta \to 0$ as $Pe_{\dot{\gamma}} \to \infty$. Furthermore, particles in this strong flow regime spin rapidly owing to the dominant fluid vorticity compared to Brownian reorientation. This leads to a more uniform number density distribution across the channel and thus $U^{\text{eff}}/\overline{u}$ approaches unity in the large $Pe_{\dot{\gamma}}$ limit.

In figure 2.7(b), we show the average drift $U^{\text{eff}}/\overline{u}$ as a function of $Pe_{\dot{\gamma}}$ for different values of the speed ratio β in the absence of translational diffusion. For a fixed β, this represents the effect of the reorientation time τ_R on the drift. For $Pe_{\dot{\gamma}} \ll 1$, the reorientation time τ_R is much smaller than the fluid shear timescale $1/\overline{\dot{\gamma}}$, and particles lose their persistence due to the rapid random reorientation and behave like passive particles without self-propulsion. As a result, the effective velocity approaches the passive limit, $U^{\text{eff}}/\overline{u} \to 1$ as $Pe_{\dot{\gamma}} \to 0$ regardless of the speed ratio β.

For $Pe_{\dot{\gamma}} \gg 1$, the reorientation time τ_R is large and particles follow nearly deterministic trajectories with small fluctuations from Brownian rotation. One can recover the purely ballistic case discussed in the previous section by taking the limit $Pe_{\dot{\gamma}} \to \infty$ with a finite β (e.g., $\tau_R \to \infty$).

It is important to distinguish between Brownian reorientation and rotation by fluid vorticity. Brownian reorientation is random and unbiased while the rotation due to the fluid vorticity is deterministic and biased. In order to move upstream, active particles have to be aligned against the flow so that it can swim upstream due to self-propulsion. This orientational bias towards the upstream, as discussed in the previous section, is achieved by the deterministic rotation from the fluid vorticity in the presence of a confining boundary. With other parameters fixed, Brownian reorientation becomes weaker as τ_R increases (D_R decreases, $Pe_{\dot{\gamma}}$ increases), and therefore is unable to randomize the biased orientation generated by the fluid vorticity. As a result, the average drift shown in figure 2.7(b) decreases monotonically as a function of $Pe_{\dot{\gamma}}$, becoming negative—upstream swimming—and asymptotes to the non-Brownian limit at large $Pe_{\dot{\gamma}}$.

We showed the variation of $U^{\text{eff}}/\overline{u}$ as a function of $Pe_{\dot{\gamma}}$ with different dimensionless parameters being fixed in figure 2.7(a) and (b). When ℓ/H is fixed, upstream drift is observed for small $Pe_{\dot{\gamma}}$. On the other hand, upstream drift is achieved for large $Pe_{\dot{\gamma}}$ when β is fixed. We emphasize that to interpret the results properly, one has to be precise about what parameters are fixed.

In addition to the two competing reorientation mechanisms characterized by $Pe_{\dot{\gamma}}$, the speed ratio β also plays an important role in determining the swimming behavior. In figure 2.7(c), we show the variation of $U^{\text{eff}}/\overline{u}$ as a function of β for different values of $Pe_{\dot{\gamma}}$. For small β (e.g., $\beta = 0.5$), active particles move downstream ($U^{\text{eff}}/\overline{u} > 0$) for all values of $Pe_{\dot{\gamma}}$. The transition from downstream to upstream swimming ($U^{\text{eff}}/\overline{u} < 0$) is observed for larger β only. For a given $Pe_{\dot{\gamma}}$, the average drift $U^{\text{eff}}/\overline{u}$ decreases monotonically and becomes negative as β increases. We note that for $\beta = 0$, i.e., the particles are passive, the orientational degree of freedom becomes decoupled from the translational, and we recover the passive limit: $U^{\text{eff}}/\overline{u} \to 1$ as $\beta \to 0$.

2.3.3 Finite translational and rotational diffusion

We now examine the distribution and swimming behavior of ABPs with finite translational and rotational diffusivities in the presence of a pressure-driven flow. To illustrate the effect of translational diffusivity (D_T) on the behavior of active particles, we show in figure 2.8 the average number density n^0, average streamwise polar order m_x^0 and the average probability distribution g_0 (Recall that $n_0 = \int g_0 d\boldsymbol{q}$.) at the top wall for different $Pe = U_f H/D_T$ with $\beta = U_s/U_f = 2$ and $Pe_{\dot{\gamma}} = 2U_f\tau_R/H = 10$. The $D_T = 0$ case discussed in the previous section is the limit $Pe \to \infty$ and $\beta, Pe_{\dot{\gamma}} < \infty$. With β and $Pe_{\dot{\gamma}}$ fixed at finite values, the variation of translational diffusivity D_T is represented in dimensionless form by the variation of Pe. In other words, Pe goes down as D_T increases and $Pe \ll 1$ implies that the translational diffusion dominates over the fluid advection. In this strong diffusion limit, the steady state probability profile cannot sustain a large gradient across the channel due to the smoothing effect of diffusion. As a result, in figure 2.8(a)-(b) we observe a mostly uniform number density and polar order for $Pe = 0.1$. As Pe increases, translational diffusion becomes less important and we observe the development of boundary layers at the wall in both the average number density and polar order distribution. At large Pe, ABPs exhibit strong accumulation and upstream polarization at the

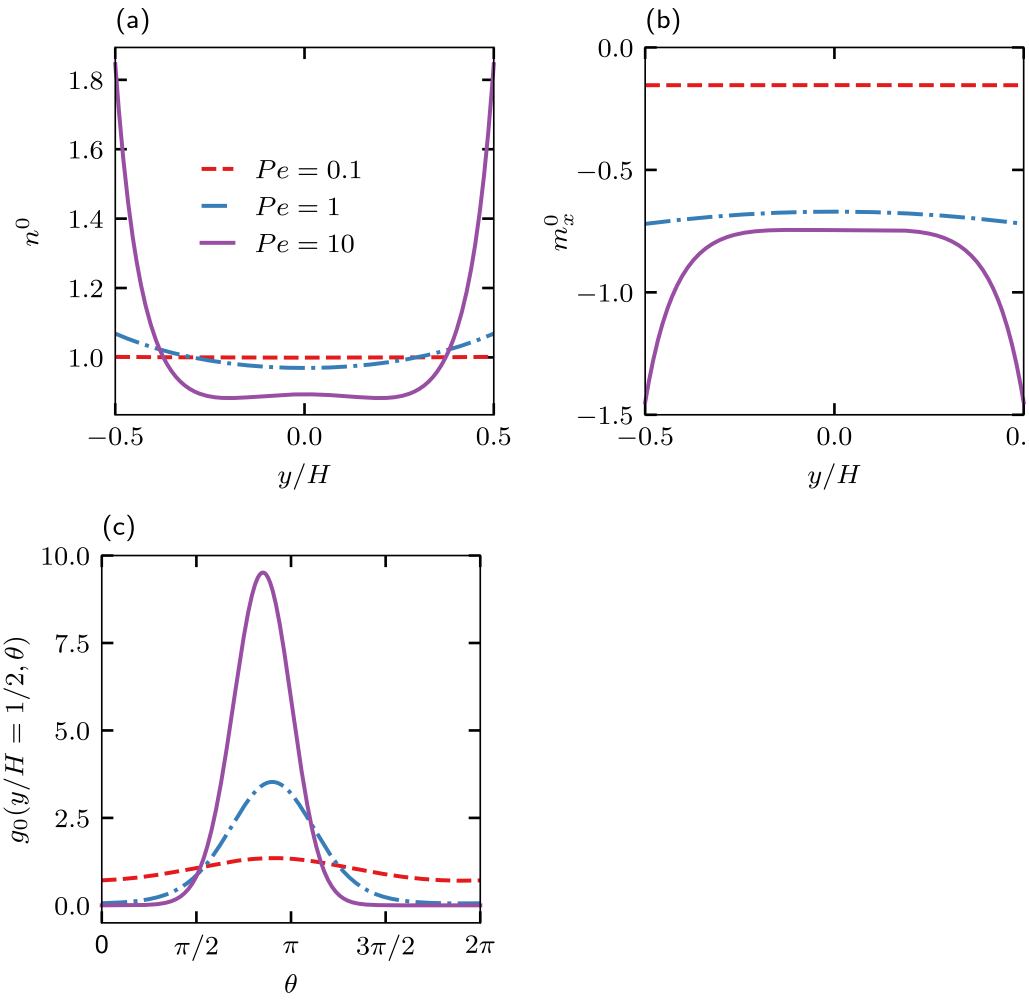

Figure 2.8: Effect of translational diffusivity D_T on the average field distributions. (a) Average number density distribution across the channel for different values of $Pe = U_f H/D_T$. (b) Average streamwise polar order distribution across the channel for different values of Pe. (c) The average field g_0 as a function of θ at the top wall $(y/H = 1/2)$ for different values of Pe. The solutions presented are obtained from the finite element calculation with $\beta = U_s/U_f = 2$ and $Pe_{\dot{\gamma}} = 2U_f\tau_R/H = 10$.

wall. In figure 2.8(c), the average field g_0 at the top wall is plotted as a function of the orientation angle θ for different Péclet numbers. Recall that an ABP with the orientation angle $\theta = \pi/2$ is pointing normally into the top wall and an ABP with $\theta = \pi$ is pointing upstream parallel to the wall. In the strong diffusion limit ($Pe \ll 1$), only a weak variation of g_0 as a function of θ is observed. Similar to the orientational order distribution across the channel, the probability at the wall develops a large gradient and the peak shifts towards the upstream direction as Pe increases.

We note that even though the streamwise polar order $m_x^0 < 0$ for $Pe = 0.1$, it is not strong enough to overcome the fluid advection, which leads to a net downstream motion ($U^{\text{eff}} > 0$). The dependence of the average drift $U^{\text{eff}}/\overline{u}$ on Pe is made quantitative in figure 2.9. Here, the dashed lines are solutions from the moment equations, the circles are solutions from FEM and the crosses are solutions from BD simulations. The horizontal dash-dotted line represents the drift velocity of passive particles, $U^{\text{eff}} = \overline{u}$. Results from BD and FEM agree very well while solution from the moment equations deviates from BD (or FEM) for $Pe_{\dot{\gamma}} = 10$ at large Pe as seen in figure 2.9(a). The moment method truncating after the nematic order is not sufficient to capture this behavior. One can show that our simple truncated expansions of the average and fluctuation fields given in equation 2.23 lead to isotropic closures to the third moments of g_0 and d_0 (Saintillan and Shelley 2013). Because this truncation does not incorporate the effect of the external flow field even though particles rotate according to Jeffery's equation, it is only a good approximation when the average and fluctuation fields are not far away from isotropy. Therefore, care must be taken when using these isotropic closures in the presence of an external flow.

For fixed finite β and $Pe_{\dot{\gamma}}$ as shown in figure 2.9(a), the increase of Pe is understood as the decrease in the translational diffusivity D_T. The effective drift $U^{\text{eff}}/\overline{u}$ approaches unity in the limit $Pe \to 0$ ($D_T \to \infty$) because the particle number density becomes uniform owing to strong translational diffusion. For small Pe, ABPs have a net downstream motion. A transition from downstream to upstream motion occurs at a larger Pe where more particles accumulate at the wall. Because the fluid vorticity is the greatest at the wall while the fluid velocity is zero, particles at the wall are able to swim upstream with a larger net speed. As a result, for a given β and $Pe_{\dot{\gamma}}$, the effective drift velocity $U^{\text{eff}}/\overline{u}$ decreases monotonically as a function of Pe and reaches a plateau at large Pe. The limit of $Pe \to \infty$ with fixed $\beta, Pe_{\dot{\gamma}} < \infty$ asymptotes to the case of no translational diffusion explored in the previous section.

The variation of $U^{\text{eff}}/\overline{u}$ as a function of Pe depends qualitatively on how the parameter space is sampled. By keeping β and $Pe_{\dot{\gamma}}$ constant as shown in figure 2.9(a), the variation of Pe is understood as the variation of the translational diffusivity alone. In figure 2.9(b), to investigate the effect of the flow speed U_f on the average drift, we fix $\ell/\delta = U_s\tau_R/\sqrt{D_T\tau_R}$, $\ell/H = U_s\tau_R/H$ and vary Pe. In this case, Pe increases as the flow speed U_f increases. Noting that ℓ/δ characterizes the activity level of ABPs, a suspension with $\ell/\delta = 30$ is in the highly active regime. The competition between upstream swimming and downstream advection gives rise to a non-monotonic vari-

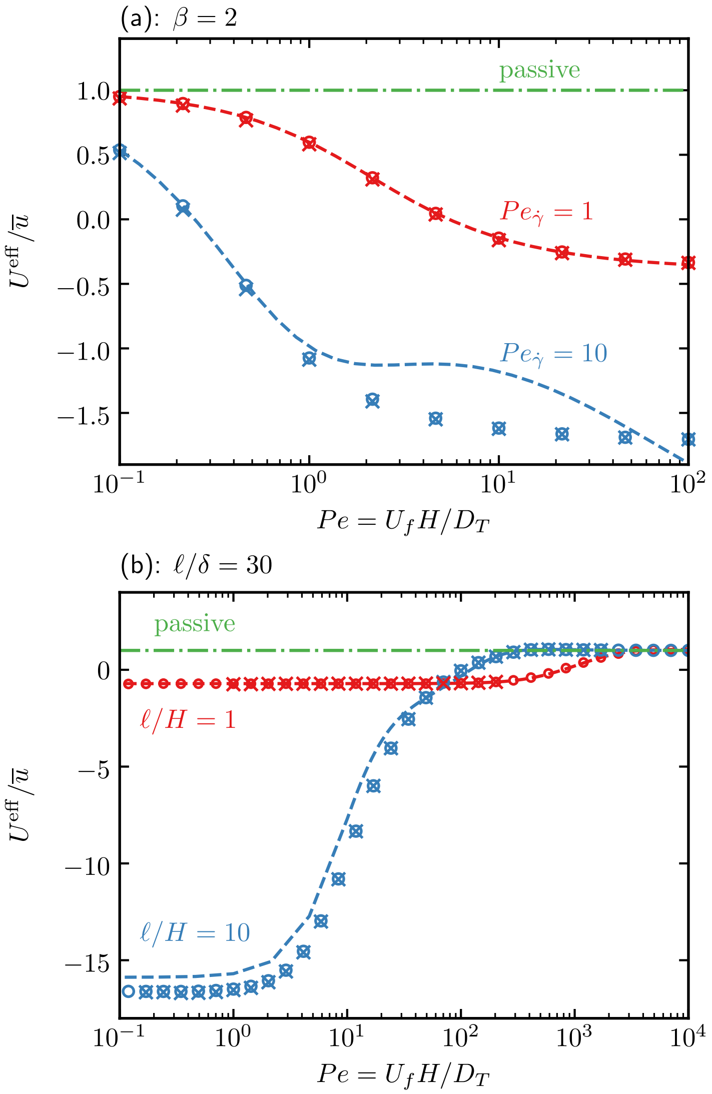

Figure 2.9: (a) Average drift $U^{\text{eff}}/\overline{u}$ of ABPs as a function of $Pe = U_f H/D_T$ for $Pe_{\dot\gamma} = 2U_f\tau_R/H = 1$ (red) and $Pe_{\dot\gamma} = 10$ (blue) with fixed $\beta = U_s/U_f = 2$. (b) Average drift $U^{\text{eff}}/\overline{u}$ of ABPs as a function of the Péclet number for $\ell/H = U_s\tau_R/H = 1$ (red) and $\ell/H = 10$ (blue) with fixed $\ell/\delta = U_s\tau_R/\sqrt{D_T\tau_R} = 30$. Circles are from FEM, while dashed lines denote results from the moment equations. Results from Brownian dynamics are indicated by crosses. The dash-dotted green line is the effective drift of passive particles.

ation of the drift velocity as a function of Péclet number. As discussed earlier, the effective drift vanishes ($U^{\text{eff}} = 0$) when the flow is absent ($Pe = 0$). For weak flow ($Pe \ll 1$), upstream swimming dominates over downstream advection and the drift becomes negative. Upstream swimming is particularly strong for large confinement,

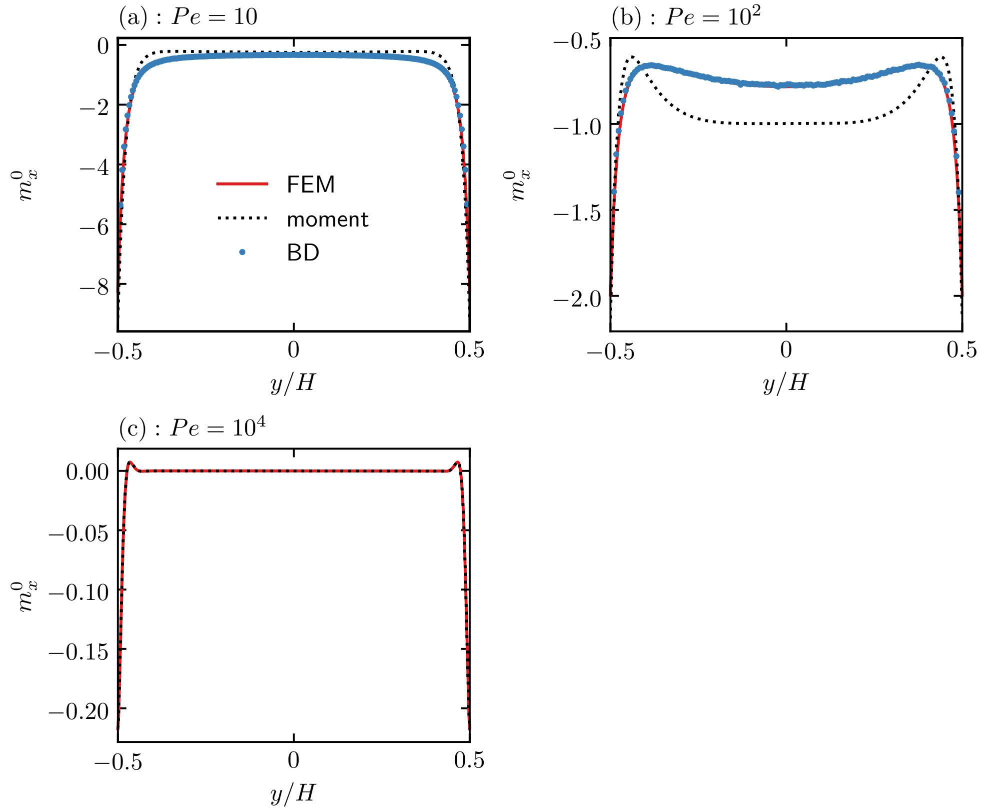

Figure 2.10: The average polar order distribution (m_x^0) across the channel for different Péclet numbers ($Pe = U_f H/D_T$) with $\ell/H = U_s\tau_R/H = 10$ and $\ell/\delta = U_s\tau_R/\sqrt{D_T\tau_R} = 30$. The red solid lines are solution from FEM, the black dashed lines are from moment equations and the blue dots are results from BD simulation.

e.g., $\ell/H = 10$ in figure 2.9(b). In the strong flow ($Pe \gg 1$) limit, the advection of ABPs by the ambient flow is much stronger than the self-propelling speed. Besides, the accumulation of ABPs at the wall is greatly reduced as Pe increases. As a result, the drift velocity approaches that of a passive particle for large Pe. As a function of the flow speed, the average drift U^{eff} of ABPs with high activity first decreases to a negative value and then increases to approach the passive limit $\overline{u}$. We note that the ratio $U^{\text{eff}}/\overline{u}$ approaches a nonzero value in the limit $U_f \to 0$. Because we scaled the dimensional average drift using $\overline{u}$, the ratio $U^{\text{eff}}/\overline{u}$ is a monotonically increasing function of Pe as shown in figure 2.9(b). We note that the non-monotonicity of the average drift refers to the variation of the dimensional quantity U^{eff} as a function of Pe. In appendix 2.8, the effect of non-spherical shape on the average drift of ABPs is discussed.

In figure 2.10, we present the average polar order distribution in x-direction (m_x^0) across the channel for different Péclet numbers for a very active suspension ($\ell/\delta = 30$) with $\ell/H = 10$. As the flow strength (Pe) increases, upstream swimming becomes weaker. For $Pe = 10$, the time scale of rotation by flow vorticity at the wall and random rotation by Brownian motion is comparable ($Pe_{\dot{\gamma}} = 2Pe(\ell/H)^2(\ell/\delta)^{-2} \approx 2.22$). In this regime, the flow vorticity at the wall only biases the orientation of ABPs towards the upstream. In the strong flow limit ($Pe \gg 1$), the time scale for rotation by flow vorticity is much smaller than the Brownian reorientation time τ_R even in the bulk. As a result, the persisting motion of an ABP vanishes because of the fast spinning due to vorticity.

This fast spinning by vorticity also affects the number density distribution. At large Pe where flow is strong, ABPs at the wall are quickly reoriented by vorticity without relying on rotary diffusion to escape into the bulk flow. This leads to a more uniform distribution of particles across the channel at large Pe. In figure 2.11, we present the average number density distribution n^0 across the channel for different Péclet numbers with $\ell/H = 10$ and $\ell/\delta = 30$. Indeed, we observe a reduction of wall accumulation as the Péclet number increases. The reduction of wall accumulation in the presence of flow has also been observed by Chilukuri et al. (2014) for a model microswimmer consists of two beads connected by a stiff spring. Another interesting feature is the non-monotonic variation of number density across the channel at large Péclet number. At $Pe = 100$, a weak accumulation of particles at the channel centerline is observed. This centerline accumulation is due to strong confinement. If we decrease ℓ/H or increase ℓ/δ, the bulk number density will become more uniform. For $Pe = 10^4$, figure 2.11(c), a local depletion of particles is observed near the wall before the number density increases at the wall. In bulk flow, the number density is uniform due to the vanishing swimming motion. In Brownian dynamics simulation, we observe that ABPs can be trapped near the wall when the flow is strong. An ABP approaching the upper wall will be rotating counterclockwise. Instead of escaping into the bulk once orientated upstream, an ABP comes back to the wall again due to the rapid rotation by flow vorticity. It will repeat this process until random Brownian motion kicks it outside this region and it can escape to the bulk. As a result, we still observe a small amount of wall accumulation and a region of depletion because ABPs here either go back to the wall or escape into the bulk.

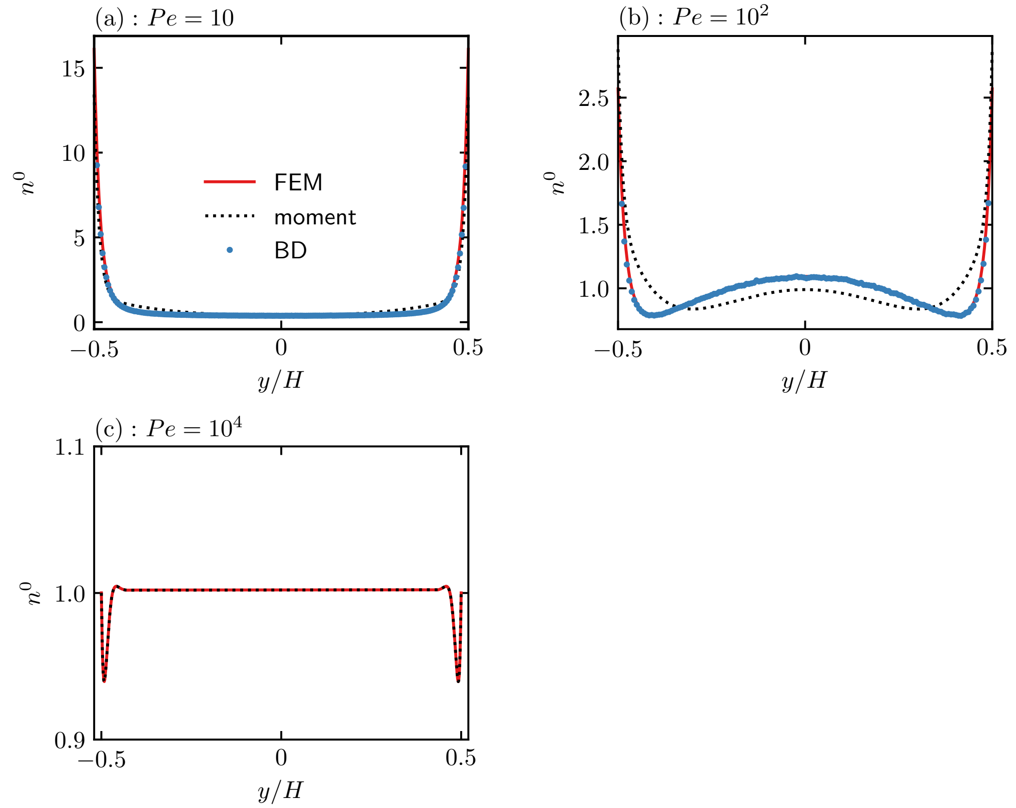

Figure 2.11: The average number density distribution (n^0) across the channel for different Péclet numbers ($Pe = U_f H/D_T$) with $\ell/H = U_s\tau_R/H = 10$ and $\ell/\delta = U_s\tau_R/\sqrt{D_T\tau_R} = 30$. The red solid lines are solution from FEM, the black dashed lines are from moment equations and the blue dots are results from BD simulation.

2.4 Longitudinal dispersion

We now turn our attention to the effect of flow on longitudinal dispersion of ABPs in a channel. The average drift considered in the previous section characterizes the mean motion of ABPs along the channel. In contrast, the effective dispersivity measures the variation of particle motion in the longitudinal direction compared to the mean. In this section, we first discuss the effective longitudinal dispersion when the translational diffusivity $D_T = 0$, in which case the classical Taylor dispersion is absent. We then discuss the general case with finite D_T.

2.4.1 Dispersion in the absence of translational diffusion

In this section, we explore the long-time longitudinal diffusive behavior of active particles in the presence of flow in the absence of translational diffusion, $D_T = 0$.

For passive particles with $D_T = 0$, there is no long-time diffusive motion. Their behavior is purely deterministic and ballistic, that is, being advected downstream with the local flow speed. But for active particles, there is long-time diffusive behavior from the coupling between the diffusive sampling of orientation space due to Brownian rotation and the orientational dependence of the self-propelling velocity $U_s\boldsymbol{q}$. In other words, the dispersion of active particles with $D_T = 0$ consists of the swim diffusivity D^{swim} alone while the presence of an external flow modulates the effective speed in a run and the effective reorientation time τ_{eff} of the effective long-time random walk process. Recall that the longitudinal dispersion coefficient becomes the free-space swim diffusivity ($D^{\text{eff}} = D_0^{\text{swim}} \equiv U_s^2\tau_R/2$) if the flow is also absent ($U_f = 0$). This coupling of rotation to translation does not exist for passive particles that do not self-propel. Therefore, Brownian sampling of the orientation space becomes irrelevant to the consideration of the effective dispersion for passive particles.

To reveal the effect of flow on the longitudinal dispersion of active particles, we show in figure 2.12(a) the effective dispersion coefficient scaled by the free space swim diffusivity as a function of $Pe_{\dot{\gamma}} = 2U_f\tau_R/H$ for different strengths of confinement $\ell/H = U_s\tau_R/H$. The same quantity is plotted as a function of $Pe_{\dot{\gamma}}$ for different values of $\beta = U_s/U_f$ in figure 2.12(b) and as a function of β for different values of $Pe_{\dot{\gamma}}$ in figure 2.12(c). Dash-dotted horizontal lines represent the case in which the effective dispersivity is identical to that in free space, $D^{\text{eff}} = D_0^{\text{swim}}$. For fixed ℓ/H as shown in figure 2.12(a), the variation of $Pe_{\dot{\gamma}}$ is understood as the variation of the flow speed U_f. For fixed β as shown in figure 2.12(b), the variation of $Pe_{\dot{\gamma}}$ is the variation of the reorientation time τ_R. In figure 2.12(c) where $Pe_{\dot{\gamma}}$ is fixed, the variation of β corresponds to the variation of the swim speed U_s.

In the presence of a pressure-driven flow, the effective longitudinal dispersivity is altered in an interesting and nontrivial fashion. As shown in figure 2.12(a), the effective dispersivity $D^{\text{eff}}/D_0^{\text{swim}}$ is a non-monotonic function of the flow speed: the effective dispersivity D^{eff} can be either enhanced ($D^{\text{eff}}/D_0^{\text{swim}} > 1$) or hindered ($D^{\text{eff}}/D_0^{\text{swim}} < 1$) compared to D_0^{swim}. To understand this non-monotonic behavior, consider the effective long-time random walk process of the ABPs in the presence of pressure-driven flow. In addition to the fluid vorticity that modifies the effective reorientation time τ_{eff}, the fluid advection affects the effective speed in a run. Recall that the effect of vorticity on orientation is characterized by $Pe_{\dot{\gamma}}$ and the effect of flow speed is characterized by β. For a given ℓ/H, β decreases as the flow speed

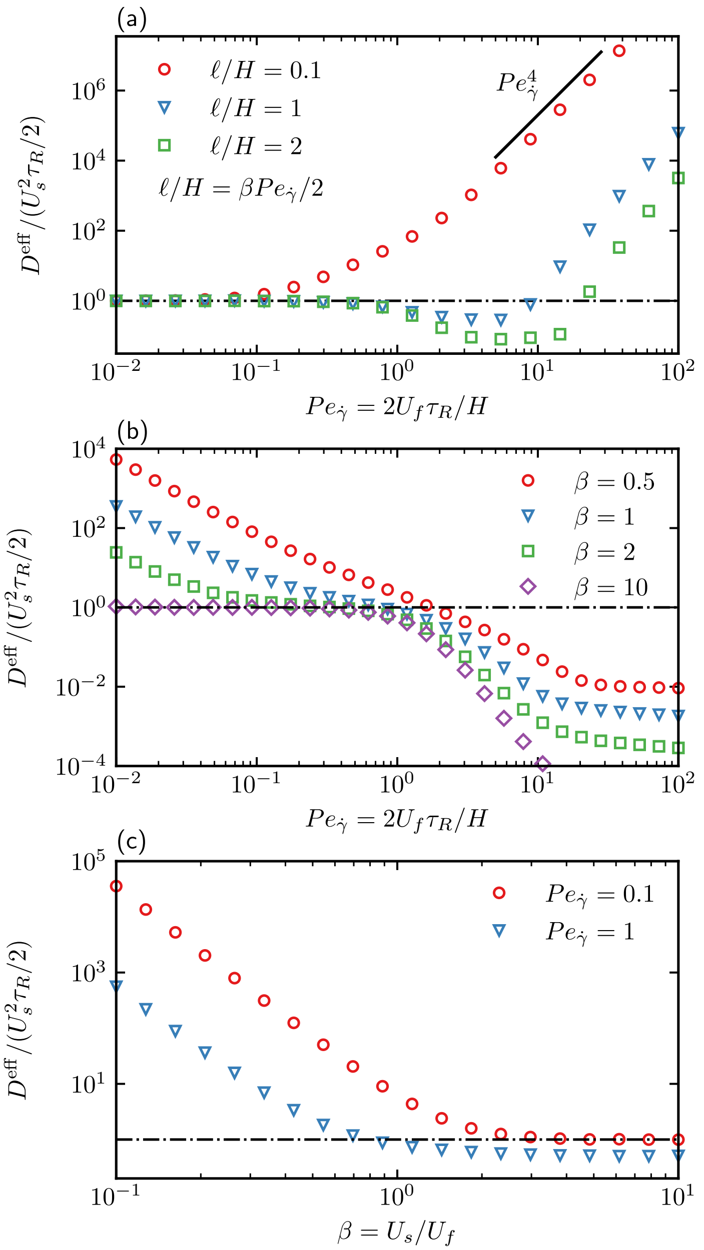

Figure 2.12: Variation of the effective longitudinal dispersivity $D^{\text{eff}}/(U_s^2\tau_R/2)$ in the absence of translational diffusion ($D_T = 0$) as a function of the flow speed U_f, the reorientation time τ_R and the swim speed U_s are shown in (a), (b) and (c), respectively. (a) Effective longitudinal dispersivity $D^{\text{eff}}/(U_s^2\tau_R/2)$ as a function of $Pe_{\dot{\gamma}} = 2U_f\tau_R/H$ for $\ell/H = U_s\tau_R/H = \{0.1, 1, 2\}$. (b) Effective longitudinal dispersivity $D^{\text{eff}}/(U_s^2\tau_R/2)$ as a function of $Pe_{\dot{\gamma}}$ for $\beta = U_s/U_f = \{0.5, 1, 2, 10\}$. (c) Effective longitudinal dispersion coefficient $D^{\text{eff}}/(U_s^2\tau_R/2)$ as a function of β for $Pe_{\dot{\gamma}} = \{0.1, 1\}$. The results shown are obtained from BD simulations. The horizontal dash-dotted lines are $D^{\text{eff}} = U_s^2\tau_R/2$, i.e., the free space swim diffusivity.

(i.e., $Pe_{\dot{\gamma}}$) increases since $\ell/H = \beta Pe_{\dot{\gamma}}/2$. When the flow is weak ($Pe_{\dot{\gamma}} \ll 1$), we have $\beta \gg 1$ and the advection is dominated by swimming and we recover the free space swim diffusivity, $D^{\text{eff}} \to U_0^2\tau_R/2$ as $Pe_{\dot{\gamma}} \to 0$ with ℓ/H fixed. For strong flow ($Pe_{\dot{\gamma}} \gg 1$), the effective reorientation time is reduced owing to the fluid vorticity but the effective speed in a run increases due to fluid advection. The effect of fluid advection dominates and the longitudinal dispersion is greatly enhanced.

The two competing effects originating from the background flow gives rise to the non-monotonic behavior. For $\ell/H = 0.1$, the fluid advection becomes important ($\beta \sim O(1)$) for even small $Pe_{\dot{\gamma}}$ (~ 0.1) where the effect of the fluid vorticity is still weak. In this case, the dispersivity increases monotonically as a function of $Pe_{\dot{\gamma}}$. For $\ell/H = \{1, 2\}$, the effect of vorticity becomes important at $Pe_{\dot{\gamma}} \sim O(1)$ and we observe an initial decrease in the dispersivity due to a reduction of the effective reorientation time. As the fluid advection becomes dominant ($\beta < 1$), $Pe_{\dot{\gamma}} \sim 10$, the dispersivity increases as $Pe_{\dot{\gamma}}$ increases.

In the large $Pe_{\dot{\gamma}}$ limit for $\ell/H = 0.1$, we observe a strong dependence of the effective longitudinal dispersion on the flow speed, $D^{\text{eff}}/D_0^{\text{swim}} \sim Pe_{\dot{\gamma}}^4$. Interestingly, this giant longitudinal dispersion has also been observed by Dehkharghani et al. (2019) in the dispersion of active particles with $D_T = 0$ in flow through a periodic porous media. Due to the rapid spinning from the fluid vorticity, active particles are not confined in the transverse direction since their effective run length ℓ^{eff} is reduced such that $\ell^{\text{eff}} \ll H$. In a constant vorticity field in an unbounded domain, the transverse dispersion coefficient of active particles is reduced. In the large $Pe_{\dot{\gamma}}$ limit, this reduction follows the scaling $D_\perp/D_0^{\text{swim}} \sim 1/Pe_{\dot{\gamma}}^2$ (Dehkharghani et al. 2019; Takatori and Brady 2014). Making use of the scaling in the classical Taylor dispersion process, $D^{\text{eff}} \sim U_f^2H^2/D_\perp$, we have $D^{\text{eff}}/D_0^{\text{swim}} \sim U_f^2H^2Pe_{\dot{\gamma}}^2/(U_s^4\tau_R^2) \sim Pe_{\dot{\gamma}}^4(\ell/H)^{-4}$ in the large $Pe_{\dot{\gamma}}$ limit. For a fixed ℓ/H, we recover the scaling $D^{\text{eff}}/D_0^{\text{swim}} \sim Pe_{\dot{\gamma}}^4$. In figure 2.12(a) for $\ell/H = 0.1$, this limiting behavior is achieved for $Pe_{\dot{\gamma}} > 10$. For larger ℓ/H, we expect the same quartic scaling in $Pe_{\dot{\gamma}}$ as $Pe_{\dot{\gamma}} \to \infty$. In the range of $Pe_{\dot{\gamma}}$ sampled in figure 2.12(a), this scaling is not achieved yet for $\ell/H = 1, 2$.

To explore the effect of the reorientation time τ_R, in figure 2.12(b) we fix β and plot the longitudinal dispersivity as a function of $Pe_{\dot{\gamma}}$. Physically, the variation of $Pe_{\dot{\gamma}}$ with β fixed corresponds to the variation of the importance of the fluid vorticity while keeping the advective effect of the flow fixed. For $Pe_{\dot{\gamma}} < 1$, Brownian reorientation is the fast time scale and rotation by the fluid vorticity is less important. On the other hand, rotation by the fluid vorticity becomes dominant for $Pe_{\dot{\gamma}} > 1$. The effective reorientation time τ_{eff} is reduced and thus the dispersivity decreases monotonically as $Pe_{\dot{\gamma}}$ increases. For $Pe_{\dot{\gamma}} \ll 1$, the dominant reorientation mechanism is Brownian and the enhancement of longitudinal dispersion for small β is due to the increase in the effective speed in the random walk from the fluid advection. The no-flow limit where $D^{\text{eff}} \to D_0^{\text{swim}}$ is recovered as the flow speed $U_f \to 0$, which in terms of the dimensionless parameters is obtained by taking the limit $\beta \to \infty$ and $Pe_{\dot{\gamma}} \to 0$. This no-flow limit is effectively recovered with $\beta = 10$ and $Pe_{\dot{\gamma}} \ll 1$ as marked by the diamond symbols in figure 2.12(b).

At this point the difference between Taylor dispersion of passive matter and active particles without translational diffusion should be noted. In the passive case, the longitudinal dispersion is always enhanced by the flow. In contrast, the pressure-driven flow can either enhance or hinder the longitudinal dispersion of active particles.

In figure 2.12(c), we show the dispersivity as a function of the speed ratio β for fixed values of $Pe_{\dot{\gamma}}$. This corresponds to a variation of the effect of the fluid advection while keeping the effect of the fluid vorticity fixed. In terms of dimensional parameters, this is a variation of the swim speed U_s while keeping other parameters fixed. As the swim speed increases, the effective run speed transitions from the fluid speed to the swim speed and the effective longitudinal dispersion decreases monotonically. The limiting value of the dispersivity in the large β limit depends on $Pe_{\dot{\gamma}}$. If $Pe_{\dot{\gamma}}$ is small (e.g., $Pe_{\dot{\gamma}} = 0.1$), Brownian reorientation dominates and we recover the no-flow limit (D_0^{swim}). If $Pe_{\dot{\gamma}}$ is larger (e.g., $Pe_{\dot{\gamma}} = 1$), the effective reorientation time is reduced and the longitudinal dispersivity is less than D_0^{swim}.

2.4.2 Dispersion with finite translational diffusion

We now consider the general case of ABPs with finite translational diffusion. For active particles with $D_T = 0$ as explored in the previous section, the background flow affects longitudinal particle dispersion through the rotation by vorticity in orientation space and advection in physical space. In addition to this effective modulation of the swim diffusivity, ABPs with finite D_T also experience the classical Taylor dispersion that occurs in physical space alone. Therefore, the dispersion of ABPs reflects the combined effects of the pressure-driven flow on the particle dynamics in both orientational and physical space.

For given activity level ℓ/δ and confinement strength ℓ/H, the variation of Pe corresponds to the variation of the flow speed U_f with other dimensional quantities being fixed. We present in figure 2.13(a) the effective longitudinal dispersivity

D^{eff}/D_T as a function of Péclet number for a suspension with low activity, $\ell/\delta = 2$, and two different confinement strengths $\ell/H = \{1, 10\}$. The same quantities are presented in figure 2.13(b) for a very active suspension characterized by $\ell/\delta = 30$.

Similar to the variation of the effective drift $U^{\text{eff}}/\overline{u}$ as a function of Pe with fixed ℓ/δ and ℓ/H shown in figure 2.9(b), we observe a non-monotonic variation of the effective longitudinal dispersivity D^{eff}/D_T as a function of the Péclet number. Notice that the effective dispersivity has three contributions, the translational diffusivity (D_T), fluctuation of the stream-wise swimming motion ($-U_s\overline{\tilde{m}_x}$) and fluctuation in the number density weighted by the flow ($-\overline{u\tilde{n}}$). Recall that in the absence of D_T, only the fluctuation in the swimming motion remains and the effective dispersivity reduces to the swim diffusivity if the flow speed is also zero. For small Péclet number, the flow is very weak and the dispersion is dominated by the fluctuation in self-propulsion. We have $D^{\text{eff}} \to D_T + D_0^{\text{swim}}$ as $Pe \to 0$. The dispersivity in this region is insensitive to the variation in confinement ℓ/H as discussed earlier for the no-flow case ($Pe = 0$).

In the large Péclet number limit, the advective effect dominates and the effective dispersion approaches that of the classical Taylor dispersion of passive particles. A minimum in the effective dispersivity is obtained when the effect of advection by the ambient flow is comparable to the self-propulsion of ABPs.

To understand the physical origin of this non-monotonic variation in the effective dispersivity, we consider two separate problems. First, by neglecting the advection ($\boldsymbol{u}_f = \boldsymbol{0}$), we remove the effect of classical Taylor dispersion and consider the effect of vorticity alone. As one increases strength of the vorticity, the effective reorientation time decreases due to the spinning motion while the random walk speed is unchanged. This reduced effective reorientation time gives rise to decreasing swim diffusivity. As $Pe \to \infty$ for fixed finite ℓ/δ and ℓ/H, $Pe_{\dot{\gamma}} \to \infty$, and the swim diffusivity $D^{\text{swim}} \to 0$. Next, we neglect the swimming motion of ABPs ($U_s = 0$) and simply recover the classical Taylor dispersion problem. In the classical Taylor dispersion problem, the effective dispersivity increases monotonically as a function of the Péclet number. By combining these two separate problems, the total effective dispersivity becomes non-monotonic as a function of the Péclet number. In other words, increasing of the flow strength diminishes the swim diffusivity while at the same time generates shear-induced dispersion. It is this competition that gives rise to the non-monotonic variation in the effective longitudinal dispersion of ABPs in a pressure-driven flow.

(a): $\ell/\delta = 2,$ low activity

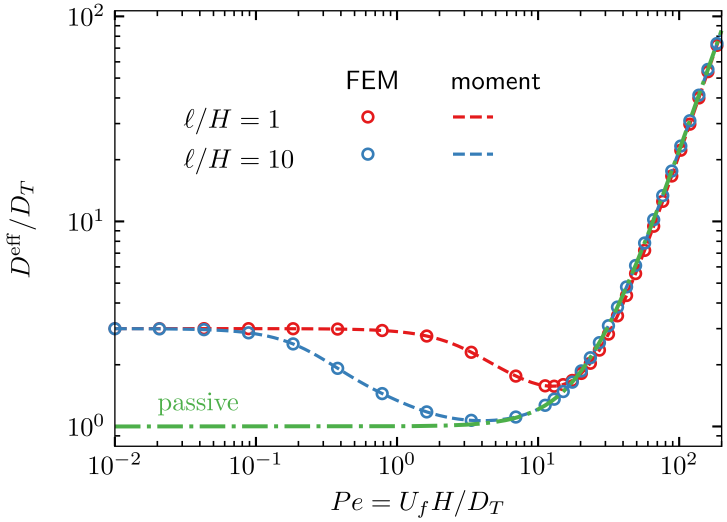

(b): $\ell/\delta = 30,$ high activity

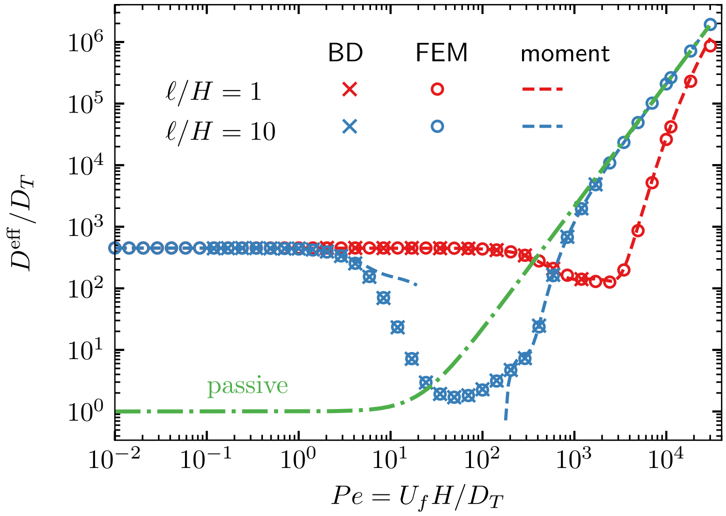

Figure 2.13: Effective longitudinal dispersivity D^{eff}/D_T as a function of $Pe = U_f H/D_T$ for (a) $\ell/\delta = U_s\tau_R/\sqrt{D_T\tau_R} = 2$ and (b) $\ell/\delta = 30$ and different confinement strengths (red: $\ell/H = U_s\tau_R/H = 1$; blue: $\ell/H = 10$). Circles are results from FEM and dashed lines are solution from moment equations. Results from BD simulation are marked by cross symbols. In regions of comparably large activity and flow strength, the moment equations do not agree with FEM or BD simulation. The classical dispersion for passive particles are plotted in a dash-dotted green line.

The above physical argument suggests the consideration of $Pe_{\dot{\gamma}}$ that characterizes how strong the biased rotation by vorticity is compared to random Brownian reorientation. Noting that $Pe_{\dot{\gamma}}$ is proportional to Pe for fixed ℓ/H and ℓ/δ from the relation $Pe_{\dot{\gamma}} = 2Pe(\ell/H)^2(\ell/\delta)^{-2}$. We can define a critical condition $Pe_{\dot{\gamma}} \sim 1$ where the rotational effect of the fluid vorticity becomes comparable to Brownian reorientation. If we consider a fixed activity level (e.g. $\ell/\delta = 30$ shown in figure 2.13(b)), we can predict the relative location of the minimal effective dispersivity when the confinement ℓ/H varies. For a fixed ℓ/δ, we require $(\ell/H)_1^2 Pe_1 \sim (\ell/H)_2^2 Pe_2$ where the subscripts 1 and 2 denote different confinement strengths. Using parameters in figure 2.13(b), we have $Pe_2/Pe_1 \sim 10^2$. Here, subscript 1 denotes $\ell/H = 10$ and 2 denotes $\ell/H = 1$. Similarly, we can consider a fixed confinement, say $\ell/H = 1$, and different activity level. By the same argument, we have $Pe_2/Pe_1 \sim 900$ with 2 denoting $\ell/\delta = 30$ and 1 being $\ell/\delta = 1$.

To recover the classical Taylor dispersion analytically, we set $U_s = 0$ in the moment equations and obtain $n^0 \equiv 1$. In other words, the average number density of passive particles is uniform across the channel as expected. The average drift is simply the average flow velocity $U^{\text{eff}} = 2U_f/3$. The fluctuating field number density can then be obtained

$$\tilde{n}(y) = -\frac{U_f H^2}{720 D_T}\left[7 - 120\left(\frac{y}{H}\right)^2 + 240\left(\frac{y}{H}\right)^4\right]. \tag{2.28}$$

Taking an average of $\tilde{n}$ weighted by the flow field, we recover the effective longitudinal dispersivity for passive particles $D^{\text{eff}}/D_T = 1 + 2Pe^2/945$. The numerical factor is different from that given in Brenner and Edwards (2013) due to their definition of the Péclet number based on the average instead of the maximum flow velocity. The effective dispersivity for passive particles as a function of Péclet number is plotted in figure 2.13 with a dash-dotted green line. In appendix 2.8, the effect of non-spherical shape on the longitudinal dispersion of ABPs is considered.

In figure 2.14, we show the variation of $D^{\text{eff}}/D_0^{\text{swim}}$ as a function of $Pe_{\dot{\gamma}}$ for $\ell/H = 2$ and different values of ℓ/δ. The blue cross markers are results for active particles with $D_T = 0$ ($\ell/\delta = \infty$), which has been shown in figure 2.12(a) with square markers. Decreasing ℓ/δ corresponds to increasing the translational diffusivity of the ABPs. The strong non-monotonic variation of the effective dispersion coefficient as a function of the flow speed ($Pe_{\dot{\gamma}}$) is observed when translational diffusion is weak (ℓ/δ is large). Due to the presence of classical Taylor dispersion for active particles with finite D_T, the non-monotonicity becomes weaker as D_T increases (ℓ/δ decreases).

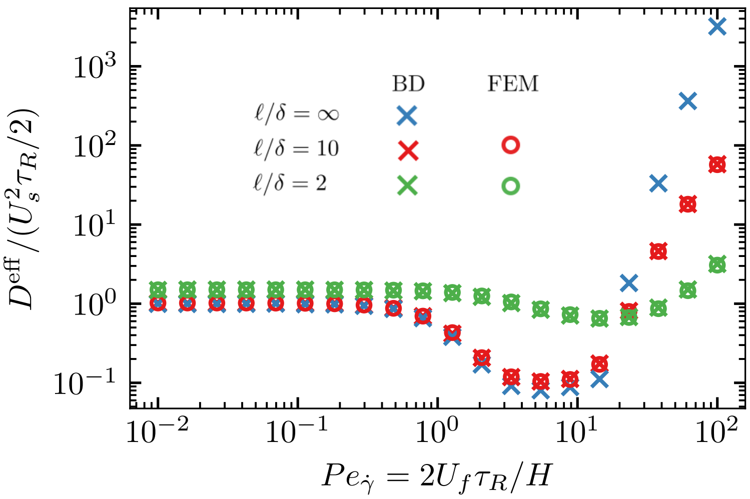

Figure 2.14: The effective longitudinal dispersion coefficient $D^{\text{eff}}/(U_s^2\tau_R/2)$ as a function of $Pe_{\dot{\gamma}}$ for different values of ℓ/δ. The degree of confinement is fixed, $\ell/H = 2$. For a given $Pe_{\dot{\gamma}}$ and ℓ/H, decreasing ℓ/δ corresponds to increasing the translational diffusivity.

2.5 Conclusion

In this Chapter, we have presented a combined analytical and numerical investigation of the effective longitudinal advection and dispersion of non-interacting isotropic ABPs in a planar Poiseuille flow. Using a generalized Taylor dispersion approach, we derived an effective longitudinal advection-diffusion equation for the cross-sectional average number density. The average drift and effective longitudinal dispersivity are then related to the average and fluctuating field moments, respectively. Our results from this continuum perspective are corroborated by Brownian dynamics simulations of the equations of motion for each active particle. Compared to the BD simulation, the continuum approach exposes the mathematical structure of the problem and elucidates the mechanism from which the observed upstream swimming and dispersive behavior emerges.

Self-propulsion of ABPs leads to interesting behavior in the average drift and effective longitudinal dispersion distinct from those of passive particles. Instead of being advected downstream, ABPs can swim upstream due to the biased rotation from the fluid vorticity. In the absence of flow, fluctuations in self-propulsion alone give rise to enhanced dispersion compared to the translational diffusivity. On the other hand, the combination of flow and activity can lead to a non-monotonic variation of the effective longitudinal dispersion with changing flow strength. By tuning the relative magnitudes of flow and self-propulsion, the long-time effective dispersivity of ABPs can be minimized.

Both upstream swimming and non-monotonic dispersion examined in this Chapter have received considerable attention in previous work using different model swimmers or methods. We have shown that the essential physics required to produce upstream swimming and non-monotonic dispersion are captured by the simple spherical ABP model. Regardless of the type of microorganisms or artificial active particles, the flow effects included in this work are universally present. As a result, the spherical ABP model provides a basis for the understanding of the transport of active particles in channel flow. In addition, the simplicity of the spherical ABP model allows the development of a continuum theory, which is challenging for active swimmers with complex body geometry.

Several previous work have studied the dynamics of non-spherical particles such as rod-like or beads-spring swimmers. To understand the effect of shape anisotropy, we consider a spheroidal particle and model the orientation dynamics using Jeffery's equation (Jeffery 1922). In the Smoluchowski equation, we need to include the additional effect of alignment from the rate-of-strain tensor $\boldsymbol{E}$ and write the rotational flux as $\boldsymbol{j}^R = \frac{1}{2}\boldsymbol{\omega}P + B\boldsymbol{q} \times (\boldsymbol{E} \cdot \boldsymbol{q})P - D_R \nabla_R P$. When $\boldsymbol{q}$ is aligned with one of the eigenvectors of $\boldsymbol{E}$, the dot product $\boldsymbol{E} \cdot \boldsymbol{q}$ is parallel to $\boldsymbol{q}$ and the term $\boldsymbol{q} \times (\boldsymbol{E} \cdot \boldsymbol{q})$ vanishes. The dimensionless parameter B quantifies the shape of the particle. For a sphere, $B = 0$. In the strong flow limit, the average drift of a non-spherical particle still approaches that of the passive particles. The effect of the alignment is to enhance upstream swimming when the flow is weak. Because the alignment do not modify the dispersion mechanism, we only expect a weak dependence of the longitudinal dispersion on the shape anisotropy. The effect of particle shape on the average drift and effective longitudinal dispersion is shown in figure 2.15 in appendix 2.8.

In addition to recovering the upstream swimming and non-monotonic dispersive behavior discovered by previous work, we systematically examined the effect of the flow speed, the swim speed, the reorientation time and the translational diffusivity on the dynamics of ABPs in Poiseuille flow. In particular, we studied the dynamics of active particles in the absence of translational diffusion, which has not been analyzed in detail previously. Under weak confinement, active particles without D_T experiences giant Taylor dispersion where $D^{\text{eff}}/D_0^{\text{swim}} \sim Pe_{\dot{\gamma}}^4$ for $Pe_{\dot{\gamma}} \gg 1$. We showed that a non-monotonic variation in longitudinal dispersion is also observed in the absence of D_T for confined active particles. For ABPs with finite D_T, we showed that $D^{\mathrm{eff}}/D_T \sim Pe^2$ for $Pe \gg 1$. For a fixed ℓ/δ and ℓ/H, this scaling for finite D_T can be alternatively written as $D^{\mathrm{eff}}/D_0^{\mathrm{swim}} \sim Pe_{\dot{\gamma}}^2$ using the relation $Pe_{\dot{\gamma}} = 2Pe(\ell/H)^2(\ell/\delta)^{-2}$. This difference in scaling reveals the singular nature of the limit $D_T \to 0$.

To conclude, we note that wall accumulation and upstream swimming have practical implications such as biofilm formation and bacteria infection. The results we have shown complement our understanding of the dynamics of active particles in Poiseuille flow and provide insights into the effective design of biomedical systems that aim to reduce infection or biofilm formation.

2.6 Appendix: The orientational moments

We substitute the moment expansion of g_0 and d_0 into equations (2.18) and (2.19) and take orientational moments to obtain the moment equations. The following identities are useful:

$$\int q_i q_j d\boldsymbol{q} = \pi\delta_{ij}, \qquad \int q_i q_j q_k q_l d\boldsymbol{q} = \frac{\pi}{4}(\delta_{ij}\delta_{kl} + \delta_{ik}\delta_{jl} + \delta_{il}\delta_{jk}), \tag{2.29}$$

where δ_{ij} is the Kronecker delta. At steady state, the average field moments satisfy

$$\frac{d}{dy}\left(U_s m_y^0 - D_T\frac{dn^0}{dy}\right) = 0, \tag{2.30}$$

$$\frac{d}{dy}\left(U_s Q_{yx}^0 - D_T\frac{dm_x^0}{dy}\right) + D_R m_x^0 + \frac{1}{2}\omega m_y^0 = 0, \tag{2.31}$$

$$\frac{d}{dy}\left(\frac{1}{2}U_s n^0 + U_s Q_{yy}^0 - D_T\frac{dm_y^0}{dy}\right) + D_R m_y^0 - \frac{1}{2}\omega m_x^0 = 0, \tag{2.32}$$

$$\frac{d}{dy}\left(\frac{1}{4}U_s m_y^0 - D_T\frac{dQ_{yy}^0}{dy}\right) + 4D_R Q_{yy}^0 - \omega Q_{yx}^0 = 0, \tag{2.33}$$

$$\frac{d}{dy}\left(\frac{1}{4}U_s m_x^0 - D_T\frac{dQ_{yx}^0}{dy}\right) + 4D_R Q_{yx}^0 + \omega Q_{yy}^0 = 0. \tag{2.34}$$

Here, $\omega = 8U_f y/H^2$ is the scalar vorticity. The no-flux boundary conditions at $y = \pm H/2$ are given by

$$U_s m_y^0 - D_T \frac{dn^0}{dy} = 0, \tag{2.35}$$

$$U_s Q_{yx}^0 - D_T \frac{dm_x^0}{dy} = 0, \tag{2.36}$$

$$\frac{1}{2}U_s n^0 + U_s Q_{yy}^0 - D_T \frac{d}{dy} m_y^0 = 0, \tag{2.37}$$

$$\frac{1}{4}U_s m_y^0 - D_T \frac{dQ_{yy}^0}{dy} = 0, \tag{2.38}$$

$$\frac{1}{4}U_s m_x^0 - D_T \frac{dQ_{yx}^0}{dy} = 0. \tag{2.39}$$

The steady-state moment equations for the fluctuating field are

$$\frac{d}{dy}\left(U_s \tilde{m}_y - D_T \frac{d\tilde{n}}{dy}\right) = (U^{\text{eff}} - u)n^0 - U_s m_x^0, \tag{2.40}$$

$$\frac{d}{dy}\left(U_s \tilde{Q}_{yx} - D_T \frac{d\tilde{m}_x}{dy}\right) + D_R \tilde{m}_x + \frac{1}{2}\omega \tilde{m}_y = (U^{\text{eff}} - u)m_x^0 - U_s\left(Q_{xx}^0 + \frac{1}{2}n^0\right), \tag{2.41}$$

$$\frac{d}{dy}\left(\frac{1}{2}U_s \tilde{n} + U_s \tilde{Q}_{yy} - D_T \frac{d\tilde{m}_y}{dy}\right) + D_R \tilde{m}_y - \frac{1}{2}\omega \tilde{m}_x = (U^{\text{eff}} - u)m_y^0 - U_s Q_{yx}^0, \tag{2.42}$$

$$\frac{d}{dy}\left(\frac{1}{4}U_s \tilde{m}_y - D_T \frac{d\tilde{Q}_{yy}}{dy}\right) + 4D_R \tilde{Q}_{yy} - \omega \tilde{Q}_{yx} = (U^{\text{eff}} - u)Q_{yy}^0 + \frac{1}{4}U_s m_x^0, \tag{2.43}$$

$$\frac{d}{dy}\left(\frac{1}{4}U_s \tilde{m}_x - D_T \frac{d\tilde{Q}_{yx}}{dy}\right) + 4D_R \tilde{Q}_{yx} + \omega \tilde{Q}_{yy} = (U^{\text{eff}} - u)Q_{yx}^0 - \frac{1}{4}U_s m_y^0. \tag{2.44}$$

Similar to the average field moments, the fluctuating field moments satisfy the no-flux conditions at the wall:

$$U_s \tilde{m}_y - D_T \frac{d\tilde{n}}{dy} = 0, \tag{2.45}$$

$$U_s \tilde{Q}_{yx} - D_T \frac{d\tilde{m}_x}{dy} = 0, \tag{2.46}$$

$$\frac{1}{2}U_s \tilde{n} + U_s \tilde{Q}_{yy} - D_T \frac{d\tilde{m}_y}{dy} = 0, \tag{2.47}$$

$$\frac{1}{4}U_s \tilde{m}_y - D_T \frac{d\tilde{Q}_{yy}}{dy} = 0, \tag{2.48}$$

$$\frac{1}{4}U_s \tilde{m}_x - D_T \frac{d\tilde{Q}_{yx}}{dy} = 0. \tag{2.49}$$

The normalization requires

$$\frac{1}{H}\int_{-H/2}^{H/2} n^0 dy = 1 \text{ and } \int_{-H/2}^{H/2} \tilde{n} dy = 0. \tag{2.50}$$

We solve these equations in Matlab using a Chebyshev collocation method (Trefethen 2000). Equation (2.30) along with its boundary condition (2.35) is analytically integrated once to obtain a first order equation

$$U_s m_y^0 - D_T \frac{dn^0}{dy} = 0. \tag{2.51}$$

To solve the average filed moment equations (2.31)–(2.34) and (2.51), we start from a guess for $n^0(-H/2)$ as a boundary condition and update the guess based on a root finding algorithm such that the normalization condition is satisfied within a tolerance of 10^{-6}. A similar approach for the fluctuating field equations is used.

2.7 Appendix: Brownian dynamics simulation

The motion of ABPs is governed by the overdamped Langevin equations as presented in equations (2.24) and (2.25). In 2D, we can parameterize the orientation vector by an orientation angle θ such that $\boldsymbol{q} = \cos\theta \boldsymbol{e}_x + \sin\theta \boldsymbol{e}_y$. The discretized Langevin equation is given by

$$\begin{aligned}
\Delta x &= u_f(y_n)\Delta t + U_s \cos\left[\theta(t_n)\right]\Delta t + \Delta x^B, \\
\Delta y &= U_s \sin\left[\theta(t_n)\right]\Delta t + \Delta y^B, \\
\Delta \theta &= \frac{1}{2}\omega(y_n)\Delta t + \Delta\theta^B,
\end{aligned} \tag{2.52}$$

where Δx is the particle displacement in x-direction over the time step Δt from t_n to t_{n+1}. Similarly, Δy is the displacement in y-direction and $\Delta\theta$ is the angular displacement. The Brownian displacement Δx^B (or Δy^B) is sampled from a white noise with a mean of 0 and variance of $2D_T\Delta t$. Similarly, the rotary Brownian displacement $\Delta\theta^B$ has a mean of 0 and variance of $2\Delta t/\tau_R$. The subscript n denotes the current time, and $t_{n+1} = t_n + \Delta t$. The position and orientation of a particle at t_{n+1} is then given by $x_{n+1} = x_n + \Delta x$, $y_{n+1} = y_n + \Delta y$, $\theta_{n+1} = \theta_n + \Delta\theta$. The position y_{n+1} is then corrected according to the potential-free algorithm if it overlaps with the channel wall. In our definition, the parameter H already includes the radius of the particle. In other words, when the center position of the particles exceeds $\pm H/2$, we move the particle back such that its center position is at $\pm H/2$. The particle size do not appear explicitly in the potential-free algorithm. We note that the radius of the ABPs is assumed to be negligible compared to the width of the channel. As a result, the ABPs experience zero background flow at contact with the wall.

In most simulations, we use a time step $\Delta t = 10^{-3} t_{\min}$ where $t_{\min}$ is the smallest time scale in the problem, which is estimated via $t_{\min} = \min(\tau_R, H^2/D_T, H/U_s, H/U_f)$. Simulations were run for a duration of $100 t_{\max}$ where $t_{\max}$ is the largest time scale in the problem. All simulations are performed using an in-house GPU-accelerated code consisting of $102,400$ active Brownian particles.

2.8 Appendix: Non-spherical particles

In figure 2.15(a), we show the average drift as a function of Pe for different values of B. For an ellipsoidal particle of major axis a and minor axis b, the shape factor is defined as $B = (r^2 - 1)/(r^2 + 1)$, where the aspect ratio $r = a/b$. For a sphere ($a = b$), we have $B = 0$. For a rod-like particle, $r \to \infty$ and $B \to 1$. As B increases from 0 to 1, the particle shape changes from a sphere to a rod. In the weak flow limit, alignment from the rate-of-strain tensor enhances upstream swimming of non-spherical particles. In figure 2.15(b), we show the effective longitudinal dispersion coefficient as a function of Pe for different values of B. We only observe a weak dependence of the dispersion on particle shape. We note that the same no-flux boundary condition for spherical ABPs ($\boldsymbol{e}_y \cdot \boldsymbol{j}^T = 0$ at the wall) is used in the Smoluchowski equation for non-spherical particles.

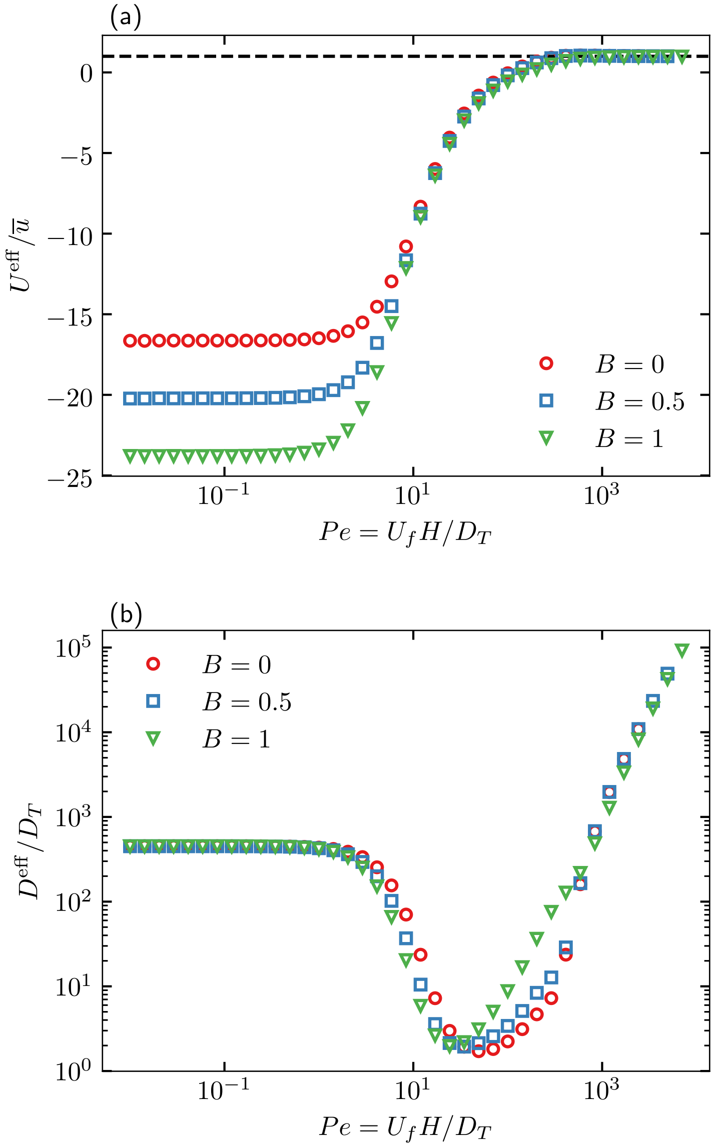

Figure 2.15: (a) The average drift $U^{\text{eff}}/\overline{u}$ as a function of Pe for different values of B. The black dashed line is the result for passive Brownian particles, $U^{\text{eff}}/\overline{u} \equiv 1$. (b) The effective longitudinal dispersion coefficient D^{eff}/D_T as a function of Pe for different values of B. In both panels, $\ell/H = 10$ and $\ell/\delta = 30$. Results are obtained from FEM simulation of the Smoluchowski equation.

Chapter 3

DYNAMICS OF AN ACTIVE ELLIPSOID IN A POISEUILLE FLOW

3.1 Introduction

In the previous Chapter, we developed a generalized Taylor dispersion approach to characterize the effective longitudinal transport of active Brownian spheres in a Poiseuille flow. However, many biological microswimmers such as *E. coli* have a nonspherical shape, which is often modeled as a prolate spheroid. Neglecting hydrodynamic interactions of the spheroid with the channel walls, the orientational dynamics of a prolate spheroid in pressure-driven flow is often modeled by Jeffery's equation (Jeffery 1922). Compared to a spherical particle that rotates with the local angular velocity of the flow, the spheroid experiences the additional effect of alignment from the rate-of-strain tensor.

In general, the interactions of a rigid particle with the channel walls include both hydrodynamic and steric effects. Even though we neglect hydrodynamic interactions, the steric interaction of a nonspherical particle with the channel walls is nontrivial. From a continuum perspective, the dynamics of an active Brownian particle is governed by the Smoluchowski equation and the steric interaction with the channel walls is enforced via boundary conditions. For spherical active Brownian particles of radius a as we considered in the previous Chapter, this is simply the no-flux condition: take the top wall located at $y = H/2$ as an example, the boundary condition is $\boldsymbol{e}_y \cdot \boldsymbol{j}_T = 0$ at $y = H/2 - a$, i.e. no flux of particle centers into the wall at a distance of the particle's radius away from the wall.

For a spheroid (or any nonspherical particle) in contact with a planar wall, the center position of the particle is coupled to its orientation. If the characteristic dimension of the spheroid is much smaller than the width of the channel, this orientation-dependent steric interaction is often neglected (Bees and Croze 2010; Croze et al. 2013; Zöttl and Stark 2013; Ezhilan and Saintillan 2015; Junot et al. 2019; Jiang and Chen 2019; 2021; Kumar et al. 2021). In this approach, the difference between the dynamics of spheroidal and spherical particles originate solely from the alignment effect of the rate-of-strain tensor, which we have explored in section 2.8 of the previous Chapter. To capture the orientation-dependent steric interaction, Nitsche and Brenner (1990) developed a generalized no-flux condition that applies locally at the hyperspace boundaries of the configuration space. This boundary condition comes naturally by integrating the Smoluchowski equation over the entire accessible phase space and demanding that the normal component of the generalized flux vector vanishes at each boundary point so as to conserve probability. The generalized no-flux condition of Nitsche and Brenner has been used to study the dynamics of nonspherical particles confined in a channel (Chen and Thiffeault 2021) and in planar Poiseuille flow (Ezhilan and Saintillan 2015).

While the generalized no-flux condition of Nitsche and Brenner guarantees that the particle does not overlap with the boundary, it does not take into consideration the contact-induced alignment of nonspherical particles with the wall. To see this, consider a spheroid approaching the wall at an oblique angle. Instead of staying in contact with the wall while maintaining its orientation, the spheroid is rotated such that its major axis aligns with the wall due to the torque induced by the off-center contact force. In this Chapter, we present a computational approach based on the micromechanical equations of motion subject to the geometric constraint of no overlap between the spheroid and the channel walls. Using this approach, we can resolve the steric interaction between the spheroid and the channel walls.

3.2 Problem formulation

We consider a rigid and active prolate spheroidal particle that swims with an intrinsic speed U_s along its major axis $\boldsymbol{p}$ ($\boldsymbol{p} \cdot \boldsymbol{p} = 1$)[1] in a planar Poiseuille flow between two parallel plates separated by a distance H. The spheroidal particle has a semi-major axis of length a and a semi-minor axis of length b, $a \geq b$. The parabolic flow profile is given by

$$\boldsymbol{u}_f = u_f(y)\boldsymbol{e}_x = U_f\left(1 - 4\frac{y^2}{H^2}\right)\boldsymbol{e}_x, \quad -\frac{H}{2} \leq y \leq \frac{H}{2}, \tag{3.1}$$

with the maximum fluid velocity U_f at the centerline of the channel ($y = 0$).

In this Chapter, we neglect hydrodynamic interactions but emphasize steric interactions of the active particle with the channel walls. Collision of the particle with a wall is assumed to be hard and has a single point of contact. At this contact point, the wall exerts a normal force that prevents the particle from penetrating the wall. When the spheroidal particle collides with a planar wall from an oblique angle, the normal

---

[1] In this Chapter, $\boldsymbol{q}$ is used to denote the generalized coordinate and $\boldsymbol{p}$ is used to denote the swimming direction of an active particle.

collisional force induces a torque that tends to align the major axis of the particle with the wall. This collision-induced alignment relies on the shape anisotropy and therefore is absent for a spherical particle.

In the absence of hydrodynamic interactions with the wall, we use the free-space resistance tensors of a single spheroidal particle to model the low Reynolds number dynamics. The force and torque balances on the spheroidal particle are given by, respectively,

$$-\boldsymbol{R}_{FU}\cdot\left(\boldsymbol{U}-\boldsymbol{u}_f-U_s\boldsymbol{p}\right)+\boldsymbol{F}_B+\boldsymbol{F}_C=\boldsymbol{0}, \tag{3.2}$$

$$-\boldsymbol{R}_{L\Omega}\cdot\left(\boldsymbol{\Omega}-\boldsymbol{\Omega}_f\right)+\boldsymbol{L}_B+\boldsymbol{L}_C=\boldsymbol{0}, \tag{3.3}$$

where $\boldsymbol{U}$ ($\boldsymbol{\Omega}$) is the instantaneous linear (angular) velocity; they satisfy the kinematic relations

$$\dot{\boldsymbol{x}}=\boldsymbol{U} \quad \text{and} \quad \dot{\boldsymbol{p}}=\boldsymbol{\Omega}\times\boldsymbol{p} \tag{3.4}$$

with the over-dot denoting the time derivative. For a prolate spheroid in free space, the resistance tensors can be written as

$$\boldsymbol{R}_{FU}=6\pi\mu a\left[X^A\boldsymbol{pp}+Y^A(\boldsymbol{I}-\boldsymbol{pp})\right], \tag{3.5}$$

$$\boldsymbol{R}_{L\Omega}=8\pi\mu a^3\left[X^C\boldsymbol{pp}+Y^C(\boldsymbol{I}-\boldsymbol{pp})\right], \tag{3.6}$$

where μ is the viscosity, and X^A, Y^A, X^C and Y^C are scalar resistance functions of Kim and Karrila (1991). For completeness, the resistance functions are listed here:

$$X^A=\frac{8}{3}e^3\left[-2e+(1+e^2)L\right]^{-1}, \tag{3.7}$$

$$Y^A=\frac{16}{3}e^3\left[2e+(3e^2-1)L\right]^{-1}, \tag{3.8}$$

$$X^C=\frac{4}{3}e^3(1-e^2)\left[2e-(1-e^2)L\right]^{-1}, \tag{3.9}$$

$$Y^C=\frac{4}{3}e^3(2-e^2)\left[-2e+(1+e^2)L\right]^{-1}, \tag{3.10}$$

where

$$L(e)=\ln\left(\frac{1+e}{1-e}\right) \tag{3.11}$$

and

$$e=\sqrt{a^2-b^2}/a \tag{3.12}$$

is the eccentricity.

Because a spheroid has three mutually perpendicular planes of symmetry (orthotropic), there is no translation-rotation coupling ($\boldsymbol{R}_{UL}=\boldsymbol{R}_{\Omega F}=\boldsymbol{0}$) in free-space.

The force ($\boldsymbol{F}_C$) and torque ($\boldsymbol{L}_C$) due to collision is only present when a collision is active. We model the angular velocity due to the background flow using Jeffery's equation (Jeffery 1922; Bretherton 1962)

$$\boldsymbol{\Omega}_f = \frac{1}{2}\boldsymbol{\omega} + \beta \boldsymbol{p} \times (\boldsymbol{E} \cdot \boldsymbol{p}), \tag{3.13}$$

where $\boldsymbol{\omega} = \nabla \times \boldsymbol{u}_f$ is the fluid vorticity and $\beta = (r^2 - 1)/(r^2 + 1)$ is the Bretherton constant characterizing the shape of the particle. The aspect ratio of the spheroid is $r = a/b \geq 1$. For a spherical particle, $a = b$ and $\beta = 0$; in the limit of an infinitely thin spheroid, $a/b \longrightarrow \infty$ and $\beta \longrightarrow 1$. The second term on the right-hand side of equation (3.13) represents alignment of $\boldsymbol{p}$ due to the local rate-of-strain tensor $\boldsymbol{E} = \frac{1}{2}(\nabla \boldsymbol{u}_f + (\nabla \boldsymbol{u}_f)^\intercal)$; this contribution to the angular velocity vanishes when $\boldsymbol{p}$ is aligned with one of the eigenvectors of $\boldsymbol{E}$.

3.2.1 Constrained equation of motion in 3D

To simulate the particle dynamics governed by equations (3.2) and (3.3) in 3D, it is more convenient to represent the orientational degrees of freedom using the normalized quaternion $\boldsymbol{\theta} = (s, \boldsymbol{v})^T$, a composition of a scalar $s \in \mathbb{R}$ and a vector $\boldsymbol{v} \in \mathbb{R}^3$ that satisfy the unit-norm constraint $\boldsymbol{\theta} \cdot \boldsymbol{\theta} = s^2 + \boldsymbol{v} \cdot \boldsymbol{v} = 1$. For a given deterministic angular velocity $\boldsymbol{\Omega}(t)$, the kinematics of rotational motion in terms of the quaternion $\boldsymbol{\theta}(t)$ satisfies

$$\dot{\boldsymbol{\theta}} = \boldsymbol{\Psi} \boldsymbol{\Omega}, \tag{3.14}$$

where

$$\boldsymbol{\Psi} = \frac{1}{2} \begin{bmatrix} -\boldsymbol{v}^\intercal \\ s\boldsymbol{I} - \boldsymbol{P} \end{bmatrix} \tag{3.15}$$

is a 4×3 matrix composed of elements of the quaternion $\boldsymbol{\theta}(t)$ (Delong et al. 2015). Here, $\boldsymbol{P}$ is a skew-symmetric matrix with elements $P_{ij} = \epsilon_{ikj} v_k$ and ϵ_{ijk} is the Levi-Civita tensor in three dimensions.

Delong et al. (2015) formulated the Ito Langevin equation of motion for a Brownian particle using the generalized coordinates $\boldsymbol{q} = (\boldsymbol{x}, \boldsymbol{\theta})^\intercal$. Following their approach, we write the equation of motion of an active Brownian spheroid in Poiseuille flow as

$$\dot{\boldsymbol{q}} = \tilde{\boldsymbol{\Psi}} \begin{bmatrix} U_s \boldsymbol{p} \\ 0 \end{bmatrix} + \tilde{\boldsymbol{\Psi}} \begin{bmatrix} \boldsymbol{u}_f \\ \boldsymbol{\Omega}_f \end{bmatrix} + \tilde{\boldsymbol{\Psi}} \boldsymbol{\mathcal{M}} \boldsymbol{\mathcal{F}}_c + \sqrt{2k_B T} \tilde{\boldsymbol{\Psi}} \boldsymbol{\mathcal{M}}^{1/2} \boldsymbol{\mathcal{W}} + k_B T \nabla_{\boldsymbol{q}} \cdot \left(\tilde{\boldsymbol{\Psi}} \boldsymbol{\mathcal{M}} \tilde{\boldsymbol{\Psi}}^\intercal \right), \tag{3.16}$$

where $\tilde{\boldsymbol{\Psi}} = \mathrm{diag}(\boldsymbol{I}, \boldsymbol{\Psi}) \in \mathbb{R}^{7\times6}$ is a block-diagonal matrix and $\boldsymbol{\mathcal{F}}_c \in \mathbb{R}^6$ is the generalized force vector (force and torque) due to collision with the boundary. In equation (3.16), the total velocity consists of the intrinsic swimming velocity, the linear and angular fluid velocities, the velocity due to collision with the wall ($\boldsymbol{\mathcal{U}}_c = \boldsymbol{\mathcal{M}}\boldsymbol{\mathcal{F}}_c$) and the velocity due to Brownian motion. The yet unknown collisional force (and velocity $\boldsymbol{\mathcal{U}}_c$) ensures that the particle does not penetrate the wall. Because the mobility tensor depends on the configuration $\boldsymbol{q}$, the Brownian velocity has two contributions as given by the last two terms in equation (3.16). In particular, the last term represents the Brownian drift due to the gradient of the mobility tensor. The "square root" of the mobility matrix is defined via the fluctuation-dissipation relation, $\boldsymbol{\mathcal{M}}^{1/2}\left(\boldsymbol{\mathcal{M}}^{1/2}\right)^{\intercal} = \boldsymbol{\mathcal{M}}$, and $\boldsymbol{\mathcal{W}}(t) \in \mathbb{R}^6$ is a vector of independent unit-variance white noise processes.

Following previous works on potential-free collision resolution (Tasora et al. 2008; Tasora and Anitescu 2011; Yan et al. 2019), we formulate the contact dynamics of a spheroid with the channel walls as an optimization problem based on geometric constraint. Collisions of the particle with a wall are assumed to be inelastic; the particle and the wall can remain in contact after collisions. We emphasize that during contact, the collisional force is normal to both the particle surface and the wall at the point of contact and friction is ignored. Before considering the collisional force, a description of the geometric condition of non-overlap is needed. This can be achieved by defining a gap function $\Phi_l(\boldsymbol{q})$ for a pair of objects labeled l—in our case the pair consists of the spheroid and one of the walls—such that $\Phi_l = 0$ if the pair is at contact and $\Phi_l > 0$ if the pair is not at contact. This purely geometric gap function can be written explicitly for a spheroid confined between two parallel plates,

$$\Phi_\pm(\boldsymbol{q}) = \frac{H}{2} \mp \boldsymbol{e}_y^{\intercal}\boldsymbol{x} - \left(\boldsymbol{e}_y^{\intercal}\boldsymbol{R}\boldsymbol{\Lambda}^{-1}\boldsymbol{R}^{\intercal}\boldsymbol{e}_y\right)^{1/2}, \tag{3.17}$$

where $\boldsymbol{\Lambda} = \mathrm{diag}(1/a^2, 1/b^2, 1/b^2)$, $\boldsymbol{e}_y = (0, 1, 0)^{\intercal}$ and $\boldsymbol{R}$ is the orthonormal rotation matrix (See section 3.5 for the derivation). The gap function Φ_+ (Φ_-) gives the minimum distance between any point on the spheroid and the upper (lower) wall for a given accessible particle configuration $\boldsymbol{q}$. In the case of a sphere, $a = b$ and the gap function for the upper wall reduces to the familiar expression $\Phi_+ = H/2 - y - a$.

If the pair l is at contact, $\Phi_l = 0$, the contact force is nonzero; denoting the force magnitude by γ_l, we have $\gamma_l > 0$. On the other hand, if the pair l is not at contact, we have $\Phi_l > 0$ and $\gamma_l = 0$. As a result, Φ_l and γ_l satisfies the so-called complementarity condition and is usually denoted by the notation

$$0 \leq \boldsymbol{\Phi} \perp \boldsymbol{\gamma} \geq 0, \tag{3.18}$$

where $\boldsymbol{\Phi} \in \mathbb{R}^{n_c}$ denotes the minimal separation distances between all possible collision pairs (n_c) and $\boldsymbol{\gamma} \in \mathbb{R}^{n_c}$ is the corresponding contact force magnitudes.

The contact force magnitude is mapped to the contact force via the director matrix $\boldsymbol{\mathcal{D}}$ such that

$$\boldsymbol{\mathcal{F}} = \boldsymbol{\mathcal{D}}\boldsymbol{\gamma}, \tag{3.19}$$

where the director matrix is a purely geometric quantity and given by (Tasora et al. 2008)

$$\nabla_q \boldsymbol{\Phi} = \boldsymbol{\mathcal{D}}^T. \tag{3.20}$$

Equations (3.16) and (3.18) complete the formulation of the constrained equation of motion for an active particle in the presence of a boundary. To simulate the constrained Langevin dynamics of the particle, a time discretization scheme is required.

3.2.2 Constrained equation of motion in 2D

The general formulation in the previous section still applies in 2D except that the orientation space is now represented by a single orientation angle θ such that the swimming direction $\boldsymbol{p} = \cos\theta \boldsymbol{e}_x + \sin\theta \boldsymbol{e}_y$. Realizing that in 2D $\boldsymbol{\Omega} = \Omega \boldsymbol{e}_z$ and $\dot{\boldsymbol{p}} = \dot{\theta}\boldsymbol{e}_z \times \boldsymbol{p}$, the orientational kinematic relation in (3.4) reduces to the familiar form $\dot{\theta} = \Omega$. The Langevin equation of motion analogous to (3.16) in 2D can be written as

$$\dot{\boldsymbol{q}} = \begin{bmatrix} U_s \boldsymbol{p} \\ 0 \end{bmatrix} + \begin{bmatrix} \boldsymbol{u}_f \\ \Omega_f \end{bmatrix} + \boldsymbol{\mathcal{M}}\boldsymbol{\mathcal{F}}_c + \sqrt{2k_BT}\boldsymbol{\mathcal{M}}^{1/2}\boldsymbol{\mathcal{W}} + k_BT\nabla_{\boldsymbol{q}} \cdot \boldsymbol{\mathcal{M}}, \tag{3.21}$$

where the generalized coordinate $\boldsymbol{q} = (\boldsymbol{x}, \theta)^{\intercal} \in \mathbb{R}^3$.

For many active matter systems, the swim diffusivity is often much larger than the thermal diffusivity. As a result, we neglect the thermal translational and rotational Brownian motion. Furthermore, a biological microswimmer may ‘decide’ to change its orientation by, for example, actuating the flagella on a different side of its body without disturbing the flow; we model this process using a rotary diffusion process with the rotary diffusivity D_R. Since the origin of D_R is biological rather than thermal in origin, it is independent of the thermal energy k_BT.

Under the above assumptions, equation (3.21) becomes

$$\dot{\boldsymbol{q}} = \begin{bmatrix} U_s \boldsymbol{p} \\ 0 \end{bmatrix} + \begin{bmatrix} \boldsymbol{u}_f \\ \Omega_f \end{bmatrix} + \boldsymbol{\mathcal{M}}\boldsymbol{\mathcal{F}}_c + \begin{bmatrix} 0 \\ \sqrt{2D_R}\mathcal{W} \end{bmatrix}, \tag{3.22}$$

where $\mathcal{W}$ is a unit-variance white noise process satisfying

$$\langle \mathcal{W} \rangle = 0 \quad \text{and} \quad \langle \mathcal{W}(0)\mathcal{W}(t) \rangle = \delta(t). \tag{3.23}$$

From equation (3.13), the scalar angular velocity due to the flow can be shown to be

$$\Omega_f = \frac{4U_f y}{H^2} \left[1 - \beta \cos(2\theta)\right]. \tag{3.24}$$

3.2.3 Time discretization

We discretize equation (3.22) using the Euler-Maruyama scheme. For a time step size Δt, we have at $t_k = k\Delta t$

$$\frac{\boldsymbol{q}^{k+1} - \boldsymbol{q}^k}{\Delta t} = \begin{bmatrix} U_s \boldsymbol{p}^k \\ 0 \end{bmatrix} + \begin{bmatrix} \boldsymbol{u}_f^k \\ \Omega_f^k \end{bmatrix} + \boldsymbol{\mathcal{M}}^k \boldsymbol{\mathcal{F}}_c^k + \begin{bmatrix} 0 \\ \sqrt{2D_R/\Delta t}W \end{bmatrix}, \tag{3.25}$$

where W is a pseudorandom number with zero mean and unit variance. To resolve the potential boundary collisions, we require

$$0 \leq \boldsymbol{\Phi}\left(\boldsymbol{q}^{k+1}\right) \perp \gamma^k \geq 0. \tag{3.26}$$

Because the minimum gap function $\boldsymbol{\Phi}$ is a nonlinear function of $\boldsymbol{q}$, the above formulation constitutes a nonlinear complementarity problem. Following the work of Yan et al. (2019), the complementarity problem is linearized and solved as a linear complementarity problem.

A straightforward dimensional analysis reveals that the problem is governed by four dimensionless groups: (i) the size of the ellipsoid compared to the channel a/H, (ii) the aspect ratio of the ellipsoid $r = a/b$, (iii) the confinement in the absence of flow $\ell/H = U_s\tau_R/H$, and (iv) the comparison of the flow speed and the swim speed U_f/U_s.

3.3 Deterministic dynamics

To probe the effect of the contact force/torque on the dynamics of the ellipsoid, we first present results in the absence of random noises ($D_R = 0$). In figure 3.1 we show the time evolution of the position and orientation of the ellipsoid as it interacts with the top wall of the channel for (a) no flow, (b) weak flow and (c) stronger flow. The simulation is started from the position $y/H = 0.3$ and orientation $\theta = \pi/4$. In the absence of flow, the ellipsoid swim towards the top wall following the initial orientation until it reaches the wall. Because the ellipsoid comes into contact with the wall at an oblique angle, the contact force is off-center and induces a net torque

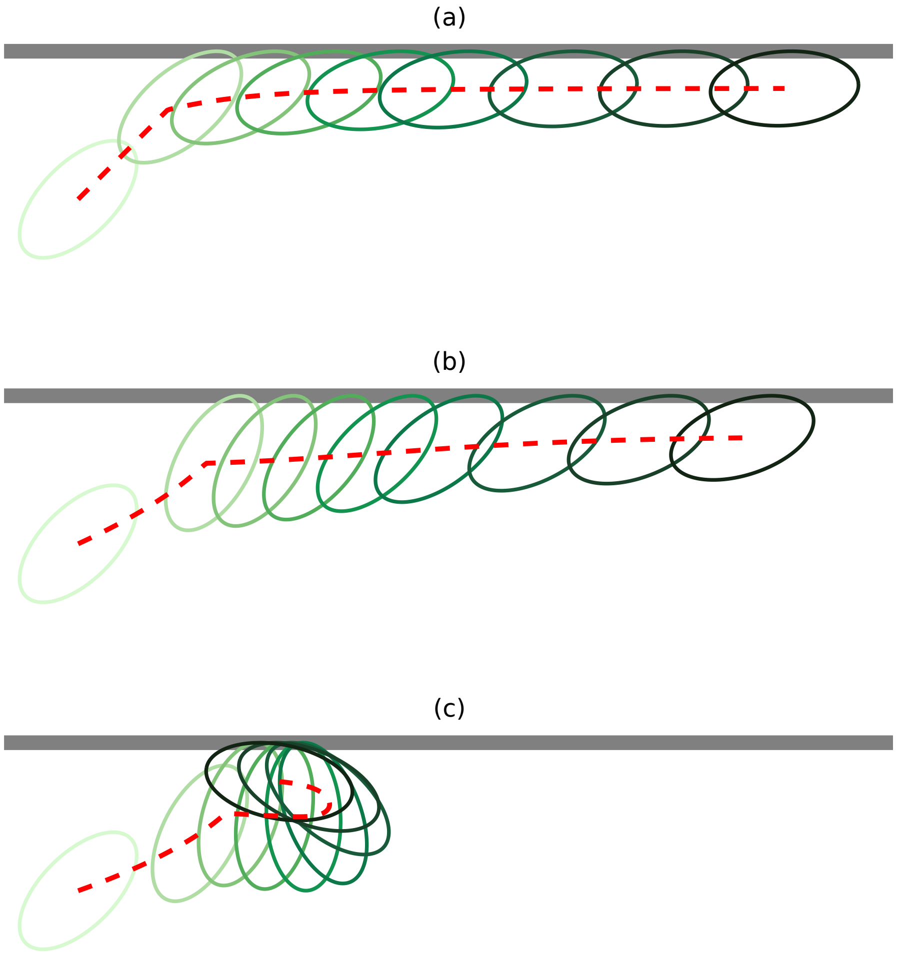

Figure 3.1: Interaction of an active ellipsoid ($a/H = 0.1, a/b = 2$) without noise in 2D with the top wall of the channel for (a) no flow, (b) weak flow, and (c) stronger flow. The red dashed line denotes the trajectory of the center of the ellipsoid. The color gradient of the ellipsoids denotes the evolution of time (from light to dark). The simulation is started from the initial condition $y/H = 0.3$ and $\theta = \pi/4$. The bottom wall of the channel is not shown.

on the ellipsoid that tends to align the major axis of the ellipsoid with the channel wall. As can be seen from figure 3.1(a), the contact torque rotates the ellipsoid such that at later times it becomes aligned with the wall. Once aligned horizontally ($\theta = 0$), the contact force and torque vanishes and the particle keeps swimming towards the right while maintaining contact with the wall. In other words, at long times the ellipsoid in figure 3.1(a) reaches the fixed point $(H/2 - b, 0)$ in the (y, θ) phase space.

For weak flow shown in figure 3.1(b), the ellipsoid is rotated counterclockwise towards the upstream (left) direction; it will then reach the wall with an orientation angle $\pi/4 < \theta < \pi/2$. Because at contact its orientation angle is less than $\pi/2$, the contact torque induces a clockwise rotation towards the downstream. At long times, the particle exhibits a nonzero orientation angle determined by the balance of the torque due to flow and the contact torque. As a result, the particle moves downstream while keeps pushing against the wall. If the flow is strong, as shown in figure 3.1(c), the particle approaches the wall with an angle close to $\pi/2$ and the contact torque is weak. Therefore, the flow torque is able to rotate the particle such that $\theta > \pi/2$. Once $\theta > \pi/2$, the contact torque reverses its direction to be counterclockwise and acts to further rotate the ellipsoid. The ellipsoid is then rotated towards the upstream direction and is able to escape into the bulk of the channel. At long times, the trajectory reaches a limit cycle in the (y, θ) space.

To classify the behavior of the system in the absence of noise, in figure 3.2 we show the phase plot for varying initial position y and U_f/U_s. Initially, the particle is pointing towards the downstream, $\theta = 0$. Because the angular velocity due to flow at the channel centerline ($y = 0$) is zero, a particle with the initial position $y = 0$ and orientation $\theta = 0$ will stay on the channel centerline; therefore ($y = 0, \theta = 0$) is a fixed point in the phase space [2]. If the particle starts slightly above the centerline, for large flow speed it will reach a limit cycle at long times. If the particle starts near the wall, it will approach the wall and follow a trajectory similar to those shown in figure 3.1(b). As the flow speed (therefore the rotation due to flow) increases, the range of initial y positions that allow the particle to reach the limit cycle is widened. In figure 3.3, the phase-space trajectories and the long-time limit cycles are presented for several values of U_f/U_s.

---

[2] This fixed point is unstable (Peng and Brady 2020).

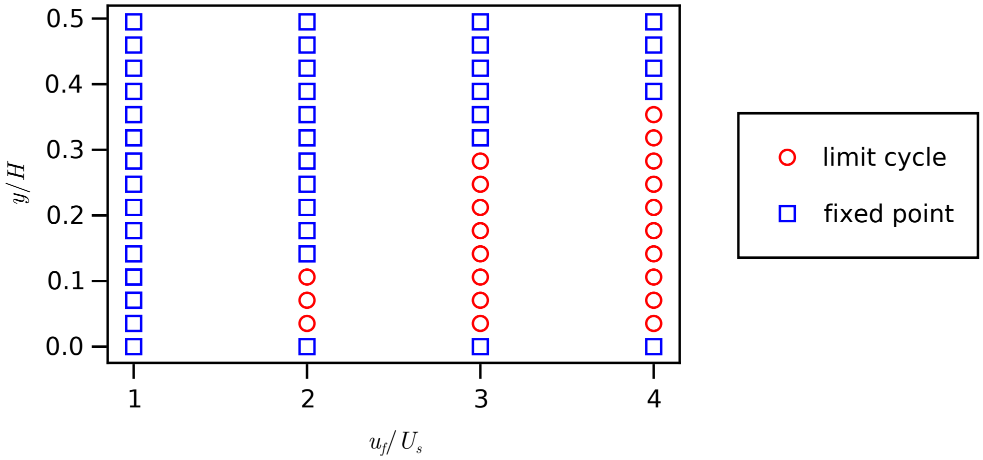

Figure 3.2: Classification of the long-time particle dynamics in the (y, θ) phase space. All simulations are started with the initial orientation $\theta = 0$. The dimensions of the ellipsoid are given by $a/H = 0.01, a/b = 2$.

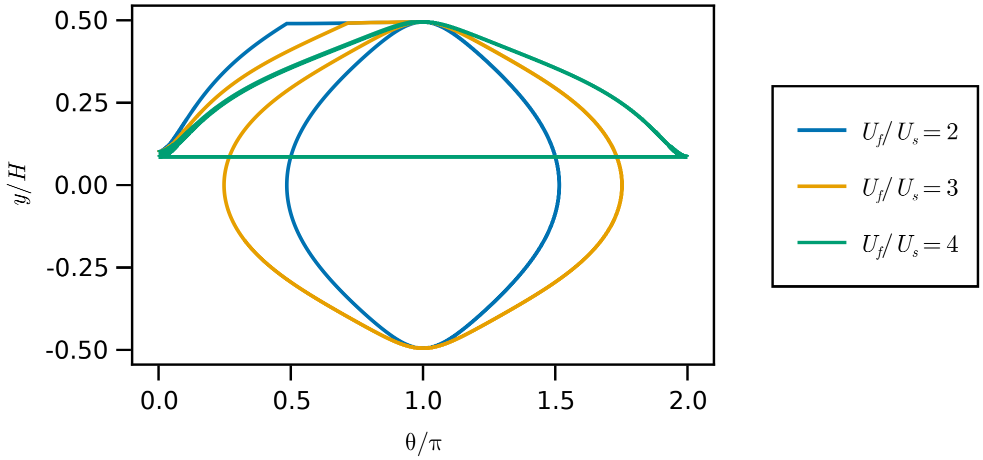

Figure 3.3: Example phase-space trajectories of an active ellipsoid. The dimensions of the ellipsoid are given by $a/H = 0.01, a/b = 2$.

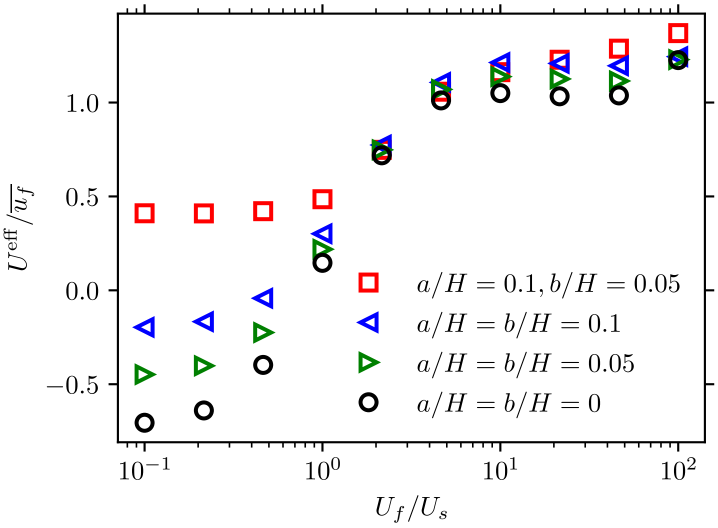

Figure 3.4: The average drift $U^{\mathrm{eff}}/\overline{u_f}$ as a function of the dimensionless flow speed U_f/U_s for different particle shapes. For all results, $\ell/H = U_s\tau_R/H = 1.0$. The average flow speed $\overline{u_f} = 2U_f/3$.

3.4 Effective transport

We now turn to the effective longitudinal transport of active ellipsoids in the absence of translational diffusion but with finite rotational diffusion. In figure 3.4, we plot the non-dimensional average drift $U^{\mathrm{eff}}/\overline{u_f}$ as a function of the dimensionless flow speed U_f/U_s for different particle shapes. The average flow speed across the channel $\overline{u_f} = 2U_f/3$ is achieved for passive point Brownian particles. For passive Brownian spheres, the average drift with a uniform number density distribution is given by

$$U^{\mathrm{eff}} = \left[\frac{2}{3} - \frac{4}{3}\left(\frac{a}{H}\right)^2 + \frac{4}{3}\left(\frac{a}{H}\right)\right] U_f, \tag{3.27}$$

which is obtained by averaging the flow velocity from $-H/2 + a$ to $H/2 - a$. For small but nonzero a/H, the average drift of passive Brownian spheres is larger than the average flow speed $2U_f/3$ because particles are excluded from the walls by a distance of a.

As shown in figure 3.4, the average drift of active spheres increases as a function of a/H. In the small U_f/U_s limit, active spheres with $a/H = \{0.1, 0.05, 0\}$ are able to exhibit a net upstream speed. For $a/H = 0$, the upstream swimming speed is the largest because a particle with $a/H = 0$ can reach the wall where the flow speed is zero. For active ellipsoids, the average drift is positive. This suppression of

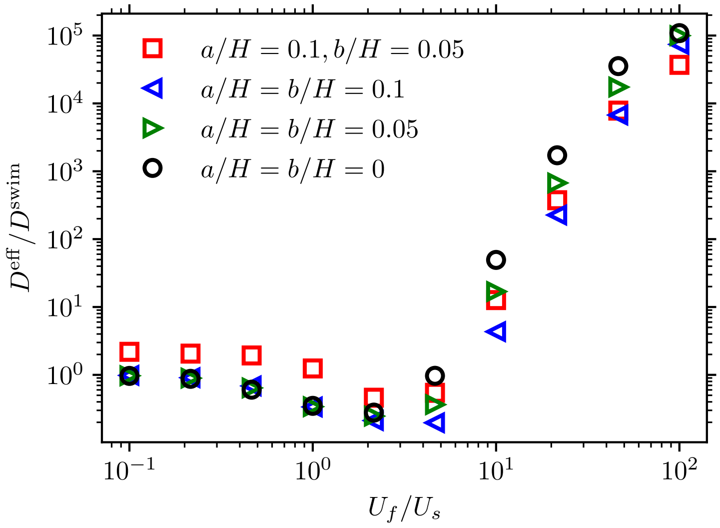

Figure 3.5: The effective longitudinal dispersion $D^{\mathrm{eff}}/D^{\mathrm{swim}}$ as a function of the dimensionless flow speed U_f/U_s for different particle shapes. For all results, $\ell/H = U_s\tau_R/H = 1.0$.

upstream swimming is due to the interaction between the ellipsoid and the channel walls as shown in figures 3.1(a) and (b).

In figure 3.5, we present the dimensionless effective longitudinal dispersion $D^{\mathrm{eff}}/D^{\mathrm{swim}}$ as a function of U_f/U_s for different particle shapes. For spherical/point particles, in the small flow limit, the dispersion is due to activity and given by the swim diffusivity $D^{\mathrm{swim}} = U_s^2\tau_R/2$. The size of the sphere does not affect the swim diffusivity. For active ellipsoid, however, the steric interaction with the wall increases the swim diffusivity.

3.5 Appendix: Minimum separation between a spheroid and a planar wall

In its body frame, the surface of a spheroid is parametrized by

$$\boldsymbol{X}^{\intercal}\boldsymbol{\Lambda}\boldsymbol{X} = 1, \tag{3.28}$$

where $\boldsymbol{\Lambda} = \mathrm{diag}(1/a^2, 1/b^2, 1/b^2)$ and $\boldsymbol{X}$ is the Cartesian coordinates in the body frame. Using the rotation matrix $\boldsymbol{R}$, the spheroidal surface in the lab frame is $\boldsymbol{y} = \boldsymbol{x} + \boldsymbol{R}\boldsymbol{X}$, where $\boldsymbol{x}$ is the Cartesian coordinates of the geometric center in the lab frame. In the lab frame, equation (3.28) becomes

$$(\boldsymbol{y} - \boldsymbol{x})^{\intercal}\, \boldsymbol{R}\boldsymbol{\Lambda}\boldsymbol{R}^{\intercal}\, (\boldsymbol{y} - \boldsymbol{x}) = 1, \tag{3.29}$$

where we have used the orthogonality condition $\boldsymbol{R}\boldsymbol{R}^{\intercal} = \boldsymbol{R}^{\intercal}\boldsymbol{R} = \boldsymbol{I}$.

The outward vector that is normal to the spheroidal surface is in the direction of the vector $\boldsymbol{R}\boldsymbol{\Lambda}\boldsymbol{R}^{\intercal}(\boldsymbol{y}-\boldsymbol{x})$. For the upper wall located at $y = H/2$, its upward unit normal vector is $\boldsymbol{e}_y$. At the point on the spheroid that has a minimum separation with the wall, the normal vectors must be parallel, which gives

$$\boldsymbol{R}\boldsymbol{\Lambda}\boldsymbol{R}^{\intercal}(\boldsymbol{y}-\boldsymbol{x}) = \lambda_+\boldsymbol{e}_y. \tag{3.30}$$

Inverting equation (3.30) for $\boldsymbol{y}-\boldsymbol{x}$ and inserting into equation (3.29), we obtain the positive solution

$$\lambda_+ = \frac{1}{\sqrt{\boldsymbol{e}_y^{\intercal}\boldsymbol{R}\boldsymbol{\Lambda}^{-1}\boldsymbol{R}^{T}\boldsymbol{e}_y}}. \tag{3.31}$$

From equation (3.30), the point of minimum separation on the spheroid is $\boldsymbol{y}^* = \boldsymbol{x} + \lambda_+\boldsymbol{R}\boldsymbol{\Lambda}^{-1}\boldsymbol{R}^{\intercal}\boldsymbol{e}_y$. As a result, we obtain

$$\Phi_+ = \frac{H}{2} - \boldsymbol{e}_y^{\intercal}\boldsymbol{y}^*, \tag{3.32}$$

which upon inserting the solution to λ_+ from (3.31) becomes equation (3.17) in the main text. Following the same procedure, the minimum separation between the spheroid and the lower wall located at $y = -H/2$ can be obtained.

Equation (3.17) is valid in both two and three dimensions. In 2D, by parametrizing $\boldsymbol{p} = \cos\theta\boldsymbol{e}_x + \sin\theta\boldsymbol{e}_y$ with $\theta \in [0, 2\pi)$ being the orientation angle, we can write the minimum separation as

$$\Phi_\pm(\boldsymbol{x}, \theta) = \frac{H}{2} \mp y - \sqrt{b^2\cos^2\theta + a^2\sin^2\theta}. \tag{3.33}$$

The gradients of $\Phi_\pm$ with respect to the configuration space variables are

$$\nabla_x\Phi_\pm = (0, \mp 1)^{\intercal} \quad \text{and} \quad \frac{\partial\Phi_\pm}{\partial\theta} = -\frac{(a^2-b^2)\sin\theta\cos\theta}{\sqrt{b^2\cos^2\theta + a^2\sin^2\theta}}. \tag{3.34}$$

Chapter 4

TRAPPED-PARTICLE MICRORHEOLOGY

In microrheology, the local rheological properties such as viscoelasticity of a complex fluid are inferred from the free or forced motion of embedded colloidal probe particles. Theoretical machinery developed for forced-probe microrheology of colloidal suspensions focused on either constant-force (CF) or constant-velocity (CV) probes while in experiments neither the force nor the kinematics of the probe is fixed. More importantly, the constraint of CF or CV introduces a difficulty in the meaningful quantification of the fluctuations of the probe due to a thermodynamic uncertainty relation. It is known that for a Brownian particle trapped in a harmonic potential well, the product of the standard deviations of the trap force and the particle position is dk_BT in d dimensions with k_BT being the thermal energy. As a result, if the force (position) is not allowed to fluctuate, the position (force) fluctuation becomes infinite. To allow the measurement of fluctuations, in this work we consider a microrheology model in which the embedded probe is dragged along by a moving harmonic potential so that both its position and the trap force are allowed to fluctuate. Starting from the full Smoluchowski equation governing the dynamics of N hard active Brownian particles, we derive a pair Smoluchowski equation describing the dynamics of the probe as it interacts with one bath particle by neglecting hydrodynamic interactions among particles in the dilute limit. From this, we determine the mean and the variance (i.e., fluctuation) of the probe position in terms of the pair probability distribution. As an example, we characterize the fluctuations of a passive Brownian probe in a bath of passive Brownian particles. For the case of an active probe and no bath particles, we show that the fluctuation includes an active contribution in addition to dk_BT. In the presence of bath particles, we show that our model reduces to the CF or CV microrheology when appropriate limits are taken.

4.1 Introduction

Rheology is the study of flow and deformation of complex materials in response to an applied force. Traditional (bulk) rheological measurements are performed by shearing a macroscopic sample of the material confined between two solid surfaces, such as in the cone and plate rheometer. Bulk rheological studies such as shear rheometry provide a measurement of the macroscopic rheological behavior of complex materials.

Recently, particle-tracking microrheology has become a standard tool for studying the mechanical properties of materials on a much smaller scale. In contrast to bulk rheology, microrheology only requires a small sample volume and can be used to quantify spatial heterogeneity. As a result, microrheology is particularly useful for examining soft biological materials. For example, classical bulk rheometry cannot be used to probe the microenvironment inside living cells without disrupting their mechanical structure while particle-tracking microrheology can be performed (Wilhelm et al. 2003; Nawaz et al. 2012; Berret 2016; Ayala et al. 2016; Hu et al. 2017).

To aid in the understanding of experimental measurements and in the prediction of colloidal microrheology, Squires and Brady (2005) developed a theoretical framework in which a colloidal probe is pulled through a suspension of neutrally buoyant bath colloids. This model has been used and generalized to study the microrheology of passive colloids (Khair and Brady 2005; 2006; Meyer et al. 2006; Zia and Brady 2010; Swan and Zia 2013; Zia 2018) and active colloids (Burkholder and Brady 2019; 2020). When the external pulling force is absent, the probe 'collides' with bath particles as it undergoes Brownian motion—the so-called tracer diffusion problem. To characterize the nonlinear response, forced microrheology is considered in which an external force, often larger than the thermodynamic restoring force, is applied to the probe. Within forced microrheology, two operating modes—constant-force (CF) and constant-velocity (CV)—are often considered from a theoretical perspective. In the CF mode, the probe is driven by a constant external force $\boldsymbol{F}^{\text{ext}}$ and the velocity of the probe is fluctuating. Conversely, for a CV probe, the probe velocity $\boldsymbol{U}_1$ is a constant vector (Therefore, the position of the probe is known at all times.) and the force required to maintain such a steady motion must fluctuate.

To characterize the micro-viscous response of colloidal suspensions, an effective microviscosity η^{eff} can be defined using the Stokes drag law. For a spherical probe of radius a in the CF mode, this is given by $F^{\text{ext}} = 6\pi\eta^{\text{eff}}\langle U_1\rangle$, where $\langle U_1\rangle$ the probe velocity in the direction of $\boldsymbol{F}^{\text{ext}}$ averaged over Brownian fluctuations. The ratio between the effective microviscosity and the solvent viscosity, η^{eff}/η, is the main quantity of interest in colloidal microrheology. For the CV mode, the average external force is used in the definition of the effective microviscosity: $\langle F^{\text{ext}}\rangle = 6\pi\eta^{\text{eff}}U_1$. In order to measure the microviscoelastic response of suspensions, an oscillatory driving force is considered (Khair and Brady 2005).

While the CF (or CV) model is successful in quantifying the mean velocity (or mean force) of a probe driven through colloidal suspensions. The fluctuation from this mean value is largely unexplored. Taking the CV mode as an example, one could calculate the variance of the mean force using the probe-distorted microstructure. The questions is what does this variance physically imply? In particular, how does this variance relate to the fluctuations in the suspension? In an experimental setting, neither the force nor the velocity of the probe is fixed; they are both allowed to fluctuate (Meyer et al. 2006; Weihs et al. 2006; Cicuta and Donald 2007; Yao et al. 2009).

To mimic the experimental realization more closely and motivate later discussions, consider the simple case of an isolated Brownian particle in a harmonic trap that is centered at the origin (arbitrary). In this physical picture, both the position and the velocity of the particle is fluctuating. A statistical mechanical description can be adopted in which one defines the probability density, $P(\boldsymbol{r}, t)$, of finding the particle at position $\boldsymbol{r}$ relative to the fixed trap at time t. Conservation of probability dictates that $P(\boldsymbol{r}, t)$ is governed by the Smoluchowski equation, which reads $\partial P/\partial t + \nabla \cdot \boldsymbol{j} = 0$, where the flux vector $\boldsymbol{j} = P\boldsymbol{F}^{\text{trap}}/\zeta - D_T \nabla P$. Here, $\boldsymbol{F}^{\text{trap}}$ is the trap force and for a harmonic trap is given by $\boldsymbol{F}^{\text{trap}} = -k\boldsymbol{r}$ with k being the spring constant; ζ is the drag coefficient and D_T is the thermal diffusivity given by the Stokes-Einstein-Sutherland relation, $\zeta D_T = k_B T$, where $k_B T$ is the thermal energy. The mean external force exerted on the Brownian particle is $\langle \boldsymbol{F}^{\text{trap}} \rangle = \int \boldsymbol{F}^{\text{trap}} P d\boldsymbol{r} = -k \int \boldsymbol{r} P d\boldsymbol{r} = -k\langle \boldsymbol{r} \rangle$. Because the trap is harmonic, the mean force is proportional to the mean displacement with $-k$ being the constant of proportionality. For a fixed trap, the mean position (therefore the mean force) is zero, $\langle \boldsymbol{r} \rangle = \boldsymbol{0}$. The variance of the force, $\mathrm{Var}\left(\boldsymbol{F}^{\text{trap}}\right) = k^2\, \mathrm{Var}(\boldsymbol{r})$. A straightforward calculation leads to the result

$$\mathrm{Var}(\boldsymbol{r}) = \frac{k_B T}{k} \boldsymbol{I}, \tag{4.1}$$

where $\boldsymbol{I}$ is the identity tensor. Introducing the shorthand $\Delta \boldsymbol{F}^{\text{trap}} = \boldsymbol{F}^{\text{trap}} - \langle \boldsymbol{F}^{\text{trap}} \rangle$, we can write the fluctuation relation as

$$\left\langle (\Delta \boldsymbol{F}^{\text{trap}})^2 \right\rangle^{1/2} \left\langle (\Delta \boldsymbol{r}_1)^2 \right\rangle^{1/2} = d k_B T, \tag{4.2}$$

where d is the spatial dimensionality.

Equation (4.2) is a fundamental result and a few comments on its implications are in order. First, by harmonically trapping a particle immersed in a solvent, the product of the standard deviations of the trap force and the particle position gives precisely the thermal fluctuations of the solvent—dk_BT. Second, one can decrease the uncertainty in the position by increasing the stiffness of the trap [see equation (4.1)]. However, the trade-off is that the fluctuation in the force must increase due to (4.2). Said differently, this constitutes a thermodynamic uncertainty relation in which one cannot decreases the fluctuations in both the force and the position simultaneously. If the fluctuation in the position vanishes (infinitely stiff trap), the fluctuation in the force blows up.

We note that (4.2) is observed elsewhere. For example, consider an ideal Gaussian polymer chain with one end localized in a harmonic trap. The fluctuations of the trap force and the position from the trap center satisfies an identical relation (Wang 2017).

We are now in a position to consider the fluctuations in the microrheology problem. Instead of considering either CF or CV, we must allow both the position of and the force on the probe to fluctuate in order to have a meaningful quantification of fluctuations. Equation (4.2) also implies that we should consider the position not the velocity of the probe. In the CF mode, therefore, the quantity of interest for fluctuations is the variance of the position of the probe, which is just the force-induced tracer diffusion problem. That is, the tracer diffusivity under the influence of a constant force should be considered—not the variance of the velocity. For the CV mode, the position of the probe is also prescribed and the fluctuation in the force is infinite. As a result, in the CV mode the computed variance of the force does not have a physical meaning.

In this Chapter, to closely mimic the setup of microrheological experiments, we consider a trapped-particle microrheology model in which the colloidal probe particle is driven by a translating harmonic trap. Because biological materials examined by microrheology such as the microenvironment inside living cells often contain active 'particles', we model the suspension as an active colloidal suspension. The colloidal particles in an active suspension are able to self-propel, which can be a model for either biologically active microswimmers or synthetic phoretic particles. This active colloidal suspension model also includes passive (not self-propelled) colloidal systems, which can be obtained by setting the swim speed to zero.

4.2 Mechanics of active Brownian suspensions

Consider a colloidal suspension consisting of N particles dispersed in an incompressible Newtonian fluid (solvent) of dynamic viscosity η. The particles could be active and are subject to fluctuating thermal (Brownian) forces from the solvent. Furthermore, the inertia of the fluid and the particles are assumed to be negligible. In this low Reynolds number regime, the fluid dynamics is governed by the linear Stokes equations and the probability distribution of the particles are described by the Smoluchowski equation. In general, all N particles could be active, and we model them as active Brownian particles. The probability distribution for finding the N particles in positions $\{\boldsymbol{x}_\alpha\}$ and orientations $\{\boldsymbol{q}_\alpha\}$ at a given time t is denoted as $P_N(\boldsymbol{x}^N, \boldsymbol{q}^N, t)$ where $\alpha = 1, \cdots, N$ is the particle label. In the laboratory frame of reference, the N-particle Smoluchowski equation is given by

$$\frac{\partial P_N}{\partial t} + \sum_{\alpha=1}^{N} \nabla_\alpha^T \cdot \boldsymbol{j}_\alpha^T + \sum_{\alpha=1}^{N} \nabla_\alpha^R \cdot \boldsymbol{j}_\alpha^R = 0, \tag{4.3}$$

where $\nabla_\alpha^T = \partial/\partial \boldsymbol{x}_\alpha$ is the spatial gradient operator with respect to the position vector ($\boldsymbol{x}_\alpha$) of particle α in the laboratory frame and $\nabla_\alpha^R = \boldsymbol{q}_\alpha \times (\partial/\partial \boldsymbol{q}_\alpha)$ is the orientational gradient operator of particle α. The translational and rotational fluxes in equation (4.3) are, respectively, given by $\boldsymbol{j}_\alpha^T = \boldsymbol{U}_\alpha P_N$ and $\boldsymbol{j}_\alpha^R = \boldsymbol{\Omega}_\alpha P_N$, where $\boldsymbol{U}_\alpha$ ($\boldsymbol{\Omega}_\alpha$) is the instantaneous linear (angular) velocity of particle labeled α relative to the laboratory frame. The conservation of probability is

$$\int_{\Gamma_N} P_N d\Gamma^N = 1, \tag{4.4}$$

where $d\Gamma^N = \prod_{\alpha=1}^{N} d\Gamma_\alpha$ denotes the volume element of the N-particle phase space and $d\Gamma_\alpha = d\boldsymbol{x}_\alpha d\boldsymbol{q}_\alpha$ is the volume element of the phase space of particle α.

In the absence of a background flow, the linear and angular velocities of any active particle α are given by

$$\begin{pmatrix} \boldsymbol{U}_\alpha - \boldsymbol{U}_\alpha^0 \\ \boldsymbol{\Omega}_\alpha - \boldsymbol{\Omega}_\alpha^0 \end{pmatrix} = \sum_{\beta=1}^{N} \boldsymbol{\mathcal{M}}_{\alpha\beta} \cdot \begin{pmatrix} \boldsymbol{F}_\beta^e + \boldsymbol{F}_\beta^P - k_B T \nabla_\beta^T \ln P_N \\ \boldsymbol{L}_\beta^e + \boldsymbol{L}_\beta^P - k_B T \nabla_\beta^R \ln P_N \end{pmatrix} + \begin{pmatrix} 0 \\ -D_\alpha^R \nabla_\alpha^R \ln P_N \end{pmatrix}, \tag{4.5}$$

where $\boldsymbol{\mathcal{M}}_{\alpha\beta}$ is the configuration-dependent grand hydrodynamic mobility tensor coupling the linear and angular velocity of particle α to the force and torque exerted on particle β. Note that for general particle shapes $\boldsymbol{\mathcal{M}}_{\alpha\beta}$ is a function of the instantaneous N-particle configuration—both positions and orientations. The forces on any particle β include the external force $\boldsymbol{F}_\beta^e$, the interparticle colloidal force $\boldsymbol{F}_\beta^P$ and the thermal or entropic force $-k_B T \nabla_\beta^T \ln P_N$. Similarly, the torques on any particle β include the external torque $\boldsymbol{L}_\beta^e$, the interparticle colloidal torque $\boldsymbol{L}_\beta^P$ and the thermal torque $-k_B T \nabla_\beta^R \ln P_N$. The interparticle colloidal forces and torques are assumed to be conservative. For the case of hard-sphere interactions, the interparticle forces reduce to no-flux boundary conditions at any surface of contact between particles.

In equation (4.5), the activity of any particle α is modeled by its undisturbed swim linear velocity $\boldsymbol{U}_\alpha^0$ and angular velocity $\boldsymbol{\Omega}_\alpha^0$ regardless of the presence of any other particles. For the case of simple ABPs, the swim angular velocity is often taken to be zero, $\boldsymbol{\Omega}_\alpha^0 = \boldsymbol{0}$. Furthermore, a biological microswimmer may "decide" to change its orientation $\boldsymbol{q}_\alpha$ by, for example, actuating the flagella on a different side of its body without disturbing the flow. In this process, the body of the microswimmer does not turn. For nonspherical particles, this process means that the swim orientation $\boldsymbol{q}_\alpha$ is usually different from the orientation of the particle shape, in which case the shape orientation needs to be included as an additional phase space variable. For spherical particles, only the swim orientation matters and no such difficulty is introduced. This reorientation process of any particle α is independent of the motion of other particles and is modeled by a simple rotary diffusion with a constant rotary diffusivity D_α^R. The reorientation time is $\tau_\alpha^R = 1/D_\alpha^R$, which defines the active run or persistence length of an ABP: $\ell_\alpha = U_\alpha^0 \tau_\alpha^R$. Because this reorientation process is biological rather than thermal in origin, D_α^R is not constrained by the fluctuation-dissipation theorem and may be inferred from experimental data.

4.3 Moving trap microrheology

In the context of microrheology, the particle with label 1 is identified as the probe particle. This particle could be a new particle placed into the suspension or one of the suspension particles tagged as the probe. Particles labeled $2 - N$ are referred to as bath particles. In the following, we consider a suspension of neutrally buoyant, hard and active colloidal spheres with identical radii. The probe may have a different radius than the bath particles. Instead of fixing the external force $\boldsymbol{F}_1^e$ or the velocity $\boldsymbol{U}_1$, the probe particle is trapped in a translating harmonic potential well. Denoting the position vector of the center of the potential well as $\boldsymbol{x}_0(t)$, we have $d\boldsymbol{x}_0/dt = \boldsymbol{U}^{\text{trap}}(t)$, where $\boldsymbol{U}^{\text{trap}}(t)$ is the prescribed velocity of the moving trap relative to the laboratory frame. The trap force $\boldsymbol{F}_1^e$ is assumed to be only a function of the relative position between the probe and the potential well. All bath particles experience no external forces or torques. We first consider a general derivation in which all particles are ABPs and the probe is a tagged ABP in the suspension.

In the constant-force or constant-velocity mode of microrheology, the position of the probe does not matter, and the system is statistically homogeneous. In contrast, the introduction of a moving trap defines a specific origin in the system and the position of the probe relative to the trap needs to be considered explicitly. To this end, we first change to a coordinate system moving with the instantaneous trap velocity and measure all particle positions relative to the trap. This change of variables is written as $\boldsymbol{z}_\alpha = \boldsymbol{z}_\alpha(\{\boldsymbol{x}\}, t) = \boldsymbol{x}_\alpha - \int_0^t \boldsymbol{U}^{\mathrm{trap}}(s)ds - \boldsymbol{x}_0(0)$ for any α and $t' = t'(\{\boldsymbol{x}\}, t) = t$. Using the chain rule we obtain $\partial/\partial t = -\sum_{\alpha=1}^N \boldsymbol{U}^{\mathrm{trap}} \cdot \partial/\partial \boldsymbol{z}_\alpha + \partial/\partial t'$ and $\partial/\partial \boldsymbol{x}_\alpha = \partial/\partial \boldsymbol{z}_\alpha$. The Smoluchowski equation (4.3) in the new coordinate system becomes

$$\frac{\partial P_N}{\partial t'} + \sum_{\alpha=1}^{N} \frac{\partial}{\partial \boldsymbol{z}_\alpha} \cdot \left(\boldsymbol{j}_\alpha^T - \boldsymbol{U}^{\mathrm{trap}} P_N \right) + \sum_{\alpha=1}^{N} \nabla_\alpha^R \cdot \boldsymbol{j}_\alpha^R = 0, \tag{4.6}$$

where $\boldsymbol{j}_\alpha^T$ and $\boldsymbol{j}_\alpha^R$ remain unchanged. In the context of microrheology, it is more convenient to measure the positions of all bath particles relative to that of the probe. We therefore introduce another change of variables such that for the probe $\boldsymbol{r}_1 = \boldsymbol{r}_1(\boldsymbol{z}^N, t') = \boldsymbol{z}_1$ and $\boldsymbol{r}_\alpha = \boldsymbol{r}_\alpha(\boldsymbol{z}^N, t') = \boldsymbol{z}_\alpha - \boldsymbol{z}_1$ for all bath particles ($\alpha = 2, \cdots, N$). In this coordinate system, the probe position is measured relative to the trap and the positions of all bath particles are measured relative to the probe. The change of variables allows us to write $\partial/\partial \boldsymbol{z}_1 = \partial/\partial \boldsymbol{r}_1 - \sum_{\alpha=2}^N \partial/\partial \boldsymbol{r}_\alpha$ and $\partial/\partial \boldsymbol{z}_\alpha = \partial/\partial \boldsymbol{r}_\alpha$ for $\alpha = 2, \cdots, N$. The Smoluchowski equation (4.6) transforms to

$$\frac{\partial P_N}{\partial t} + \nabla_1^T \cdot \left(\boldsymbol{j}_1^T - \boldsymbol{U}^{\mathrm{trap}} P_N \right) + \sum_{\alpha=2}^{N} \nabla_\alpha^T \cdot \left(\boldsymbol{j}_\alpha^T - \boldsymbol{j}_1^T \right) + \sum_{\alpha=1}^{N} \nabla_\alpha^R \cdot \boldsymbol{j}_\alpha^R = 0. \tag{4.7}$$

It is understood that in equation (4.7) we have used t for the time variable and $\nabla_\alpha^T = \partial/\partial \boldsymbol{r}_\alpha$ for any α. Formally, the probability density in equation (4.7) is the conditional probability of find all particles at a given configuration provided that the trap is at $\boldsymbol{x}_0$ at time t, i.e., $P_N = P_N\left(\boldsymbol{r}^N, \boldsymbol{q}^N, t | \boldsymbol{x}_0, t\right)$. The translational flux of particle α can be written as

$$\begin{aligned} \boldsymbol{j}_\alpha^T = & U_\alpha^0 \boldsymbol{q}_\alpha P_N + \boldsymbol{M}_{\alpha 1}^{UF} \cdot \boldsymbol{F}_1^e P_N - \sum_{\beta=1}^{N} \left(\boldsymbol{D}_{\alpha\beta}^{UF} - \boldsymbol{D}_{\alpha 1}^{UF} \right) \cdot \nabla_\beta^T P_N - \boldsymbol{D}_{\alpha 1}^{UF} \cdot \nabla_1^T P_N \\ & - \sum_{\beta=1}^{N} \boldsymbol{D}_{\alpha\beta}^{UL} \cdot \nabla_\beta^R P_N, \end{aligned} \tag{4.8}$$

where we have taken $\boldsymbol{U}_\alpha^0 = U_\alpha^0 \boldsymbol{q}_\alpha$ and used the Stokes-Einstein-Sutherland relations $\boldsymbol{D}_{\alpha\beta}^{UF} = k_B T \boldsymbol{M}_{\alpha\beta}^{UF}, \boldsymbol{D}_{\alpha\beta}^{UL} = k_B T \boldsymbol{M}_{\alpha\beta}^{UL}$. For all accessible configurations, the interparticle forces are zero and the hard-particle interaction between two spheres do not induce torques. Similarly, the rotary flux of particle α is given by

$$\begin{aligned}\boldsymbol{j}_\alpha^R =&\boldsymbol{M}_{\alpha 1}^{\Omega F}\cdot\boldsymbol{F}_1^e P_N-\sum_{\beta=1}^{N}\left(\boldsymbol{D}_{\alpha\beta}^{\Omega F}-\boldsymbol{D}_{\alpha 1}^{\Omega F}\right)\cdot\nabla_\beta^T P_N-\boldsymbol{D}_{\alpha 1}^{\Omega F}\cdot\nabla_1^T P_N\\ &-\sum_{\beta=1}^{N}\boldsymbol{D}_{\alpha\beta}^{\Omega L}\cdot\nabla_\beta^R P_N-D_\alpha^R\nabla_\alpha^R P_N.\end{aligned}\tag{4.9}$$

The Smoluchowski equation (4.7) together with the flux expressions (4.8) and (4.9) fully specify the N-particle phase space dynamics. Some comments regarding equations (4.7)-(4.9) are in order. First, the above derivation is an extension of the model considered by Squires and Brady (2005) for passive Brownian suspensions. We have generalized their model to a suspension of ABPs in which one of the particles are tagged as the probe that is driven by a translating trap. Realizing that the grand mobility tensor does not depend on the swim orientation vectors of spherical particles, one can set $\boldsymbol{U}_\alpha^0 = 0$ and integrate over the orientations of all particles to obtain the trapped probe microrheology problem of a passive Brownian suspension. Note that even for passive suspensions, if the probe or the bath particles are non-spherical, their shape orientations need to be included in the above formulation. Second, the hydrodynamic interactions between all N-particles are included in the grand mobility tensor. In particular, this leads to the fact that a gradient in orientation space of particle β induces a translational flux of particle α, and vice versa, due to the hydrodynamic translation-rotation coupling. Third, due to the dependence on particle orientations, the phase space of N ABPs has a dimension of $5N$: the physical space has a dimension of $3N$ and the orientation space has a dimension of $2N$ if the orientation of each particle is parametrized by the azimuthal and polar angles.

4.3.1 Mean and fluctuation of the probe position

The average position or mean displacement of the probe relative to the trap is defined by

$$\langle\boldsymbol{r}_1\rangle(t)=\int\boldsymbol{r}_1 P_N d\Gamma^N,\tag{4.10}$$

where the angle bracket denotes integration against P_N over the configuration space of all particles. Multiplying equation (4.7) by $\boldsymbol{r}_1$ and integrating over the configuration space Γ^N, we obtain

$$\begin{aligned}\frac{\partial\langle\boldsymbol{r}_1\rangle}{\partial t}+\boldsymbol{U}^{\text{trap}} =& U_1^0\langle\boldsymbol{q}_1\rangle+\left\langle\boldsymbol{M}_{11}^{UF}\cdot\boldsymbol{F}_1^e\right\rangle-\left\langle\boldsymbol{D}_{11}^{UF}\cdot\nabla_1^T\ln P_N\right\rangle\\&-\sum_{\beta=1}^{N}\left\langle\left(\boldsymbol{D}_{1\beta}^{UF}-\boldsymbol{D}_{11}^{UF}\right)\cdot\nabla_\beta^T\ln P_N\right\rangle.\end{aligned}\tag{4.11}$$

Similarly, the mean squared displacement, a second order tensor, is governed by

$$\frac{\partial\langle\boldsymbol{r}_1\boldsymbol{r}_1\rangle}{\partial t}+\boldsymbol{U}^{\text{trap}}\langle\boldsymbol{r}_1\rangle+\langle\boldsymbol{r}_1\rangle\boldsymbol{U}^{\text{trap}}=\int\left(\boldsymbol{j}_1^T\boldsymbol{r}_1+\boldsymbol{r}_1\boldsymbol{j}_1^T\right)d\Gamma^N,\tag{4.12}$$

where the integral

$$\begin{aligned}\int\boldsymbol{j}_1^T\boldsymbol{r}_1 d\Gamma^N =\quad & U_1^0\langle\boldsymbol{q}_1\boldsymbol{r}_1\rangle+\left\langle\boldsymbol{M}_{11}^{UF}\cdot\boldsymbol{F}_1^e\boldsymbol{r}_1\right\rangle-\left\langle\boldsymbol{D}_{11}^{UF}\cdot\left(\nabla_1^T\ln P_N\right)\boldsymbol{r}_1\right\rangle\\&-\sum_{\beta=1}^{N}\left\langle\left(\boldsymbol{D}_{1\beta}^{UF}-\boldsymbol{D}_{11}^{UF}\right)\cdot\left(\nabla_\beta^T\ln P_N\right)\boldsymbol{r}_1\right\rangle.\end{aligned}\tag{4.13}$$

The main quantities of interest in the trapped probe microrheology problem are the mean displacement $\langle\boldsymbol{r}_1\rangle$ and the fluctuation

$$\text{Cov}(\boldsymbol{r}_1,\boldsymbol{r}_1)=\left\langle\Delta\boldsymbol{r}_1\Delta\boldsymbol{r}_1\right\rangle=\left\langle\boldsymbol{r}_1\boldsymbol{r}_1\right\rangle-\langle\boldsymbol{r}_1\rangle\langle\boldsymbol{r}_1\rangle,\tag{4.14}$$

where we have introduced the shorthand $\Delta\boldsymbol{r}_1=\boldsymbol{r}_1-\langle\boldsymbol{r}_1\rangle$ and $\text{Cov}(\boldsymbol{r}_1,\boldsymbol{r}_1)$ denotes the covariance tensor of $\boldsymbol{r}_1$. For a harmonic trap, the mean force is related to the mean displacement via $\langle\boldsymbol{F}_1^e\rangle=-k\langle\boldsymbol{r}_1\rangle$ and similarly the fluctuation in the force is given by $\left\langle\Delta\boldsymbol{F}_1^e\Delta\boldsymbol{F}_1^e\right\rangle=k^2\langle\Delta\boldsymbol{r}_1\Delta\boldsymbol{r}_1\rangle$.

4.3.2 The pair problem

The generalized pair distribution function g_2 (See section 4.6.) is governed by

$$\frac{\partial g_2}{\partial t}+\nabla_1^T\cdot\left(\boldsymbol{j}_1^T-\boldsymbol{U}^{\text{trap}}g_2\right)+\nabla_2^T\cdot\left(\boldsymbol{j}_2^T-\boldsymbol{j}_1^T\right)+\sum_{\alpha=1}^{2}\nabla_\alpha^R\cdot\boldsymbol{j}_\alpha^R=0,\tag{4.15}$$

$$\boldsymbol{j}_1^T=U_1^0\boldsymbol{q}_1g_2+\frac{1}{\zeta_1}\boldsymbol{F}_1^e g_2+D_1^T\nabla_2^T g_2-D_1^T\nabla_1^T g_2,\tag{4.16}$$

$$\boldsymbol{j}_2^T=U_2^0\boldsymbol{q}_2g_2-D_2^T\nabla_2^T g_2,\tag{4.17}$$

$$\boldsymbol{j}_\alpha^R=-D_\alpha^R\nabla_\alpha^R g_2.\tag{4.18}$$

At contact, $r_2=R_c$, no relative flux is allowed,

$$\boldsymbol{n}_2\cdot\left(\boldsymbol{j}_2^T-\boldsymbol{j}_1^T\right)=0.\tag{4.19}$$

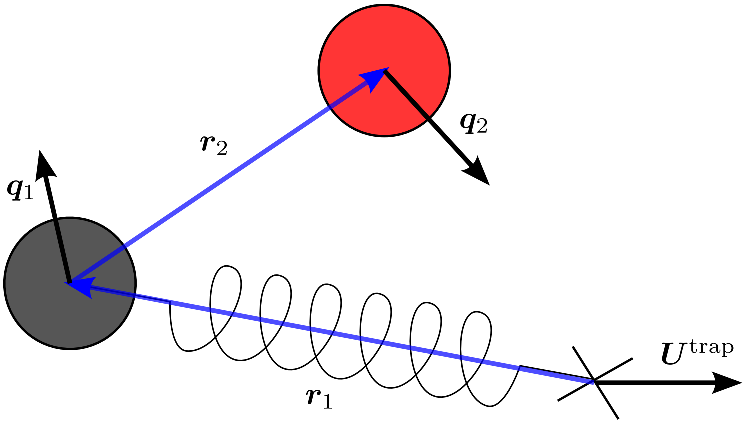

Figure 4.1: Schematic of the pair problem of a spherical probe particle in a moving harmonic trap interacting with a spherical bath particle. Both the probe and the bath particles can be active.

Far away from the probe, the bath distribution is undisturbed by the probe and the probe distribution is that in the absence of the bath particles,

$$g_2(\boldsymbol{r}_2, \boldsymbol{q}_2, \boldsymbol{r}_1, \boldsymbol{q}_1, t) \to \frac{1}{\Omega_b} P_1(\boldsymbol{r}_1, \boldsymbol{q}_1, t) \quad \text{as} \quad |\boldsymbol{r}_2| \to \infty, \tag{4.20}$$

where Ω_b is the total solid angle of the orientation space of the bath particle. In 3D, $\Omega_b = 4\pi$. Far away from the trap, the probability vanishes

$$g_2 \to 0 \quad \text{as} \quad |\boldsymbol{r}_1| \to \infty. \tag{4.21}$$

The conservation equation (4.4) becomes

$$\int g_2 d\Gamma_1 d\Gamma_2 = \frac{N-1}{n_b}, \tag{4.22}$$

and the mean of any quantity defined in equation (4.10) is given by

$$\langle(\cdot)\rangle = \frac{n_b}{N-1} \int (\cdot) g_2 d\Gamma_1 d\Gamma_2. \tag{4.23}$$

Equation (4.11) governing the mean displacement becomes

$$\frac{\partial \langle \boldsymbol{r}_1 \rangle}{\partial t} + \frac{1}{\tau_k} \langle \boldsymbol{r}_1 \rangle = -\boldsymbol{U}^{\text{trap}} + U_1^0 \langle \boldsymbol{q}_1 \rangle + n_b D_1^T \left\langle \nabla_2 \ln g_2 \right\rangle, \tag{4.24}$$

where we have defined the viscoelastic timescale

$$\tau_k = \frac{\zeta_1}{k}, \tag{4.25}$$

which is set by the balance between the viscous force $\zeta_1 \partial \langle \boldsymbol{r}_1 \rangle / \partial t$ and the elastic force $k\langle \boldsymbol{r}_1 \rangle$. Using the divergence theorem and the far-field condition (4.20), the last term on the rhs of (4.24) can be written as

$$n_b D_1^T \left\langle \nabla_2 \ln g_2 \right\rangle = n_b D_1^T \int d\boldsymbol{q}_2 d\Gamma_1 \oint_{S_c} \boldsymbol{n}_2 \frac{n_b}{N-1} g_2 dS_2, \tag{4.26}$$

where $S_c = \{\boldsymbol{r}_2 : |\boldsymbol{r}_2| = R_c\}$ is the contact surface and $\boldsymbol{n}_2$ is the unit normal vector of S_c that points out of particle 2.

As shown in appendix 4.7, the position fluctuation of the probe is governed by

$$\frac{1}{2}\frac{\partial\,\mathrm{Cov}(\boldsymbol{r}_1, \boldsymbol{r}_1)}{\partial t} + \frac{1}{\tau_k}\mathrm{Cov}(\boldsymbol{r}_1, \boldsymbol{r}_1) = D_1^T \boldsymbol{I} + \left[U_1^0\,\mathrm{Cov}(\boldsymbol{q}_1, \boldsymbol{r}_1) + n_b D_1^T \left\langle \nabla_2 \left(\ln g_2\right) \Delta \boldsymbol{r}_1 \right\rangle\right]^{\mathrm{sym}}, \tag{4.27}$$

where the covariance of $\boldsymbol{q}_1$ and $\boldsymbol{r}_1$ satisfies

$$\begin{aligned}\frac{\partial\,\mathrm{Cov}(\boldsymbol{q}_1, \boldsymbol{r}_1)}{\partial t} + \left(\frac{1}{\tau_k} + \frac{d-1}{\tau_1^R}\right)\mathrm{Cov}(\boldsymbol{q}_1, \boldsymbol{r}_1) =& U_1^0\,\mathrm{Cov}(\boldsymbol{q}_1, \boldsymbol{q}_1) \\ &+ n_b D_1^T \left\langle \Delta \boldsymbol{q}_1 \nabla_2 \ln g_2 \right\rangle.\end{aligned} \tag{4.28}$$

Regardless of the presence of the trap or the bath particles, at long times ($t \longrightarrow \infty$) the net polar and nematic orders of the probe are given by $\langle \boldsymbol{q}_1 \rangle = \boldsymbol{0}$ and $\left\langle \boldsymbol{q}_1 \boldsymbol{q}_1 \right\rangle = \boldsymbol{I}/d$, respectively (see appendix 4.7). As a result, $\mathrm{Cov}(\boldsymbol{q}_1, \boldsymbol{q}_1) = \boldsymbol{I}/d$ at long times.

It is convenient to consider the rank m polyadic spatial moment tensor

$$\boldsymbol{M}_m(\boldsymbol{r}_2, \boldsymbol{q}_2, \boldsymbol{q}_1, t) = \int \underbrace{\boldsymbol{r}_1 \cdots \boldsymbol{r}_1}_{m} g_2 d\boldsymbol{r}_1, \quad (m = 0, 1, 2, ...). \tag{4.29}$$

Multiplying equation (4.15) by the m-adic product of $\boldsymbol{r}_1$ and integrating over the physical space of the probe, we obtain

$$\begin{aligned}&\frac{\partial \boldsymbol{M}_m}{\partial t} - m\left[U_1^0 \boldsymbol{q}_1 \boldsymbol{M}_{m-1} - \frac{k}{\zeta_1}\boldsymbol{M}_m + (m-1)D_1^T \boldsymbol{M}_{m-2}\boldsymbol{I} + D_1^T \nabla_2^T \boldsymbol{M}_{m-1} - \boldsymbol{U}^{\mathrm{trap}} \boldsymbol{M}_{m-1}\right]^{\mathrm{sym}} \\ &+\nabla_2^T \cdot \left(\boldsymbol{U}_r \boldsymbol{M}_m - D_r^T \nabla_2^T \boldsymbol{M}_m + \frac{k}{\zeta_1}\boldsymbol{M}_{m+1}\right) \\ &-mD_1^T \left[\nabla_2^T \boldsymbol{M}_{m-1}\right]^{\mathrm{sym}} - \sum_{\alpha=1}^{2} D_\alpha^R \nabla_\alpha^R \cdot \nabla_\alpha^R \boldsymbol{M}_m = \boldsymbol{0},\end{aligned} \tag{4.30}$$

where we have defined the relative swim velocity and the relative diffusivity as, respectively,

$$\boldsymbol{U}_r = U_2^0 \boldsymbol{q}_2 - U_1^0 \boldsymbol{q}_1, \quad D_r^T = D_1^T + D_2^T, \tag{4.31}$$

whereas $[\boldsymbol{A}]^{\mathrm{sym}}$ denotes the symmetric part of any rank m Cartesian tensor $\boldsymbol{A}$ such that

$$[\boldsymbol{A}]^{\mathrm{sym}}_{i_1 i_2 \cdots i_m} = \frac{1}{m!} \sum_{\sigma \in \mathfrak{S}_m} A_{i_{\sigma 1} i_{\sigma 2} \cdots i_{\sigma m}}, \tag{4.32}$$

in which $\mathfrak{S}_m$ is the set containing the $m!$ permutations of indices. For $m = 2$, this reduces to the familiar definition of the symmetric part of a rank 2 tensor, $\boldsymbol{A}^{\mathrm{sym}} = (\boldsymbol{A} + \boldsymbol{A}^{\intercal})/2$. For any rank m tensor $\boldsymbol{A}$, its symmetric part $[\boldsymbol{A}]^{\mathrm{sym}}$ is invariant under a permutation of all indices. In equation (4.30), $\boldsymbol{M}_m$ for $m < 0$ is understood to be zero.

At contact, $r_2 = R_c$, the no-flux boundary condition is satisfied:

$$\boldsymbol{n}_2 \cdot \left(\boldsymbol{U}_r \boldsymbol{M}_m - D_r^T \nabla_2^T \boldsymbol{M}_m + \frac{k}{\zeta_1} \boldsymbol{M}_{m+1} \right) - m D_1^T \left[\boldsymbol{n}_2 \boldsymbol{M}_{m-1} \right]^{\mathrm{sym}} = \boldsymbol{0}. \tag{4.33}$$

The far-field condition for the spatial moment of rank m is

$$\boldsymbol{M}_m \to \frac{1}{\Omega_b} \boldsymbol{\Phi}_m(\boldsymbol{q}_1, t) \quad \text{as} \quad r_2 \to \infty, \tag{4.34}$$

where

$$\boldsymbol{\Phi}_m(\boldsymbol{q}_1, t) = \int \underbrace{\boldsymbol{r}_1 \cdots \boldsymbol{r}_1}_{m} P_1(\boldsymbol{r}_1, \boldsymbol{q}_1, t) d\boldsymbol{r}_1 \tag{4.35}$$

is the rank m spatial moment of the single particle probability P_1 of the probe. Discussion of the single particle behavior and the method to obtain $\boldsymbol{\Phi}_m$ is deferred to section 4.3.3.

From (4.24) and (4.102), to obtain the mean and mean-squared displacements, one only needs to calculate the zeroth and first spatial moments, respectively. On the other hand, the definitions of mean and mean-squared displacements allow us to write $\langle \boldsymbol{r}_1 \rangle = [n_b/(N-1)] \int \boldsymbol{M}_1 d\boldsymbol{q}_1 d\Gamma_2$ and $\langle \boldsymbol{r}_1 \boldsymbol{r}_1 \rangle = [n_b/(N-1)] \int \boldsymbol{M}_2 d\boldsymbol{q}_1 d\Gamma_2$. Because in obtaining $\langle \boldsymbol{r}_1 \boldsymbol{r}_1 \rangle$ only the integral of $\boldsymbol{M}_2$ is required, it's not necessary to first calculate the distribution of $\boldsymbol{M}_2$ explicitly before carrying out the integration. Instead, one can show that integrating equation (4.30) for $m = 2$ leads to the same equation as (4.102). Due to the presence of the harmonic trap force, the equation for $\boldsymbol{M}_m$ is coupled to $\boldsymbol{M}_{m+1}$. To truncate this infinite set of equations and obtain a finite set of closed equations, a closure model may be used.

To see the structure of the spatial moments more clearly, we write out the first few moment equations explicitly using (4.30). The zeroth moment, $M_0 = \int g_2 d\boldsymbol{r}_1$, satisfies the equation

$$\frac{\partial M_0}{\partial t} + \nabla_2^T \cdot \left[\boldsymbol{U}_r M_0 - D_r^T \nabla_2^T M_0 + \frac{k}{\zeta_1} \boldsymbol{M}_1 \right] - \sum_{\alpha=1}^{2} D_\alpha^R \nabla_\alpha^R \cdot \nabla_\alpha^R M_0 = 0, \tag{4.36}$$

and the normalization $\int M_0 d\boldsymbol{q}_1 d\Gamma_2 = (N-1)/n_b$. In addition to being advected by the relative velocity $\boldsymbol{U}_r$ in the physical space of the bath particle, M_0 is forced by the trap via the divergence of the first moment. The equation governing the evolution of the first spatial moment is

$$\begin{aligned}&\frac{\partial \boldsymbol{M}_1}{\partial t} - \left(U_1^0 \boldsymbol{q}_1 M_0 - \frac{k}{\zeta_1}\boldsymbol{M}_1 + D_1^T \nabla_2^T M_0\right) + \boldsymbol{U}^{\text{trap}} M_0 \\ &+\nabla_2^T \cdot \left[\boldsymbol{U}_r \boldsymbol{M}_1 - D_r^T \nabla_2^T \boldsymbol{M}_1 + \frac{k}{\zeta_1}\boldsymbol{M}_2 - D_1^T \boldsymbol{I} M_0\right] \\ &- \sum_{\alpha=1}^{2} D_\alpha^R \nabla_\alpha^R \cdot \nabla_\alpha^R \boldsymbol{M}_1 = \boldsymbol{0}. \end{aligned} \tag{4.37}$$

Similarly, the second moment is governed by

$$\begin{aligned}&\frac{\partial \boldsymbol{M}_2}{\partial t} - 2\left[U_1^0 \boldsymbol{q}_1 \boldsymbol{M}_1 - \frac{k}{\zeta_1}\boldsymbol{M}_2 + D_1^T M_0 \boldsymbol{I} + D_1^T \nabla_2^T \boldsymbol{M}_1 - \boldsymbol{U}^{\text{trap}} \boldsymbol{M}_1\right]^{\text{sym}} \\ &+\nabla_2^T \cdot \left[\boldsymbol{U}_r \boldsymbol{M}_2 - D_r^T \nabla_2^T \boldsymbol{M}_2 + \frac{k}{\zeta_1}\boldsymbol{M}_3\right] \\ &-2D_1^T \left[\nabla_2^T \boldsymbol{M}_1\right]^{\text{sym}} - \sum_{\alpha=1}^{2} D_\alpha^R \nabla_\alpha^R \cdot \nabla_\alpha^R \boldsymbol{M}_2 = \boldsymbol{0}. \end{aligned} \tag{4.38}$$

4.3.3 The probe distribution in the absence of bath particles

The lowest level problem in the above formulation is the single particle problem of the probe interacting with the trap. One can formulate this single particle problem by neglecting all bath particles or taking the limit $\phi_b \to 0$ in the above N-particle formulation. The single particle probability $P_1(\boldsymbol{r}_1, \boldsymbol{q}_1, t|\boldsymbol{x}_0, t)$ of the active probe satisfies

$$\frac{\partial P_1}{\partial t} + \nabla_1^T \cdot \left(\frac{1}{\zeta_1}\boldsymbol{F}_1^e P_1 - D_1^T \nabla P_1 - \boldsymbol{U}^{\text{trap}} P_1 + U_1^0 \boldsymbol{q}_1 P_1\right) - D_1^R \nabla_1^R \cdot \nabla_1^R P_1 = 0, \tag{4.39}$$

where the conservation of probability dictates that $\int P_1 d\Gamma_1 = 1$ and the harmonic trap force $\boldsymbol{F}_1^e = -k\boldsymbol{r}_1$.

The rank m ($m = 0, 1, \ldots$) spatial moment of P_1 defined by (4.35) satisfies

$$\begin{aligned}&\frac{\partial \boldsymbol{\Phi}_m}{\partial t} - m\left[U_1^0 \boldsymbol{q}_1 \boldsymbol{\Phi}_{m-1} - \frac{k}{\zeta_1}\boldsymbol{\Phi}_m + (m-1) D_1^T \boldsymbol{\Phi}_{m-2} \boldsymbol{I} - \boldsymbol{U}^{\text{trap}} \boldsymbol{\Phi}_{m-1}\right]^{\text{sym}} \\ &- D_1^R \nabla_1^R \cdot \nabla_1^R \boldsymbol{\Phi}_m = \boldsymbol{0}, \end{aligned} \tag{4.40}$$

where $\boldsymbol{\Phi}_m$ for $m < 0$ is defined to be zero. Different from equation (4.30) in which the moment $\boldsymbol{M}_m$ is coupled to $\boldsymbol{M}_{m+1}$, the rank m spatial moment of P_1 only depends on lower order moments, which leads to a set of closed equations. The solution to the preceding equation provides the far-field condition for $\boldsymbol{M}_m$ as given by equation (4.34).

The zeroth order spatial moment Φ_0 is the net orientational distribution, which is unaffected by the trap and is governed by the orientational diffusion equation:

$$\frac{\partial \Phi_0}{\partial t} - D_1^R \nabla_1^R \cdot \nabla_1^R \Phi_0 = 0, \tag{4.41}$$

where the conservation of P_1 gives $\int \Phi_0 d\boldsymbol{q}_1 = 1$. At long times, the solution is simply the uniform distribution, $\Phi_0(\boldsymbol{q}_1, t \to \infty) = 1/(4\pi)$.

The above formulation also allows us to consider the mean and fluctuation of the probe displacement in the absence of bath particles. Equation (4.11) or (4.24) in the absence of bath particles reduces to

$$\frac{\partial \langle \boldsymbol{r}_1 \rangle}{\partial t} + \frac{1}{\tau_k} \langle \boldsymbol{r}_1 \rangle = -\boldsymbol{U}^{\text{trap}} + U_1^0 \langle \boldsymbol{q}_1 \rangle, \tag{4.42}$$

where for the single particle $\langle \boldsymbol{r}_1 \rangle = \int \boldsymbol{r}_1 P_1 d\Gamma_1 = \int \boldsymbol{\Phi}_1 d\boldsymbol{q}_1$. Similarly, equation (4.12) or (4.102) for the single particle becomes

$$\frac{1}{2}\frac{\partial \langle \boldsymbol{r}_1 \boldsymbol{r}_1 \rangle}{\partial t} + \frac{1}{\tau_k} \big\langle \boldsymbol{r}_1 \boldsymbol{r}_1 \big\rangle = D_1^T \boldsymbol{I} + \left[U_1^0 \big\langle \boldsymbol{q}_1 \boldsymbol{r}_1 \big\rangle - \boldsymbol{U}^{\text{trap}} \langle \boldsymbol{r}_1 \rangle \right]^{\text{sym}}. \tag{4.43}$$

It can be seen from equations (4.42) and (4.43) that in order to calculate the mean and mean-squared displacements, one needs to obtain the net polar order $\langle \boldsymbol{q}_1 \rangle$ and the covariance of the position and orientation $\text{Cov}(\boldsymbol{q}_1, \boldsymbol{r}_1)$. The governing equation for $\text{Cov}(\boldsymbol{q}_1, \boldsymbol{r}_1)$ follows from (4.28) and is given by

$$\frac{\partial\, \text{Cov}(\boldsymbol{q}_1, \boldsymbol{r}_1)}{\partial t} + \frac{1}{\tau_k} \text{Cov}(\boldsymbol{q}_1, \boldsymbol{r}_1) + \frac{d-1}{\tau_1^R} \text{Cov}(\boldsymbol{q}_1, \boldsymbol{r}_1) = U_1^0\, \text{Cov}(\boldsymbol{q}_1, \boldsymbol{q}_1) \tag{4.44}$$

which depends on the net nematic order $\langle \boldsymbol{q}_1 \boldsymbol{q}_1 \rangle$.

At steady state, it is shown that $\langle \boldsymbol{q}_1 \rangle = \boldsymbol{0}$ and $\langle \boldsymbol{q}_1 \boldsymbol{q}_1 \rangle = \boldsymbol{I}/d$, where $d = 2, 3$ is the dimensionality of the physical space. This allows us to obtain

$$\begin{aligned} \langle \boldsymbol{r}_1 \rangle &= -\frac{\zeta_1 \boldsymbol{U}^{\text{trap}}}{k}, && (4.45) \\ \text{Cov}(\boldsymbol{q}_1, \boldsymbol{r}_1) &= \frac{U_1^0}{dk/\zeta_1 + d(d-1) D_1^R} \boldsymbol{I}, && (4.46) \\ \langle \boldsymbol{r}_1 \boldsymbol{r}_1 \rangle &= \frac{\zeta_1^2}{k^2} \boldsymbol{U}^{\text{trap}} \boldsymbol{U}^{\text{trap}} + \frac{\zeta_1 D_1^T}{k} \boldsymbol{I} + \frac{\zeta_1 D_1^{\text{swim}}}{k} \frac{1}{1 + \frac{k \tau_1^R}{\zeta_1} \frac{1}{d-1}} \boldsymbol{I}, && (4.47) \end{aligned}$$

where $D_1^{\text{swim}} = \left(U_1^0\right)^2 \tau_1^R/[d(d-1)]$ is the swim diffusivity of a freely swimming ABP (Takatori et al. 2014; Takatori and Brady 2014). The average position of the ABP relative to the trap is given by the balance between the average trap force $k\langle \boldsymbol{r}_1\rangle$ and the viscous drag $\zeta_1 \boldsymbol{U}^{\text{trap}}$. If the trap is strong, $k \to \infty$, the ABP is tightly confined and pushing against the trap 'boundary'. On the other hand, for $k \to 0$, the average position of the ABP becomes unbounded. Solving the steady state first and then taking the limit $k \to 0$ in (4.45) is singular because in the absence of the trap ($k = 0$) the average position is unbounded and at long times the particle motion is diffusive. For $k \equiv 0$, we are simply measuring the motion of an ABP in a frame of reference moving with velocity $\boldsymbol{U}^{\text{trap}}$ relative to the laboratory frame, which gives $d\langle \boldsymbol{r}_1\rangle/dt = -\boldsymbol{U}^{\text{trap}}$.

Takatori et al. (2016) studied the transient and long-time dynamics of self-propelled Janus particles in a fixed acoustic trap. They showed that the experimentally measured density distribution of Janus particles follow closely the theoretical predictions using a harmonic trap. Equation (4.47) in the absence of $\boldsymbol{U}^{\text{trap}}$ agrees with that obtained in Takatori et al. (2016).

The fluctuation relation is given by

$$\left\langle (\Delta \boldsymbol{F}_1^e)^2 \right\rangle^{1/2} \left\langle (\Delta \boldsymbol{r}_1)^2 \right\rangle^{1/2} = d\left[k_B T + \frac{k_s T_s}{1 + \tau_1^R/[(d-1)\tau_k]}\right], \tag{4.48}$$

where the thermal energy $k_B T = \zeta_1 D_1^T$ and analogously an *active* energy scale $k_s T_s$ has been defined such that $k_s T_s = \zeta_1 D_1^{\text{swim}}$ (Takatori et al. 2014). In equation (4.48), the fluctuation consists of the thermal (passive) energy $d k_B T$ and an active energy contribution. This active energy is different from $k_s T_s$ due to the presence of the harmonic trap, which introduces an orientational decorrelation timescale τ_k in addition to the reorientation time τ_1^R of the ABP. For a weak trap, $\tau_1^R/\tau_k \ll 1$, the decorrelation occurs on the timescale of τ_1^R, and the active contribution scales as $\zeta_1 \left(U_1^0\right)^2 \tau_1^R$. As a result, the fluctuation $\left\langle (\Delta \boldsymbol{F}_1^e)^2 \right\rangle^{1/2} \left\langle (\Delta \boldsymbol{r}_1)^2 \right\rangle^{1/2} \to d(k_B T + k_s T_s)$ as $\tau_1^R/\tau_k \to 0$. When $\tau_1^R/\tau_k \gg 1$, the relevant timescale is τ_k, and the active contribution scales as $\zeta_1 \left(U_1^0\right)^2 \tau_k$. In this limit, the ABP is pushing against the edge of the potential well and the fluctuation comes from passive Brownian motion alone, $\left\langle (\Delta \boldsymbol{F}_1^e)^2 \right\rangle^{1/2} \left\langle (\Delta \boldsymbol{r}_1)^2 \right\rangle^{1/2} \to d k_B T$ as $\tau_1^R/\tau_k \to \infty$.

Regardless of the trap strength, the product of the square root of the fluctuations in the force and the position is always bounded. For a strong trap, the position fluctuation vanishes, $\left\langle \Delta \boldsymbol{r}_1 \Delta \boldsymbol{r}_1 \right\rangle = O(1/k) \to 0$, but the force fluctuation blows up linearly since $\langle \Delta \boldsymbol{F}_1^e \Delta \boldsymbol{F}_1^e \rangle = O(k) \to \infty$ as $k \to \infty$. Conversely, the position fluctuation grows unboundedly while the force fluctuation vanishes as $k \to 0$.

In the weak trap limit, equation (4.48) can be equivalently written as

$$\frac{k}{\zeta_1} \langle \Delta \boldsymbol{r}_1 \Delta \boldsymbol{r}_1 \rangle = \frac{\langle \Delta \boldsymbol{r}_1 \Delta \boldsymbol{r}_1 \rangle}{\tau_k} \to \boldsymbol{D}_1^{\text{eff}} \quad \text{as} \quad \frac{\tau_1^R}{\tau_k} \to 0, \tag{4.49}$$

where $\boldsymbol{D}_1^{\text{eff}} = D_1^T \boldsymbol{I} + D_1^{\text{swim}} \boldsymbol{I}$ is the long-time effective dispersion tensor of the ABP in the absence of the trap (see appendix 4.8 for the asymptotic analysis). This relation implies the equivalence of the position fluctuation divided by τ_k in the limit of vanishing harmonic trapping force and the effective dispersion of a free ABP. In other words, one could calculate the position fluctuation in a trap and then take the limit of $\langle \Delta \boldsymbol{r}_1 \Delta \boldsymbol{r}_1 \rangle / \tau_k$ as $k \to 0$ to obtain the long-time dispersion tensor that the particle would have in the absence of the trap, or vice versa. Because the trap is weak, the ABP is able to explore space via both thermal fluctuation and its undisturbed active run-and-reorientation, both processes contribute to the position fluctuation. In the presence of bath particles, this equivalence still holds in which $\boldsymbol{D}_1^{\text{eff}}$ is the dispersion tensor of the probe affected by collisions with bath particles (i.e., tracer dispersion).

4.3.4 A weak trap

For a weak trap, $\epsilon = \tau_1^R / \tau_k = k \tau_1^R / \zeta_1 \ll 1$, the probe is allowed to explore and reorient freely before reaching the 'boundary' of the potential well. The viscoelastic timescale τ_k is well separated from the reorientation timescale τ_1^R. In the intermediate timescale characterized by $t/\tau_1^R \gg 1$ and $t/\tau_k \ll 1$, the probe has explored the suspension but has not reached the boundary of the potential; we expect a diffusive behavior of the probe. At times much longer than the viscoelastic timescale ($t/\tau_k \gg 1$), the variance of the probe position becomes bounded due to the trapping force. Therefore, the motion of the probe exhibits a transition from diffusive to bounded behavior.

The separation of the two timescales allows us to consider a multiple-scale analysis. By defining the fast variable $t_1 = t$ and the slow variable $t_2 = \epsilon t$, we have $\partial / \partial t = \partial / \partial t_1 + \epsilon \partial / \partial t_2$. Regular perturbation expansions of the pair probability distribution and its spatial moments in terms of ϵ are written as

$$g_2 = g_2^{(0)} + \epsilon g_2^{(1)} + \cdots, \tag{4.50}$$

$$\boldsymbol{M}_m = \boldsymbol{M}_m^{(0)} + \epsilon \boldsymbol{M}_m^{(0)} + \cdots, \tag{4.51}$$

where $\boldsymbol{M}_m^{(k)}$ is the rank m spatial moment of $g_2^{(k)}$.

At $O(1)$, the zeroth moment satisfies

$$\frac{\partial M_0^{(0)}}{\partial t_1} + \nabla_2^T \cdot \left(\boldsymbol{U}_r M_0^{(0)} - D_r^T \nabla_2^T M_0^{(0)}\right) - \sum_{\alpha=1}^{2} D_\alpha^R \nabla_\alpha^R \cdot \nabla_\alpha^R M_0^{(0)} = 0, \tag{4.52}$$

$$\boldsymbol{n}_2 \cdot \left(\boldsymbol{U}_r M_0^{(0)} - D_r^T \nabla_2^T M_0^{(0)}\right) = 0, \quad \boldsymbol{r}_2 \in S_c. \tag{4.53}$$

Similarly, the first moment at this order is given by

$$\begin{aligned}&\frac{\partial \boldsymbol{M}_1^{(0)}}{\partial t_1} - \left(U_1^0 \boldsymbol{q}_1 M_0^{(0)} + D_1^T \nabla_2^T M_0^{(0)}\right) + \boldsymbol{U}^{\text{trap}} M_0^{(0)} \\ &+ \nabla_2^T \cdot \left(\boldsymbol{U}_r \boldsymbol{M}_1^{(0)} - D_r^T \nabla_2^T \boldsymbol{M}_1^{(0)} - D_1^T \boldsymbol{I} M_0^{(0)}\right) \\ &- \sum_{\alpha=1}^{2} D_\alpha^R \nabla_\alpha^R \cdot \nabla_\alpha^R \boldsymbol{M}_1^{(0)} = \boldsymbol{0},\end{aligned} \tag{4.54}$$

$$\boldsymbol{n}_2 \cdot \left(\boldsymbol{U}_r \boldsymbol{M}_1^{(0)} - D_r^T \nabla_2^T \boldsymbol{M}_1^{(0)} - D_1^T \boldsymbol{I} M_0^{(0)}\right) = 0, \quad \boldsymbol{r}_2 \in S_c. \tag{4.55}$$

Expanding the covariances in a similar fashion,

$$\text{Cov}(\boldsymbol{r}_1, \boldsymbol{r}_1) = \text{Cov}^{(0)}(\boldsymbol{r}_1, \boldsymbol{r}_1) + \epsilon\, \text{Cov}^{(1)}(\boldsymbol{r}_1, \boldsymbol{r}_1) + \cdots, \tag{4.56}$$

we obtain at $O(1)$

$$\frac{1}{2}\frac{\partial\, \text{Cov}^{(0)}(\boldsymbol{r}_1, \boldsymbol{r}_1)}{\partial t_1} = D_1^T \boldsymbol{I} + \left[U_1^0\, \text{Cov}^{(0)}(\boldsymbol{q}_1, \boldsymbol{r}_1) + n_b D_1^T \langle \nabla_2 \left(\ln g_2^{(0)}\right) \Delta \boldsymbol{r}_1 \rangle\right]^{\text{sym}}, \tag{4.57}$$

and

$$\frac{\partial\, \text{Cov}^{(0)}(\boldsymbol{q}_1, \boldsymbol{r}_1)}{\partial t_1} + \frac{d-1}{\tau_1^R} \text{Cov}^{(0)}(\boldsymbol{q}_1, \boldsymbol{r}_1) = U_1^0\, \text{Cov}(\boldsymbol{q}_1, \boldsymbol{q}_1) + n_b D_1^T \langle \Delta \boldsymbol{q}_1 \nabla_2 \ln g_2^{(0)} \rangle. \tag{4.58}$$

Note that $\text{Cov}(\boldsymbol{q}_1, \boldsymbol{q}_1)$ is not affected by the presence of the trap (see appendix 4.7) and therefore only has the $O(1)$ term in the small-ϵ expansion.

Equations (4.52)–(4.58) govern the dynamics of a probe in a bath of active particles in the absence of the trapping force (The presence of $\boldsymbol{U}^{\text{trap}}$ in (4.54) is only due to the fact that we are in a frame of reference moving with $\boldsymbol{U}^{\text{trap}}$ relative to the laboratory frame). This problem is the so-called tracer—an active one—dispersion in an active Brownian suspension. Even in the absence of the trap, the correlation between $\boldsymbol{q}_1$ and $\boldsymbol{r}_1$ has a steady-state (time-independent) solution due to the presence of the decorrelation time τ_1^R in equation (4.58). Dropping the time derivative in (4.58) at steady state, we obtain

$$\mathrm{Cov}^{(0)}(\boldsymbol{q}_1, \boldsymbol{r}_1) = \frac{\ell_1}{d(d-1)}\boldsymbol{I} + \frac{\tau_1^R}{d-1} n_b D_1^T \left\langle \Delta \boldsymbol{q}_1 \nabla_2 \ln g_2^{(0)} \right\rangle, \tag{4.59}$$

where it is understood that the steady-state distribution of $g_2^{(0)}$ is used. Therefore, equation (4.57) is written as

$$\boldsymbol{D}_1^{\mathrm{eff}} = \left(D_1^T + D_1^{\mathrm{swim}}\right)\boldsymbol{I} + n_b D_1^T \left[\frac{\ell_1}{d-1}\left\langle \Delta \boldsymbol{q}_1 \nabla_2 \ln g_2 \right\rangle + \left\langle \Delta \boldsymbol{r}_1 \nabla_2 \ln g_2 \right\rangle\right]^{\mathrm{sym}}, \tag{4.60}$$

where $\boldsymbol{D}_1^{\mathrm{eff}} = \partial\, \mathrm{Cov}^{(0)}(\boldsymbol{r}_1, \boldsymbol{r}_1)/(2\partial t_1)$ is the long-time dispersivity of the probe in the absence of the trapping force. As expected, one could obtain the same results by setting $\boldsymbol{F}_1^e = \boldsymbol{0}$ from the outset (see section 4.4.2).

So long as the trapping force is not identically zero, the probe will eventually reach the boundary of the trap. This confinement happens at very large distances from the trap (or at long times).

4.3.5 A strong trap

For a strong trap, the viscoelastic time scale $\tau_k = \zeta_1/k$ is much smaller than other timescales (e.g., the reorientation time) of the problem. Due to the strong trapping force, both the mean and the variance of the probe have a steady-state solution that is time independent.

The position fluctuation governed by equation (4.27) at steady state becomes

$$\frac{k}{\zeta_1}\mathrm{Cov}(\boldsymbol{r}_1, \boldsymbol{r}_1) = D_1^T \boldsymbol{I} + \left[U_1^0 \mathrm{Cov}(\boldsymbol{q}_1, \boldsymbol{r}_1) + n_b D_1^T \left\langle \nabla_2 (\ln g_2)\, \Delta \boldsymbol{r}_1 \right\rangle\right]^{\mathrm{sym}}. \tag{4.61}$$

Similarly, $\mathrm{Cov}(\boldsymbol{q}_1, \boldsymbol{r}_1)$ defined in (4.28) is given by

$$\frac{k}{\zeta_1}\mathrm{Cov}(\boldsymbol{q}_1, \boldsymbol{r}_1) = U_1^0 \boldsymbol{I}/d + n_b D_1^T \left\langle \Delta \boldsymbol{q}_1 \nabla_2 \ln g_2 \right\rangle. \tag{4.62}$$

Because the last term in the preceding equation is finite as $k \to \infty$, $\mathrm{Cov}(\boldsymbol{q}_1, \boldsymbol{r}_1)$ is small and on the order of $1/k$.

On the other hand, the relative deviation of the probe position from the average position is small, $\Delta|\boldsymbol{r}_1|/\langle|\boldsymbol{r}_1|\rangle \ll 1$, which leads to

$$\begin{aligned} \boldsymbol{M}_1(\boldsymbol{r}_2, \boldsymbol{q}_2, t) &= \int \boldsymbol{r}_1 g_2 d\boldsymbol{r}_1 = \left\langle \boldsymbol{r}_1 \right\rangle M_0 + \int \Delta \boldsymbol{r}_1 g_2 d\boldsymbol{r}_1 \\ &= \left\langle \boldsymbol{r}_1 \right\rangle M_0 + O(\Delta|\boldsymbol{r}_1|/\langle|\boldsymbol{r}_1|\rangle), \end{aligned} \tag{4.63}$$

where the decomposition $\boldsymbol{r}_1 = \langle \boldsymbol{r}_1 \rangle + \Delta \boldsymbol{r}_1$ is used. Noting that

$$\left\langle \nabla_2 \left(\ln g_2 \right) \Delta \boldsymbol{r}_1 \right\rangle = \frac{n_b}{N-1} \int d\boldsymbol{q}_1 d\boldsymbol{q}_2 \oint_{S_c} \left(\boldsymbol{M}_1 - \langle \boldsymbol{r}_1 \rangle M_0 \right) dS_2, \tag{4.64}$$

we conclude that the last two terms on the rhs of (4.61) are small. To leading-order, the fluctuation in the strong-trap limit is given by

$$\frac{k}{\zeta_1} \operatorname{Cov}(\boldsymbol{r}_1, \boldsymbol{r}_1) = D_1^T \boldsymbol{I}, \tag{4.65}$$

regardless of the presence of the bath particles.

4.4 Constant-force and constant-velocity microrheology

The moving-trap microrheology model includes the constant-force and constant-velocity microrheology models.

4.4.1 Constant-force microrheology

To recover the constant-force microrheology problem, instead of a harmonic trapping force, we apply a constant force to the probe particle, $\boldsymbol{F}_1^e = const$, and set the trap velocity $\boldsymbol{U}^{\text{trap}} = \boldsymbol{0}$. In this mode of operation, the main quantity of interest is the average velocity $\langle \boldsymbol{U}_1 \rangle$ of the probe in response to the constant external driving force. By definition, $\langle \boldsymbol{U}_1 \rangle = \partial \langle \boldsymbol{r}_1 \rangle / \partial t$, which can be obtained by considering the rhs of equation (4.11). Because the trap is absent, the position $\boldsymbol{r}_1$ defines an arbitrary origin in the laboratory frame of reference and the system is statistically homogeneous. As a result, the conditional probability $P_{N-1/1}$ defined by

$$P_N \left(\boldsymbol{r}^N, \boldsymbol{q}^N, t \right) = P_{N-1/1}(\boldsymbol{r}^{N-1}, \boldsymbol{q}^{N-1}, t | \boldsymbol{r}_1, \boldsymbol{q}_1, t) P_1(\boldsymbol{r}_1, \boldsymbol{q}_1, t) \tag{4.66}$$

is not a function of $\boldsymbol{r}_1$. (Note that in general $P_{N-1/1}$ is a function of $\boldsymbol{q}_1$.) The third term on the rhs of equation (4.11) becomes

$$- \left\langle \boldsymbol{D}_{11}^{UF} \cdot \nabla_1^T \ln P_N \right\rangle = - \int d\Gamma^{N-1} P_{N-1/1} \boldsymbol{D}_{11}^{UF} \cdot \int d\Gamma_1 \nabla_1^T P_1 = \boldsymbol{0}, \tag{4.67}$$

where we have used the divergence theorem and the fact that P_1 vanishes at infinity. Further manipulations allow us to write equation (4.11) as

$$\begin{aligned} \langle \boldsymbol{U}_1 \rangle =& U_1^0 \langle \boldsymbol{q}_1 \rangle + \left\langle \boldsymbol{M}_{11}^{UF} \right\rangle \cdot \boldsymbol{F}_1^e \\ & - \sum_{\beta=1}^{N} \int d\Gamma_1 P_1 \int d\Gamma^{N-1} \left(\boldsymbol{D}_{1\beta}^{UF} - \boldsymbol{D}_{11}^{UF} \right) \cdot \nabla_\beta^T P_{N-1/1}. \end{aligned} \tag{4.68}$$

If all N particles are not active, equation (4.68) upon integration over Γ_1 reduces to the average velocity relation originally obtained by Squires and Brady (2005, equation A4) for passive colloids.

Neglecting hydrodynamic interactions in the dilute limit, the average velocity becomes

$$\langle \boldsymbol{U}_1 \rangle = \frac{1}{\zeta_1}\boldsymbol{F}_1^e + U_1^0 \langle \boldsymbol{q}_1 \rangle + n_b D_1^T \big\langle \nabla_2 \ln g_2 \big\rangle, \tag{4.69}$$

where the zeroth spatial moment, $M_0(\boldsymbol{q}_1, \boldsymbol{r}_2, \boldsymbol{q}_2, t) = \int g_2 d\boldsymbol{r}_1$, is needed in order to calculate the average velocity of the probe. At long times, $\langle \boldsymbol{q}_1 \rangle = \boldsymbol{0}$.

In the CF mode of microrheology, the equation governing the spatial moment $\boldsymbol{M}_m$ is similar to (4.30) and can be shown to be

$$\begin{aligned}
&\frac{\partial \boldsymbol{M}_m}{\partial t} - m\left[U_1^0 \boldsymbol{q}_1 \boldsymbol{M}_{m-1} + \frac{1}{\zeta_1}\boldsymbol{F}_1^e \boldsymbol{M}_{m-1} + (m-1)D_1^T \boldsymbol{M}_{m-2}\boldsymbol{I} + D_1^T \nabla_2^T \boldsymbol{M}_{m-1}\right]^{\text{sym}} \\
&+\nabla_2^T \cdot \left(\boldsymbol{U}_r \boldsymbol{M}_m - D_r^T \nabla_2^T \boldsymbol{M}_m - \frac{1}{\zeta_1}\boldsymbol{F}_1^e \boldsymbol{M}_m\right) \\
&-m D_1^T \left[\nabla_2^T \boldsymbol{M}_{m-1}\right]^{\text{sym}} - \sum_{\alpha=1}^{2} D_\alpha^R \nabla_\alpha^R \cdot \nabla_\alpha^R \boldsymbol{M}_m = \boldsymbol{0}.
\end{aligned} \tag{4.70}$$

Here, because the force is constant, the moment equation at rank m only depends on moments of lower ranks and the system up to any rank is a closed set of equations. At contact, $r_2 = R_c$, we have the no-flux boundary condition

$$\boldsymbol{n}_2 \cdot \left(\boldsymbol{U}_r \boldsymbol{M}_m - D_r^T \nabla_2^T \boldsymbol{M}_m - \frac{1}{\zeta_1}\boldsymbol{F}_1^e \boldsymbol{M}_m\right) - m D_1^T \left[\boldsymbol{n}_2 \boldsymbol{M}_{m-1}\right]^{\text{sym}} = \boldsymbol{0}. \tag{4.71}$$

The far-field condition as $r_2 \to \infty$ is unchanged and given by equation (4.34), where $\boldsymbol{\Phi}_m$ for constant force satisfies

$$\begin{aligned}
&\frac{\partial \boldsymbol{\Phi}_m}{\partial t} - m\left[U_1^0 \boldsymbol{q}_1 \boldsymbol{\Phi}_{m-1} + \frac{\boldsymbol{F}_1^e}{\zeta_1}\boldsymbol{\Phi}_{m-1} + (m-1)D_1^T \boldsymbol{\Phi}_{m-2}\boldsymbol{I}\right]^{\text{sym}} \\
&- D_1^R \nabla_1^R \cdot \nabla_1^R \boldsymbol{\Phi}_m = \boldsymbol{0}.
\end{aligned} \tag{4.72}$$

To find the average velocity given in equation (4.69), one needs to consider equations (4.70) and (4.72) for $m = 0$. At long times, $\Phi_0 = 0$.

We note that in the above general formulation, both the probe particle and the bath particle are ABPs. By setting $U_1^0, U_2^0 = 0$ and integrating out the orientational degrees of freedom of the probe and the bath particle, we obtain the CF microrheology problem of a passive Brownian probe in a passive Brownian suspension, which has been considered by Squires and Brady (2005). On the other hand, the CF microrheology of a passive Brownian probe in an active Brownian suspension ($U_1^0 = 0, U_2^0 \neq 0$) is studied by Burkholder and Brady (2019).

Taking $m = 0$ in equation (4.70) in the absence of the external force ($\boldsymbol{F}_1^e = \boldsymbol{0}$), we obtain

$$\frac{\partial M_0}{\partial t} + \nabla_2^T \cdot \left(\boldsymbol{U}_r M_0 - D_r^T \nabla_2^T M_0\right) - \sum_{\alpha=1}^{2} D_\alpha^R \nabla_\alpha^R \cdot \nabla_\alpha^R M_0 = 0. \tag{4.73}$$

Treating the probe as one of the suspension particles, this zeroth spatial moment is the pair-correlation function of an active Brownian suspension (subject to proper normalization) in the dilute limit by neglecting all higher order correlations. Equation (4.73) governing the pair-correlation at steady state in 2D has been studied (Poncet et al. 2021; Dhont et al. 2021).

4.4.2 Force-induced tracer dispersion

In the constant-force mode of microrheology, it is also of importance to consider the force-induced dispersion of the probe particle. In this context, the probe is often referred to as the tracer, i.e., force-induced tracer dispersion. If no external force is applied, $\boldsymbol{F}_1^e = \boldsymbol{0}$, the problem is simply called tracer dispersion. The long-time dispersion tensor of the tracer in the presence of bath particles can be written as

$$\begin{aligned}\boldsymbol{D}_1^{\text{eff}} &= \lim_{t\to\infty} \frac{1}{2}\frac{d}{dt}\text{Cov}(\boldsymbol{r}_1, \boldsymbol{r}_1) \\ &= \lim_{t\to\infty} \frac{1}{2}\left[\frac{\partial}{\partial t}\langle \boldsymbol{r}_1\boldsymbol{r}_1\rangle - \langle \boldsymbol{U}_1\rangle\langle \boldsymbol{r}_1\rangle - \langle \boldsymbol{r}_1\rangle\langle \boldsymbol{U}_1\rangle\right],\end{aligned} \tag{4.74}$$

where the covariance tensor of $\boldsymbol{r}_1$ is governed by

$$\frac{1}{2}\frac{d}{dt}\text{Cov}(\boldsymbol{r}_1, \boldsymbol{r}_1) = D_1^T \boldsymbol{I} + \left[U_1^0 \text{Cov}(\boldsymbol{q}_1, \boldsymbol{r}_1) + n_b D_1^T \left\langle \Delta \boldsymbol{r}_1 \nabla_2 \ln g_2 \right\rangle\right]^{\text{sym}}, \tag{4.75}$$

and the covariance of $\boldsymbol{q}_1$ and $\boldsymbol{r}_1$ satisfies

$$\frac{d}{dt}\text{Cov}(\boldsymbol{q}_1, \boldsymbol{r}_1) + \frac{d-1}{\tau_1^R}\text{Cov}(\boldsymbol{q}_1, \boldsymbol{r}_1) = U_1^0 \text{Cov}(\boldsymbol{q}_1, \boldsymbol{q}_1) + n_b D_1^T \left\langle \Delta \boldsymbol{q}_1 \nabla_2 \ln g_2 \right\rangle. \tag{4.76}$$

At long times, we then obtain the dispersion tensor as

$$\boldsymbol{D}_1^{\text{eff}} = \left(D_1^T + D_1^{\text{swim}}\right)\boldsymbol{I} + n_b D_1^T \left[\frac{\ell_1}{d-1}\left\langle \Delta \boldsymbol{q}_1 \nabla_2 \ln g_2 \right\rangle + \left\langle \Delta \boldsymbol{r}_1 \nabla_2 \ln g_2 \right\rangle\right]^{\text{sym}}, \tag{4.77}$$

where $\ell_1 = U_1^0 \tau_1^R$ is the run length of the active probe. In the preceding equation, the first bracketed term on the rhs is the dispersion tensor of a single ABP in free space and the terms proportional to n_b is the additional contribution due to the excluded-volume interaction with the bath particles.

Using the divergence theorem, we can relate the last two terms on the rhs of (4.77) to the zeroth and first spatial moments,

$$\left\langle \Delta \boldsymbol{q}_1 \nabla_2 \ln g_2 \right\rangle = \frac{n_b}{N-1} \int \Delta \boldsymbol{q}_1 d\boldsymbol{q}_1 d\boldsymbol{q}_2 \oint_{S_c} \boldsymbol{n}_2 M_0 dS_2, \tag{4.78}$$

$$\left\langle \Delta \boldsymbol{r}_1 \nabla_2 \ln g_2 \right\rangle = \frac{n_b}{N-1} \int d\boldsymbol{q}_1 d\boldsymbol{q}_2 \oint_{S_c} \left(\boldsymbol{M}_1 - \langle \boldsymbol{r}_1 \rangle M_0 \right) \boldsymbol{n}_2 dS_2, \tag{4.79}$$

where $\langle \boldsymbol{r}_1 \rangle = [n_b/(N-1)] \int \boldsymbol{M}_1 d\boldsymbol{q}_1 d\Gamma_2$. Therefore, one only needs to solve for M_0 and $\boldsymbol{M}_1$ in equation (4.70) in order to calculate the dispersion tensor.

The above formulation for the forced-induced dispersion of an active tracer in an active suspension is a direct extension of the generalized Taylor dispersion theory (GTDT). In particular, we have used the statistical moment method of Frankel and Brenner (1989). An equivalent approach is to derive the mean velocity and the dispersion tensor by first transforming the unbounded coordinate $\boldsymbol{r}_1$ into the Fourier space and consider a small wave-number expansion (Zia and Brady 2010).

By setting $U_1^0, U_2^0 = 0$ and integrating over the orientational degrees of freedom of both the probe and the bath particles, we recover the equations governing the force-induced dispersion of a passive probe in a passive suspension (Zia and Brady 2010). To recover the problem of a passive free tracer in an active suspension studied by Burkholder and Brady (2017), one can set $\boldsymbol{F}_1^e = \boldsymbol{0}$, $U_1^0 = 0$ and integrate over the orientational degrees of freedom of the probe.

4.4.3 Constant-velocity microrheology

To obtain the equations for the CV microrheology problem, we first consider the probe to have deterministic dynamics with $U_1^0 = 0$, $D_1^T = 0$ and $D_1^R = 0$. Equation (4.24) at steady-state then leads to $k\langle \boldsymbol{r}_1 \rangle / \zeta_1 = -\boldsymbol{U}^{\text{trap}}$. Furthermore, we consider the limit of a strong trap in which case the probe tightly follows the trap velocity. In this limit, the probe velocity is the trap velocity to leading-order and we then achieve a CV probe.

To see this, we first decompose the position of the probe via $\boldsymbol{r}_1 = \langle \boldsymbol{r}_1 \rangle + \Delta \boldsymbol{r}_1$. In the strong trap limit, the deviation of the probe from the mean position is small, $\Delta |\boldsymbol{r}_1| / \langle |\boldsymbol{r}_1| \rangle \ll 1$. To leading-order, (4.63) allows us to obtain the first spatial moment as $k\boldsymbol{M}_1/\zeta_1 = -\boldsymbol{U}^{\text{trap}} M_0$ (this relation can also be viewed as a closure for the spatial moments). Substitution of this relation into (4.36) leads to

$$\frac{\partial M_0}{\partial t} + \nabla_2^T \cdot \left(U_2^0 \boldsymbol{q}_2 M_0 - D_1^T \nabla_2^T M_0 - \boldsymbol{U}^{\text{trap}} M_0 \right) - D_2^R \nabla_2^R \cdot \nabla_2^R M_0 = 0. \tag{4.80}$$

Similarly, the no-flux condition at contact ($\boldsymbol{r}_2 \in S_c$) is

$$\boldsymbol{n}_2 \cdot \left(U_2^0 \boldsymbol{q}_2 M_0 - D_1^T \nabla_2^T M_0 - \boldsymbol{U}^{\text{trap}} M_0 \right) = 0. \tag{4.81}$$

Equation (4.80) describes the distribution of the bath particle measured in a frame of reference that is co-moving with $\boldsymbol{U}^{\text{trap}}$. Realizing that the probe velocity is the same as the 'trap', $\boldsymbol{U}^{\text{probe}} = \boldsymbol{U}^{\text{trap}}$, this is the CV microrheology of an active Brownian suspension. We note that in (4.80) [cf. (4.36)] the relative velocity is $U_2^0 \boldsymbol{q}_2 - \boldsymbol{U}^{\text{trap}}$ and the relative diffusivity is D_1^T because the probe has prescribed kinematics.

The CV microrheology of an active Brownian suspension governed by (4.80) and (4.81) has been studied by Burkholder and Brady (2020). To recover the CV microrheology of a passive Brownian suspension considered by Squires and Brady (2005), one only needs to set $U_2^0 = 0$ and integrate over the orientational degrees of freedom of the bath ABP.

4.5 Fluctuations in a passive suspension

For a passive spherical probe in a passive suspension of Brownian spheres, $U_1^0, U_2^0 = 0$, the orientational degrees of freedom of both the probe and the bath particles do not matter. As a result, the pair distribution is given by $g(\boldsymbol{r}_1, \boldsymbol{r}_2, t) = \int g_2(\boldsymbol{r}_1, \boldsymbol{q}_1, \boldsymbol{r}_2, \boldsymbol{q}_2, t) d\boldsymbol{q}_1 d\boldsymbol{q}_2$, which only depends on the spatial coordinates of the probe and the bath particle. Because a constant velocity of translation of the harmonic trap does not affect the position fluctuation of the probe, without loss of generality we set the trap speed to be zero, $\boldsymbol{U}^{\text{trap}} = \boldsymbol{0}$.

Equation (4.15) at steady state under the above conditions reduces to

$$\nabla_1 \cdot \left(-\frac{k}{\zeta_1} \boldsymbol{r}_1 g + D_1 \nabla_2 g - D_1 \nabla_1 g \right) + \nabla_2 \cdot \left(\frac{k}{\zeta_1} \boldsymbol{r}_1 g + D_1 \nabla_1 g - D_r \nabla_2 g \right) = 0, \tag{4.82}$$

where we have dropped the superscript 'T' denoting translation. The no-flux condition at contact, $r_2 = R_c$, is given by

$$\boldsymbol{n}_2 \cdot \left(\frac{k}{\zeta_1} \boldsymbol{r}_1 g + D_1 \nabla_1 g - D_r \nabla_2 g \right) = 0. \tag{4.83}$$

The far-field conditions for $r_2 \to \infty$ and $r_1 \to \infty$ can be obtained from (4.20) and (4.21), respectively. In the absence of the bath particles, the positional distribution of the probe at steady state is Boltzmann and given by $P_1(\boldsymbol{r}_1) = C_1 \exp(-V^{\text{trap}}/k_BT)$, where $V^{\text{trap}} = k\boldsymbol{r}_1 \cdot \boldsymbol{r}_1/2$ is the potential energy of the trap and C_1 is a normalization constant such that the total probability is conserved, $\int P_1 d\boldsymbol{r}_1 = 1$.

The pair distribution governed by (4.82) still has a high dimensionality even without considering the orientational degrees of freedom, as is the case for a passive probe in a passive suspension. To make numerical progress, we consider the system to be in 2D, in which case the normalization constant is given by $C_1 = k/(2\pi k_BT)$. The normalization also reveals an important entropic length scale, $\sqrt{k_BT/k}$, which characterizes the spreading of the probability because $k\langle \boldsymbol{r}_1\boldsymbol{r}_1\rangle = k_BT\boldsymbol{I}$ (regardless of the dimensionality) in the absence of the bath particles.

By setting $\boldsymbol{U}_\alpha^0 = 0$ and integrating out the orientational degrees of freedom, we define the spatial moment for passive particles as $\boldsymbol{N}_m(\boldsymbol{r}_2, t) = \int \boldsymbol{M}_m d\boldsymbol{q}_1 d\boldsymbol{q}_2$. The equation governing the evolution of $\boldsymbol{N}_m$ is readily obtained by integrating over $\boldsymbol{q}_1$ and $\boldsymbol{q}_2$ in equation (4.30). At steady state, the zeroth spatial moment satisfies

$$\nabla_2^T \cdot \left(-D_r^T \nabla_2^T N_0 + \frac{k}{\zeta_1}\boldsymbol{N}_1\right) = 0. \tag{4.84}$$

The preceding equation is accompanied by the no-flux condition

$$\boldsymbol{n}_2 \cdot \left(-D_r^T \nabla_2^T N_0 + \frac{k}{\zeta_1}\boldsymbol{N}_1\right) = 0 \quad \text{for} \quad \boldsymbol{r}_2 \in S_c, \tag{4.85}$$

the far-field condition

$$N_0 \to 1 \quad \text{as} \quad |\boldsymbol{r}_2| \to \infty, \tag{4.86}$$

and the normalization $\int N_0 d\boldsymbol{r}_2 = (N-1)/n_b$. Using equation (4.24), we obtain at steady state

$$\frac{k}{\zeta_1}\langle \boldsymbol{r}_1\rangle = \frac{n_b}{N-1} n_b D_1^T \oint_{r_2=R_c} \boldsymbol{n}_2 N_0 dS_2. \tag{4.87}$$

The first spatial moment is governed by

$$\frac{k}{\zeta_1}\boldsymbol{N}_1 - D_1^T \nabla_2^T N_0 + \nabla_2^T \cdot \left(-D_r^T \nabla_2^T \boldsymbol{N}_1 + \frac{k}{\zeta_1}\boldsymbol{N}_2 - D_1^T \boldsymbol{I} N_0\right) = \boldsymbol{0}, \tag{4.88}$$

where similarly the no-flux condition is

$$\boldsymbol{n}_2 \cdot \left(-D_r^T \nabla_2^T \boldsymbol{N}_1 + \frac{k}{\zeta_1}\boldsymbol{N}_2 - D_1^T \boldsymbol{I} N_0\right) = 0 \quad \text{for} \quad \boldsymbol{r}_2 \in S_c, \tag{4.89}$$

and the far-field condition is given by

$$\boldsymbol{N}_1 \to \boldsymbol{0} \quad \text{as} \quad |\boldsymbol{r}_2| \to \infty. \tag{4.90}$$

Using $\boldsymbol{N}_1$, one can calculate the mean-squared displacement via

$$\frac{k}{\zeta_1}\langle \boldsymbol{r}_1\boldsymbol{r}_1\rangle = D_1^T\boldsymbol{I} + 2\frac{n_b}{N-1}n_b D_1^T \oint_{r_2=R_c} [\boldsymbol{n}_2\boldsymbol{N}_1]^{\mathrm{sym}}\, dS_2. \tag{4.91}$$

The second spatial moment is governed by

$$\begin{aligned} &-2\left[-\frac{k}{\zeta_1}\boldsymbol{N}_2 + D_1^T N_0\boldsymbol{I} + D_1^T\nabla_2^T\boldsymbol{N}_1\right]^{\mathrm{sym}} \\ &+\nabla_2^T\cdot\left[-D_r^T\nabla_2^T\boldsymbol{N}_2 + \frac{k}{\zeta_1}\boldsymbol{N}_3\right] - 2D_1^T\left[\nabla_2^T\boldsymbol{N}_1\right]^{\mathrm{sym}} = \boldsymbol{0}, \\ \boldsymbol{n}_2\cdot&\left[-D_r^T\nabla_2^T\boldsymbol{N}_2 + \frac{k}{\zeta_1}\boldsymbol{N}_3\right] - 2D_1^T\left[\boldsymbol{n}_2\boldsymbol{N}_1\right]^{\mathrm{sym}} = \boldsymbol{0}. \end{aligned} \tag{4.92}$$

The far-filed condition for $\boldsymbol{N}_2$ is given by

$$\boldsymbol{N}_2 \to \frac{\zeta_1 D_1^T}{k}\boldsymbol{I} \quad \text{as} \quad |\boldsymbol{r}_2| \to \infty. \tag{4.93}$$

4.6 Derivation of the pair problem

We integrate equation (4.7) over the relative positions and the orientations of the bath particles labeled from 3 to N to obtain

$$\begin{aligned} \frac{\partial P_2}{\partial t} &+ \nabla_1^T\cdot\int\left(\boldsymbol{j}_1^T - \boldsymbol{U}^{\mathrm{trap}}P_N\right)d\Gamma^{N-2} + \nabla_2^T\cdot\int\left(\boldsymbol{j}_2^T - \boldsymbol{j}_1^T\right)d\Gamma^{N-2} \\ &+ \sum_{\alpha=1}^{2}\nabla_\alpha^R\cdot\int \boldsymbol{j}_\alpha^R d\Gamma^{N-2} = 0, \end{aligned} \tag{4.94}$$

where $d\Gamma^{N-2}$ is a shorthand for $\prod_{\beta=3}^{N} d\Gamma_\beta$ and $P_2 = \int P_N d\Gamma^{N-2}$. In deriving the preceding equation, the divergence theorem and the no-flux condition are used to eliminate the terms $\int \nabla_\beta^T\cdot\left(\boldsymbol{j}_\beta^T - \boldsymbol{j}_1^T\right)d\Gamma^{N-2}$ for $\beta = 3, ..., N$. In addition, the relation $\int \nabla_\alpha^R\cdot \boldsymbol{j}_\alpha^R d\boldsymbol{q}_\alpha = 0$ is used.

To proceed further, we define the conditional probability of finding the remaining $N-2$ particles ($P_{N-2/2}$) given the configuration of the probe and the *first* bath particle:

$$P_N(\boldsymbol{r}^N, \boldsymbol{q}^N, t) = P_{(N-2)/2}\left(\boldsymbol{r}^{N-2}, \boldsymbol{q}^{N-2}, t|\boldsymbol{r}_2, \boldsymbol{q}_2, \boldsymbol{r}_1, \boldsymbol{q}_1, t\right)P_2(\boldsymbol{r}_2, \boldsymbol{q}_2, \boldsymbol{r}_1, \boldsymbol{q}_1, t). \tag{4.95}$$

Notice that the conditional probability is conserved, $\int P_{N-2/2} d\Gamma^{N-2} = 1$. In equation (4.94), for $\alpha = 1$ or 2, we have

$$\begin{aligned}\int \boldsymbol{j}_\alpha^T d\Gamma^{N-2} =& U_\alpha^0 \boldsymbol{q}_\alpha P_2 + \left\langle \boldsymbol{M}_{\alpha 1}^{UF} \right\rangle_{N-2/2} \cdot \boldsymbol{F}_1^e P_2 - \left\langle \boldsymbol{D}_{\alpha 2}^{UF} - \boldsymbol{D}_{\alpha 1}^{UF} \right\rangle_{N-2/2} \cdot \nabla_2^T P_2 \\ & - \sum_{\beta=2}^{N} \left\langle \left(\boldsymbol{D}_{\alpha\beta}^{UF} - \boldsymbol{D}_{\alpha 1}^{UF} \right) \cdot \nabla_\beta^T \ln P_{N-2/2} \right\rangle_{N-2/2} P_2 \\ & - \left\langle \boldsymbol{D}_{\alpha 1}^{UF} \cdot \nabla_1^T \ln P_{N-2/2} \right\rangle_{N-2/2} P_2 - \left\langle \boldsymbol{D}_{\alpha 1}^{UF} \right\rangle_{N-2/2} \cdot \nabla_1^T P_2 \\ & - \sum_{\beta=1}^{2} \left\langle \boldsymbol{D}_{\alpha\beta}^{UL} \cdot \nabla_\beta^R \ln P_{N-2/2} \right\rangle P_2 - \sum_{\beta=1}^{2} \left\langle \boldsymbol{D}_{\alpha\beta}^{UL} \right\rangle \cdot \nabla_\beta^R P_2, \end{aligned} \qquad (4.96)$$

and

$$\begin{aligned}\int \boldsymbol{j}_\alpha^R d\Gamma^{N-2} =& \left\langle \boldsymbol{M}_{\alpha 1}^{\Omega F} \right\rangle_{N-2/2} \cdot \boldsymbol{F}_1^e P_2 - \left\langle \boldsymbol{D}_{\alpha 2}^{\Omega F} - \boldsymbol{D}_{\alpha 1}^{\Omega F} \right\rangle_{N-2/2} \cdot \nabla_2^T P_2 \\ & - \sum_{\beta=2}^{N} \left\langle \left(\boldsymbol{D}_{\alpha\beta}^{\Omega F} - \boldsymbol{D}_{\alpha 1}^{\Omega F} \right) \cdot \nabla_\beta^T \ln P_{N-2/2} \right\rangle_{N-2/2} P_2 \\ & - \left\langle \boldsymbol{D}_{\alpha 1}^{\Omega F} \cdot \nabla_1^T \ln P_{N-2/2} \right\rangle_{N-2/2} P_2 - \left\langle \boldsymbol{D}_{\alpha 1}^{\Omega F} \right\rangle_{N-2/2} \cdot \nabla_1^T P_2 \\ & - \sum_{\beta=1}^{2} \left\langle \boldsymbol{D}_{\alpha\beta}^{\Omega L} \cdot \nabla_\beta^R \ln P_{N-2/2} \right\rangle P_2 \\ & - \sum_{\beta=1}^{2} \left\langle \boldsymbol{D}_{\alpha\beta}^{\Omega L} \right\rangle \cdot \nabla_\beta^R P_2 - D_\alpha^R \nabla_\alpha^R P_2, \end{aligned} \qquad (4.97)$$

where we have used the fact that the mobility tensors are independent of $\boldsymbol{q}^N$ for spheres, i.e., $\boldsymbol{M}_{\alpha\beta} = \boldsymbol{M}_{\alpha\beta}(\boldsymbol{r}_2, ...\boldsymbol{r}_N)$.

In the dilute limit, neglecting the terms involving the gradients of $\ln P_{N-2/2}$ and using the pair mobility tensor in the absence of other particles in place of $\langle \boldsymbol{M} \rangle_{N-2/2}$, we obtain

$$\frac{\partial P_2}{\partial t} + \nabla_1^T \cdot \left(\boldsymbol{j}_1^T - \boldsymbol{U}^{\mathrm{trap}} P_2 \right) + \nabla_2^T \cdot \left(\boldsymbol{j}_2^T - \boldsymbol{j}_1^T \right) + \sum_{\alpha=1}^{2} \nabla_\alpha^R \cdot \boldsymbol{j}_\alpha^R = 0, \qquad (4.98)$$

where using the same symbols as before

$$\begin{aligned}\boldsymbol{j}_\alpha^T &= U_\alpha^0 \boldsymbol{q}_\alpha P_2 + \boldsymbol{M}_{\alpha 1}^{UF} \cdot \boldsymbol{F}_1^e P_2 - \left(\boldsymbol{D}_{\alpha 2}^{UF} - \boldsymbol{D}_{\alpha 1}^{UF}\right) \cdot \nabla_2^T P_2 \\ &\quad - \boldsymbol{D}_{\alpha 1}^{UF} \cdot \nabla_1^T P_2 - \sum_{\beta=1}^{2} \boldsymbol{D}_{\alpha\beta}^{UL} \cdot \nabla_\beta^R P_2 \qquad (4.99) \\ \boldsymbol{j}_\alpha^R &= \boldsymbol{M}_{\alpha 1}^{\Omega F} \cdot \boldsymbol{F}_1^e P_2 - \left(\boldsymbol{D}_{\alpha 2}^{\Omega F} - \boldsymbol{D}_{\alpha 1}^{\Omega F}\right) \cdot \nabla_2^T P_2 - \boldsymbol{D}_{\alpha 1}^{\Omega F} \cdot \nabla_1^T P_2 \\ &\quad - \sum_{\beta=1}^{2} \boldsymbol{D}_{\alpha\beta}^{\Omega L} \cdot \nabla_\beta^R P_2 - D_\alpha^R \nabla_\alpha^R P_2. \qquad (4.100)\end{aligned}$$

In the absence of hydrodynamic interactions, we have $\boldsymbol{M}_{\alpha\beta}^{UF} = \boldsymbol{I}\delta_{\alpha\beta}/\zeta_\alpha^T$, $\boldsymbol{M}_{\alpha\beta}^{\Omega L} = \boldsymbol{I}\delta_{\alpha\beta}/\zeta_\alpha^R$, and $\boldsymbol{M}_{\alpha\beta}^{UL}, \boldsymbol{M}_{\alpha\beta}^{\Omega F} = \boldsymbol{0}$, where $\delta_{\alpha\beta}$ is the Kronecker delta. The conditional probability of finding a bath particle, $\rho_{1/1}(\boldsymbol{r}_2, \boldsymbol{q}_2, t|\boldsymbol{r}_1, \boldsymbol{q}_1, t)$, can be related to P_2 via the relation $\rho_{1/1} = (N-1)P_{1/1}$, where $P_{1/1}$ is defined by $P_2 = P_{1/1}P_1$. The factor of $N-1$ comes from the process of removing the "labels" of the $N-1$ bath particles. From this, the joint probability density of finding a bath particle at $\boldsymbol{r}_2$, $\boldsymbol{q}_2$ and the probe at $\boldsymbol{r}_1$, $\boldsymbol{q}_1$ is defined as $\rho_2 = \rho_{1/1}P_1$. Furthermore, we define a generalized pair-distribution function g_2 such that

$$\rho_2 = \rho_{1/1}P_1 = n_b g_{1/1} P_1 = n_b g_2, \qquad (4.101)$$

where $n_b = (N-1)/V$ is the number density of bath particles.

This generalized pair distribution is still governed by equation (4.98) with g_2 in place of P_2. In the absence of hydrodynamic interactions, equations (4.98)-(4.100) reduce to equations (4.15)-(4.18) given in the text.

4.7 Derivation of the variance relations

For the pair problem, equation (4.12) governing the mean-squared displacement reduces to

$$\begin{aligned}\frac{1}{2}\frac{\partial\langle \boldsymbol{r}_1\boldsymbol{r}_1\rangle}{\partial t} + \frac{1}{\tau_k}\left\langle \boldsymbol{r}_1\boldsymbol{r}_1\right\rangle =& D_1^T\boldsymbol{I} + \left[U_1^0\left\langle \boldsymbol{q}_1\boldsymbol{r}_1\right\rangle - \boldsymbol{U}^{\text{trap}}\langle \boldsymbol{r}_1\rangle\right]^{\text{sym}} \\ &+ n_b D_1^T\left[\left\langle \nabla_2\left(\ln g_2\right)\boldsymbol{r}_1\right\rangle\right]^{\text{sym}}. \qquad (4.102)\end{aligned}$$

Using equations (4.24) and (4.102), one can show that the position fluctuation of the probe is governed by

$$\begin{aligned}\frac{1}{2}\frac{\partial\,\mathrm{Cov}(\boldsymbol{r}_1,\boldsymbol{r}_1)}{\partial t} + \frac{1}{\tau_k}\mathrm{Cov}(\boldsymbol{r}_1,\boldsymbol{r}_1) =& D_1^T\boldsymbol{I} + U_1^0\left[\mathrm{Cov}(\boldsymbol{q}_1,\boldsymbol{r}_1)\right]^{\text{sym}} \\ &+ n_b D_1^T\left[\left\langle \nabla_2\left(\ln g_2\right)\Delta\boldsymbol{r}_1\right\rangle\right]^{\text{sym}}, \qquad (4.103)\end{aligned}$$

where $\mathrm{Cov}(\boldsymbol{q}_1, \boldsymbol{r}_1) = \langle \boldsymbol{q}_1\boldsymbol{r}_1\rangle - \langle \boldsymbol{q}_1\rangle\langle \boldsymbol{r}_1\rangle$ and recall that $\Delta\boldsymbol{r}_1 = \boldsymbol{r}_1 - \langle \boldsymbol{r}_1\rangle$. To calculate the covariance of $\boldsymbol{q}_1$ and $\boldsymbol{r}_1$ appearing in equation (4.103), we need $\langle \boldsymbol{q}_1\boldsymbol{r}_1\rangle$, $\langle \boldsymbol{q}_1\rangle$ and $\langle \boldsymbol{r}_1\rangle$.

The net polar order of the probe satisfies

$$\frac{\partial\langle \boldsymbol{q}_1\rangle}{\partial t} + \frac{d-1}{\tau_1^R}\langle \boldsymbol{q}_1\rangle = \boldsymbol{0}, \tag{4.104}$$

where $d(=2,3)$ is the dimensionality of the problem. It can be seen that the net polar order of the probe is not affected by the trap or the bath particles. The full solution to (4.104) is readily obtained as

$$\langle \boldsymbol{q}_1\rangle(t) = \exp\left[-(d-1)t/\tau_1^R\right]\langle \boldsymbol{q}_1\rangle(0), \tag{4.105}$$

where any initial net polar order $\langle \boldsymbol{q}_1\rangle(0)$ decays away exponentially due to the rotary diffusion.

The average of $\boldsymbol{q}_1\boldsymbol{r}_1$ is governed by

$$\begin{aligned}\frac{\partial\left\langle \boldsymbol{q}_1\boldsymbol{r}_1\right\rangle}{\partial t} + \frac{1}{\tau_k}\left\langle \boldsymbol{q}_1\boldsymbol{r}_1\right\rangle + \frac{d-1}{\tau_1^R}\left\langle \boldsymbol{q}_1\boldsymbol{r}_1\right\rangle = &- \langle \boldsymbol{q}_1\rangle\boldsymbol{U}^{\mathrm{trap}} + U_1^0\left\langle \boldsymbol{q}_1\boldsymbol{q}_1\right\rangle \\ &+ n_b D_1^T\left\langle \boldsymbol{q}_1\nabla_2 \ln g_2\right\rangle,\end{aligned} \tag{4.106}$$

where $\langle \boldsymbol{q}_1\rangle$ is given by (4.104) and $\left\langle \boldsymbol{q}_1\boldsymbol{q}_1\right\rangle$ satisfies

$$\frac{\partial\left\langle \boldsymbol{q}_1\boldsymbol{q}_1\right\rangle}{\partial t} + \frac{2d}{\tau_1^R}\left[\left\langle \boldsymbol{q}_1\boldsymbol{q}_1\right\rangle - \frac{1}{d}\boldsymbol{I}\right] = \boldsymbol{0}. \tag{4.107}$$

Similarly to $\langle \boldsymbol{q}_1\rangle$, the net nematic order of the probe regardless of the presence of the trap or the bath particles is given by

$$\langle \boldsymbol{Q}_1\rangle(t) = \exp\left[-2dt/\tau_1^R\right]\boldsymbol{Q}_1(0), \tag{4.108}$$

where we have defined the net trace-free nematic tensor $\langle \boldsymbol{Q}_1\rangle = \left\langle \boldsymbol{q}_1\boldsymbol{q}_1\right\rangle - \boldsymbol{I}/d$.

At long times ($t \to \infty$), there is no net polar order of the probe, $\langle \boldsymbol{q}_1\rangle = \boldsymbol{0}$ and the net nematic order is isotropic, $\left\langle \boldsymbol{q}_1\boldsymbol{q}_1\right\rangle = \boldsymbol{I}/d$.

Using equations (4.24), (4.104) and (4.106), we obtain

$$\begin{aligned}\frac{\partial\,\mathrm{Cov}(\boldsymbol{q}_1, \boldsymbol{r}_1)}{\partial t} + \left(\frac{1}{\tau_k} + \frac{d-1}{\tau_1^R}\right)\mathrm{Cov}(\boldsymbol{q}_1, \boldsymbol{r}_1) =& U_1^0\,\mathrm{Cov}(\boldsymbol{q}_1, \boldsymbol{q}_1) \\ &+ n_b D_1^T\left\langle \Delta\boldsymbol{q}_1\nabla_2 \ln g_2\right\rangle,\end{aligned} \tag{4.109}$$

where $\Delta\boldsymbol{q}_1 = \boldsymbol{q}_1 - \langle \boldsymbol{q}_1\rangle$.

4.8 Asymptotic analysis of the probe in the absence of bath particles

In equation (4.44), the timescale of transient decay τ can be defiend by

$$\frac{1}{\tau} = \frac{d-1}{\tau_1^R} + \frac{1}{\tau_k} = \frac{d-1+\epsilon}{\tau_1^R}, \tag{4.110}$$

where $\epsilon = \tau_1^R/\tau_k = k\tau_1^R/\zeta_1$. Using this definition, the solution of (4.44) is given by

$$\begin{aligned} \mathrm{Cov}(\boldsymbol{q}_1, \boldsymbol{r}_1)(t) =& e^{-t/\tau}\,\mathrm{Cov}(\boldsymbol{q}_1, \boldsymbol{r}_1)(0) \\ & + U_1^0 \int_0^t \exp\left(-\frac{t-s}{\tau}\right) \mathrm{Cov}(\boldsymbol{q}_1, \boldsymbol{q}_1)(s) ds. \end{aligned} \tag{4.111}$$

From equation (4.108), the preceding equation becomes

$$\begin{aligned} \mathrm{Cov}(\boldsymbol{q}_1, \boldsymbol{r}_1)(t) \quad = \quad & e^{-t/\tau}\,\mathrm{Cov}(\boldsymbol{q}_1, \boldsymbol{r}_1)(0) + \frac{U_1^0 \tau \boldsymbol{I}}{d}\left(1 - e^{-t/\tau}\right) \\ & - \frac{\ell_1}{d+1-\epsilon}\left(e^{-2dt/\tau_R} - e^{-t/\tau}\right)\langle \boldsymbol{Q}_1\rangle(0). \end{aligned} \tag{4.112}$$

In the long-time limit ($t/\tau_R \gg 1$ and $t/\tau \gg 1$), we obtain equation (4.46) in the text. Using equation (4.103) in the absence of bath particles, we obtain

$$\begin{aligned} \mathrm{Cov}(\boldsymbol{r}_1, \boldsymbol{r}_1)(t) \quad = \quad & e^{-2t/\tau_k}\,\mathrm{Cov}(\boldsymbol{r}_1, \boldsymbol{r}_1)(0) + \tau_k \left(D_1^T + \frac{\left(U_1^0\right)^2 \tau}{d} \right) \boldsymbol{I} \left(1 - e^{-2t/\tau_k}\right) \\ & + 2U_1^0 \int_0^t \exp\left[-2\frac{t-s}{\tau_k}\right] \left[\mathrm{Cov}'(\boldsymbol{q}_1, \boldsymbol{r}_1)(s)\right]^{\mathrm{sym}} ds, \end{aligned} \tag{4.113}$$

where $\mathrm{Cov}'(\boldsymbol{q}_1, \boldsymbol{r}_1)(s) = \mathrm{Cov}(\boldsymbol{q}_1, \boldsymbol{r}_1)(s) - U_1^0 \tau \boldsymbol{I}/d$ is the time-dependent (transient) part of the covariance of $\boldsymbol{q}_1$ and $\boldsymbol{r}_1$. The integral in (4.113) can be carried out explicitly but is not important for the following discussion.

In the presence of the harmonic trap, the system exhibit two timescales that are important: the reorientation time τ_1^R and the viscoelastic timescale τ_k; their relative importance is characterized by the parameter ϵ. In the weak-trap limit, $\epsilon \to 0$, the two timescales are well-separated. It is useful to define the fast time variable $t_1 = t$ and the slow time variable $t_2 = \epsilon t$. We now consider the limit $\epsilon \to 0$ and the intermediate timescale in which the ABP has experienced many reorientations due to rotary diffusion but hasn't reached the 'boundary' of the trap, i.e., $t_1/\tau_1^R \gg 1$ but $t_2/\tau_1^R = \epsilon t/\tau_R \ll 1$.

Differentiating equation (4.113) leads to

$$\begin{aligned}\frac{d}{dt}\operatorname{Cov}(\boldsymbol{r}_1,\boldsymbol{r}_1)(t) =& \frac{-2}{\tau_k}e^{-2t/\tau_k}\operatorname{Cov}(\boldsymbol{r}_1,\boldsymbol{r}_1)(0) + 2\left(D_1^T + \frac{\left(U_1^0\right)^2\tau}{d}\right)\boldsymbol{I}e^{-2t/\tau_k} \\ &+ 2U_1^0\left[\operatorname{Cov}'(\boldsymbol{q}_1,\boldsymbol{r}_1)(t)\right]^{\text{sym}} \\ &+ 2U_1^0\frac{-2}{\tau_k}\int_0^t \exp\left[-2\frac{t-s}{\tau_k}\right]\left[\operatorname{Cov}'(\boldsymbol{q}_1,\boldsymbol{r}_1)(s)\right]^{\text{sym}}\,ds.\end{aligned} \tag{4.114}$$

Since $1/\tau_k = \epsilon/\tau_1^R$ and

$$\frac{t}{\tau_k} = \frac{t_2}{\epsilon\tau_k} = \frac{t_2}{\tau_1^R} \ll 1 \quad \text{and} \quad \frac{t}{\tau} = \frac{t_1}{\tau_1^R}(d+1-\epsilon) \gg 1, \tag{4.115}$$

we have

$$e^{-2t/\tau_k} = e^{-2t_2/\tau_1^R} = 1 + O(t_2/\tau_1^R) \qquad \frac{\left(U_1^0\right)^2\tau}{d} = \frac{U_1^0\ell_1}{d(d-1)}\left[1+O(\epsilon)\right]. \tag{4.116}$$

Therefore, equation (4.114) at leading order is

$$\frac{1}{2}\frac{d}{dt}\operatorname{Cov}(\boldsymbol{r}_1,\boldsymbol{r}_1)(t) = \left(D_1^T + \frac{U_1^0\ell_1}{d(d-1)}\right)\boldsymbol{I} = \left(D_1^T + D_1^{\text{swim}}\right)\boldsymbol{I}. \tag{4.117}$$

It is clear that in the weak-trap limit in this intermediate timescale, the ABP exhibit diffusive behavior with the free-space dispersivity $D_1^T + D_1^{\text{swim}}$.

We now consider the weak-trap limit but at long-times, $t/\tau_1^R \gg 1, t/\tau_k \gg 1$. So long as the trap strength is not identically zero, the ABP will eventually ($t/\tau_k \gg 1$) experience the confinement of the trap. Using equation (4.113), we obtain at long times

$$\frac{1}{\tau_k}\operatorname{Cov}(\boldsymbol{r}_1,\boldsymbol{r}_1) \to \left(D_1^T + D_1^{\text{swim}}\right)\boldsymbol{I}. \tag{4.118}$$

In the strong-trap limit ($\epsilon \to \infty$) and at long times, we have $\tau/\tau_1^R = O(1/\epsilon)$ and the position fluctuation of the probe $\operatorname{Cov}(\boldsymbol{r}_1,\boldsymbol{r}_1)/\tau_k = D_1^T$.

4.9 Solution for a passive probe in a passive suspension

Equation (4.82) in 2D is most convenient for numerical analysis in a polar coordinate system in which the angle between $\boldsymbol{r}_2$ and $\boldsymbol{r}_1$ is defined as β. To see this, we first consider the polar angles defined relative to a Cartesian frame of reference (see

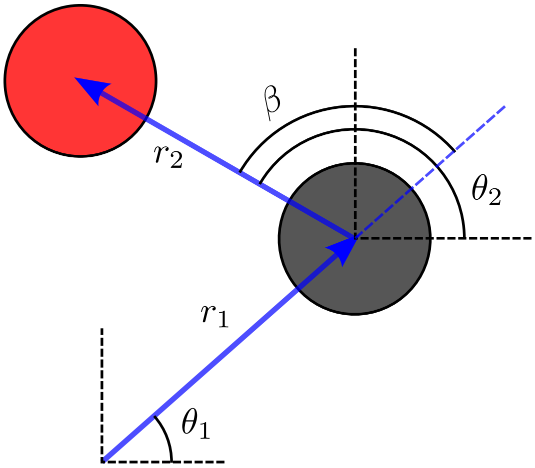

Figure 4.2: Definitions of the polar coordinate system and the relative angle $\beta = \theta_2 - \theta_1$.

figure 4.2) in which $g = g(r_1, \theta_1, r_2, \theta_2)$. Introducing the change of variables such that $\alpha = \theta_1$ and $\beta = \theta_2 - \theta_1$, one can show that g_2 in this new coordinate system is not a function of α, i.e., $g = g(r_1, r_2, \beta)$.

Noting that $\partial/\partial\theta_1 = \partial/\partial\alpha - \partial/\partial\beta$ and $\partial/\partial\theta_2 = \partial/\partial\beta$, equation (4.82) is written as

$$\begin{aligned}&-2g - \frac{r_1}{r_2}\sin\beta\frac{\partial g}{\partial\beta} - \left[\frac{1}{r_1^2} + \left(1 + \frac{D_2}{D_1}\right)\frac{1}{r_2^2} + \frac{2\cos\beta}{r_1 r_2}\right]\frac{\partial^2 g}{\partial\beta^2}\\&- \left[\left(1 + \frac{D_2}{D_1}\right)\frac{1}{r_2} - r_1\cos\beta\right]\frac{\partial g}{\partial r_2} - 2\sin\beta\frac{\partial}{\partial\beta}\left(\frac{1}{r_1}\frac{\partial g}{\partial r_2} + \frac{1}{r_2}\frac{\partial g}{\partial r_1}\right)\\&- \left(1 + \frac{D_2}{D_1}\right)\frac{\partial^2 g}{\partial r_2^2} - \left(\frac{1}{r_1} + r_1\right)\frac{\partial g}{\partial r_1} + 2\cos\beta\frac{\partial^2 g}{\partial r_1\partial r_2} - \frac{\partial^2 g}{\partial r_1^2} = 0, \quad (4.119)\end{aligned}$$

where r_1, r_2 and g are rendered dimensionless using the length scale $\sqrt{k_B T/k}$. The no-flux condition (4.83) becomes

$$r_1\cos\beta g - \frac{\sin\beta}{r_1}\frac{\partial g}{\partial\beta} - \left(1 + \frac{D_2}{D_1}\right)\frac{\partial g}{\partial r_2} + \cos\beta\frac{\partial g}{\partial r_1} = 0 \quad \text{at} \quad r_2 = \frac{R_c}{\sqrt{k_B T/k}}. \quad (4.120)$$

Far away from the probe, the probe distribution is undisturbed from its equilibrium:

$$g \to \frac{1}{2\pi}\exp\left(-\frac{1}{2}r_1^2\right) \quad \text{as} \quad r_2 \to \infty. \quad (4.121)$$

Far away from the trap, the probability vanishes:

$$g \to 0 \quad \text{as} \quad r_1 \to \infty. \quad (4.122)$$

Because $\zeta_1 D_1 = \zeta_2 D_2 = k_B T$, we have $D_2/D_1 = a/b$.

Chapter 5

CONSTANT-VELOCITY MICRORHEOLOGY

Particle-tracking microrheology of dilute active (self-propelled) colloidal suspensions is studied by considering the external force required to maintain the steady translation of an immersed constant-velocity colloidal probe. If the probe speed is zero, the suspension microstructure is isotropic but exhibits a boundary accumulation of active bath particles at contact due to their self-propulsion. As the probe moves through the suspension, the microstructure is distorted from the non-equilibrium isotropic state, which allows us to define a microviscosity for the suspension using the Stokes drag law. For a slow probe, we show that active suspensions exhibit a swim-thinning behavior in which their microviscosity is gradually lowered from that of passive suspensions as the swim speed increases. When the probe speed is fast, the suspension activity is obscured by the rapid advection of the probe and the measured microviscosity is indistinguishable from that of passive suspensions. Generally for finite activity, the suspension exhibits a force-thinning behavior—though with a lower zero-forcing plateau—as a function of the probe speed. These behaviors originate from the interplay between the suspension activity and the hard-sphere excluded volume interaction between the probe and a bath particle. We show that for *pullers*, the disturbance due to their hydrodynamic stresslets pulls the probe forward provided that the density of particles is larger in the front of the probe than that in the back. Therefore, the microviscosity can become *negative* if the hydrodynamic stresslet is sufficiently strong. This is in contrast to the bulk shear rheology of active suspensions, where a negative viscosity is only observed for pushers. In addition, if the disturbance flow due to the translating probe is considered, we show that again the microviscosity can become negative. This is due to the coupling between vorticity-induced reorientation and swimming of active particles, which allows the number density in the back of the probe to be larger than that in the front.

5.1 Introduction

In the past few decades, colloidal active matter systems such as motile bacteria and synthetic Janus particles immersed in a viscous solvent have evolved into a vibrant field of study (Lauga and Powers 2009; Ramaswamy 2010; Marchetti et al. 2013;

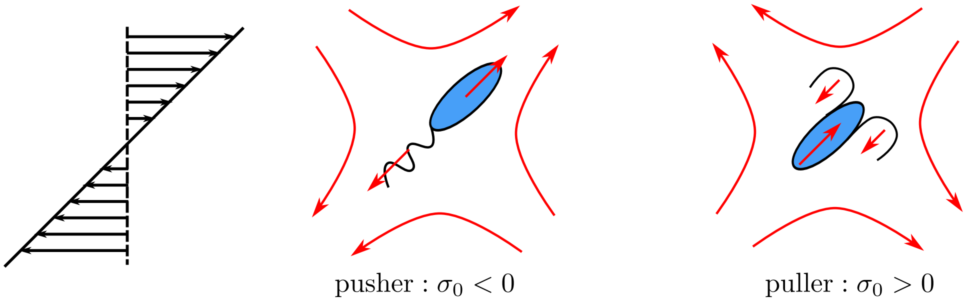

Figure 5.1: Schematic of a simple shear flow and the force dipoles of a pusher and a puller.

Elgeti et al. 2015; Bechinger et al. 2016). Owing to their ability to self-propel, active colloids exhibit a cascade of striking properties not observed in equilibrium colloidal systems such as accumulation at no-flux boundaries (Wensink and Löwen 2008; Li and Tang 2009; Elgeti and Gompper 2013; Yan and Brady 2015b), upstream swimming in Poiseuille flow (Hill et al. 2007; Kaya and Koser 2009; 2012; Zöttl and Stark 2012; Peng and Brady 2020), and the existence of a steady-state spontaneous flow in the absence of any external forces (Lushi et al. 2012; Guo et al. 2018).

The macroscopic (bulk) rheological response of active colloidal suspensions is also distinct from that of passive colloids. In particular, experiments (López et al. 2015; Chui et al. 2021) and theoretical studies (Hatwalne et al. 2004; Haines et al. 2009; Saintillan 2010; Ryan et al. 2011; Loisy et al. 2018) have shown that the low-Pe shear (weak shear) viscosity of dilute active suspensions consisting of *anisotropic* and *pusher* (tail-actuated) microswimmers can be zero—or even negative. This apparent negative viscosity has been attributed to the interaction between the hydrodynamic stresslet induced by the force dipoles of an active particle and the applied simple shear flow. To see this, consider a self-propelled pusher or puller microswimmer in a simple shear flow (see figure 5.1 for a schematic). The straining-component of the flow tends to align the microswimmer along the extensional axis of shear. With this alignment, the flow induced by a pusher acts to "stretch" the fluid further, which results in a reduced shear viscosity. For a puller swimmer, the induced flow acts against the imposed shear and an increase in the shear viscosity is observed. According to Jeffery's equation describing the orientational dynamics of an ellipsoidal particle in simple shear (Jeffery 1922), this alignment effect is only present for non-spherical particles and therefore one expects the shear viscosity of active spheres to be non-negative.

Bulk rheological studies such as simple shear provide a measurement of the global (suspension averaged) rheological behavior of colloidal suspensions. In the context of biological active matter such as cellular environments, the active "particles" are often subjected to spatially *localized* cues and biochemical signals rather than to bulk flow or body forces. These localized behaviors lead to an inherently heterogeneous intracellular environment with differing material properties such as spatial variations in viscosity and elasticity. In addition, classical bulk rheology equipment cannot be used to probe the microenvironment inside individual living cells without disrupting their mechanical structure. To address such challenges, microrheological techniques have been developed. In microrheology, the local rheological properties such as viscoelasticity of a complex fluid are inferred from the free (thermal) or forced motion of "probe" particles. The probes can be either embedded colloidal particles or tagged organelles and molecules existing in the biological material. The study of the deformation or flow of biological materials at small length scales has been termed bio-microrheology and deemed a frontier in microrheology (Weihs et al. 2006). Indeed, particle-tracking microrheology has been widely used in experimental measurements to characterize the rheological properties inside living cells (Wilhelm et al. 2003; Nawaz et al. 2012; Berret 2016; Ayala et al. 2016; Hu et al. 2017).

To aid in the understanding of experimental measurements and in the prediction of colloidal microrheology, Squires and Brady (2005) developed a theoretical framework in which a colloidal probe is pulled through a suspension of neutrally buoyant bath colloids (see figure 5.2 for a schematic). If the external pulling force is absent, this problem is often referred to as tracer diffusion and is classified as passive (no external forcing) microrheology. To characterize the nonlinear response, an external force, often larger than the thermodynamic restoring force, is applied to the probe and we call this problem forced microrheology [1]. Within forced microrheology, two operating modes—constant-force (CF) and constant-velocity (CV)—are often considered from a theoretical perspective. In the CF mode, the external force $\boldsymbol{F}^{\text{ext}}$ applied to the probe is a constant while the position of the probe is fluctuating. Conversely for the CV mode, the velocity $\boldsymbol{U}^{\text{ext}}$ is a constant (therefore the position of the probe is known) and the external force required to maintain such a steady motion must fluctuate. The framework of Squires and Brady (2005) has been extended and used to study the microrheology of passive (not self-propelled) colloidal

---

[1] Traditionally, this is called *active* microrheology in contrast to the passive mode. In the context of active matter, however, this terminology of active microrheology conflicts with that of active matter and we thus use the term forced microrheology.

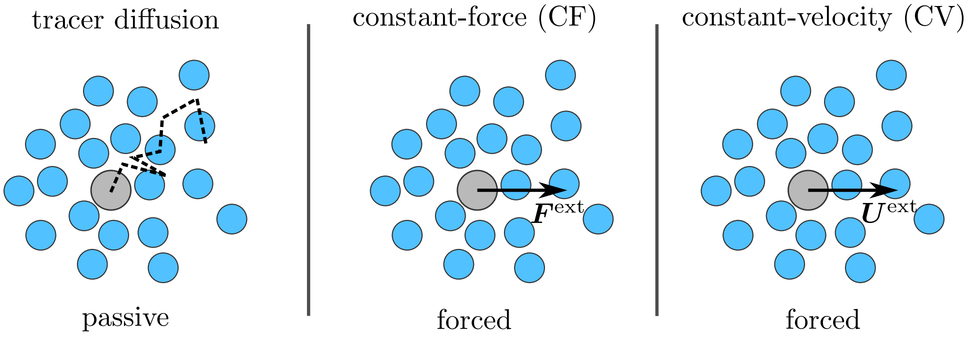

Figure 5.2: Schematic of different operating modes of colloidal microrheology. The gray particle is the probe and the blue particles are the bath particles. In the passive mode, the MSD of the probe is measured. In the forced modes, the probe is driven by an external force, either constant (CF mode) or fluctuating (CV mode).

suspensions (Khair and Brady 2005; 2006; Meyer et al. 2006; Zia and Brady 2010; Swan and Zia 2013; Zia 2018).

In contrast to passive colloids, the study of the microrheology of active colloids is more recent and their microrheological response is less well understood. Recent experimental and theoretical studies have shown that in the absence of external forcing, a Brownian tracer can undergo enhanced diffusive motion at long times due to the activity (e.g., self-propulsion) of the bath particles (Jepson et al. 2013; Miño et al. 2013; Morozov and Marenduzzo 2014; Burkholder and Brady 2017). If the bath particles are passive, it is known that the long-time diffusive motion of the tracer is hindered resulting from the "collisions" between the probe and the bath particles. This means that for active bath particles the activity-induced enhancement is more than enough to overcome the steric hindrance, which is present regardless of the activity of the bath particles. In the absence of hydrodynamic interactions (HI), Burkholder and Brady (2017) showed that such enhanced diffusive motion can result from the interplay between the bath activity and the probe-bath steric interactions.

In forced microrheology, the viscous response of the suspension can be characterized by the effective microviscosity η^{eff}. Taking the CV mode as an example, one can relate the average external force to the probe velocity via $\langle \boldsymbol{F}^{\text{ext}} \rangle = 6\pi\eta^{\text{eff}} a \boldsymbol{U}_1$, where a is the radius of the spherical probe and $\boldsymbol{U}_1$ is the prescribed constant probe velocity. In the absence of HI, the microviscosity of passive colloids exhibit a force-thinning behavior as a function of the probe speed—the microscopic analogue of shear-thinning (Squires and Brady 2005). When the short-range hydrodynamic lubrication is considered, a force-thickening behavior can be observed (Swan and

Zia 2013) at large probe speed. For active Brownian suspensions without HI in the dilute limit, Burkholder and Brady studied the forced microrheology by solving the Smoluchowski equation governing the distribution of active Brownian bath particles relative to the probe using a closure approximation. In particular, in the low probe speed limit a swim-thinning behavior is predicted (Burkholder and Brady 2019) and in the high probe speed limit the microviscosity becomes indistinguishable from that of passive suspensions because the swimming motion is obscured by the much faster probe advection (Burkholder and Brady 2020).

Following previous works (Burkholder and Brady 2017; 2019; 2020), we consider active colloidal suspensions modeled as monodisperse spherical active Brownian particles (ABPs) of radii b. The ABP model is one of the simplest descriptions for self-propelled particles. Furthermore, we study the CV mode of microrheology in which the probe (particle 1), which is a spherical colloidal particle of radius a, has a prescribed constant velocity $\boldsymbol{U}_1$. In addition to the thermal Brownian motion with diffusivity D_2, the bath ABP (particle 2) self-propels with its intrinsic "swim" speed U_2 in a direction $\boldsymbol{q}$, as illustrated in figure 5.3. The orientation of swimming $\boldsymbol{q}$ changes on a reorientation timescale τ_R that results from either continuous random Brownian rotations or the often-observed discrete tumbling events of bacteria. The inverse of reorientation time defines a rotary diffusivity, $D_R = 1/\tau_R$. One important intrinsic length scale due to activity is the run or persistence length $\ell = U_s \tau_R$. Even for an isolated spherical ABP, the self-propulsion introduces a coupling between its orientational and translational dynamics, which is absent for a passive Brownian sphere.

To characterize the microstructural deformation of the active suspension and the resulting viscous response, in the present work we solve the *full* Smoluchowski equation governing the probability distribution of a single ABP relative to the translating probe. This is done in the dilute limit in which only the interactions between the probe and one of the bath ABPs matter. Furthermore, we neglect hydrodynamic interactions between the probe and the ABP and focus on the interplay between the bath activity and the probe-ABP steric interaction. Resolving the full probability distribution allows us to examine the microstructure and the microviscosity in the full range of the ABP swim speeds and the probe speeds.

For a passive Brownian suspension, recall that the microviscosity η^{micro} [see equations (5.20) and (5.21)] exhibits a force-thinning behavior as a function of the probe Péclet number $Pe = U_1 R_c / D_2$, where $R_c = a + b$ (Squires and Brady 2005). The asymptotic results in the small and large Pe limits are: $\eta^{\text{micro}} \to 1$ as $Pe \to 0$ and $\eta^{\text{micro}} \to 1/2$ as $Pe \to \infty$. For active suspensions, if the probe speed is much faster than the swim speed, the activity of the suspension is obscured by the probe advection and one recovers the passive result: $\eta^{\text{micro}} \to 1/2$ as $Pe \to \infty$. As such, the most interesting regime for the microrheology of active suspensions is small and intermediate Pe.

When the speed of the probe is small, the suspension is in the linear response regime (linear in terms of the probe speed, or Pe; see section 5.3) and the microviscosity obtained in this limit is called the zero-forcing microviscosity, η_0^{micro} [see equation (5.38)]. Corroborating the observations of Burkholder and Brady (2019), we show that η_0^{micro} decreases as the swim speed increases; therefore the zero-forcing microviscosity exhibits a swim-thinning behavior. In the limit of no swimming, the passive result is recovered: $\eta_0^{\text{micro}} \to 1$ as $Pe_s = U_2 R_c / D_2 \to 0$. When the swim speed is large, we show via a boundary-layer analysis of the Smoluchowski equation that $\eta_0^{\text{micro}} \to 1/2$ as $Pe_s \to \infty$. Generally for finite activity, the microviscosity exhibits a force-thinning behavior as a function of Pe but with a reduced η_0^{micro} due to swim-thinning.

Because an active particle or microswimmer propels itself without exerting a net force on the surrounding fluid, it generates a dipolar disturbance flow (hydrodynamic stresslet). We show that the dipolar disturbance flow can either enhance or hinder the motion of the probe depending on the sign of the stresslet (pusher or puller). The disturbance from a puller located in front of the probe acts to pull the probe forward, therefore facilitates the probe motion and can give rise to a negative microviscosity. This behavior is opposite to that observed in bulk rheology, where only pushers can exhibit a negative shear viscosity. Our analysis is consistent with the work of Foffano et al. (2012), where the microrheology of an active nematic is considered. Using a continuum approach based on an active liquid crystal model, they showed that the flow field due to pullers in front of the probe can facilitate the probe motion.

Finally, by considering the disturbance flow due to the steady motion of the probe—the classical Stokes flow outside a translating sphere—while treating the ABPs as point particles hydrodynamically, we reveal another mechanism for *negative* microviscosity. Because the probe disturbance flow has a nonzero curvature, particularly near the probe, the ABPs are advected by the flow and rotated by the fluid vorticity. The advection near the probe means that particles that would otherwise be "stuck" at the front of the probe can be transported to the back, which acts to lower the difference between the densities in the front and in the back; this ultimately leads to a reduction in the suspension microviscosity. The advection-induced reduction does not rely on the activity of the bath particles and therefore is also present for passive Brownian suspensions.

In addition to this advective effect enjoyed by bath particles regardless of activity, active bath particles that would otherwise escape into the bulk from the sides (e.g., top and bottom) of the probe are reoriented towards the back of the probe due to the fluid vorticity. If the swim speed is large enough, this reorientation allows them to swim towards the back of the probe and then “push” the probe from behind. This reorientation by vorticity is responsible for upstream swimming of active particles in Poiseuille flow (Peng and Brady 2020) and in the current problem the same mechanism leads to a negative microviscosity. The reorientation by vorticity, of course, is irrelevant for the translational motion of a passive bath particle.

Recalling that at large Pe, the activity does not matter and the microviscosity cannot be negative. Therefore, active suspensions can exhibit a force-thickening behavior with a negative low-Pe plateau and a non-negative high-Pe plateau. This is in contrast to passive suspensions in which force-thickening is often associated with the short-range hydrodynamic lubrication (i.e., pair hydrodynamic interaction between the probe and a bath particle), which occurs at large Pe (Swan and Zia 2013). For ABPs in the presence of the probe disturbance flow, force-thickening originates from the interaction between swimming and the disturbance flow.

To obtain the results outlined thus far, in section 5.2 we formulate the problem from the Smoluchowski perspective. From the Smoluchowski equation governing the probability distribution of an ABP relative to the translating probe, we show that the microviscosity can be defined by the bath particle number density distribution at contact. A perturbation analysis at small Pe (section 5.3) allows us to derive equations governing the leading-order $[O(Pe)]$ microstructure deformation, which gives rise to the zero-forcing microviscosity η_0^{micro}. In this small Pe limit, we further consider the limit of fast swimming ($Pe_s \gg 1$) and show that η_0^{micro} exhibits a swim-thinning behavior. In section 5.4, we discuss the numerical methods used to solve the full Smoluchowski equation. To corroborate our analysis and numerical results from the Smoluchowski equation, in section 5.5 we consider Brownian dynamics (BD) simulations. In section 5.6, we present the microviscosity as a function of the probe speed, the swim speed, and the reorientation time. We show that the results obtained by solving the Smoluchowski equation agree well with those from BD.

In section 5.7, we consider the effect of the active hydrodynamic stresslet and then the effect of the probe disturbance flow. We conclude in section 5.8.

5.2 Problem formulation

We consider a dilute suspension of ABPs where only the pair-wise interactions between the probe and a single ABP matter. At this level, the suspension microstructure in the presence of a probe is described by the pair probability distribution $P_2(\boldsymbol{x}_1, \boldsymbol{x}_2, \boldsymbol{q}, t)$, where the positions of the probe ($\boldsymbol{x}_1$) and the ABP ($\boldsymbol{x}_2$) are in the laboratory frame. Because the probe has prescribed kinematics, i.e., constant-velocity, the position of the probe does not matter and the system is statistically homogeneous (Squires and Brady 2005). Conditioning the pair probability on the position of the probe, we then have

$$P_2(\boldsymbol{x}_1, \boldsymbol{x}_2, \boldsymbol{q}, t) = P_{1/1}(\boldsymbol{r}, \boldsymbol{q}, t|\boldsymbol{z}, t)P_1(\boldsymbol{z}, t) = P_{1/1}(\boldsymbol{r}, \boldsymbol{q}, t)P_1(\boldsymbol{z}, t), \tag{5.1}$$

where $\boldsymbol{r} = \boldsymbol{x}_2 - \boldsymbol{x}_1$, $\boldsymbol{z} = \boldsymbol{x}_1$. In other words, the conditional probability density function $P_{1/1}$ does not depend on the position of the probe in the laboratory frame. As a result, it is most convenient to consider the conditional probability distribution of the ABP in a co-moving frame that is attached to the probe particle. In this relative frame, the Smoluchowski equation governing the conservation of ABPs is written as (Burkholder and Brady 2019; 2020)

$$\frac{\partial P_{1/1}(\boldsymbol{r}, \boldsymbol{q}, t)}{\partial t} + \nabla_r \cdot \left(\boldsymbol{j}_2^T - \boldsymbol{j}_1^T\right) + \nabla_R \cdot \boldsymbol{j}_2^R = 0. \tag{5.2}$$

In the absence of hydrodynamic interactions between the probe and the ABP, the translational and rotational fluxes in the Smoluchowski equation (5.2), respectively, are

$$\boldsymbol{j}_2^T - \boldsymbol{j}_1^T = \left(U_2\boldsymbol{q} - \boldsymbol{U}_1\right) P_{1/1} - D_2\nabla_r P_{1/1}, \tag{5.3}$$

$$\boldsymbol{j}_2^R = -D_R\nabla_R P_{1/1}. \tag{5.4}$$

Notice that it is the flux of ABPs relative to the probe that appears in the equation so as to obey Galilean invariance. In the CV mode of microrheology, the relative diffusivity is simply the diffusivity of the ABP (D_2) instead of the sum of diffusivities of the probe and the ABP as in the CF mode of microrheology (Squires and Brady 2005). Because we neglect hydrodynamic interactions, the probe and ABP interact sterically due to their hard-sphere nature. That is, at the surface of contact ($|\boldsymbol{r}| = R_c = a + b$), the relative translational flux of particle centers vanishes:

$$\boldsymbol{n} \cdot \left(\boldsymbol{j}_2^T - \boldsymbol{j}_1^T\right) = 0, \tag{5.5}$$

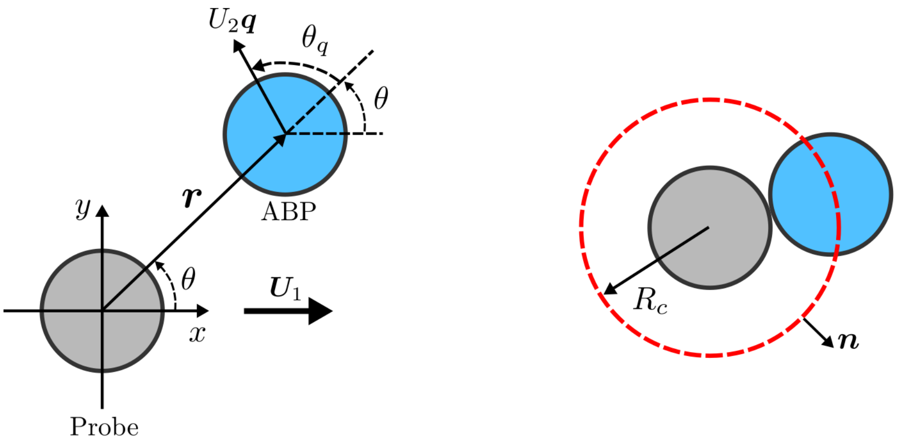

Figure 5.3: Schematic of a probe particle driven at a constant velocity $\boldsymbol{U}_1$ and an active Brownian bath particle in 2D. The ABP swims with a constant speed U_2 in a direction $\boldsymbol{q}$. The radius of contact is R_c and $\boldsymbol{n}$ is the unit normal vector pointing from the probe into the ABP suspension.

where $\boldsymbol{n}$ is the unit normal vector as shown in figure 5.3.

Far from the probe, the suspension microstructure is undisturbed, giving

$$P_{1/1} \to \frac{n^\infty}{\Omega_d}, \tag{5.6}$$

where n^∞ is the number density in the undisturbed ABP suspension, which has the units of number per volume (or area in 2D), and Ω_d is the total solid angle of the orientation space in d dimensions.

Equation (5.2) together with its flux expressions (5.3)-(5.4) and boundary conditions (5.5)-(5.6) govern the disturbance of the suspension microstructure due to the CV probe. In the absence of activity, by setting $U_2 = 0$ and integrating out the orientational degree of freedom, one can recover the CV microrheology problem for passive Brownian suspensions considered by Squires and Brady (2005).

In the CV mode of microrheology, the main quantity of interest is the external force required to maintain such a steady probe motion. Due to the fluctuating nature of the ABP suspension, the external force averaged over Brownian fluctuations is considered. For an active Brownian suspension, this has been shown to be (Burkholder and Brady 2019)

$$\left\langle F^{\text{ext}} \right\rangle = \zeta_1 U_1 + k_B T \oint_{r=R_c} \boldsymbol{n} \cdot \hat{\boldsymbol{U}}_1 P_{1/1} dS d\boldsymbol{q}, \tag{5.7}$$

where ζ_1 is the Stokes drag of the probe, $k_B T$ is the thermal energy, and $\hat{\boldsymbol{U}}_1$ is the direction of the probe motion, $\hat{\boldsymbol{U}}_1 = \boldsymbol{U}_1/|\boldsymbol{U}_1|$. The only difference between equation (5.7) and that obtained for a passive Brownian suspension (Squires and Brady 2005) is the additional integration over the orientational degrees of freedom of the active bath particle. In equation (5.7), only the net force in the direction of the probe motion is considered because the net force in the transverse direction vanishes due to symmetry. The applied external force in a hard-sphere passive colloidal suspension is larger than the Stokes drag ($\zeta_1 U_1$) of the probe due to the fact that in order to maintain a constant velocity the probe has to push away bath particles along its trajectory. To quantify this increase in the applied force, it is convenient to consider the dimensionless viscosity increment defined as

$$\frac{\Delta\eta}{\eta} = \frac{\left\langle F^{\mathrm{ext}} \right\rangle - \zeta_1 U_1}{\zeta_1 U_1}, \tag{5.8}$$

where an effective microscopic viscosity can be defined via $F^{\mathrm{ext}} = 6\pi\eta^{\mathrm{eff}} a U_1$ and equivalently $\Delta\eta/\eta = (\eta^{\mathrm{eff}} - \eta)/\eta$ with η being the viscosity of the solvent. By definition, the viscosity increment vanishes in the absence of bath particles.

A dimensional analysis reveals four timescales that govern the microrheology of active Brownian suspensions: (1) the diffusive timescale $\tau_D = R_c^2/D_2$, (2) the swim timescale $\tau_s = R_c/U_2$, (3) the advective timescale $\tau_{\mathrm{adv}} = R_c/U_1$, and (4) the reorientation time $\tau_R = 1/D_R$. Comparing the other three timescales with the diffusive timescale gives three dimensionless groups. The first one is the swim Péclet number given by

$$Pe_s = \frac{\tau_D}{\tau_s} = \frac{U_2 R_c}{D_2}. \tag{5.9}$$

The second dimensionless group is the Péclet number of the probe (using the diffusivity of the ABP)

$$Pe = \frac{\tau_D}{\tau_{\mathrm{adv}}} = \frac{U_1 R_c}{D_2}. \tag{5.10}$$

Finally, comparing τ_R with τ_D defines the third parameter:

$$\gamma = \left(\frac{\tau_D}{\tau_R}\right)^{1/2} = \frac{R_c}{\delta}, \tag{5.11}$$

where $\delta = \sqrt{D_2 \tau_R}$ is the microscopic diffusive step taken by the ABP on the reorientation timescale τ_R.

To render the equations dimensionless, we scale lengths by R_c and time by τ_D and define the dimensionless probability distribution (or the suspension microstructure) g such that

$$P_{1/1}(\boldsymbol{r}, \boldsymbol{q}, t) = n^{\infty} g(\boldsymbol{r}, \boldsymbol{q}, t). \tag{5.12}$$

From equations (5.2), (5.3), and (5.4), we obtain the Smoluchowski equation for the microstructure as

$$\frac{\partial g}{\partial t} + \nabla_r \cdot \left[\left(Pe_s \boldsymbol{q} - Pe \hat{\boldsymbol{U}}_1 \right) g - \nabla_r g \right] - \gamma^2 \nabla_R^2 g = 0. \tag{5.13}$$

The no-flux condition (5.5) becomes

$$\boldsymbol{n} \cdot \left[\left(Pe_s \boldsymbol{q} - Pe \hat{\boldsymbol{U}}_1 \right) g - \nabla_r g \right] = 0 \quad \text{at} \quad r = 1, \tag{5.14}$$

and the far-field condition (5.6) translates into

$$g \to \frac{1}{\Omega_d} \quad \text{as} \quad r \to \infty. \tag{5.15}$$

Making use of the Stokes-Einstein-Sutherland relation, $k_B T = D_2 \zeta_2 = D_2 6 \pi \eta b$ and the definition of volume fraction $\phi = 4\pi b^3 n^\infty / 3$ in 3D, we obtain from (5.7) and (5.8) the scaled viscosity increment

$$\frac{\Delta \eta}{\phi \eta} = \frac{3}{4\pi} \frac{D_2 R_c^2}{a b^2 U_1} \oint_{r=1} \boldsymbol{n} \cdot \hat{\boldsymbol{U}}_1 n dS, \tag{5.16}$$

where

$$n(\boldsymbol{r}, t) = \int g(\boldsymbol{r}, \boldsymbol{q}, t) d\boldsymbol{q} \tag{5.17}$$

is the dimensionless number density which tends to unity as $r \to \infty$. Noting that

$$\frac{D_2 R_c^2}{a b^2 U_1} = \frac{(1+\alpha)^3}{\alpha Pe}, \tag{5.18}$$

and $\alpha = a/b$, we obtain

$$\frac{\Delta \eta}{\phi \eta} = \frac{3}{4\pi} \frac{(1+\alpha)^3}{\alpha Pe} \oint_{r=1} \boldsymbol{n} \cdot \hat{\boldsymbol{U}} n dS. \tag{5.19}$$

Noting that the microstructure only depends on the contact radius R_c instead of the sizes of both the probe and the ABP [see equation (5.13)], the only dependence of the scaled viscosity increment $\Delta\eta/(\phi\eta)$ on the size ratio α is in the prefactor before the integral in equation (5.19). Therefore, for convenience we define the so-called effective microviscosity coefficient as

$$\eta^{\text{micro}} = \frac{\Delta \eta}{\phi \eta} \frac{2\alpha}{(1+\alpha)^3} = \frac{3}{2\pi Pe} \hat{\boldsymbol{U}}_1 \cdot \oint_{r=1} \boldsymbol{n} n dS. \tag{5.20}$$

Here, a factor of 2 is introduced in front of the factor $\alpha/(1+\alpha)^3$ so that for a passive Brownian suspension $\eta^{\text{micro}} \to 1$ as $Pe \to 0$ (Squires and Brady 2005). By construction, η^{micro} does not depend on the size ratio α. In 2D, we use the area fraction $\phi = n^\infty \pi b^2$ and obtain a similar definition

$$\eta^{\text{micro}} = \frac{\Delta\eta}{\phi\eta}\frac{\alpha}{(1+\alpha)^2} = \frac{1}{\pi Pe}\hat{\boldsymbol{U}}_1 \cdot \oint_{r=1} \boldsymbol{n} n dS. \tag{5.21}$$

Hereinafter, we use microviscosity and microviscosity coefficient interchangeably to refer to the effective microviscosity coefficient defined above.

Because the bath particles are active, the phase space of the microstructure includes both the relative position $\boldsymbol{r}$ and the orientation $\boldsymbol{q}$. The high dimensionality of the phase space is challenging for the numerical simulation of the Smoluchowski equation (5.13). In 3D, by parametrizing the orientation vector $\boldsymbol{q}$ using the polar and azimuthal angles of a spherical coordinate system, the phase space has a dimensionality of 5: three dimensional in space and two dimensional in orientation. As shown in previous work (Yan and Brady 2015b; Burkholder and Brady 2019), the dimensionality only affects the solution of the Smoluchowski equation in a quantitative manner. In this Chapter we focus on the microrheology of ABPs in 2D.

5.2.1 The Smoluchowski equation in 2D

Equation (5.13) is most convenient for analysis in a polar coordinate system for the physical space and in a relative angular coordinate system for the orientation space in which $\boldsymbol{q} = \cos\theta_q \boldsymbol{e}_r + \sin\theta_q \boldsymbol{e}_\theta$ (see figure 5.3 for a schematic). Here, $\boldsymbol{e}_r = \cos\theta \boldsymbol{e}_x + \sin\theta \boldsymbol{e}_y$ is the radial basis vector in the polar coordinate system and $\boldsymbol{e}_\theta$ is the basis vector in the angular (θ) direction. Without loss of generality, we take $\hat{\boldsymbol{U}}_1 = \boldsymbol{e}_x$ so that the probe moves in the positive x direction. In this (r, θ, θ_q) coordinate system, equation (5.13) is written explicitly as

$$\begin{aligned} &\left(Pe_s \cos\theta_q - Pe\cos\theta\right)\frac{\partial g}{\partial r} + \left(Pe_s \sin\theta_q + Pe\sin\theta\right)\frac{1}{r}\left(\frac{\partial g}{\partial \theta} - \frac{\partial g}{\partial \theta_q}\right) \\ &- \frac{1}{r}\frac{\partial}{\partial r}r\frac{\partial g}{\partial r} - \frac{1}{r^2}\left(\frac{\partial^2 g}{\partial \theta^2} - 2\frac{\partial^2 g}{\partial\theta\partial\theta_q} + \frac{\partial^2 g}{\partial \theta_q^2}\right) - \gamma^2\frac{\partial^2 g}{\partial\theta_q^2} = 0, \end{aligned} \tag{5.22}$$

$$\left(Pe_s \cos\theta_q - Pe\cos\theta\right) g - \frac{\partial g}{\partial r} = 0 \quad \text{at} \quad r = 1, \tag{5.23}$$

$$g \to \frac{1}{2\pi} \quad \text{as} \quad r \to \infty. \tag{5.24}$$

5.3 A slow probe

5.3.1 Perturbation expansion of the microstructure

For a slow probe, $Pe \ll 1$, the suspension microstructure is only slightly displaced from the state in which the probe is held fixed in a bath of ABPs. This allows us to consider the microstructure in the perturbation series $g = g_0(\boldsymbol{r}, \boldsymbol{q}) + Pe g_1(\boldsymbol{r}, \boldsymbol{q}) + \cdots$, where in any dimension we have at $O(1)$:

$$\nabla_r \cdot (Pe_s \boldsymbol{q} g_0 - \nabla_r g_0) - \gamma^2 \nabla_R^2 g_0 = 0, \tag{5.25}$$

$$\boldsymbol{n} \cdot (Pe_s \boldsymbol{q} g_0 - \nabla_r g_0) = 0 \quad \text{at} \quad r = 1, \tag{5.26}$$

$$g_0 \to \frac{1}{\Omega_d} \quad \text{as} \quad r \to \infty. \tag{5.27}$$

The $O(Pe)$ equation is nonhomogeneous, i.e., forced by the probe advection of the g_0 field, which reads

$$\nabla_r \cdot (Pe_s \boldsymbol{q} g_1 - \nabla_r g_1) - \gamma^2 \nabla_R^2 g_1 = \hat{\boldsymbol{U}}_1 \cdot \nabla_r g_0, \tag{5.28}$$

$$\boldsymbol{n} \cdot (Pe_s \boldsymbol{q} g_1 - \nabla_r g_1) = \boldsymbol{n} \cdot \hat{\boldsymbol{U}}_1 g_0 \quad \text{at} \quad r = 1, \tag{5.29}$$

$$g_1 \to 0 \quad \text{as} \quad r \to \infty. \tag{5.30}$$

In 2D, equations (5.25)-(5.29) can be written explicitly in the (r, θ, θ_q) frame. To this end, we first write the perturbation series as $g = g_0(r, \theta_q) + Pe g_1(r, \theta, \theta_q) + \cdots$. At $O(1)$, the probe is held stationary (zero velocity) and the problem reduces to that of ABPs in the exterior of a disk (Yan and Brady 2015b), which exhibits spherical symmetry and thus g_0 is independent of the angular position θ. The probability distribution of ABPs outside a fixed probe is governed by

$$Pe_s \cos\theta_q \frac{\partial g_0}{\partial r} - Pe_s \sin\theta_q \frac{1}{r}\frac{\partial g_0}{\partial \theta_q} - \frac{1}{r}\frac{\partial}{\partial r} r \frac{\partial g_0}{\partial r} - \left(\frac{1}{r^2} + \gamma^2\right)\frac{\partial^2 g_0}{\partial \theta_q^2} = 0, \tag{5.31}$$

$$Pe_s \cos\theta_q g_0 - \frac{\partial g_0}{\partial r} = 0 \quad \text{at} \quad r = 1, \tag{5.32}$$

$$g_0 \to \frac{1}{2\pi} \quad \text{as} \quad r \to \infty. \tag{5.33}$$

The first effect of the probe motion appears at $O(Pe)$, which is governed by

$$\begin{aligned}
&Pe_s \cos\theta_q \frac{\partial f_1}{\partial r} + Pe_s \sin\theta_q \frac{1}{r}\left(f_2 - \frac{\partial f_1}{\partial \theta_q}\right) \\
&- \frac{1}{r}\frac{\partial}{\partial r} r \frac{\partial f_1}{\partial r} - \frac{1}{r^2}\left(-f_1 - 2\frac{\partial f_2}{\partial \theta_q} + \frac{\partial^2 f_1}{\partial \theta_q^2}\right) - \gamma^2 \frac{\partial^2 f_1}{\partial \theta_q^2} = \frac{\partial g_0}{\partial r},
\end{aligned} \tag{5.34}$$

$$\begin{aligned}
&Pe_s \cos\theta_q \frac{\partial f_2}{\partial r} + Pe_s \sin\theta_q \frac{1}{r}\left(-f_1 - \frac{\partial f_2}{\partial \theta_q}\right) \\
&- \frac{1}{r}\frac{\partial}{\partial r} r \frac{\partial f_2}{\partial r} - \frac{1}{r^2}\left(-f_2 + 2\frac{\partial f_1}{\partial \theta_q} + \frac{\partial^2 f_2}{\partial \theta_q^2}\right) - \gamma^2 \frac{\partial^2 f_2}{\partial \theta_q^2} = \frac{1}{r}\frac{\partial g_0}{\partial \theta_q},
\end{aligned} \tag{5.35}$$

where $g_1(r,\theta,\theta_q) = f_1(r,\theta_q)\cos\theta + f_2(r,\theta_q)\sin\theta$. The no-flux condition reduces to

$$Pe_s \cos\theta_q f_1 - \frac{\partial f_1}{\partial r} = g_0, \quad Pe_s \cos\theta_q f_2 - \frac{\partial f_2}{\partial r} = 0, \quad \text{at} \quad r = 1. \tag{5.36}$$

Using equation (5.21), we obtain

$$\eta_0^{\text{micro}} = \int f_1(r=1,\theta_q)d\theta_q, \tag{5.37}$$

where

$$\eta_0^{\text{micro}} = \lim_{Pe\to 0} \eta^{\text{micro}} \tag{5.38}$$

is the microviscosity in the limit $Pe \to 0$, or the zero-forcing microviscosity. The $O(Pe)$ number density, $n_1(\boldsymbol{r}) = \int g_1 d\boldsymbol{q}$, has the form $n_1(\boldsymbol{r}) = \hat{\boldsymbol{U}}_1 \cdot \boldsymbol{r} p_3(r)$ due to symmetry, where p_3 is an unknown scalar function of r (see section 5.9). From this and (5.21), we see that $\eta_0^{\text{micro}} = p_3(1)$ in 2D.

In general, η_0^{micro} for active Brownian suspensions is a function of Pe_s and γ. For passive suspensions ($Pe_s = 0$), the orientational distribution is uniform and the density at $O(Pe)$ is $n_1 = \hat{\boldsymbol{U}}_1 \cdot \boldsymbol{e}_r / r$ in 2D, which gives $\eta_0^{\text{micro}} = 1$. If the suspension is weakly active, we expect the zero-forcing microviscosity to approach that of a passive suspension. That is, $\eta_0^{\text{micro}} \to 1$ as $Pe_s \to 0$.

5.3.2 Fast-swimming ABPs

We now consider the suspension microstructure and the zero-forcing microviscosity in the fast-swimming limit characterized by $Pe_s \gg 1$. The rotational diffusivity is assumed to be finite, $\gamma \sim O(1)$. In this high Pe_s limit, translational diffusion is only important in a boundary layer near the probe. The boundary layer thickness is dictated by the balance between the swimming flux into the probe and the diffusive flux down the concentration gradient, which gives a thickness of $O(Pe_s^{-1} R_c)$. Therefore, we define a stretched boundary layer coordinate $\rho = (r-1)/\epsilon$, $\epsilon = 1/Pe_s$, such that $\rho \sim O(1)$ as $r \to 1$ and $\epsilon \to 0$.

In the boundary layer, the governing equation for $g_0(\rho,\theta,\theta_q)$ becomes

$$\begin{aligned} &\cos\theta_q \frac{\partial g_0}{\partial \rho} - \sin\theta_q \frac{\epsilon}{1+\rho\epsilon}\frac{\partial g_0}{\partial \theta_q} - \frac{\epsilon}{1+\rho\epsilon}\frac{\partial g_0}{\partial \rho} \\ &- \frac{\partial^2 g_0}{\partial \rho^2} - \epsilon^2\left(\gamma^2 + \frac{1}{(1+\rho\epsilon)^2}\right)\frac{\partial^2 g_0}{\partial \theta_q^2} = 0, \end{aligned} \tag{5.39}$$

$$\cos\theta_q g_0 - \frac{\partial g_0}{\partial \rho} = 0 \quad \text{at} \quad \rho = 0, \tag{5.40}$$

$$g_0 \to \frac{1}{2\pi} \quad \text{as} \quad \rho \to \infty. \tag{5.41}$$

To study the microstructure for a stationary probe in the fast swimming limit, we pose the perturbation expansion $g_0 = \epsilon^{-1} g_0^{(-1)} + g_0^{(0)} + \epsilon g_0^{(1)} + o(\epsilon)$, where the leading order microstructure is $O(1/\epsilon)$ (singular) as $\epsilon \to 0$ (Yan and Brady 2018; Peng et al. 2021). Inserting this expansion into equation (5.39) yields equations for $g_0^{(k)}$ $(k = -1, 0, \cdots)$.

The solution to $g_0^{(-1)}$ can be readily obtained as

$$g_0^{(-1)} = A_1(\theta_q) e^{\rho \cos\theta_q}. \tag{5.42}$$

Here, A_1 is an unknown function of θ_q that will be determined from the solution at the next order. Because the distribution is $O(1)$ far from the probe, we require $g_0^{(-1)} \to 0$ as $\rho \to \infty$. This means that the solution is only valid in the region $\cos\theta_q < 0$. Outside this region in orientation space, the solution is zero at this order. Physically, this is due to the fact that ABPs in contact with the probe have to point towards the probe, i.e. $\boldsymbol{q} \cdot \boldsymbol{e}_r = \cos\theta_q < 0$, because otherwise they would swim away.

At $O(1)$, we have

$$\cos\theta_q \frac{\partial g_0^{(0)}}{\partial \rho} - \frac{\partial^2 g_0^{(0)}}{\partial \rho^2} = \sin\theta_q \frac{\partial g_0^{(-1)}}{\partial \theta_q} + \frac{\partial g_0^{(-1)}}{\partial \rho}, \tag{5.43}$$

$$\cos\theta_q g_0^{(0)} - \frac{\partial g_0^{(0)}}{\partial \rho} = 0 \quad \text{at} \quad \rho = 0, \tag{5.44}$$

$$g_0^{(0)} \to \frac{1}{2\pi} \quad \text{as} \quad \rho \to \infty. \tag{5.45}$$

The far-field condition on $g_0^{(0)}$ ensures proper matching with the constant solution outside the boundary layer. The general solution can be written as

$$g_0^{(0)} = \left(B_1(\theta_q)\rho + B_2(\theta_q)\rho^2 \right) e^{\rho\cos\theta_q} + C_1(\theta_q) e^{\rho\cos\theta_q} + \frac{1}{2\pi}, \tag{5.46}$$

where

$$B_1 = -A_1 \sec^2\theta_q - \tan\theta_q \frac{dA_1}{d\theta_q}, \tag{5.47}$$

$$B_2 = \frac{1}{2} A_1 \sin\theta_q \tan\theta_q \tag{5.48}$$

and the far-field condition is already enforced. Making use of the no-flux condition at $\rho = 0$, we obtain an ordinary differential equation for A_1:

$$\frac{\cos\theta_q}{2\pi} + A_1 \sec^2\theta_q + \tan\theta_q \frac{dA_1}{d\theta_q} = 0. \tag{5.49}$$

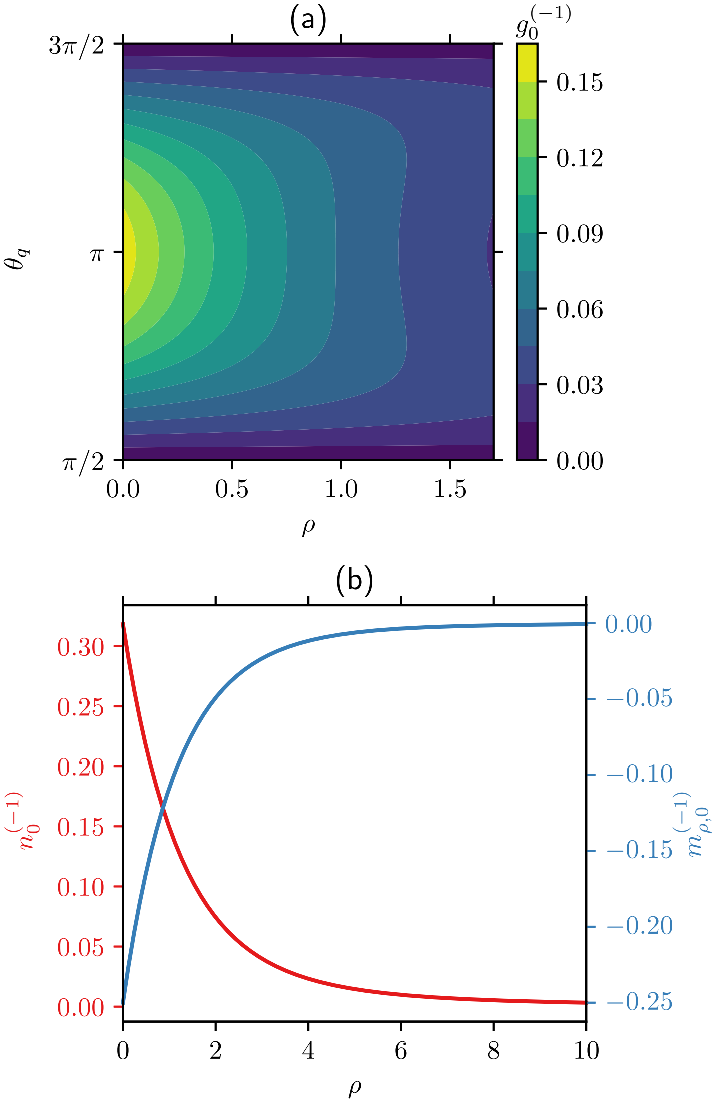

Figure 5.4: (a): Contour plot of the leading-order distribution function $g_0^{(-1)}$ as a function of ρ and θ_q. (b): The leading-order number density $n_0^{(-1)}$ and polar order in the radial direction $m_{\rho,0}^{(-1)}$ as a function of ρ.

Requiring regularity of A_1 at $\theta_q = \pi$, we can integrate the above equation to obtain $A_1 = -\cos\theta_q/(2\pi)$.

In figure 5.4(a) we plot the leading-order probability distribution $g_0^{(-1)}$ as a function of ρ and θ_q. In figure 5.4(b) , we show the number density $n_0^{(-1)} = \int g_0^{(-1)} d\theta_q$ and the radial polar order $m_{\rho,0}^{(-1)} = \int g_0^{(-1)} \cos\theta_q d\theta_q$ as a function of ρ. In the boundary layer, ABPs are pointing into the probe, because otherwise they would swim away. As a result, we observe an accumulation at contact ($\rho = 0$) and a negative radial polar order. The following asymptotic behaviors can be obtained near contact:

$$n_0^{(-1)} = \frac{1}{\pi} - \frac{\rho}{4} + O(\rho^2) \quad \text{and} \quad m_{\rho,0}^{(-1)} = -\frac{1}{4} + \frac{2\rho}{3\pi} + O(\rho^2) \quad \text{as} \quad \rho \to 0. \tag{5.50}$$

It is worth noting that the boundary layer structure is identical in 2D and 3D. One can show that in 3D the leading order probability density is given by $g_0^{-1} = \boldsymbol{q}\cdot\boldsymbol{e}_r \exp(\boldsymbol{q}\cdot\boldsymbol{e}_r\rho)/(-8\pi)$, which differs from (5.42) only by a numerical factor due to the dimensionality.

To determine the function C_1 in equation (5.46), we again need the solution at the next order. So far in this section we have considered the asymptotic behavior of the probability distribution of ABPs outside a a fixed probe in the large Pe_s limit. This problem has been solved by Yan and Brady (2015b) using a $\boldsymbol{Q} = \boldsymbol{0}$ (defined by $\boldsymbol{Q} = \int g(\boldsymbol{qq} - \boldsymbol{I}/d)d\boldsymbol{q}$) closure and Brownian dynamics simulations. We note that the $\boldsymbol{Q}$ closure gives the correctly scaling for the number density, i.e., the number density at contact scales as Pe_s for large Pe_s, but does not give quantitatively correct results over the full range of Pe_s.

We now consider the microstructure disturbance due to the weak probe motion and the zero-forcing microviscosity in the high Pe_s limit. The governing equations for f_1 and f_2 in the boundary layer can be obtained in a similar fashion to the approach described above for g_0. At leading order, the disturbance fields are finite, i.e., $O(\epsilon^0)$, and are expanded as

$$f_1(\rho,\theta_q) = f_1^{(0)} + \epsilon f_1^{(1)} + O(\epsilon^2), \tag{5.51}$$

$$f_2(\rho,\theta_q) = f_2^{(0)} + \epsilon f_2^{(1)} + O(\epsilon^2). \tag{5.52}$$

The governing equation for $f_1^{(0)}$ is

$$\cos\theta_q \frac{\partial f_1^{(0)}}{\partial \rho} - \frac{\partial^2 f_1^{(0)}}{\partial \rho^2} = \frac{\partial g_0^{(-1)}}{\partial \rho}, \tag{5.53}$$

$$\cos\theta_q f_1^{(0)} - \frac{\partial f_1^{(0)}}{\partial \rho} = g_0^{(-1)} \quad \text{at} \quad \rho = 0, \tag{5.54}$$

$$f_1^{(0)} \to 0 \quad \text{as} \quad \rho \to \infty. \tag{5.55}$$

The solution is given by

$$f_1^{(0)} = \frac{1}{2\pi}\rho\cos\theta_q e^{\rho\cos\theta_q} + A_2(\theta_q)e^{\rho\cos\theta_q}, \tag{5.56}$$

which is only valid for $\cos\theta_q < 0$. To determine A_2, we need the solutions to $f_2^{(0)}$ and $f_1^{(1)}$. Imposing regularity of $f_1^{(0)}$ at $\theta_q = \pi$, one can show that $A_2 = 1/(2\pi)$. Finally, using equation (5.37), we obtain the zero-forcing microviscosity in the fast-swimming limit:

$$\eta_0^{\text{micro}} \to \frac{1}{2} \quad \text{as} \quad Pe_s \to \infty. \tag{5.57}$$

5.3.3 Zero-forcing microviscosity

To obtain the microstructure in the zero Pe limit for arbitrary values of Pe_s, we solve equations (5.31), (5.34) and (5.35) numerically using a Fourier-Laguerre spectral method (see section 5.4). For large Pe_s, the discretization of the equations needs to conform with the boundary layer structure as discussed in the previous section in order to yield accurate numerical result. To this end, for $Pe_s > 10$, instead of discretizing r, the boundary layer coordinate ρ is discretized and used in the numerical solution.

As shown in equation (5.37), the contact distribution of f_1 determines the zero-forcing microviscosity. More precisely, η_0^{micro} is the area under the curve $f(r = 1, \theta_q)$ from $\theta_q = 0$ to $\theta_q = 2\pi$. For a passive suspension, $Pe_s \equiv 0$, one can readily show that $f_1(r = 1, \theta_q) \equiv 1/(2\pi)$, in which case the area under the curve is unity hence $\eta_0^{\text{micro}} = 1$. For large Pe_s, the contact distribution of f_1 obtained from equation (5.56) is $f_1(r = 1, \theta_q) = 1/(2\pi)$ for $\boldsymbol{q} \cdot \boldsymbol{e}_r < 0$ and zero otherwise. In other words, the contact value of f_1 for large Pe_s is the same as the limit of $Pe_s \to 0$ but only in half of the domain of θ_q. Therefore, the zero-forcing microviscosity approaches $1/2$ as $Pe_s \to \infty$. In figure 5.5 we plot the contact distribution of f_1 as a function of θ_q for several values of Pe_s obtained from the numerical solutions. The leading-order asymptotic solution in the large Pe_s limit is plotted as a solid line.

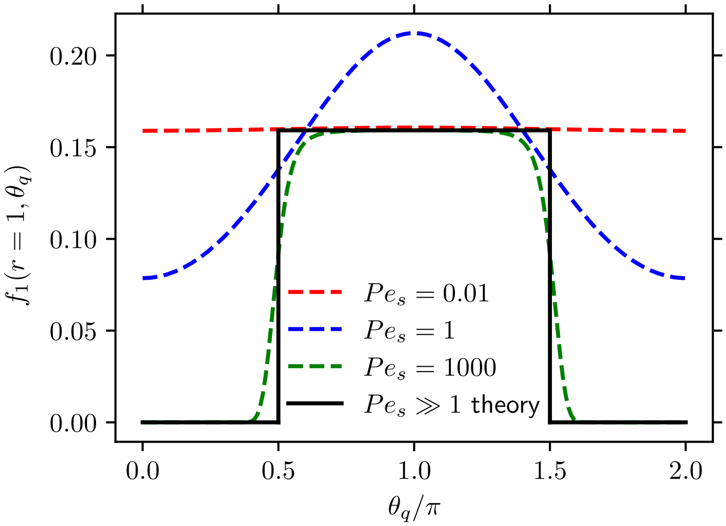

Figure 5.5: The function $f_1(r = 1, \theta_q)$ as a function of θ_q for several values of Pe_s and $\gamma = 1$. The large Pe_s asymptotic solution given by equation (5.56) is plotted as a solid line. The zero-forcing microviscosity is the area under the curve as can be seen from equation (5.37).

In figure 5.6 we present the zero-forcing microviscosity as a function of Pe_s for several values of γ. As alluded to earlier, the zero-forcing microviscosity exhibits a swim-thinning behavior. That is, η_0^{micro} in general decreases with increasing swim speed, or Pe_s. The onset of swim-thinning occurs at $O(Pe_s^2)$ for small Pe_s (see section 5.10). An outlier in this general behavior appears when γ^2 is comparable to Pe_s and both are large, $Pe_s \sim \gamma^2 \gg 1$. This can be seen from the results in figure 5.6 for $\gamma = 10$, in which case η_0^{micro} decreases below $1/2$ before increasing and asymptoting to the large Pe_s value of $1/2$. An asymptotic analysis in the limit $Pe_s \gg 1$ while $Pe_s/\gamma^2 = O(1)$ shows that the boundary layer thickness remains the same but an additional forcing term due to rotary diffusion appears in equation (5.43). The addition of this new term renders the boundary layer equations analytically intractable.

5.4 Numerical solution of the Smoluchowski equation

To obtain the suspension microstructure over the full range of Pe, a numerical solution of the full Smoluchowski equation (5.22) together with its boundary conditions (5.23) and (5.24) is required. In this section, we develop a Fourier-Laguerre spectral method in which the physical space angular position θ and the orientation angle θ_q are resolved analytically using a truncated double Fourier series expansion. To this

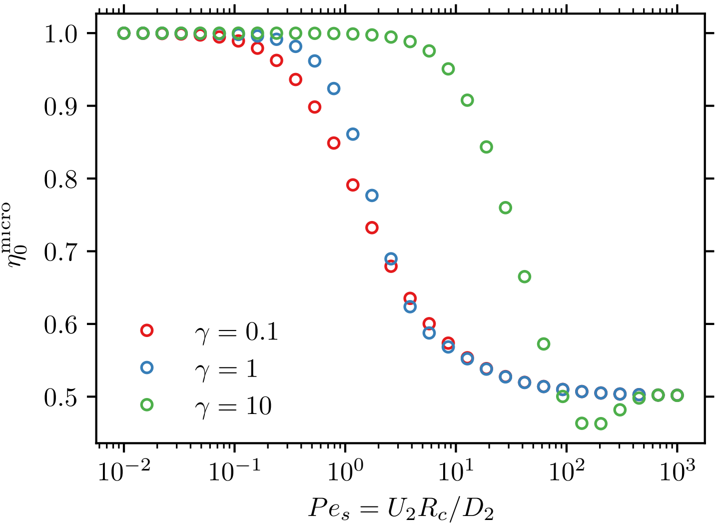

Figure 5.6: The zero-forcing microviscosity $\eta_0^{\rm micro}$ as a function of Pe_s for several values of γ.

end, we first approximate the microstructure at steady state as a truncated double Fourier series as

$$g(r,\theta,\theta_q) \approx \sum_{m=-M}^{M} \sum_{n=-N}^{N} C_{m,n}(r) e^{im\theta} e^{in\theta_q}, \tag{5.58}$$

where $i^2 = -1$ is the imaginary unit and $C_{m,n}(r)$ is the Fourier mode indexed by m and n. Inserting equation (5.58) into (5.22), at steady state we obtain a system of $(2N+1)(2M+1)$ coupled ordinary differential equations (ODEs) for the radially-varying Fourier modes:

$$\begin{aligned} &\frac{Pe_s}{2}\frac{d}{dr}\left(C_{m,n+1} + C_{m,n-1}\right) + \frac{Pe_s}{2r}\left[(n+1-m)C_{m,n+1} + (m-(n-1)C_{m,n-1}\right] \\ &-\frac{Pe}{2}\frac{d}{dr}\left(C_{m+1,n} + C_{m-1,n}\right) + \frac{Pe}{2r}\left[(n-(m+1)C_{m+1,n} + (m-1-n)C_{m-1,n}\right] \\ &-\frac{1}{r}\frac{d}{dr}r\frac{dC_{m,n}}{dr} + \frac{m^2+n^2-2mn}{r^2}C_{m,n} + \gamma^2 n^2 C_{m,n} = 0. \end{aligned} \tag{5.59}$$

Here, any Fourier mode $C_{m,n}$ that exceeds the range $-M \le m \le M, -N \le n \le N$ is simply discarded. Similarly, the no-flux condition (5.23) becomes

$$\frac{Pe_s}{2}\left(C_{m,n+1} + C_{m,n-1}\right) - \frac{Pe}{2}\left(C_{m+1,n} + C_{m-1,n}\right) - \frac{dC_{m,n}}{dr} = 0 \quad \text{at} \quad r = 1, \tag{5.60}$$

and the far-filed condition (5.24) is

$$C_{m,n} \to \begin{cases} \frac{1}{2\pi} & m = n = 0 \\ 0 & \text{otherwise} \end{cases} \quad \text{as} \quad r \to \infty. \tag{5.61}$$

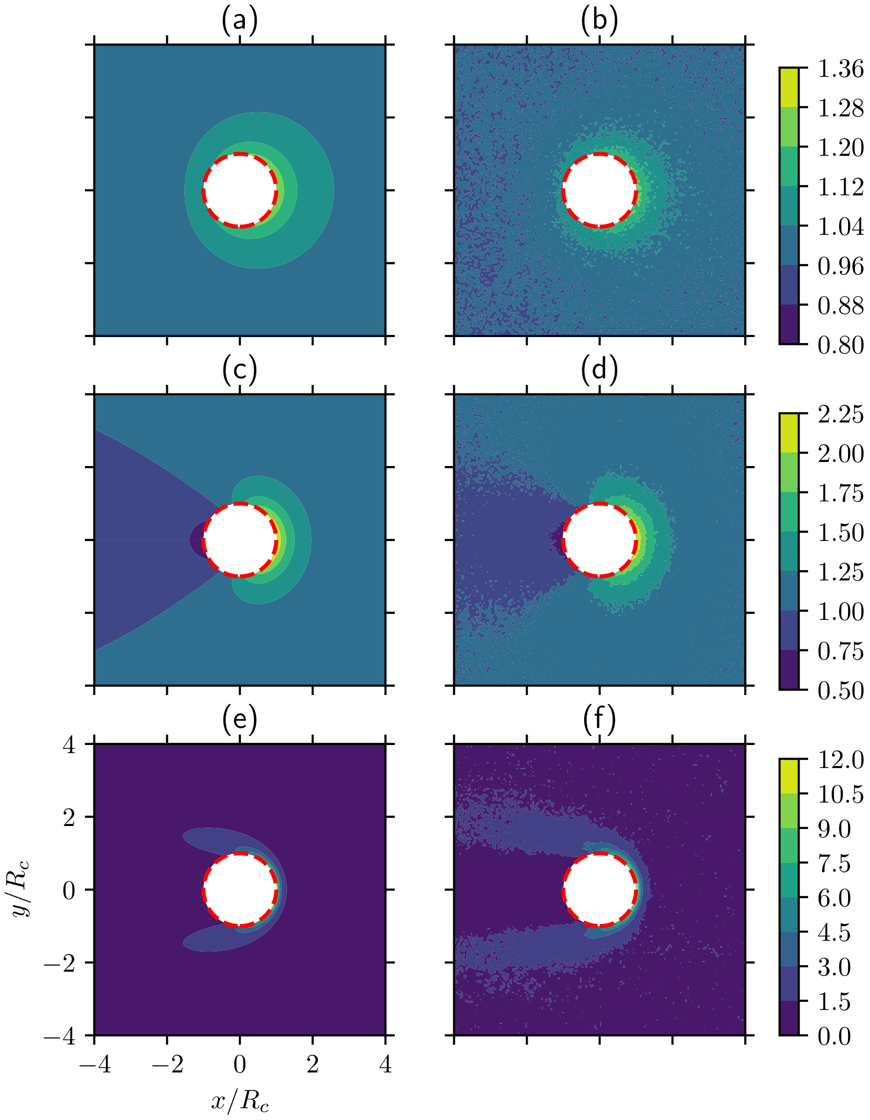

Figure 5.7: Contour plots of the number density distribution around the probe for different values of $Pe = U_1 R_c/D_2$ with $Pe_s = U_2 R_c/D_2 = 1, \gamma = R_c/\delta = 1$ obtained from the numerical solution of the Smoluchowski equation [(a), (c), (e)] and BD [(b), (d), (f)]. For the top panels (a)-(b), $Pe = 0.1$; (c)-(d): $Pe = 1$, and (e)-(f): $Pe = 10$. All panels have identical x and y limits and are thus only shown in (e). Panels in each row have the same color bar and are shown on the right. The red disk with a white fill represents the circle of contact with radius R_c.

We solve the system of ODEs in (5.59) using spectral collocation of the Laguerre functions at the Laguerre-Gauss-Radau quadrature nodes (Shen et al. 2011). The Laguerre function of order n is defined by $\hat{L}_n(x) = e^{-x/2} L_n(x)$, where $L_n(x)$ is the Laguerre polynomial satisfying the recurrence relation $(n+1)L_{n+1} = (2n + 1 -$

$x)L_n - nL_{n-1}$ and $L_0(x) = 1, L_1(x) = 1 - x$. The orthogonality condition of the Laguerre functions is given by $\int_0^{+\infty} \hat{L}_j(x)\hat{L}_k(x)dx = \delta_{jk}$ where δ_{jk} is the Kronecker delta. It is clear that all Laguerre functions vanish at infinity. To accommodate this natural boundary condition, we define the shifted Fourier modes $\tilde{C}_{m,n}$ such that $\tilde{C}_{0,0} = C_{0,0} - 1/(2\pi)$ and $\tilde{C}_{m,n} = C_{m,n}$ otherwise. It is straightforward to rewrite the ODEs in (5.59) and the no-flux condition (5.60) in terms of $\tilde{C}_{m,n}$. For $Pe, Pe_s \lesssim 10$, the ODEs in terms of $\tilde{C}_{m,n}$ is solved after shifting the radial coordinate $r \to r - 1$ so that it falls into the natural domain $[0, \infty)$ of the Laguerre functions. For $Pe_s \gtrsim 10$, there exists an accumulation boundary layer near the wall as considered in the previous section; in this case a stretched coordinate $\rho = (r - 1)Pe_s$ is used and the ODEs are written in terms of ρ before applying the spectral collocation. For a fast-moving probe, $Pe \gg 1$, there exists a boundary layer of thickness $O(1/Pe)$ in the front sector of the probe with density in the boundary layer growing like Pe as $Pe \to \infty$, just like the case of a probe moving in a passive Brownian suspension (Squires and Brady 2005). For $Pe \gtrsim 10$, we use the stretched coordinate $\rho = (r - 1)Pe$ for the spectral collocation.

Because the resulting discretized linear system has a very large dimension and the spectral differentiation matrix is dense, the matrix system is not formed explicitly. We solve the linear system iteratively using a matrix-free generalized minimal residual method (GMRES).

In figure 5.7 we plot the number density distribution (Recall $n = \int g d\boldsymbol{q}$) in a region around the probe for several values of Pe with $Pe_s = 1$ and $\gamma = 1$. Contours on the left [(a), (c), (e)] are obtained from the numerical solutions of the Smoluchowski equation and are compared to the results obtained from BD (See section 5.5 for details on BD.) on the right [(b), (d), (f)]. The Pe numbers from the top to the bottom are, respectively, 0.1, 1, and 10. A square grid is used to sample the number density distribution and is averaged over several hundred frames at long times. Despite the noise, the density distribution sampled from BD agrees well with that obtained from solving the Smoluchowski equation. The number density and radial polar order ($m_r = \int g\boldsymbol{q} \cdot \boldsymbol{e}_r d\boldsymbol{q}$) distributions at contact corresponding to the microstructures shown in figures 5.7(a), 5.7(c) and 5.7(e) are shown in figure 5.8.

When the speed of the probe is zero, i.e., $Pe = 0$, the microstructure (hence the density) is isotropic, which is simply the distribution of ABPs outside a fixed sphere (Yan and Brady 2015b). Because the suspension is active, the density is not uniform in space but exhibits a boundary accumulation at contact. In order for ABPs to

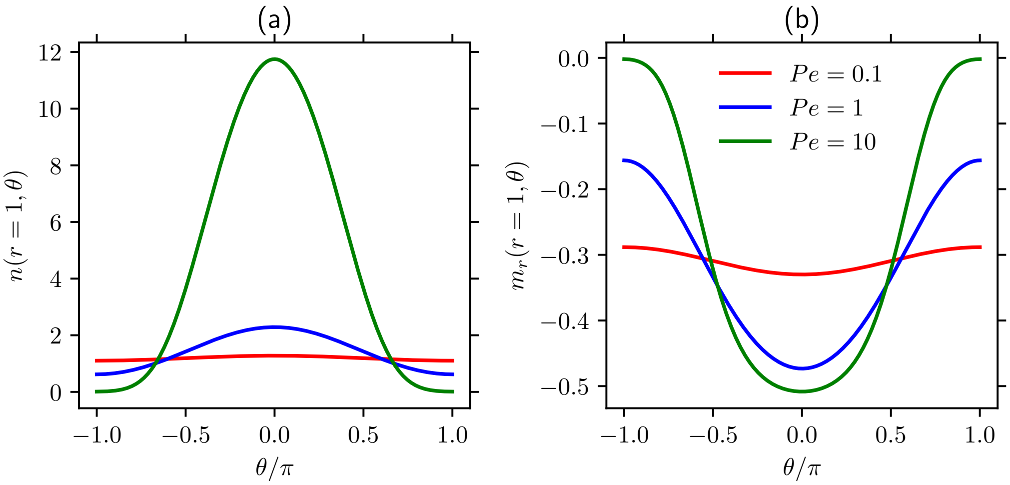

Figure 5.8: Contact values of (a) the number density and (b) the radial polar order as a function of the angular position θ for several values of $Pe = U_1 R_c / D_2$. Panels (a) and (b) share the same legends and are only shown in (b). For all lines plotted, $Pe_s = U_2 R_c / D_2 = 1$ and $\gamma = R_c/\delta = 1$. The front of the probe is at $\theta = 0$ and the back is $\theta = \pm\pi$.

accumulate at the boundary, they must exhibit a net polar order pointing into the boundary ($m_r < 0$) because otherwise they swim away. In the absence of activity ($Pe_s = 0$), the number density is uniform. When the probe is set into motion in an active suspension, the microstructure is perturbed from its isotropic steady state (For an active suspension, this steady state is not in a thermodynamic equilibrium.). For small Pe such as that shown in figure 5.7(a), the microstructure is only slightly perturbed from the isotropic state and has been characterized in section 5.3. As Pe increases, a prominently non-uniform density distribution develops at contact with an accumulation at the front and a depletion in the back of the probe as can be seen in figure 5.8(a). Because the density becomes depleted in the back, the polar order also decreases in the back (in absolute value) and increases in the front of the probe as shown in figure 5.8(b).

For passive Brownian suspensions, the buildup of particles in the front of the probe is solely due to the advection of the probe. When the suspension is active, this advective effect is still present. In figure 5.9 we plot the contact density at $Pe = 10$ for a passive suspension and for active suspensions with $Pe_s = 1$ and $Pe_s = 10$. For $Pe_s = 1$, the swim speed is small compared to that of the probe and the contact density is almost the same as that of the passive suspension. For $Pe_s = 10$, the swim speed is comparable to the probe speed and the density is elevated from that

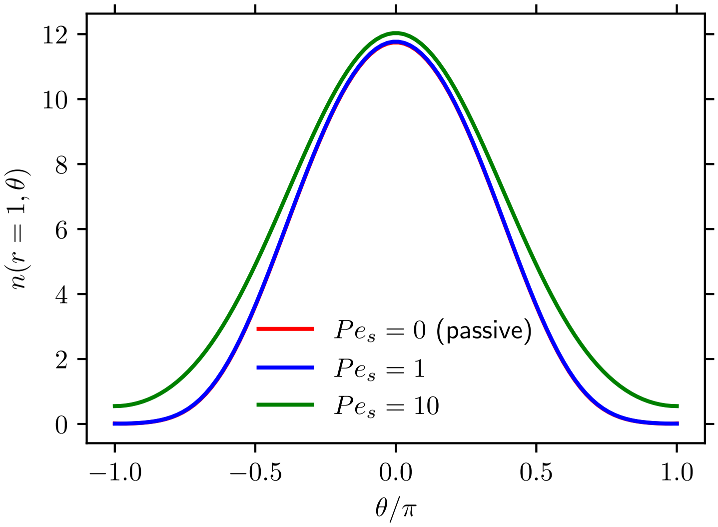

Figure 5.9: Number density at contact for several values of $Pe_s = U_2 R_c/D_2$. For all results, $\gamma = Rc/\delta = 1$ and $Pe = U_1 R_c/D_2 = 10$.

of the passive. This elevation in density represents the additional wall accumulation resulting from activity. In particular, we note that the contact density on all sides of the probe is increased.

5.5 Brownian dynamics simulation

From a particle-level perspective, the evolution of the configuration of ABPs can be described by the overdamped Langevin equations—a balance of forces and torques. In the absence of hydrodynamic interactions as we consider here, Brownian Dynamics (BD) can be used to simulate the dynamics of ABPs at the particle level. BD has been used to study the bulk rheology (Foss and Brady 2000) and microrheology (Carpen and Brady 2005) of passive colloidal suspensions. Our approach is similar to those considered by Foss and Brady (2000) and Carpen and Brady (2005) except that the orientational dynamics of each particle also needs to be tracked due to the self-propulsion of ABPs.

For each ABP, the force and torque balance in the co-moving frame is given by

$$\mathbf{0} = -\zeta_2\left(\frac{d\boldsymbol{x}}{dt} + \boldsymbol{U}_1\right) + \boldsymbol{F}^B + \boldsymbol{F}^S + \boldsymbol{F}^{HS}, \tag{5.62}$$

$$\mathbf{0} = -\zeta_R \frac{d\boldsymbol{q}}{dt} + \boldsymbol{L}^B \times \boldsymbol{q}. \tag{5.63}$$

Here, $\boldsymbol{F}^S = \zeta_2 U_s \boldsymbol{q}$ is the swim force (Takatori et al. 2014) giving rise to self-propulsion, $\boldsymbol{F}^B$ ($\boldsymbol{L}^B$) is the Brownian force (torque), $\boldsymbol{F}^{HS}$ is the hard-sphere force due to the steric interaction between the probe and the ABP, and ζ_R is the rotational hydrodynamic drag coefficient. Because both the probe and the ABP are spheres, their hard-sphere interaction do not induce a torque. However, if either the probe or the ABP (or both) is nonspherical, their hard-particle interaction can induce a torque. The hard-sphere force is present only when the probe and the ABP are in contact and is the mechanism of the enhanced viscosity in passive colloidal suspensions compared to the motion of a probe in the solvent alone. The Brownian force and torque satisfy the white-noise statistics:

$$\left\langle \boldsymbol{F}^B \right\rangle = 0, \quad \left\langle \boldsymbol{F}^B(0)\boldsymbol{F}^B(t) \right\rangle = 2D_2\zeta_2^2\delta(t)\boldsymbol{I}, \tag{5.64}$$

$$\left\langle \boldsymbol{L}^B \right\rangle = 0, \quad \left\langle \boldsymbol{L}^B(0)\boldsymbol{L}^B(t) \right\rangle = 2D_R\zeta_R^2\delta(t)\boldsymbol{I}, \tag{5.65}$$

where $\delta(t)$ is the delta function (which has the units of the inverse of time) and the angle brackets denote the ensemble average over Brownian fluctuations. We emphasize that the rotational diffusivity represents biological noises and can be varied independently from the translational diffusivity D_2. In the co-moving frame, the probe is fixed in space and appears as an obstacle for the dynamics of ABPs outside of it.

In 2D, using the parametrization $\boldsymbol{q}(t) = \cos\theta'(t)\boldsymbol{e}_x + \sin\theta'(t)\boldsymbol{e}_y$, it is straightforward to see that $d\boldsymbol{q}/dt = \boldsymbol{e}_z \times \boldsymbol{q}d\theta'/dt$ where $\boldsymbol{e}_z = \boldsymbol{e}_x \times \boldsymbol{e}_y$. As a result, equation (5.63) can be written as

$$\frac{d\theta'}{dt} = \Omega^B, \tag{5.66}$$

where the Brownian angular velocity satisfies $\left\langle \Omega^B(t) \right\rangle = 0$ and $\left\langle \Omega^B(0)\Omega^B(t) \right\rangle = 2D_R\delta(t)$.

Using the Euler-Maruyama scheme, the linear and angular equations (5.62) and (5.66) can be discretized given the time step Δt; their discrete forms at time $t = t_k = k\Delta t (k = 0, 1, ...)$ are given by

$$\boldsymbol{x}_{k+1} = \boldsymbol{x}_k + (-\boldsymbol{U}_1 + U_s\boldsymbol{q}_k)\,\Delta t + \sqrt{2D_2\Delta t}\boldsymbol{\xi}_x + \Delta\boldsymbol{x}^{HS}, \tag{5.67}$$

$$\theta'_{k+1} = \theta'_k + \sqrt{2D_R\Delta t}\xi_{\theta'}, \tag{5.68}$$

where $\boldsymbol{\xi}_x$ is a 2-vector of pseudo random numbers with each entry having zero mean and unit variance. Similarly, $\xi_{\theta'}$ is a scalar having zero mean and unit variance.

At each time step, the position of the ABP is updated first by adding the displacements due to the relative velocity $-\boldsymbol{U}_1$, the swimming, and the Brownian contributions, and second by resolving collision with the fixed probe. We use the potential-free algorithm of Heyes and Melrose (1993) in which the overlap between the probe-ABP pair is corrected by moving the ABP along the line of centers back to contact. Because the probe has prescribed kinematics (i.e., fixed), only the ABP is moved if an overlap is detected.

At this point, a contrast between the CF and CV modes of microrheology is in order. In the CF mode of microrheology, either the external force is zero (tracer dispersion) or finite, in the collision resolution step both the probe and the ABP have to be displaced in opposite directions such that Newton's third law is satisfied. In the CV mode of microrheology, because the probe is never displaced due to collision, one can have many bath particles interacting with a single probe in one simulation; these bath particles are "transparent" to each other in the sense that they can pass through each other and only interact with the probe. For the CF mode, however, the collision resolution between the probe and a bath particle might introduce a new overlap between the probe and a different bath particle due to the displacement to the probe. Therefore, if one wishes to simulate the pair-interaction between the probe and one bath particle only, one can run many independent simulations each consisting of the probe and a bath particle or simulate a system of many bath particles with low volume fraction. The results obtained in the second method is a good approximation to the pair behavior only when the system is sufficiently dilute.

In the simulation setup, the system consists of the fixed probe and N ABPs in a rectangular domain of lengths L_x and L_y where the x-axis is aligned with $\boldsymbol{U}_1$, i.e., $\hat{\boldsymbol{U}}_1 = \boldsymbol{e}_x$. The size of the simulation domain needs to be sufficiently large such that its boundary is a good approximation of the far-field [see equation (5.15)]. In particular, the domain needs to be much larger than the run length of the ABPs. At each time step, we evolve the positions and orientations of all ABPs according to equations (5.67) and (5.68) and the hard-sphere displacement of each particle is recorded when necessary. Simulations are performed using an in-house CUDA-accelerated code that runs on NVIDIA GPUs, which enables us to run a typical simulation with $O(10^5)$ ABPs. The measured area fraction of the ABPs is $\phi = N\pi b^2/(L_xL_y - \pi a^2)$. Because the ABPs are transparent to each other, the measured volume fraction has no physical interpretation and only serves to improve the measured statistics.

The force balance of the probe is $-\zeta_1\boldsymbol{U}_1 + \boldsymbol{F}^{\text{ext}} - \boldsymbol{F}^{HS} = \boldsymbol{0}$, where the hard-sphere force the ABP exerts on the probe is $-\boldsymbol{F}^{HS}$ according to Newton's third law. To maintain a constant velocity of the probe, the external force fluctuates and we are concerned with its average over the fluctuations. Noting that $\boldsymbol{F}^{HS} = \zeta_2 \Delta \boldsymbol{x}^{HS}/\Delta t$ and equation (5.8), we obtain

$$\frac{\Delta \eta}{\eta} = \frac{\zeta_2 \Delta x^{HS}}{\zeta_1 U_1 \Delta t}, \tag{5.69}$$

where Δx^{HS} is the accumulated hard-sphere displacement of all N ABPs at each time step and then averaged over many frames at sufficiently long times so that a steady state is reached. It is then straightforward to calculate η^{micro} using the first part of equation (5.21).

In figure 5.10 we show three snapshots of the BD simulation for varying probe speeds. The speed of the probe increases from the top panel to the bottom. The snapshot is windowed around the probe in order to highlight the near-field microstructure. The red solid circle denotes the circle of contact that is concentric with the probe but with radius R_c (see figure 5.3). The blue dots are the positions of the centers of the ABPs and their size do not reflect the size of ABPs in the simulation. A prominent feature of the near-field microstructure is the presence of a trailing wake behind the probe that is devoid of bath particles. To highlight the wake structure, in figure 5.10 the translational diffusion is turned off, $D_2 = 0$. In the absence of translational diffusion, the only source of noise in the dynamics of ABPs comes from the Brownian reorientation. Recall that in the simulation the probe is fixed in place while the ABPs experience a constant advection of speed U_1 to the left. To understand the development of the trailing wake, consider an ABP that is behind the probe (to the left). In order for this ABP to reach the probe from behind, the best orientation it should take is $\boldsymbol{q} = \boldsymbol{e}_x$ (pointing to the right), in which case the net speed to the right is $U_2 - U_1$. When $U_2 > U_1$, i.e., the speed of the ABPs is larger than that of the probe, ABPs with orientations near $\boldsymbol{e}_x$ can reach the probe. On the other hand, when $U_2 \leq U_1$, the speed of the ABPs is smaller than that of the probe and all ABPs will be advected further to the left. This simple physical argument suggests that the onset of a trailing wake happens when $U_2 \approx U_1$. Indeed, when the speed of the probe is smaller than that of the ABPs as shown in the top panel of figure 5.10 there is no wake. When the speed of the probe surpasses that of the ABPs, e.g. in the middle and bottom panels of figure 5.10, the trailing wake appears and becomes more extended to the left as the speed of the probe increases.

To characterize the geometry of the triangular wake, we define the wake half angle β, which is the angle between the top (or equivalently the bottom) boundary of the wake and the horizontal axis. Consider an active particle at contact with the top

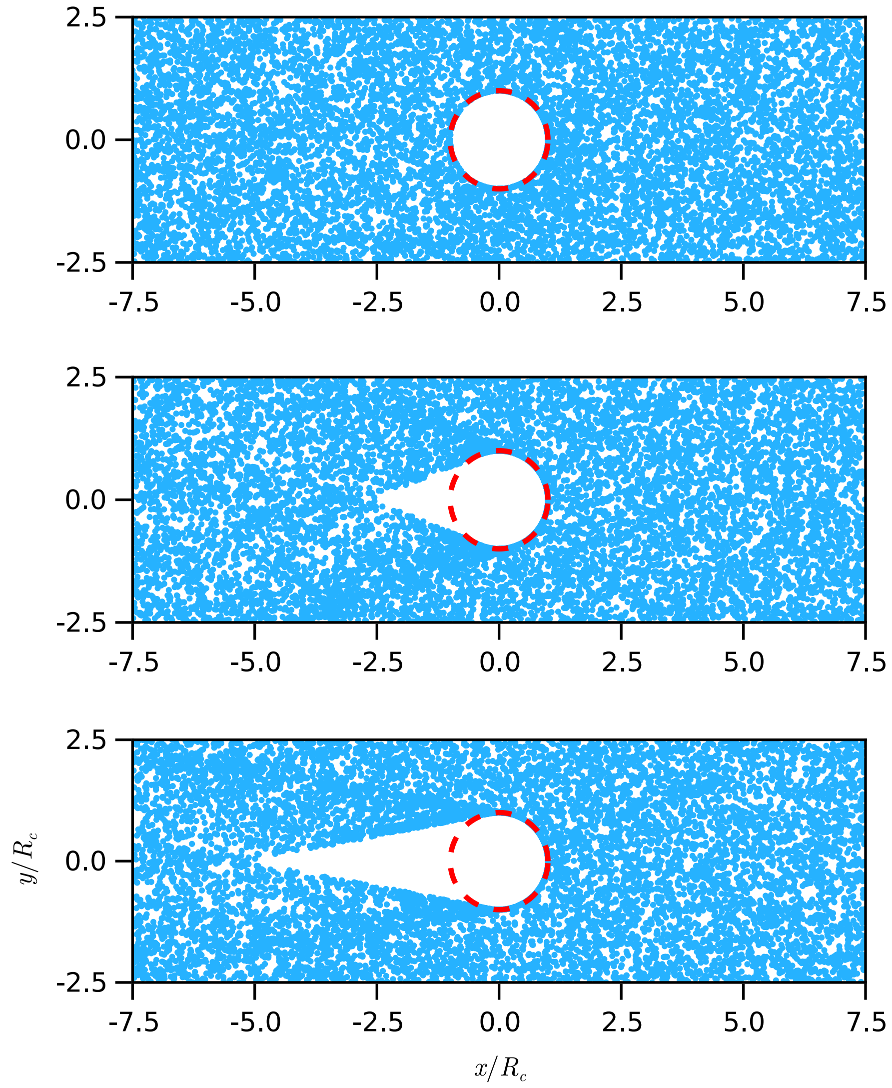

Figure 5.10: Windowed snapshots of the BD simulation showing the circle of contact (red solid line), the positions of ABPs (blue dots), and the wake structure behind the probe. In all panels, $\ell/R_c = 1$ and $D_2 = 0$. The speed of the probe increases from top to bottom: $U_1\tau_R/R_c = \{0.5, 2.5, 5\}$. The blue dots denote the center positions of the ABPs and their size in the figure does not represent the size of the ABPs in the simulation. The simulation domain is larger than the window shown and 10000 ABPs are plotted in each panel.

of the probe; in order for this particle to swim into the back of the probe it should have an orientation towards the bottom. The maximum vertical displacement is achieved with $\boldsymbol{q} = -\boldsymbol{e}_y$, in which case the ABP assumes a trajectory that has a slope given by $\tan\beta = U_2/U_1$. This simple argument is able to predict the wake half angle quantitatively. The wake half angle can be easily read off from the middle and bottom panels of figure 5.10. Taking the bottom panel as an example, from the plot we see that $\tan\beta \approx 1/5$ which is exactly the speed ratio $U_2/U_1 = 1/5$. Similarly, one can verify the prediction in the middle panel.

In the presence of translational diffusion, the wake boundary becomes less sharp because of the diffusive flux $-D_2\nabla n$ down the number density gradient, into the wake. If the swim speed is small compared to the probe speed, the wake structure with finite D_2 approaches that obtained for a passive Brownian suspension, which has been studied (Squires and Brady 2005; Carpen and Brady 2005).

In figure 5.10, periodic boundary conditions in both directions of the simulation domain are used. This is a good approximation of the far-field condition provided that the simulation domain is sufficiently long such that all prior interactions of an ABP with the probe have relaxed once the ABP reaches the boundary of the domain. When the probe speed is much larger than that of the ABPs, $U_1 \gg U_2$, the trailing wake becomes rather extended in the horizontal direction. To make use of the periodic boundary condition, the simulation domain has to be enlarged accordingly, which makes the nominal volume fraction very small and the number of particles colliding with the probe diminishing. For a fixed number of ABPs, as the probe speed increases the statistics for the hard-sphere force becomes less reliable. Notice that for $U_1 \gg U_2$, once an ABP moves past the probe to the left, the chance of it turning back to the right without exiting the left boundary and entering from the right is vanishingly small. As a result, we introduce a new boundary condition in the horizontal direction for $U_1 \gg U_2$ in which the trailing wake is cut off. Once an ABP moves past the probe to the left, it is removed from the simulation and added back from the right boundary of the domain with the bulk distribution, i.e., random orientation and y position. Similarly, if the ABP leaves the boundary from the right, instead of appearing from the left it will be put back on the right boundary with the bulk distribution. This new boundary condition allows us to reduce the domain size significantly for $U_1 \gg U_2$ but still obtain the correct microviscosity measurement.

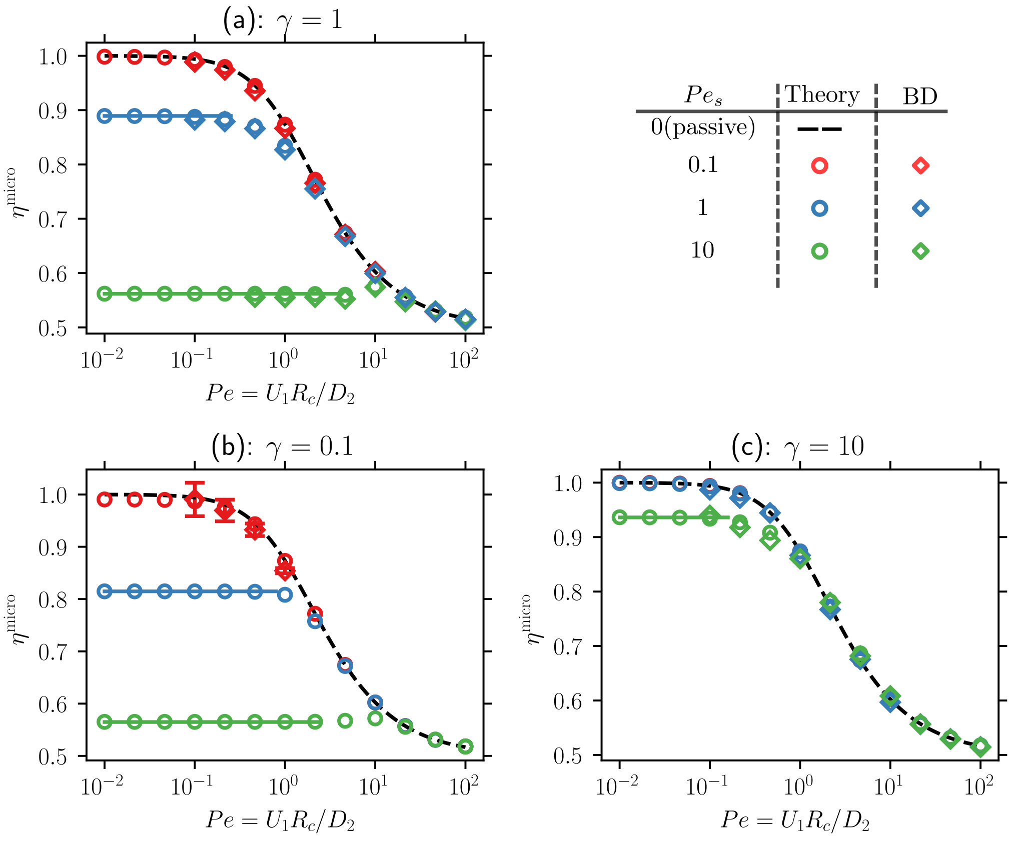

Figure 5.11: The microviscosity of ABPs as a function of $Pe = U_1 R_c / D_2$ for several values of Pe_s and γ. The dashed line denotes the results for passive Brownian suspensions ($Pe_s = 0$). Circles are results from the numerical solutions of the Smoluchowski equation and diamonds are obtained from BD. The horizontal solid lines are the zero-forcing microviscosity η_0^{micro} obtained in section 5.3. The values of γ are fixed in each panel and are given by: (a) $\gamma = 1$, (b) $\gamma = 0.1$ and (c) $\gamma = 10$. Note that in panel (c) the results for $Pe_s = 0.1$ and $Pe_s = 1$ are visually indistinguishable.

5.6 Microviscosity

In figure 5.11(a) we plot the microviscosity η^{micro} as a function of Pe for several values of Pe_s and $\gamma = 1$. The solid line denotes the microviscosity of passive Brownian suspensions ($Pe_s = 0$). Circles denote results from the numerical solution of the Smoluchowski equation and diamonds are obtained from BD. The solid horizontal lines denote the zero-forcing microviscosity discussed in section 5.3. For $Pe_s = 0.1$, the ABPs are weakly active and the microviscosity approximates that of the passive suspension. As discussed in section 5.3, when the probe speed is small ($Pe \ll 1$), the ABPs exhibit swim-thinning in which the microviscosity decreases as Pe_s increases. In the large Pe limit, the activity of the ABPs is obscured by the rapid advection of the probe speed and therefore does not affect the microviscosity as $Pe \to \infty$. That is, regardless of Pe_s (so long as it is finite), the microviscosity approaches that of the passive result of $1/2$ as $Pe \to \infty$.

For completeness, the variation of microviscosity for different values of γ are presented in figures 5.11(b) and 5.11(c). The increase of γ corresponds to the decrease in τ_R or the increase in the rotary diffusivity D_R. When γ is large, e.g., $\gamma = 10$ in 5.11(c), the rotary diffusion is strong and the particles behave more like passive particles. Therefore, the swim-thinning is less prominent and the microviscosity is closer to that of passive suspensions. Conversely for a small γ as shown in 5.11(b) for $\gamma = 0.1$, the swim-thinning is stronger compared to the case shown in 5.11(a) for $\gamma = 1$.

5.7 Effects of hydrodynamics

5.7.1 Fluid disturbance due to the active force dipole

So far in this Chapter we have considered the effect of activity, i.e., the intrinsic swim speed, on the suspension microstructure and the resulting microviscosity. Beyond the swim speed (U_2), another important characteristic of a self-propelled microswimmer or active particle is its hydrodynamic stresslet (Koch and Subramanian 2011; Saintillan and Shelley 2015). Because an active particle propels itself without applying a net force on the surrounding fluid, the disturbance flow it induces in the far field has a dipolar structure that decays as $1/r^2$ with r being the distance from the particle. Using the reciprocal theorem for Stokes flow, Lauga and Michelin (2016) proposed a general method to determine the stresslet of an active particle with a prescribed surface slip velocity distribution.

To understand the first effect of the stresslet on the suspension microviscosity, we

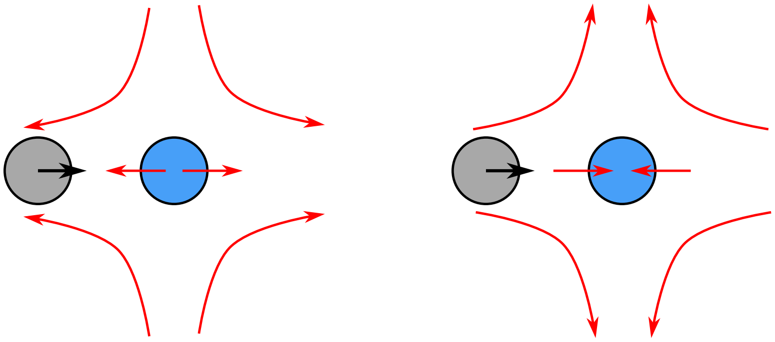

Figure 5.12: Schematic of the flow generated by a pusher (left) and by a puller (right) located in the front of the probe.

consider the far-field fluid velocity generated by an ABP. The flow field at position $\boldsymbol{x}$ in 3D due to the force dipole with strength σ_0 at $\boldsymbol{y}$ with orientation $\boldsymbol{q}$ can be written as (Saintillan and Shelley 2015)

$$\boldsymbol{u}(\boldsymbol{x};\boldsymbol{y},\boldsymbol{q}) = \frac{\sigma_0}{8\pi\eta}\boldsymbol{q}\boldsymbol{q} : \nabla_x \boldsymbol{J}(\boldsymbol{x}-\boldsymbol{y}), \tag{5.70}$$

where $\boldsymbol{J}(\boldsymbol{r}) = \boldsymbol{I}/r + \boldsymbol{r}\boldsymbol{r}/r^3$ is the Oseen–Burgers tensor. The dipole strength is a signed quantity and its magnitude for ABPs obeys the scaling relation $|\sigma_0| \sim F^{\text{swim}}b \sim \zeta_2 U_2 b \sim \eta U_2 b^2$. The sign of σ_0 depends on the positions of the thrust and drag forces relative to the swimming direction $\boldsymbol{q}$: $\sigma_0 < 0$ for a pusher particle that generates a thrust with its tail (e.g, *E. coli*), while for a puller particle such as *C. reinhardtii*, $\sigma_0 > 0$ (see figure 5.12 for a schematic).

To proceed, we only consider the effect of the dipolar flow on the drag of the probe for the *known* ABP distribution solved in the previous section. Making use of Faxén's law for a sphere (Kim and Karrila 1991), the hydrodynamic force the probe experiences can be given by $\boldsymbol{F}^H = -\zeta_1\left[\boldsymbol{U}_1 - \left(1 + a^2\nabla^2/6\right)\boldsymbol{u}\right]$. Noting the force balance, $\boldsymbol{F}^{\text{ext}} + \boldsymbol{F}^H + \boldsymbol{F}^{HS} = \boldsymbol{0}$, we only need to consider the additional drag contribution due to the dipole, which upon averaging over the distribution of the ABP is given by

$$\left\langle\left(1 + a^2\frac{\nabla^2}{6}\right)\boldsymbol{u}\right\rangle = n_3^\infty \int \left(1 + a^2\frac{\nabla^2}{6}\right)\boldsymbol{u} g_3(\boldsymbol{r}_3,\boldsymbol{q})d\boldsymbol{r}_3 d\boldsymbol{q}, \tag{5.71}$$

where the subscript 3 denotes 3D. To accommodate the above equation using the 2D solution of the ABP distribution, we place the system in a monolayer such that $n_3^\infty = N/V = N/(2bA) = n^\infty/(2b)$ and $g_3(\boldsymbol{r}_3,\boldsymbol{q}) = g(\boldsymbol{r},\boldsymbol{q})\delta(z)$. After non-dimensionalization (recall that lengths are non-dimensionalized by R_c), we obtain the dipole contribution to microviscosity as

$$\eta_{\mathrm{d}}^{\mathrm{micro}} = -\beta \int_0^{2\pi} d\theta \int_1^{\infty} f_x(r,\theta) r dr, \tag{5.72}$$

where we have defined

$$f_x = 3Q_{rr} \cos\theta \left[\frac{1}{r^2} - \frac{1}{r^4} \left(\frac{a}{R_c} \right)^2 \right] - 2Q_{rt} \sin\theta \frac{1}{r^4} \left(\frac{a}{R_c} \right)^2 \tag{5.73}$$

and

$$\beta = \frac{a\sigma_0}{16\pi^2 \eta b^2 R_c U_1} = \hat{\sigma}_0 \frac{\alpha^2}{Pe}. \tag{5.74}$$

In the above, $\hat{\sigma}_0 = \sigma_0/(16\pi^2 \eta a D_2)$ is a dimensionless measure of the dipole strength; recall that $\alpha = a/b$. In equation (5.73), $Q_{rr} = \int \boldsymbol{e}_r \boldsymbol{e}_r : (\boldsymbol{qq} - \boldsymbol{I}/2) g d\boldsymbol{q}$ is the radial component of the nematic tensor and $Q_{rt} = \int \boldsymbol{e}_r \boldsymbol{e}_\theta : (\boldsymbol{qq} - \boldsymbol{I}/2) g d\boldsymbol{q}$ is the cross component.

Notice that at this level of approximation the dipole contribution to microviscosity is proportional to $\hat{\sigma}_0$ (and thus σ_0). As a result, $\eta_{\mathrm{d}}^{\mathrm{micro}}$ for pushers and pullers have opposite signs. In figure 5.13 we plot $\eta_{\mathrm{d}}^{\mathrm{micro}}$ for pushers with $\hat{\sigma}_0 = -100$ obtained from equation (5.72) as a function of Pe. Similar to the collisional microviscosity considered in the previous section, $\eta_{\mathrm{d}}^{\mathrm{micro}}$ exhibits a force-thinning behavior. The most interesting characteristic seen in figure 5.13 is the fact that for pushers $\eta_{\mathrm{d}}^{\mathrm{micro}}$ is positive. Due to the linearity in $\hat{\sigma}_0$, this means that for *pullers* $\eta_{\mathrm{d}}^{\mathrm{micro}}$ is *negative*, which acts to reduce the microviscosity below that of the collisional result.

To understand the physical origin of such behavior, we consider the force dipole of an ABP that is in front of the probe as shown in figure 5.12. For a pusher, the flow field acts to push back the probe, which gives rise to increased microviscosity. On the other hand, for a puller the flow field pulls the probe forward which results in reduced drag and thus reduced microviscosity. Because the ABP is more likely to be in front of the probe than in the back, the above physical picture is sufficient to explain the qualitative behavior of the dipole contribution to microviscosity.

If the dipole strength of puller ABPs is sufficiently large, the suspension microviscosity can become negative, which means that the external force applied to maintain the steady probe motion is *opposite* to the direction of the probe velocity—a microscopic analogue of the bulk superfluid behavior observed in rheological measurements of active matter in the dilute regime (López et al. 2015; Chui et al. 2021). Opposite to the microscopic result, in bulk shear flow the superfluid behavior is observed only

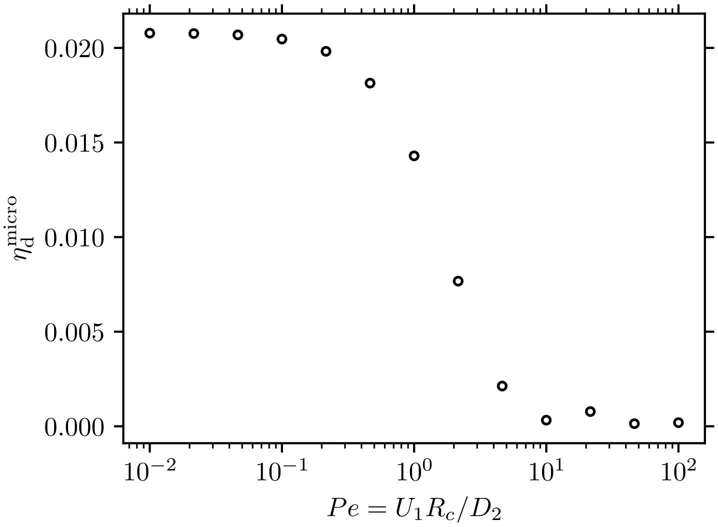

Figure 5.13: The dipole contribution to the suspension microviscosity obtained from equation (5.72). Parameters used are $\hat{\sigma}_0 = -100$ (pusher), $\alpha = 1$, $\gamma = 1$ and $Pe_s = 1$.

for *pushers*, the mechanism for which is shown in figure 5.1. For a nonspherical particle, the shear flow tends to align the particle along the extensional axis. The flow due to the pusher stresslet then acts to “stretch” the fluid further and reduces the effective shear viscosity. For active puller microswimmers, the effective shear viscosity is increased because the flow they induce acts against the imposed shear. We note that one similarity between microrheology and bulk rheology is that the reductions in viscosity in both cases are most significant in the small Pe limit—slow probe speed in microrheology and weak shear in bulk rheology.

The presence of a negative microviscosity at steady state is a unique feature for CV probes. In the CF mode of microrheology, the probe would speed up as the local viscosity decreases, and eventually moves out of the regime of negative viscosity. At steady state, therefore, the measured microviscosity is positive [2]. Foffano et al. (2012) studied the CF microrheology of an active nematic suspension modeled at the continuum level as an active liquid crystal. In the active nematics model, activity refers to the stresslet contribution to the suspension stress and the constituting individual “particles” do not self-propel (cf. ABPs). Though a negative microviscosity is not observed in Foffano et al. (2012), the authors showed that in

---

[2] The macroscopic analogue of this phenomenon is the constant strain-rate versus constant shear-stress experiments. For constant shear-stress, a negative viscosity allows the rheometer to accelerate (and thus increases the shear rate) out of the negative viscosity regime (Takatori and Brady 2017).

the puller case the active stresslet generates a flow field in front of the probe that acts to pull the probe forward, hence facilitating the probe motion. Their observation is consistent with our analysis and prediction.

5.7.2 Fluid disturbance due to the probe motion

In this section, we neglect any fluid disturbances associated with the self-propulsion of ABPs but consider the flow due to the steady motion of the probe—the Stokes flow outside a translating sphere. In this limit, the ABPs are treated hydrodynamically as point particles that do not disturb the flow. Defining $\boldsymbol{u}' = \boldsymbol{u} - \boldsymbol{U}_1$ with $\boldsymbol{u}$ being the flow field in the laboratory frame, the translational and rotational fluxes of the Smoluchowski equation (5.2) are, respectively,

$$\boldsymbol{j}_2^T - \boldsymbol{j}_1^T = (\boldsymbol{u}' + U_s\boldsymbol{q})\, P_{1/1} - D_2\nabla_r P_{1/1}, \tag{5.75}$$

$$\boldsymbol{j}_2^R = \frac{1}{2}\boldsymbol{\omega}' P_{1/1} - D_R\nabla_R P_{1/1}, \tag{5.76}$$

where $\boldsymbol{\omega}' = \nabla \times \boldsymbol{u}'$ is the vorticity of the $\boldsymbol{u}'$ field. Notice that the $\boldsymbol{u}'$ field vanishes on the surface of the probe and asymptotes to $-\boldsymbol{U}_1$ at infinity: $\boldsymbol{u}' = \boldsymbol{0}$ at $r = a$ and $\boldsymbol{u}' \to -\boldsymbol{U}_1$ as $r \to \infty$.

The ABPs in the Stokes flow of the probe experience a spatially varying fluid advection and rotate with the vorticity. Only in the far field one recovers equations (5.3) and (5.4): the vorticity vanishes and $\boldsymbol{u}' \to -\boldsymbol{U}_1$ as $r \to \infty$. For our 2D system we only need the in-plane components of the flow field, which in the polar coordinate system are written as

$$u'_r = U_1 \cos\theta \left(-1 + \frac{3a}{2r} - \frac{a^3}{2r^3}\right), \tag{5.77}$$

$$u'_\theta = U_1 \sin\theta \left(1 - \frac{3a}{4r} - \frac{a^3}{4r^3}\right). \tag{5.78}$$

Similarly, the vorticity in the z direction can be obtained as $\omega = 3aU_1 \sin\theta/(2r^2)$. Because the length scale of the flow is set by the size of the probe (radius a) while the hard sphere contact occurs at $r = R_c$, this introduces an explicit dependence on the size ratio a/R_c. Following the procedure outlined in previous sections, the Smoluchowski equation together with the flux expressions (5.75) and (5.76) is non-dimensionalized and solved numerically.

In figure 5.14 we plot the microviscosity obtained from the numerical solutions of the Smoluchowski equation in the probe disturbance flow for an active suspension with $Pe_s = 10, \gamma = 1$ (fast-swimming ABPs) and the passive suspension as a

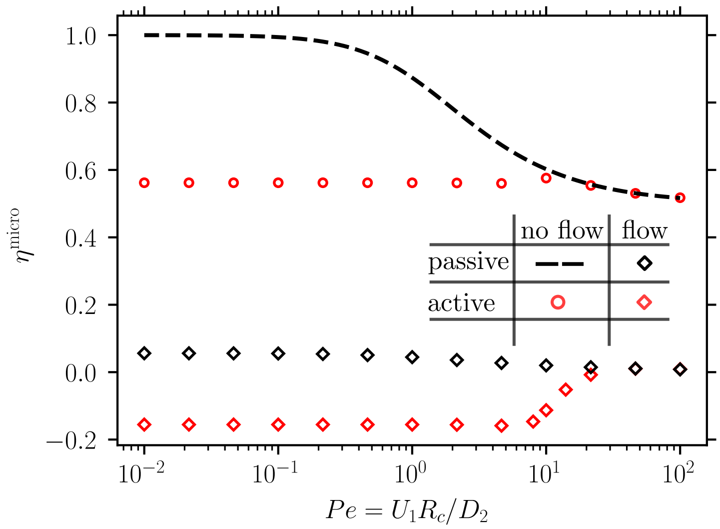

Figure 5.14: The suspension microviscosity as a function of $Pe = U_1R_c/D_2$ for fast ABPs (red) and passive Brownian particles (black) with or without considering the Stokes flow of the probe. The size ratio is $a/R_c = 0.8$. For the active results, $Pe_s = 10$ and $\gamma = 1$. In the small Pe regime for fast ABPs ($Pe_s = 10$), a negative microviscosity is observed.

function of Pe. For comparison, the results in the absence of the probe disturbance flow obtained previously (see figure 5.11) are also plotted. Comparing the passive results without (dashed line) and with (black diamonds) the probe disturbance, we see that the microviscosity is lowered over the entire range of Pe. In the small Pe limit, the microviscosity is lowered to a value close to zero (but positive). When $Pe \gg 1$, the microviscosity approaches zero. For a passive suspension, the suspension still exhibits a force-thinning behavior (though at a smaller scale). For the fast ABPs shown in red, the behavior is rather interesting: in the small Pe regime, the probe disturbance leads to a *negative* microviscosity; in the large Pe limit, the microviscosity is indistinguishable from that of the passive suspension and approaches zero as $Pe \to \infty$.

Though more significant for active suspensions, the reduction in microviscosity occurs regardless of the activity of the bath particles. This disturbance-induced reduction can be understood by examining the flow field shown in figure 5.15. In the co-moving frame of the probe, the disturbance flow is the same as that of a fixed sphere placed in the uniform background flow $-\boldsymbol{U}_1$. As one moves from infinity towards the probe, the flow field develops a transverse (y) component and the magnitude of the flow decreases because at the probe surface (a no-slip boundary) $\boldsymbol{u}'$

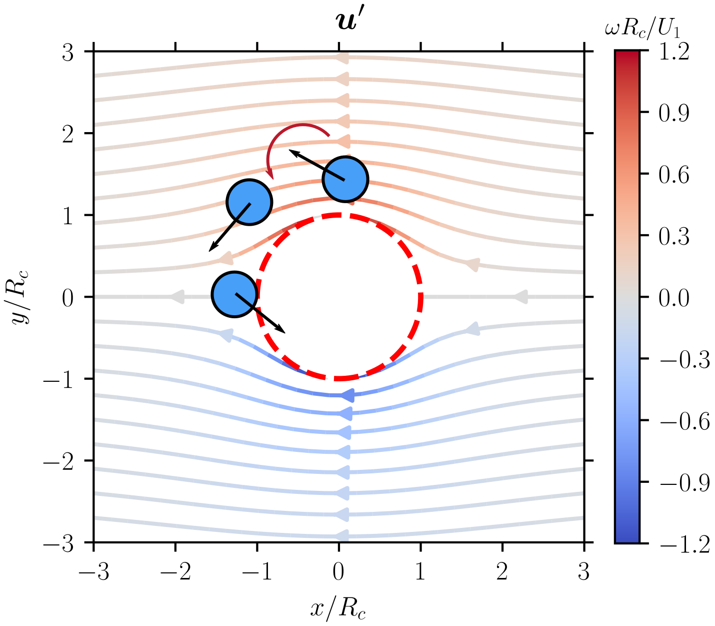

Figure 5.15: Plot of the stream lines of the flow field $\boldsymbol{u}'$. The dashed red circle is the circle of contact ($r = R_c$). The streamlines are colored according to the local fluid *vorticity* (non-dimensionalized by U_1/R_c). The blue particles from right to left is a sketch of the trajectory of an ABP under the influence of the fluid vorticity. The size of the ABP is not to scale but the contact circle and the flow/vorticity fields are. Note that $\boldsymbol{u}'$ vanishes at $r = a$, not at $r = R_c = a + b$. The ratio $a/R_c = 0.8$ is used for the flow field.

vanishes. To understand the reduction in η^{micro} for passive suspensions, recall that there is a buildup of bath particles in the front (right) of the probe due to the uniform advection $-\boldsymbol{U}_1$. When the disturbance flow is included, however, the x component of the flow vanishes at the front and near this stagnation point the streamlines (see figure 5.15) go around the probe towards the back (left) [3]. The particles that would otherwise accumulate at the front are transported to the back of the probe simply due to the advection of the flow. As a result, the advection acts to lower the difference between the number density in the front and back, thus reduces the microviscosity.

Further reductions in microviscosity for ABPs beyond that of the passive suspension as shown in figure 5.14 must be due to the interaction between the suspension activity and the disturbance flow. In the high *Pe* limit, as noted before the probe speed obscures that of the activity, and one cannot distinguish between a passive and

---

[3] A bath particle at contact with the front of the probe still experiences a weak flow speed towards the left because the contact radius $r = R_c = a + b$ is larger than the no-slip surface $r = a$.

an active suspension solely from the measurements of microviscosity. For small Pe, however, the difference between an active and a passive suspension is prominent because a *negative* microviscosity is observed as indicated by the red diamond symbols in figure 5.14. To understand the emergence of a negative microviscosity, consider an active particle near the top of the probe that is trying to move away from the probe to the upper left domain (see figure 5.15). Noting that in addition to the spatially-varying fluid velocity, the probe disturbance also introduces a vorticity field, which at the top half ($y > 0$) of the plane is positive as shown in the color bar. For the ABP at the top, it experiences a counterclockwise rotation due to the fluid vorticity, which tends to turn the swimming director $\boldsymbol{q}$ towards the back of the probe. In the small Pe limit, the $-y$ component of the swim speed is larger than the flow speed, which allows the ABP to move into the rear of the probe and pushes the probe towards the right. This vorticity-induced reorientation process near a no-slip wall has been discussed in detail by Peng and Brady (2020) in the context of upstream swimming of ABPs in Poiseuille flow. In the current problem, the reorientation and pushing lead to a negative microviscosity provided that the ABPs have a large enough swim speed. Because the flow field has mirror symmetry about the $y = 0$ axis, a similar process occurs for ABPs in the lower half of the domain.

In the large Pe limit, the timescale for reorientation by vorticity is much smaller than the active reorientation time τ_R, which significantly reduces the effective run length of ABPs (Peng and Brady 2020). Therefore, in this limit the ABPs "lose" their activity (e.g., persistence) and must have a microviscosity indistinguishable from that of the passive suspension. In the intermediate Pe regime, the above analysis means that active suspensions must exhibit a force-thickening behavior (see figure 5.14) in order to meet with the low-Pe negative plateau and the near-zero plateau of large Pe. We note that for ABPs with slow swim speed, the low-Pe plateau is still positive and a force-thinning behavior can be observed. Depending on the activity, an active suspension in the disturbance of the probe can exhibit either force-thinning or force-thickening behavior.

The above analysis is from a micromechanical perspective, which can be corroborated by examining the number density and polar order distributions at the circle of contact shown in figure 5.16. When the disturbance flow of the probe (shown in blue) is included, the density (similarly the radial polar order) in the back ($\theta = \pm\pi$) becomes higher than that in the front. Because more particles are pushing in the back than in the front, one must experience a negative microviscosity, which is con-

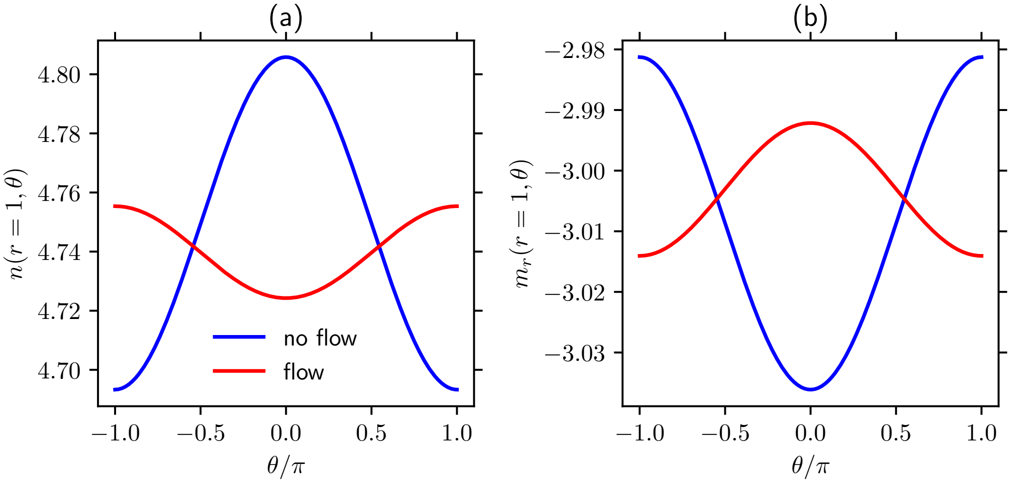

Figure 5.16: (a) The number density distribution and (b) the radial polar order distribution at contact as a function of the angular position θ around the probe in the small Pe regime. The front of the probe is at $\theta = 0$ and the back is $\theta = \pm\pi$. Parameters are $\gamma = 1, Pe_s = 10, a/R_c = 0.8$ and $Pe = 0.1$.

sistent with the micromechanical analysis. The behavior is reversed in the absence of the probe disturbance with more ABPs pushing in the front than in the back.

5.8 Concluding remarks

In this Chapter we have considered the particle-tracking microrheology of an active colloidal suspension consisting of active Brownian spheres. The tracked particle, i.e., probe, is a passive colloidal sphere. When the probe is held fixed in an active suspension, the microstructure is isotropic but not in a thermodynamic equilibrium. Because active particles self-propel, they accumulate at no-flux boundaries. In the context of microrheology when the probe is stationary, the number density at contact is higher than that in the bulk, far from the probe. Nevertheless, this isotropic state of active suspensions does not give rise to a net force on the probe, only an elevated osmotic pressure at contact compared to that in the bulk (Yan and Brady 2015b). When the probe has a nonzero speed, the suspension microstructure is no longer isotropic, even for passive suspensions. Averaging the external force over Brownian fluctuations allows us to define a microviscosity similar to that in a passive suspension. By varying the prescribed speed of a CV probe, one can distort the suspension microstructure slightly ($Pe \ll 1$) or considerably ($Pe \gg 1$) from the isotropic steady state.

In the absence of hydrodynamic interactions, the microrheological response of active suspensions originates from the interplay between the suspension activity and the excluded-volume interaction between the probe and the bath ABP. One manifestation of such a nontrivial interaction is the swim-thinning of the zero-forcing microviscosity. As the swim speed of the ABP increases, the zero-forcing microviscosity is lowered: $\eta_0^{\text{micro}} \to 1$ as $Pe_s \to 0$ and $\eta_0^{\text{micro}} \to 1/2$ as $Pe_s \to \infty$. In general, for finite activity, the suspension exhibits a force-thinning behavior similar to that of passive suspensions but with a lowered η_0^{micro}. The high Pe microviscosity of colloidal suspensions does not depend on activity due to the obscuring effect of the rapid advection of the probe. To

One interesting feature to note is that the microviscosity obtained in the successive limits $Pe \to 0$ then $Pe_s \to \infty$ is the same as the limit $Pe \to \infty$ but with Pe_s being finite (or zero). This can be understood by recalling the boundary layer structures in these two limits. For $Pe \to \infty$, there is an advective accumulation boundary layer in the front and an empty wake devoid of particles in the back regardless of activity (provided that the swimming motion is not covarying with the probe speed, i.e., $Pe_s \ll Pe$ as $Pe \to \infty$). On the other hand, in the successive limits by first talking $Pe \to 0$ and then $Pe_s \to \infty$, there is again an accumulation boundary layer (but due to swimming) for orientations pointing into the probe. At contact, there are no particles with orientations pointing away from the probe in the limit $Pe_s \to \infty$. Structurally, these two limits share the behavior that only half of the domain has particles—half of the local orientation space for the first limit and half of the physical space for the second limit. The resulting net asymmetry of the density distribution at contact in both cases are identical and gives rise to the same microviscosity.

By considering the disturbance flow of the hydrodynamic stresslet, we showed that its effect on microviscosity depends on the type of the stresslet. For bath particles that are pullers, we showed that the suspension microviscosity is lowered provided that the number density in the front of the probe is larger than that in the back. On the other hand, the flow due to pushers increases the microviscosity. This interesting result has been observed in the microrheology of active nematics (Foffano et al. 2012). More importantly, this behavior is opposite to the bulk shear rheology of active matter, where the reduction in shear viscosity is only associated with pushers. In shear rheology, this is due to the interaction between activity and the applied shear flow (single particle). For microrheology, the reduction results from the interplay between the activity, volume exclusion (two-particle interaction), and the additional effect of the flow.

Finally, we considered the disturbance flow due to the translating probe while treating ABPs as point particles that do not disturb the fluid. In this case, the combination of reorientation by vorticity and swimming allows the ABPs to be transported to the back of the probe, which leads to a negative microviscosity. This mechanism for reduced microviscosity relies on the self-propulsion of the ABPs, not the nature of the stresslet in contrast to the disturbance due to the ABPs.

It is also important to note that the negative shear viscosity relies on the nonspherical shape of the active particle. In microrheology, negative microviscosity can be observed for spherical particles as we have shown here. These differences between bulk rheology and microrheology imply that care must be taken when extrapolating the results of bulk rheology to microrheology and vice versa in the study of active matter.

To conclude, we have shown that in the absence of hydrodynamic interactions the microviscosity of active suspensions are always positive. In particular, the swim-thinning in the low-Pe limit at most can reduce the microviscosity by $1/2$, which is still positive. When some hydrodynamic effects are included, however, a negative microviscosity can be obtained. This suggests that the existence of a negative microviscosity is the result of hydrodynamic interactions between the probe and the active bath particles. In the present study, hydrodynamic interactions are only partially accounted for and the effect of full hydrodynamic interactions on the microrheology of active suspensions will be considered in a future study.

5.9 Appendix: Orientational moments for a slow probe

Though in the main text the full Smoluchowski equation is solved, it is useful to examine the symmetries of the orientational moments in the slow probe limit. The zeroth moment of equation (5.25) gives the governing equation for the $O(1)$ number density, which reads

$$\nabla_r \cdot (Pe_s \boldsymbol{m}_0 - \nabla_r n_0) = 0, \tag{5.79}$$

$$\boldsymbol{n} \cdot (Pe_s \boldsymbol{m}_0 - \nabla_r n_0) = 0 \quad \text{at} \quad r = 1, \tag{5.80}$$

$$n_0 \to 1 \quad \text{as} \quad r \to \infty. \tag{5.81}$$

Here, $n_0 = \int g_0 d\boldsymbol{q}$ is the number density and $\boldsymbol{m}_0 = \int g_0 \boldsymbol{q} d\boldsymbol{q}$ is the polar order when the probe is fixed. The polar order satisfies

$$\nabla_r \cdot \left[Pe_s \left(\boldsymbol{Q}_0 + \frac{1}{d} n_0 \boldsymbol{I} \right) - \nabla_r \boldsymbol{m}_0 \right] + (d-1)\gamma^2 \boldsymbol{m}_0 = 0, \tag{5.82}$$

$$\boldsymbol{n} \cdot \left[Pe_s \left(\boldsymbol{Q}_0 + \frac{1}{d} n_0 \boldsymbol{I} \right) - \nabla_r \boldsymbol{m}_0 \right] = \boldsymbol{0} \quad \text{at} \quad r = 1, \tag{5.83}$$

where $\boldsymbol{Q}_0 = \int (\boldsymbol{q}\boldsymbol{q} - \boldsymbol{I}/d) g_0 d\boldsymbol{q}$ is the nematic field.

The spherical symmetry of the domain dictates that (Yan and Brady 2015b)

$$n_0(\boldsymbol{r}) = p_0(r),\ \boldsymbol{m}_0(\boldsymbol{r}) = \boldsymbol{r} p_1(r),\ \boldsymbol{Q}_0(\boldsymbol{r}) = \left(\boldsymbol{r}\boldsymbol{r} - \frac{1}{d} r^2 \boldsymbol{I} \right) p_2(r), \tag{5.84}$$

where p_0-p_2 are scalar functions of the radial coordinate. One cannot solve equation (5.79) without knowledge of the polar order $\boldsymbol{m}_0$. In fact, this hierarchy of orientational moments continue indefinitely. A truncation or closure is often used to close the set of moment equations. For example, the solutions to n_0 and $\boldsymbol{m}_0$ are obtained by Yan and Brady (2015b) with the closure $\boldsymbol{Q}_0 = \boldsymbol{0}$.

As a reference, we proceed to present the solution when $\boldsymbol{Q}_0$ is included and a closure at the next order is used. The third orientational moment in 3D is

$$\tilde{\boldsymbol{B}}_0 = \int \boldsymbol{q}\boldsymbol{q}\boldsymbol{q} g_0 d\boldsymbol{q} = \boldsymbol{B}_0 + \boldsymbol{\alpha} \cdot \boldsymbol{m}_0 / 5, \tag{5.85}$$

where $\alpha_{ijkl} = \delta_{ij}\delta_{kl} + \delta_{il}\delta_{jk} + \delta_{ik}\delta_{jl}$ is an isotropic fourth order tensor. Assuming that $\boldsymbol{B}_0 = \boldsymbol{0}$, one can show that the general solutions are given by

$$p_0(r) = C_0 + \sum_{k=1}^{2} C_k \frac{1}{r} \exp\left[-\lambda_k (r-1) \right] + \frac{C_3}{r}, \tag{5.86}$$

$$p_1(r) = -\sum_{k=1}^{2} \frac{C_k}{Pe_s} \left(\frac{\lambda_k}{r^2} + \frac{1}{r^3} \right) \exp\left[-\lambda_k (r-1) \right] + \frac{C_3 Pe_s}{6\gamma^2 r^3}, \tag{5.87}$$

$$\begin{aligned} p_2(r) = {} & \sum_{k=1}^{2} C_k \frac{3\lambda_k^2 - 6\gamma^2 - Pe_s^2}{2Pe_s^2} \left(\frac{1}{r^3} + \frac{3}{\lambda_k r^4} + \frac{3}{\lambda_k^2 r^5} \right) \exp\left[-\lambda_k (r-1) \right] \\ & + \frac{C_3 Pe_s^2}{30\gamma^4 r^5}, \end{aligned} \tag{5.88}$$

where

$$\lambda_1 = \frac{\sqrt{3Pe_s^2 + 40\gamma^2 + \sqrt{9Pe_s^4 + 40\gamma^2 Pe_s^2 + 400\gamma^4}}}{\sqrt{10}}, \tag{5.89}$$

$$\lambda_2 = \frac{\sqrt{3Pe_s^2 + 40\gamma^2 - \sqrt{9Pe_s^4 + 40\gamma^2 Pe_s^2 + 400\gamma^4}}}{\sqrt{10}}. \tag{5.90}$$

The no-flux condition of n_0 means that $C_3 = 0$ and the far-field condition gives $C_0 = 1$. The other two integration constants C_1 and C_2 can be obtained from the no-flux conditions for $\boldsymbol{m}_0$ and $\boldsymbol{Q}_0$.

It is worthwhile to compare the results obtained with $\boldsymbol{Q}_0 = \boldsymbol{0}$ and $\boldsymbol{B}_0 = \boldsymbol{0}$. In particular, for $Pe_s \gg 1$ and $\gamma = O(1)$, the $\boldsymbol{Q}_0$ closure predicts the correct scaling of the number density at contact $[n_c = O(Pe_s)]$ while the $\boldsymbol{B}_0$ closure gives a finite density. This comparison implies that a higher order closure is not necessarily more accurate.

The zeroth moment of g_1 satisfies

$$\nabla_r \cdot (Pe_s \boldsymbol{m}_1 - \nabla_r n_1) = \hat{\boldsymbol{U}}_1 \cdot \nabla_r n_0, \tag{5.91}$$

$$\boldsymbol{n} \cdot (Pe_s \boldsymbol{m}_1 - \nabla_r n_1) = \boldsymbol{n} \cdot \hat{\boldsymbol{U}}_1 n_0 \quad \text{at} \quad r = 1, \tag{5.92}$$

$$n_1 \to 0 \quad \text{as} \quad r \to \infty, \tag{5.93}$$

where n_1 and $\boldsymbol{m}_1$ are similarly defined but for g_1; they are the leading-order disturbances to n_0 and $\boldsymbol{m}_0$, respectively, due to the weak probe motion. With (5.84), it is straightforward to see that the $O(Pe)$ moments satisfy

$$n_1(\boldsymbol{r}) = \hat{\boldsymbol{U}}_1 \cdot \boldsymbol{r} p_3(r), \tag{5.94}$$

$$\boldsymbol{m}_1(\boldsymbol{r}) = \hat{\boldsymbol{U}}_1 p_4(r) + \hat{\boldsymbol{U}}_1 \cdot \boldsymbol{rr} p_5(r), \tag{5.95}$$

where p_3-p_5 are unknown scalar radial functions. This is a manifestation of the so-called linear response in which the disturbance fields are proportional to the vector $\boldsymbol{U}_1$—the weak driving force.

In 2D, from (5.21), we have $\eta_0^{\text{micro}} = p_3(1)$. Similarly in 3D, (5.20) gives $\eta_0^{\text{micro}} = 2p_3(1)$. In other words, the zero-forcing microviscosity is determined from the contact value of p_3.

5.10 Appendix: The slow-swimming limit

In the slow-swimming limit, characterized by $Pe_s \ll 1$, the probability distribution of bath colloids can be expanded as

$$g(\boldsymbol{r}, \boldsymbol{q}) = g_0(\boldsymbol{r}, \boldsymbol{q}) + Pe_s g_1(\boldsymbol{r}, \boldsymbol{q}) + Pe_s^2 g_2(\boldsymbol{r}, \boldsymbol{q}) + \cdots. \tag{5.96}$$

Inserting the series into (5.13), (5.14), and (5.15), we can solve the problem order by order.

At $O(1)$, the bath colloids are not self-propelling and the governing equations in the vector form are

$$Pe\hat{\boldsymbol{U}}_1 \cdot \nabla_r n_0 + \nabla_r^2 n_0 = 0, \tag{5.97}$$

$$Pe\boldsymbol{n} \cdot \hat{\boldsymbol{U}}_1 n_0 + \boldsymbol{n} \cdot \nabla_r n_0 = 0 \quad \text{at} \quad r = 1, \tag{5.98}$$

$$n_0 \to 1 \quad \text{as} \quad r \to \infty, \tag{5.99}$$

where $n_0(\boldsymbol{r}) = \int g_0 d\boldsymbol{q}$ and $g_0 = n_0/\Omega_d$. Clearly, the equations at $O(1)$ govern the CV microrheology of passive colloids (Squires and Brady 2005).

The problem at $O(Pe_s^k)$ $(k = 1, 2, ...)$ satisfies

$$\nabla_r \cdot \left(Pe\hat{\boldsymbol{U}}_1 g_k + \nabla_r g_k\right) + \gamma^2 \nabla_R^2 g_1 = \boldsymbol{q} \cdot \nabla_r g_{k-1}, \tag{5.100}$$

$$\boldsymbol{n} \cdot \left(Pe\hat{\boldsymbol{U}}_1 g_k + \nabla_r g_k\right) = \boldsymbol{n} \cdot \boldsymbol{q} g_{k-1} \quad \text{at} \quad r = 1, \tag{5.101}$$

$$g_k \to 0 \quad \text{as} \quad r \to \infty. \tag{5.102}$$

One can see that the solution at $O(Pe_s)$ has the structure $g_1(\boldsymbol{r}, \boldsymbol{q}) = \boldsymbol{q} \cdot \boldsymbol{G}_1(\boldsymbol{r})$, where $\boldsymbol{G}_1(\boldsymbol{r})$ is a vector-valued function of $\boldsymbol{r}$. This means that the number density at $O(Pe_s)$ vanishes, $n_1 = \int g_1 d\boldsymbol{q} \equiv 0$. We note that the polar order ($\boldsymbol{m}_1 = \int \boldsymbol{q} g_1 d\boldsymbol{q}$) is nonzero and is responsible for driving a density distribution at the next order $[O(Pe_s^2)]$. This structure ultimately leads to the fact that

$$\eta^{\text{micro}}(Pe, Pe_s, \gamma) = \eta^{\text{micro}}_{\text{passive}} + Pe_s^2 \eta_2^{\text{micro}} + \cdots. \tag{5.103}$$

In other words, the swim-thinning discussed in the main text occurs at $O(Pe_s^2)$.

Chapter 6

MICROVISCOELASTICITY

6.1 Introduction

In the previous chapter, we have examined the micro-viscous response of active colloidal suspensions. This is achieved using particle-tracking microrheology in which a probe particle is pulled through the suspension at a constant velocity. In the context of bio-microrheology, the material under examination is often complex and exhibit viscoelastic behavior. To probe the viscoelastic response of materials at the microscale, the probe is often driven by an oscillatory motion (Weihs et al. 2006; Berret 2016).

From a theoretical perspective, the oscillatory microrheology of passive colloidal suspensions have been considered by Khair and Brady (2005) and Swan et al. (2014). In this chapter, we extend this analysis to active colloidal suspensions.

6.2 Theoretical framework

Consider a collection of N neutrally buoyant spherical active Brownian particles of radii b dispersed in a Newtonian solvent with viscosity η and density ρ. A probe particle of radius a is placed into the active suspension in order to measure its rheological response. The kinematics of the probe is prescribed to be oscillatory such that its instantaneous velocity at time t is given by

$$\tilde{\boldsymbol{U}}_1(t) = \boldsymbol{U}_1 Re\left[e^{i\omega t}\right], \tag{6.1}$$

where $\boldsymbol{U}_1$ is a constant vector, i ($i^2 = -1$) is the imaginary unit, ω is frequency of oscillation, and Re denotes the real part of a complex quantity. In addition to requiring the Reynolds number to be small, we assume that the Strouhal number $St = \rho\omega b^2/\eta \ll 1$ such that the fluid mechanics is described by the quasi-steady Stokes equations.

Assuming that the suspension is sufficiently dilute, we only consider the interaction between the probe and one of the bath particles. Following previous work on the microrheology of passive (Squires and Brady 2005) and active suspensions (Burkholder and Brady 2019; 2020), we neglect hydrodynamic interactions and instead focus on the steric interaction between the probe and one ABP. These

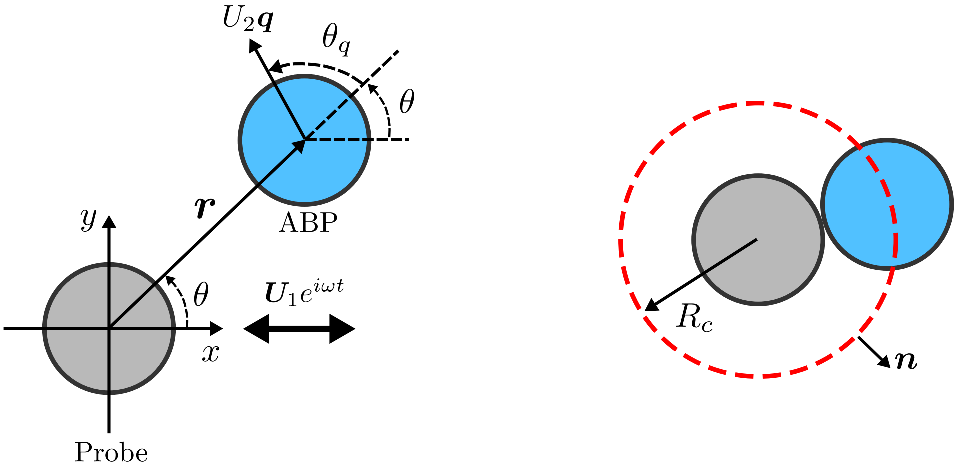

Figure 6.1: Schematic of a probe particle oscillating with the velocity $\boldsymbol{U}_1 e^{i\omega t}$ and an active Brownian bath particle in 2D. The ABP swims with a constant speed U_2 in a direction $\boldsymbol{q}$. The radius of contact is R_c and $\boldsymbol{n}$ is the unit normal vector pointing from the probe into the ABP suspension.

assumptions lead to arguably the simplest model for the microrheology of active suspensions, where insightful analytical progress can be made. In the co-moving frame attached to the probe, the suspension microstructure $g(\boldsymbol{r}, \boldsymbol{q}, t)$ is governed by the Smoluchowski equation (Burkholder and Brady 2020):

$$\frac{\partial g(\boldsymbol{r}, \boldsymbol{q}, t)}{\partial t} + \nabla_r \cdot \left(\boldsymbol{j}_2^T - \boldsymbol{j}_1^T \right) + \nabla_R \cdot \boldsymbol{j}_2^R = 0, \tag{6.2}$$

where $P_{1/1}(\boldsymbol{r}, \boldsymbol{q}, t) = n^\infty g(\boldsymbol{r}, \boldsymbol{q}, t)$ is the conditional probability of finding an ABP at a separation $\boldsymbol{r}$ from the probe with orientation $\boldsymbol{q}$ at time t and n^∞ is the undisturbed number density of the suspension.

In the absence of hydrodynamic interactions between the probe and the ABP, the translational and rotational fluxes in the Smoluchowski equation (6.2), respectively, are

$$\boldsymbol{j}_2^T - \boldsymbol{j}_1^T = \left(U_2 \boldsymbol{q} - \tilde{\boldsymbol{U}}_1 \right) g - D_2 \nabla_r g, \tag{6.3}$$

$$\boldsymbol{j}_2^R = -D_R \nabla_R g. \tag{6.4}$$

At the surface of contact ($|\boldsymbol{r}| = R_c = a + b$), the relative translational flux of particle centers vanishes:

$$\boldsymbol{n} \cdot \left(\boldsymbol{j}_2^T - \boldsymbol{j}_1^T \right) = 0, \tag{6.5}$$

where $\boldsymbol{n}$ is the unit normal vector as shown in figure 6.1. In the far field, the suspension microstructure is undisturbed, giving

$$g \longrightarrow \frac{1}{\Omega_d} \quad \text{as} \quad r \longrightarrow \infty, \tag{6.6}$$

where Ω_d is the total solid angle of the orientation space in d dimensions.

A dimensional analysis reveals five timescales that govern the oscillatory microrheology of active suspensions: (1) the diffusive timescale $\tau_D = R_c^2/D_2$, (2) the swim timescale $\tau_s = R_c/U_2$, (3) the advective timescale $\tau_{\text{adv}} = R_c/U_1$, (4) the reorientation time $\tau_R = 1/D_R$, and (5) the timescale of oscillation $1/\omega$. Four dimensionless parameters can be defined by comparing various timescales; these are given by

$$Pe_s = \frac{\tau_D}{\tau_s} = \frac{U_2 R_c}{D_2}, \; \gamma = \left(\frac{\tau_D}{\tau_R}\right)^{1/2} = \frac{R_c}{\delta}, \; Pe = \frac{\tau_D}{\tau_{\text{adv}}} = \frac{U_1 R_c}{D_2}, \; \chi = \omega \tau_D. \tag{6.7}$$

where $\delta = \sqrt{D_2 \tau_R}$ is the microscopic diffusive step taken by the ABP on the reorientation timescale τ_R. The first parameter in the above is referred to as the swim Péclet number, Pe is the Péclet number of the probe, γ is a measure of the reorientation time compared to τ_D, and χ is the comparison between the oscillation timescale and τ_D.

By scaling lengths by R_c and time by τ_D, the resulting dimensionless Smoluchowski equation is

$$\frac{\partial g}{\partial t} + \nabla_r \cdot \left[\left(Pe_s \boldsymbol{q} - Pe \hat{\boldsymbol{U}}_1 \cos(\chi t) \right) g - \nabla_r g \right] - \gamma^2 \nabla_R^2 g = 0. \tag{6.8}$$

The no-flux condition (6.5) becomes

$$\boldsymbol{n} \cdot \left[\left(Pe_s \boldsymbol{q} - Pe \hat{\boldsymbol{U}}_1 \cos(\chi t) \right) g - \nabla_r g \right] = 0 \quad \text{at} \quad r = 1, \tag{6.9}$$

and the far-field condition (6.6) remains unchanged.

To characterize the microviscoelastic response of the suspension in the dilute limit, a microviscosity can be defined. In 2D, this is given by

$$\eta^{\text{micro}} = \frac{\Delta \eta}{\phi \eta} \frac{\alpha}{(1+\alpha)^2} = \frac{1}{\pi Pe} \hat{\boldsymbol{U}}_1 \cdot \oint_{r=1} \boldsymbol{n} n dS, \tag{6.10}$$

where $\phi = n^\infty \pi b^2$ is the area fraction, $\alpha = a/b$ is the radius ratio between the probe and the bath particle, and $n = \int g d\boldsymbol{q}$ is the number density. When the probe has an oscillatory motion, the probability distribution g (therefore the microviscosity) is a function of time t. A general time-periodic oscillation can be decomposed into an infinite sum of individual Fourier modes. Here, we consider the microrheological behavior under a single mode oscillation.

For steady-probe microrheology, we have shown that the viscous response of active suspensions exhibit a swim-thinning behavior. Compared to that of passive suspensions, the microviscosity of active suspensions is lowered due to their swimming motion. Because the swimming motion is obscured by a fast probe, swim-thinning is most significant in the slow-probe regime and vanishes in the fast-probe limit. For an oscillating probe as we consider in this chapter, the swimming motion is similarly obscured in the fast-probe limit and the microviscoelastic response becomes the same as that of passive suspensions. To highlight the difference between passive and active suspensions, we therefore focus on small amplitude oscillations in this chapter.

6.3 Small amplitude oscillations

When the amplitude of oscillation is small but the frequency of oscillation is arbitrary, characterized by $Pe \ll 1$, the suspension is slightly perturbed from its isotropic steady state in which the probe is held fixed ($Pe \equiv 0$). In this low-Pe limit, the suspension microstructure at long times admits a perturbation expansion of the form

$$g(\boldsymbol{r},\boldsymbol{q},t) = g_0(\boldsymbol{r},\boldsymbol{q}) + Pe\,\tilde{g}_1(\boldsymbol{r},\boldsymbol{q})e^{i\chi t} + \cdots, \tag{6.11}$$

where at $O(1)$ the probe is not moving and g_0 is the microstructure of ABPs outside a fixed sphere. We note that, in the above to obtain the $O(Pe)$ microstructure due to the oscillation $\cos(\chi t)$, the real part of the solution should be taken. In terms of Pe, the leading-order deformation of the microstructure is in the linear response regime. Inserting equation (6.11) into the Smoluchowski equation (6.8) and the no-flux condition (6.9), we obtain the governing equations at $O(Pe)$ as

$$i\chi\tilde{g}_1 + \nabla_r\cdot(Pe_s\boldsymbol{q}\tilde{g}_1 - \nabla\tilde{g}_1) - \gamma^2\nabla_R^2\tilde{g}_1 = \hat{\boldsymbol{U}}_1\cdot\nabla_r g_0, \tag{6.12}$$

$$\boldsymbol{n}\cdot(Pe_s\boldsymbol{q}\tilde{g}_1 - \nabla_r\tilde{g}_1) = \boldsymbol{n}\cdot\hat{\boldsymbol{U}}_1 g_0 \quad \text{at} \quad r = 1, \tag{6.13}$$

$$\tilde{g}_1 \to 0 \quad \text{as} \quad r \to \infty. \tag{6.14}$$

Obviously, the only difference between (6.12) and that obtained for a steady-probe is the presence of the term $i\chi\tilde{g}_1$, which drives a frequency response.

From (6.10) and (6.11), the microviscosity can be obtained order by order. The $O(Pe)$ microstructure gives rise to the $O(1)$ microviscosity:

$$\eta_0^{\text{micro}} = \lim_{Pe\to 0}\eta^{\text{micro}} = Re\left[e^{i\chi t}\tilde{\eta}_0\right], \tag{6.15}$$

where we have defined the zero-forcing complex microviscosity (in 2D)

$$\tilde{\eta}_0 = \frac{1}{\pi}\hat{\boldsymbol{U}}_1 \cdot \oint_{r=1} \boldsymbol{n}\tilde{n}_1 dS, \tag{6.16}$$

and

$$\tilde{n}_1 = \int \tilde{g}_1 d\boldsymbol{q} \tag{6.17}$$

is the "complex" number density at $O(Pe)$.

It is useful to separate $\tilde{\eta}_0$ into its real and imaginary parts via the definition

$$\tilde{\eta}_0 = \eta' - i\eta'', \tag{6.18}$$

where $\eta' = Re\left[\tilde{\eta}_0\right]$ is the real part and $\eta'' = -Im\left[\tilde{\eta}_0\right]$ is the imaginary part. The real part corresponds to viscous dissipation while the imaginary part corresponds to elasticity. To see this more clearly, consider the probe motion given by $Re\left[e^{i\chi t}\right] = \cos(\chi t)$, which in the small amplitude limit leads to a microviscosity of the form $\eta_0^{\text{micro}} = \cos(\chi t)\eta' + \sin(\chi t)\eta''$. Notice that $\eta'\cos(\chi t)$ is the component that is in-phase (i.e., viscous) with the driving motion while $\eta'\cos(\chi t)$ is the out-of-phase component (elastic).

6.3.1 The governing equations in 2D

It is convenient to define the swim orientation angle relative to the radial basis vector $\boldsymbol{e}_r$ such that $\boldsymbol{q} = \cos\theta_q \boldsymbol{e}_r + \sin\theta_q \boldsymbol{e}_\theta$, where $\boldsymbol{e}_r = \cos\theta \boldsymbol{e}_x + \sin\theta \boldsymbol{e}_y$ and $\boldsymbol{e}_\theta = \boldsymbol{e}_z \times \boldsymbol{e}_r$. Furthermore, we take $\hat{\boldsymbol{U}}_1 = \boldsymbol{e}_x$ so that the oscillation is along the x axis of the Cartesian coordinate system (see figure 6.1). In the (r, θ, θ_q) coordinate system, equation (6.12) can be written explicitly as

$$\begin{aligned} &i\chi\tilde{g}_1 + Pe_s\cos\theta_q\frac{\partial\tilde{g}_1}{\partial r} + Pe_s\frac{\sin\theta_q}{r}\left(\frac{\partial\tilde{g}_1}{\partial\theta} - \frac{\partial\tilde{g}_1}{\partial\theta_q}\right) \\ &- \frac{1}{r}\frac{\partial}{\partial r}r\frac{\partial\tilde{g}_1}{\partial r} - \frac{1}{r^2}\left(\frac{\partial^2\tilde{g}_1}{\partial\theta^2} - 2\frac{\partial^2\tilde{g}_1}{\partial\theta\partial\theta_q} + \frac{\partial^2\tilde{g}_1}{\partial\theta_q^2}\right) \\ &- \gamma^2\frac{\partial^2\tilde{g}_1}{\partial\theta_q^2} = \cos\theta\frac{\partial g_0}{\partial r} - \frac{\sin\theta}{r}\left(\frac{\partial g_0}{\partial\theta} - \frac{\partial g_0}{\partial\theta_q}\right), \end{aligned} \tag{6.19}$$

and the boundary condition (6.13) becomes

$$Pe_s\cos\theta_q\tilde{g}_1 - \frac{\partial\tilde{g}_1}{\partial r} = \cos\theta g_0 \quad \text{at} \quad r = 1. \tag{6.20}$$

As shown in the previous chapter for the microrheology using a steady probe ($\chi \equiv 0$), the structure of the equations at $O(Pe)$ allows us to decompose the solution as

$$\tilde{g}_1(r, \theta, \theta_q) = f_1(r, \theta_q)\cos\theta + f_2(r, \theta_q)\sin\theta. \tag{6.21}$$

The solution to g_0 has been obtained in the previous chapter, which is needed to calculate the $O(Pe)$ microstructure $\tilde{g}_1$ as can be seen from equation (6.19). Using truncated Fourier series to represent f_1 and f_2 allows us to obtain a set of coupled ordinary differential equations (ODEs) for their radially-dependent Fourier modes. These ODEs are then solved numerically using a Laguerre collocation method (see section 6.5 for the details on numerics).

6.3.2 The high-frequency limit

In the limit $\chi \to \infty$, far from the probe the suspension is not disturbed, $\tilde{g}_1 = 0$. Near contact with the probe, a boundary layer emerges, which is determined by a balance between the fast oscillation $i\chi\tilde{g}_1$ and diffusion $-\partial^2\tilde{g}_1/\partial r^2$. This balance determines the boundary layer thickness and the stretched coordinate $\rho = (r-1)\chi^{1/2}$. In the boundary layer, the leading-order solution is $O(\chi^{-1/2})$:

$$\tilde{g}_1 = \chi^{-1/2} h + \cdots, \tag{6.22}$$

where h is governed by

$$ih - \frac{\partial^2 h}{\partial \rho^2} = 0, \tag{6.23}$$

$$-\frac{\partial h}{\partial \rho} = \boldsymbol{e}_r \cdot \hat{\boldsymbol{U}}_1 g_0 \quad \text{at} \quad \rho = 0, \tag{6.24}$$

$$h \to 0 \quad \text{as} \quad \rho \to \infty. \tag{6.25}$$

Here, as seen in (6.24), h is driven by the radial advective flux of the g_0 field at contact. One can show that the solution is

$$h = \frac{1-i}{\sqrt{2}} \boldsymbol{e}_r \cdot \hat{\boldsymbol{U}}_1 \exp\left(-\frac{(1+i)\rho}{\sqrt{2}}\right) g_0(|\boldsymbol{r}| = 1, \boldsymbol{q}). \tag{6.26}$$

With this, the zero-forcing microviscosity defined by equation (6.16) becomes

$$\tilde{\eta}_0 = \frac{1-i}{\sqrt{2\chi}} n_0(r=1) + o(\frac{1}{\sqrt{\chi}}) \quad \text{as} \quad \chi \to \infty, \tag{6.27}$$

where $n_0(r=1) = \int g_0(r=1) d\boldsymbol{q}$ is the number density at contact when the probe is held fixed.

6.4 The zero-forcing microviscoelasticity

In figure 6.2, we plot the zero-forcing microviscoelasticity as a function of the dimensionless frequency χ. In the small χ limit, the active suspension is viscous

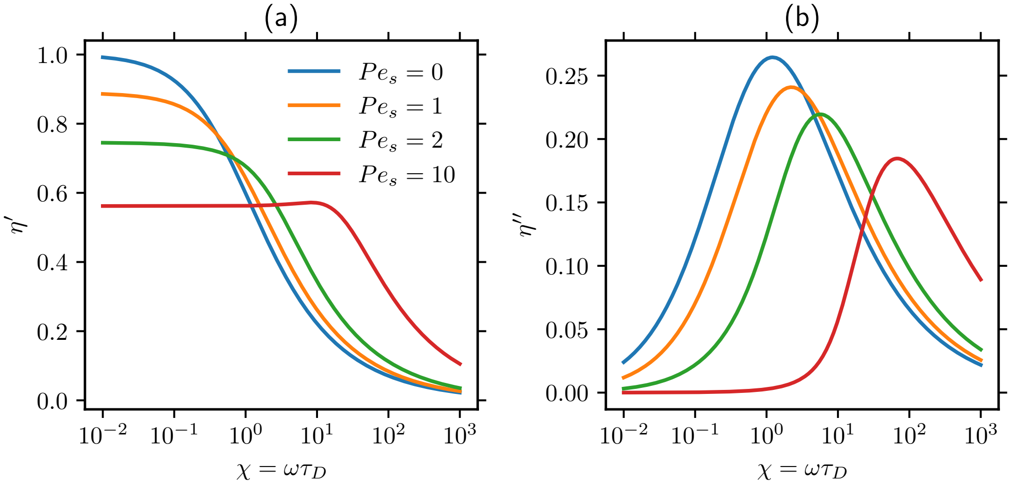

Figure 6.2: Plot of (a) the viscous part (η') and (b) the elastic part (η'') of the zero-forcing microviscosity as a function of the dimensionless oscillation frequency $\chi = \omega\tau_D$ for several values of $Pe_s = U_2 R_c/D_2$. The results are obtained from solving the governing equations numerically as discussed in section 6.5. For all results shown, $\gamma = 1$. Both panels share the same legends as shown in (a).

and the viscous part of the microviscosity exhibits a swim-thinning behavior as discussed in the previous chapter. As the frequency increases, the viscous part of the microviscosity decreases. The elastic part of the microviscosity exhibits a non-monotonic behavior as a function of χ.

In the large χ limit, both the viscous and the elastic part of the microviscosity decay as $\chi^{-1/2}$ [see equation (6.27)]. This behavior is highlighted in figure 6.3 in which $\eta'/n_0(r=1)$ and $\eta''/n_0(r=1)$ are plotted as a function of χ.

6.5 Appendix: Numerical solution to f_1 and f_2

In this section, we present the governing equations for f_1 and f_2 and their discretization used for the numerical solution. Inserting equation (6.21) into (6.19) leads to the following coupled equations:

$$\begin{aligned} &i\chi f_1 + Pe_s \cos\theta_q \frac{\partial f_1}{\partial r} + Pe_s \frac{\sin\theta_q}{r}\left(f_2 - \frac{\partial f_1}{\partial \theta_q}\right) \\ &- \frac{1}{r}\frac{\partial}{\partial r} r \frac{\partial f_1}{\partial r} - \frac{1}{r^2}\left(-f_1 - 2\frac{\partial f_2}{\partial \theta_q} + \frac{\partial^2 f_1}{\partial \theta_q^2}\right) - \gamma^2 \frac{\partial^2 f_1}{\partial \theta_q^2} = \frac{\partial g_0}{\partial r}, \end{aligned} \tag{6.28}$$

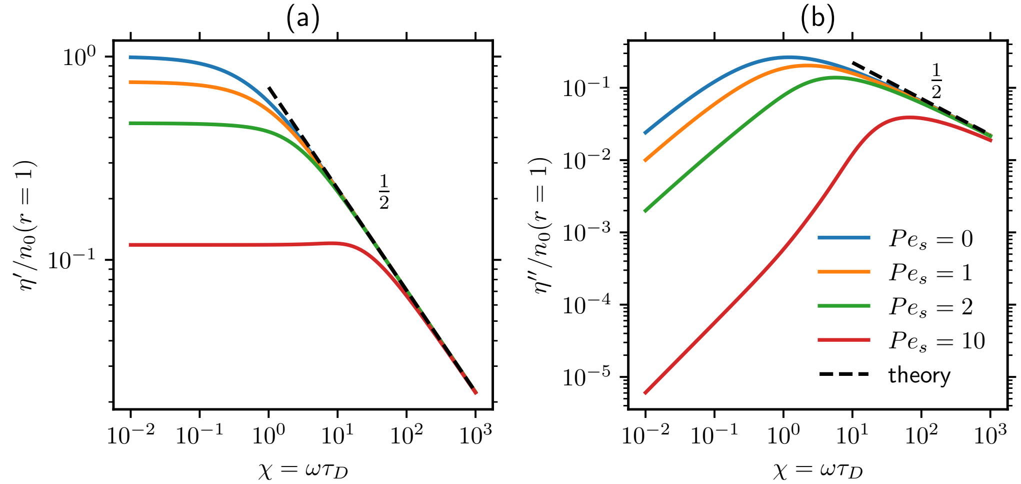

Figure 6.3: Plot of (a) the viscous part (η') and (b) the elastic part (η'') of the zero-forcing microviscosity as a function of the dimensionless oscillation frequency $\chi = \omega\tau_D$ for several values of $Pe_s = U_2R_c/D_2$. The results are obtained from solving the governing equations numerically as discussed in section 6.5. For all results shown, $\gamma = 1$.

$$\begin{aligned} &i\chi f_2 + Pe_s \cos\theta_q \frac{\partial f_2}{\partial r} + Pe_s \frac{\sin\theta_q}{r}\left(-f_1 - \frac{\partial f_2}{\partial \theta_q}\right) \\ &- \frac{1}{r}\frac{\partial}{\partial r} r \frac{\partial f_2}{\partial r} - \frac{1}{r^2}\left(-f_2 + 2\frac{\partial f_2}{\partial \theta_q} + \frac{\partial^2 f_2}{\partial \theta_q^2}\right) - \gamma^2 \frac{\partial^2 f_2}{\partial \theta_q^2} = \frac{1}{r}\frac{\partial g_0}{\partial \theta_q}. \end{aligned} \tag{6.29}$$

Similarly, the boundary condition (6.20) decomposes into

$$Pe_s \cos\theta_q f_1 - \frac{\partial f_1}{\partial r} = g_0 \quad \text{at} \quad r = 1, \tag{6.30}$$

$$Pe_s \cos\theta_q f_2 - \frac{\partial f_2}{\partial r} = 0 \quad \text{at} \quad r = 1. \tag{6.31}$$

The far-field condition is $f_1, f_2 \to 0$ as $r \to \infty$.

Following the previous chapter, we resolve the orientational operators explicitly using a truncated Fourier series, i.e.,

$$f_1(r, \theta_q) \approx \sum_{k=-K}^{K} C_{1,k}(r) e^{ik\theta_q}, \tag{6.32}$$

$$f_2(r, \theta_q) \approx \sum_{k=-K}^{K} C_{2,k}(r) e^{ik\theta_q}, \tag{6.33}$$

where K is a positive integer denoting the number of Fourier modes used in the truncated series. These expansions allow us to reduce equations (6.28) and (6.29) to a set of coupled ODEs in terms of the Fourier modes $C_{1,k}(r)$ and $C_{2,k}(r)$. The resulting ODEs are similar to those obtained in the previous chapter for the case of steady-probe microrheology except the addition of the frequency terms (e.g., $i\chi f_1$). We solve these ODEs using a spectral collocation method of the Laguerre functions, which forms an orthogonal basis in the natural domain of $[0,+\infty)$. Further details of the numerics are given in the previous chapter.

Chapter 7

ACTIVITY-INDUCED PROPULSION OF A VESICLE

Modern biomedical applications such as targeted drug delivery require a delivery system capable of enhanced transport beyond that of passive Brownian diffusion. In this work an osmotic mechanism for the propulsion of a vesicle immersed in a viscous fluid is proposed. By maintaining a steady-state solute gradient inside the vesicle, a seepage flow of the solvent (e.g., water) across the semipermeable membrane is generated which in turn propels the vesicle. We develop a theoretical model for this vesicle-solute system in which the seepage flow is described by a Darcy flow. Using the reciprocal theorem for Stokes flow it is shown that the seepage velocity at the exterior surface of the vesicle generates a thrust force which is balanced by the hydrodynamic drag such that there is no net force on the vesicle. We characterize the motility of the vesicle in relation to the concentration distribution of the solute confined inside the vesicle. Any osmotic solute is able to propel the vesicle so long as a concentration gradient is present. In the present work, we propose active Brownian particles (ABPs) as a solute. To maintain a symmetry-breaking concentration gradient, we consider ABPs with spatially varying swim speed and ABPs with constant properties but under the influence of an orienting field. In particular, it is shown that at high activity the vesicle velocity is $\boldsymbol{U} \sim [K_\perp/(\eta_e \ell_m)] \int \Pi_0^{\text{swim}} \boldsymbol{n} d\Omega$, where Π_0^{swim} is the swim pressure just outside the thin accumulation boundary layer on the vesicle interior surface, $\boldsymbol{n}$ is the unit normal vector of the vesicle boundary, $K_\perp$ is the membrane permeability, η_e is the viscosity of the solvent, and ℓ_m is the membrane thickness.

7.1 Introduction

Targeted drug delivery is an important goal of modern nanomedicine. Recent advances in the design, manufacture and control of nanocarriers have enabled the delivery of such cargoes into single cells for the purpose of imaging, diagnostics and therapeutics (West and Halas 2003; Gao et al. 2005; Rao et al. 2007; Torchilin 2012). Commonly used pharmaceutical nanocarriers include liposomes, micelles, nanoemulsions, polymeric nanoparticles, and many others (Torchilin 2012). In particular, liposomes have become an important class of carriers for the encapsulation and transport of medical cargoes because of several advantages including their biocompatibility with human cells, and the improved solubility of drugs and versatility for chemical targeting (Pattni et al. 2015), among others.

A liposome is a vesicle that has an aqueous solution core encircled by a hydrophobic membrane (lipid bilayer); hydrophilic solutes dissolved in the core cannot readily pass through the membrane while lipophilic chemicals tend to associate with the bilayer. As a result, a liposome can be loaded with hydrophilic, lipophilic and/or amphiphilic cargoes in the context of drug delivery. Recently, the Moderna vaccine developed to prevent coronavirus disease 2019 (COVID-19) has utilized a lipid based nanovesicle to encapsulate the mRNA vaccine that encodes the SARS-CoV-2 spike glycoprotein (Jackson et al. 2020).

The liposome-encapsulated medical cargo is transported passively, either via diffusion or advection due to local fluid flow, which limits its ability to overcome biological barriers. To mitigate such limitations of passive drug delivery, active drug delivery platforms using motile microrobots (or microswimmers), either synthetic or biohybrid, have been proposed (Medina-Sánchez et al. 2018; Erkoc et al. 2019; Singh et al. 2019; Bunea and Taboryski 2020). By attaching nanoparticle cargoes to the surface of a motile microswimmer, the delivery system can actively navigate, access regions that are unreachable to passive drug delivery, and be directed to the desired site using chemotaxis or an external magnetic field (Felfoul et al. 2016; Park et al. 2017). Due to self-propulsion of the microswimmer, the effective dispersion of the attached cargo is greatly enhanced, sometimes by a few orders of magnitude, compared to the long-time self diffusivity of the passively-transported cargo (Singh et al. 2017).

Instead of attaching a cargo to the surface of a microswimmer, one can also encapsulate both the cargo and the microswimmer inside the vesicle. Encapsulated microswimmers have been studied by previous works. For example, biological microswimmers and self-propelled Janus particles haven been successfully encapsulated inside engineered giant unilamellar vesicles (GUVs) (Trantidou et al. 2018; Takatori and Sahu 2020; Vutukuri et al. 2020). The encapsulated microswimmer provides the vesicle with enhanced super-diffusive motion mediated through hydrodynamic interactions between the microswimmer and the vesicle provided that the fluid is allowed to pass through the membrane of the vesicle (Marshall and Brady 2021).

In the present work we consider a system that combines the benefits of the vesicle for cargo encapsulation and the self-propulsion of microswimmers for enhanced transport. We propose an alternate model system in which the vesicle is propelled by an osmotic flow that is induced by an actively-maintained concentration gradient of a solute inside the vesicle. This kind of osmotic propulsion has been proposed as an alternate mechanism for tumor cells to migrate under strong confinement, in which case other modes of motility such as contractility is inhibited. Stroka et al. (2014) showed that through physical and biochemical processes, the tumor cell establishes a spatial gradient of solute (ions), which creates a net inflow of water at the cell leading edge and a net outflow at the cell trailing edge. As a result, this water permeation process enables the cell to migrate through narrow channels. We are specifically interested in studying the motility of the vesicle as a result of a prescribed concentration gradient of a solute that is confined inside the vesicle. Because the solute particles are not allowed to pass through the membrane, an osmotic flow of water is generated, which in turn propels the vesicle immersed in water.

The main question we wish to address in this work is: What is the motility of the vesicle system in relation to the concentration gradient of the solute? More interestingly, does the vesicle move in the same or opposite direction of the concentration gradient?

We show by explicit calculation that for a weakly permeable membrane the translational velocity of a rigid spherical vesicle becomes

$$\boldsymbol{U} = \frac{1}{4\pi}\frac{K_\perp}{\eta_e \ell_m}\int_{S^2} \Pi_0^{\text{osmo}} \boldsymbol{n} d\Omega, \tag{7.1}$$

where $\Pi_0^{\text{osmo}} = n^w k_B T$ is the osmotic pressure of the solute at the interior wall, n^w is the local number density of the solute in the absence of internal fluid flow, $k_B T$ is the thermal energy, $K_\perp$ is the membrane permeability, η_e is the viscosity of the solvent (water) and ℓ_m is the thickness of the membrane. In equation (7.1), $\boldsymbol{n}$ is the unit outward normal vector (see figure 7.1) and the integration is over the solid angle in three dimensions (3D). In this limit, the translational velocity of the vesicle is linearly proportional to the driving force—the osmotic pressure. As expected, a number density at the interior wall that breaks front-back symmetry is required in order to have a nonzero translational velocity of the vesicle.

Equation (7.1) applies generally for any osmotic solute in the weak permeability limit so that the interior fluid flow only slightly perturbs the solute distribution. For example, a linear solute gradient, $n_0 = n_0(\boldsymbol{0}) + \boldsymbol{x} \cdot \nabla n_0$, results in

$$\boldsymbol{U} = \frac{1}{3}\frac{K_\perp}{\eta_e \ell_m}(R - \ell_m) k_B T \nabla n_0, \tag{7.2}$$

where ∇n_0 is a constant vector and R is the exterior radius of the vesicle. Therefore, for the simple prescribed linear-density gradient, the vesicle translates in the same direction as the gradient in number density.

The above discussion reveals that the vesicle is able to exhibit net motion when an interior solute concentration gradient is given. A separate, but important, question is: How can such a solute gradient be maintained? For a biological cell, this is achieved by its internal physical and biochemical processes (Stroka et al. 2014). For a synthetic vesicle system for the purpose of enhanced transport, alternate methods need to be implemented in order to generate such a concentration gradient.

In this work, leveraging recent advances in the understanding of the dynamics of active matter, we propose to use active Brownian particles (ABPs) as the solute. In addition to normal thermal Brownian motion with translational diffusivity D_T, ABPs self-propel with an intrinsic 'swim' speed U_s in a direction $\boldsymbol{q}$. The orientation of the swimming direction $\boldsymbol{q}$ changes on a reorientation timescale τ_R that results from either continuous random Brownian rotations or the often-observed discrete tumbling events of bacteria. One important intrinsic length scale due to activity is the run or persistence length $\ell = U_s \tau_R$. Previous works have shown that a spatial variation in the swim speed leads to a spatial variation in the concentration (or number density) of active particles (Schnitzer 1993; Tailleur and Cates 2008; Row and Brady 2020). By tuning the swim speed distribution of ABPs confined inside the vesicle, a spherically asymmetric density distribution can emerge and lead to net motion of the vesicle.

For active particles with slow spatial variation in swim speed in 1D, Schnitzer (1993) and later Tailleur and Cates (2008) showed that the local number density n is inversely proportional to the local swim speed U_s, i.e., $nU_s = const$. This simple prediction has been validated experimentally using bacteria that swim with an intensity-dependent speed when illuminated by a spatial light pattern (Arlt et al. 2019). Row and Brady (2020) generalized this result and showed that the spatial variation in activity (e.g., swim speed) can be utilized as a pump mechanism in which fluid flows from regions of high concentration of particles to low. Employing this spatial variation, we show that encapsulated ABPs with spatially varying activity can be used to propel the vesicle.

In equations (7.1) and (7.2), the vesicle velocity appears to be linearly proportional to $k_B T$. However, this does not imply that the driving force is necessarily thermal in origin (in thermodynamic equilibrium no density gradient is present). In the case of ABPs as solute, the active (non-equilibrium) dynamics provides such a density gradient. Analogous to the Stokes-Einstein-Sutherland relation $k_BT = \zeta D_T$, where ζ is the Stokes drag coefficient, an active energy scale $k_sT_s = \zeta \tilde{D}^{\text{swim}}$ can be defined for active matter systems (Takatori et al. 2014), where $\tilde{D}^{\text{swim}} = \tilde{U}_s^2\tau_R/6$ is the swim diffusivity. We note that for ABPs with spatially varying swim speed a characteristic swim speed $\tilde{U}_s$ is used in the definition of the swim diffusivity; the local active energy $k_sT_s(\boldsymbol{x})$ can also be defined by using the local swim speed $U_s(\boldsymbol{x})$ and/or local reorientation time $\tau_R(\boldsymbol{x})$. An important parameter that quantifies the activity of ABPs is the ratio $k_sT_s/k_BT = \tilde{D}^{\text{swim}}/D_T$. For many active matter systems this ratio is very large, often exceeding 10^3 (Takatori et al. 2016). In this high activity limit, the ABPs exhibit a thin accumulation boundary layer at the interior surface of the vesicle. As we shall show in section 7.3.2, the local density at the interior wall of the vesicle can be related to the density just outside the boundary layer via the equation $n^wk_BT = n^0k_sT_s(\boldsymbol{x})f = \Pi_0^{\text{swim}}(\boldsymbol{x})f$, where Π_0^{swim} is the swim pressure just outside the boundary layer and f is a factor that depends on the ratio of the run length to the size of the vesicle. [This factor is unity for the case of ABPs on one side of an infinite planar wall (Yan and Brady 2015b).] For highly active ($k_sT_s \gg k_BT$) ABPs, equation (7.1) becomes

$$\boldsymbol{U} = \frac{1}{4\pi}\frac{K_\perp}{\eta_e\ell_m}\int_{S^2} n^0k_sT_s(\boldsymbol{x})f\boldsymbol{n}d\Omega = \frac{1}{4\pi}\frac{K_\perp}{\eta_e\ell_m}\int_{S^2}\Pi_0^{\text{swim}}\boldsymbol{n}fd\Omega, \tag{7.3}$$

showing that the velocity of the vesicle is proportional to the swim pressure. More precisely, it is the variation of the swim pressure [due to the variation in swim speed or run length $\ell(\boldsymbol{x})$] that gives rise to net motion.

Instead of using ABPs with spatially varying swim speed or run length, one can also consider using an external field that orients constant-property ABPs towards a certain direction. External fields such as chemical gradients or magnetic fields can affect the swimming behavior of microorganisms to facilitate their movement towards a favorable region. In the laboratory, an externally applied magnetic field has been used to guide nanocarriers for the purpose of targeted drug delivery (Felfoul et al. 2016; Pattni et al. 2015). In the presence of an external orienting field, even for ABPs with constant properties, the front-back symmetry is broken, and net motion of the vesicle is generated. The balance of the strength of the orienting field and the random reorientation due to rotary diffusion is characterized by the Langevin parameter, $\chi_R = \Omega_c\tau_R$, where Ω_c is the strength of the angular velocity induced by the field (Takatori and Brady 2014). Noting that the force exerted by the active particles on the wall $\boldsymbol{F}^w = k_BT\int n^w\boldsymbol{n}dS$ (Yan and Brady 2015b), we rewrite equation (7.1) as $U = K_\perp \boldsymbol{F}^W/(4\pi R^2 \eta_e \ell_m)$. In other words, we need to know the net force the active particles exert on the wall to determine the net vesicle motion. The force on the wall scales as $N^w \zeta U_s$, where N^w is the total number of particles at the wall and each particle pushes against the wall with at most its swim force ζU_s. The balance of this force due to the ABPs with the drag force of the porous vesicle moving through an external viscous fluid gives the net motion. Of particular interest is the strong-field limit, where the number of particles on the wall is on the same order as the total number of particles, $N^w/N = O(1)$, and the net speed of the vesicle is the largest, $U \sim K_\perp N \zeta U_s/(R^2 \eta_e \ell_m)$.

This last example where we argued that the vesicle motion can be deduced from the net swim force of the ABPs balancing the drag of the vesicle also applies to the so-called 'dry' active matter (Marchetti et al. 2013). Dry active matter describes bacteria (or other organisms) that crawl (or even walk) on a surface of a medium of resistivity ζ. Active particles confined to a 'container' that is able to slide along the surface in response to a lateral force will be able to push the container via their 'swim' force if there is an asymmetric distribution of ABPs. The net swim force would scale as $N^w \zeta U_s$, and the container would translate with the speed $U_c \sim N^w \zeta U_s/\zeta_c$, where ζ_c is the resistivity for sliding the container along the surface. For dry active matter there is no fluid and thus one does not have the notion of a semipermeable membrane nor a seepage velocity driven by an osmotic pressure difference. Nevertheless, the mechanics are the same: like the seepage velocity, the substrate surface must move across the container boundary as it slides along the surface, and the ABPs achieve their propulsive 'crawling' force by pushing off the substrate just like swimmers push off the fluid. Thus, at least at high activity, the results derived here apply equally well to dry active matter with an appropriate change in notation.

In the case of a spherical vesicle, its net motion is induced by an asymmetric number density distribution on the vesicle interior surface. An alternate route for the generation of net motion is to use a vesicle with an asymmetric shape. Because the accumulation of ABPs at the interior surface depends on the local curvature of the boundary, a vesicle that has a front-back asymmetry in its shape is able to exhibit net motion. Indeed, the exterior version of the problem where a passive object is immersed in a bath of active particles has been studied. It has been shown in experiments and simulations that for an object with shape asymmetry, net motion can be achieved (Sokolov et al. 2010; Kaiser et al. 2014; Yan and Brady 2018).

To obtain the results for the vesicle motility, in section 7.2 we describe the model and derive a theoretical formulation that governs the dynamics of the vesicle, the interior solute suspension and the exterior fluid flow. A Darcy-like constitutive law that models the response of the fluid seepage velocity in relation to the fluid stress differences across the membrane is used. This formulation is at the continuum level, where the vesicle is large compared to the size of the ABPs so that the interior (fluid and ABPs) is treated as a suspension; the suspension stress includes the fluid stress and the osmotic pressure of the ABPs. The exterior flow field satisfies the boundary condition that the fluid velocity at the exterior surface of the vesicle consists of the rigid body motion and a seepage velocity. Because the vesicle is force- and torque-free, we can relate the rigid body motion to the seepage velocity distribution at the exterior surface using the reciprocal theorem. This approach is similar to treatments of the swimming of microorganisms using the squirmer model (Stone and Samuel 1996) where the boundary velocity at the surface of the swimmer is decomposed into rigid-body motion and the slip velocity distribution.

In situations relevant for the vesicle model as we consider here, the interior fluid flow is often weak compared to the active self-propulsion. In section 7.3, by neglecting the interior fluid flow we show that the total (fluid and osmotic) pressure inside the vesicle is constant and the leading-order translational velocity of the vesicle is driven by the difference in the fluid pressure across the membrane. As a result, one only needs to compute the distribution of ABPs in the absence of flow and the resulting number density distribution at the interior wall is used to obtain the translational velocity. The effect of an external orienting field on the dynamics of confined ABPs and the motion of the vesicle is considered in section 7.3.4. The behavior of ABPs with slow spatial variation in their swim speed where fluid motion is explicitly considered is discussed in section 7.4. Finally, we conclude in section 7.5 with a discussion of the limitations and extensions of this vesicle-ABPs propulsion system.

7.2 Problem formulation

Consider a rigid vesicle or cell consisting of a thin membrane and a solution core immersed in an otherwise quiescent viscous fluid (see figure 7.1). The interior of the vesicle is a suspension of potentially active elements, which we model as active Brownian particles. The boundary or membrane of the vesicle is permeable to the solvent (i.e. water) but not to the solute (ABPs). In other words, the membrane is an osmotic membrane and serves as a confining boundary for the ABPs. Relative to the vesicle, the fluid domain is partitioned into interior, exterior, and the thin porous (in the membrane) regions. The solvent in all regions is identical.

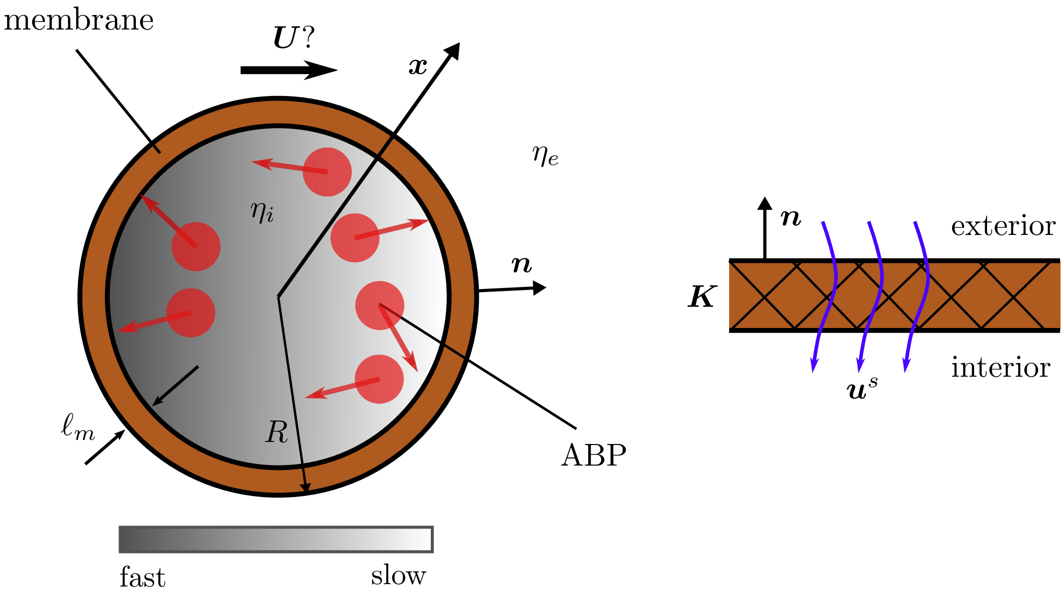

Figure 7.1: Left: A rigid spherical vesicle with a semipermeable membrane immersed in an otherwise quiescent viscous fluid. Active Brownian particles are confined inside the vesicle. Right: Schematic of the semipermeable membrane with a permeability tensor $\boldsymbol{K}$ and thickness ℓ_m. The seepage velocity in the membrane is $\boldsymbol{u}^s$, which in general depends on the local position vector.

The ABPs encapsulated inside the vesicle swim with a prescribed spatially varying swim speed, which is the driving mechanism for a spatially varying number density.

At small scales relevant to the vesicle-ABP system proposed here, the inertia of the fluid, the ABPs and the vesicle are negligible. In this low Reynolds number limit, the dynamics of the fluid is governed by the Stokes equations and there is no external force/torque on the vesicle.

7.2.1 The exterior flow

The exterior domain consists of solvent alone and its dynamics is governed by

$$\nabla \cdot \boldsymbol{\sigma}_f^e = \eta_e \nabla^2 \boldsymbol{u}^e - \nabla p_f^e = \boldsymbol{0}, \quad \nabla \cdot \boldsymbol{u}^e = 0. \tag{7.4}$$

Here, $\boldsymbol{\sigma}_f^e$ is the stress tensor, η_e is the dynamic viscosity of the solvent, p_f^e is the pressure field and $\boldsymbol{u}^e$ is the velocity field. Far from the vesicle, the fluid is undisturbed and there is no background flow:

$$p_f^e \to 0 \quad \text{and} \quad \boldsymbol{u}^e \to \boldsymbol{0} \quad \text{as} \quad r \to \infty. \tag{7.5}$$

At the exterior surface of the vesicle, we have

$$\boldsymbol{u}^e\,(\boldsymbol{x} \in S_e) = \boldsymbol{U} + \boldsymbol{\Omega} \times \boldsymbol{x} + \boldsymbol{u}^s(\boldsymbol{x}), \tag{7.6}$$

where S_e denotes the exterior surface of the vesicle, $\boldsymbol{U}$ ($\boldsymbol{\Omega}$) is the rigid-body linear (angular) velocity of the vesicle and $\boldsymbol{u}^s$ is the local seepage velocity at the exterior surface. The definition of $\boldsymbol{u}^s$ is deferred to Section 7.2.4. We note that equation (7.6) is similar to the squirmer model where the closely packed cilia tips of a microorganism are modeled as a distribution of radial and tangential velocities on the cell body, often taken to be of spherical shape (Lighthill 1952; Blake 1971).

7.2.2 The interior suspension

The particles and solvent in the interior of the vesicle are treated as a continuum and governed by

$$\nabla \cdot \boldsymbol{\sigma}^i = \eta_i \nabla^2 \boldsymbol{u}^i - \nabla P = \boldsymbol{0} \quad \text{and} \quad \nabla \cdot \boldsymbol{u}^i = 0, \tag{7.7}$$

where $\boldsymbol{\sigma}^i$ is the stress tensor, η_i is the dynamic viscosity of the suspension and $\boldsymbol{u}^i$ is the velocity field. Here, the total pressure is given by

$$P = p^i_f + nk_BT, \tag{7.8}$$

where p^i_f is the fluid pressure, n the number density of the ABPs and k_BT is the thermal energy. In our model, the only contribution to the suspension stress from the ABPs is the osmotic pressure nk_BT. We note that additional stress contributions such as the active hydrodynamic stresslet of ABPs (Saintillan and Shelley 2015) can be readily incorporated into our model. These effects play a less important role compared to the osmotic pressure and are thus neglected here. At the interior wall of the vesicle, we have

$$\boldsymbol{u}^i\,(\boldsymbol{x} \in S_i) = \boldsymbol{U} + \boldsymbol{\Omega} \times \boldsymbol{x} + \boldsymbol{u}^s(\boldsymbol{x}), \tag{7.9}$$

where S_i is the interior surface of the vesicle.

7.2.3 Dynamics of ABPs

The distribution of ABPs confined inside the vesicle is described by the probability density $\Psi(\boldsymbol{x}, \boldsymbol{q}, t)$ as a function of space $\boldsymbol{x}$, orientation $\boldsymbol{q}$ ($|\boldsymbol{q}| = 1$) and time t. The conservation of ABPs is governed by the Smoluchowski equation. At steady state, this is given by

$$\nabla \cdot \boldsymbol{j}_T + \nabla_R \cdot \boldsymbol{j}_R = 0, \tag{7.10}$$

where the translational and rotational fluxes are given by, respectively,

$$\boldsymbol{j}_T = \boldsymbol{u}^i \Psi + U_s(\boldsymbol{x}) \boldsymbol{q} \Psi - D_T \nabla \Psi, \tag{7.11}$$

$$\boldsymbol{j}_R = \frac{1}{2} \boldsymbol{\omega}^i \Psi - D_R \nabla_R \Psi. \tag{7.12}$$

Here, D_T is the thermal diffusivity of ABPs, $\boldsymbol{\omega}^i = \nabla \times \boldsymbol{u}^i$ is the vorticity vector, D_R is the rotary diffusivity, $\nabla_R = \boldsymbol{q} \times \nabla_q$ is the rotary gradient operator and $U_s(\boldsymbol{x})$ is the intrinsic swim speed of ABPs. The prescribed spatial variation of U_s is the key ingredient of our model, and is responsible for the generation of a concentration gradient of ABPs inside the vesicle. The conservation of ABPs requires that

$$\int_{V_i} \Psi d\boldsymbol{x} d\boldsymbol{q} = N, \tag{7.13}$$

where N is the total number of ABPs and V_i is the volume of the interior of the vesicle. At the interior surface of the vesicle, the flux relative to the rigid-body motion must vanish. This no-flux condition can be written as

$$\boldsymbol{n} \cdot \boldsymbol{j}_T = \boldsymbol{n} \cdot (\boldsymbol{U} + \boldsymbol{\Omega} \times \boldsymbol{x}) \Psi, \quad \boldsymbol{x} \in S_i, \tag{7.14}$$

where $\boldsymbol{n}$ is the unit normal vector as shown in figure 7.1. We note that as a model of active elements inside a cell, the rotary diffusivity D_R is biological rather than thermal in origin. As a result, D_R is independent of D_T (which is assumed to be thermal in origin). The rotary diffusivity defines a reorientation timescale $\tau_R = 1/D_R$ that characterizes the relaxation of the swimming direction. The ABPs take a step of magnitude $\ell = U_s \tau_R$, which is often called the run (or persistence) length ℓ, before its swimming direction changes significantly. Note that one might have a reorientation time $\tau_R(\boldsymbol{x})$ that is a function of position in addition to a spatially varying swim speed, as we show below that the important quantity is the run length $\ell(\boldsymbol{x})$.

7.2.4 Transport in the membrane

We treat the fluid transport in the membrane using a macroscopic approach similar to Darcy's law; however, the porous region is ultimately modelled as a thin permeable interface. To this end, we first consider the membrane as having a network stress $\boldsymbol{\sigma}^{\text{net}}$ and a fluid stress $\boldsymbol{\sigma}_f^m$. The defining characteristic of the semi-permeable membrane is that the fluid stress in the membrane balances the seepage velocity:

$$\nabla \cdot \boldsymbol{\sigma}_f^m - \eta_e \boldsymbol{R}_m \cdot \boldsymbol{u}^s = \boldsymbol{0}, \tag{7.15}$$

or $\boldsymbol{u}^s = \boldsymbol{K} \cdot \nabla \cdot \boldsymbol{\sigma}_f^m / \eta_e$, where $\boldsymbol{K} = \boldsymbol{R}_m^{-1}$ is the permeability tensor and $\boldsymbol{R}_m$ is the membrane resistivity. The remaining network stress is responsible for maintaining the osmotic pressure difference across the membrane. That is, we have the force balance on the exterior and interior surfaces, respectively,

$$\begin{aligned} \boldsymbol{\sigma}_f^e \cdot \boldsymbol{n} &= \boldsymbol{\sigma}_f^m \cdot \boldsymbol{n}, \quad \boldsymbol{x} \in S_e & (7.16) \\ \boldsymbol{\sigma}_f^i \cdot \boldsymbol{n} &= \boldsymbol{\sigma}_f^m \cdot \boldsymbol{n}, \quad \boldsymbol{x} \in S_i. & (7.17) \end{aligned}$$

Note, importantly, that at the interior surface, $\boldsymbol{\sigma}_f^i$ is the interior *fluid* stress (it does not contain the osmotic pressure).

We model the membrane as a tangentially isotropic material with the permeability tensor

$$\boldsymbol{K}(\boldsymbol{n}) = K_\perp \boldsymbol{n}\boldsymbol{n} + K_\parallel(\boldsymbol{I} - \boldsymbol{n}\boldsymbol{n}), \tag{7.18}$$

where $K_\perp$ is the normal permeability and $K_\parallel$ is the tangential one. For a thin membrane the gradient in equation (7.15) can be approximated by a finite difference in the normal direction, which after applying the boundary conditions (7.16) and (7.17) leads to

$$\boldsymbol{u}^s(\boldsymbol{n}) = \frac{\boldsymbol{K}}{\eta_e \ell_m} \cdot \left(\boldsymbol{\sigma}_f^e|_{S_e} - \boldsymbol{\sigma}_f^i|_{S_i} \right) \cdot \boldsymbol{n}. \tag{7.19}$$

Here, ℓ_m is the thickness of the membrane and the thin membrane condition is $\ell_m \ll R$ with R being the radius of the exterior surface. It is understood that in equation (7.19) $\boldsymbol{u}^s$ is a function of the local outward normal vector $\boldsymbol{n}$ (see figure 7.1). Equation (7.19) is a linear relation that specifies how a seepage velocity is generated in response to a jump in the fluid stress across the membrane.

In the absence of deviatoric stress, equation (7.19) reduces to

$$\boldsymbol{u}^s = -\frac{K_\perp}{\eta_e \ell_m} \left(p_f^e|_{S_e} - p_f^i|_{S_i} \right) \boldsymbol{n}, \tag{7.20}$$

which is the more familiar Darcy's law in terms of the fluid pressure difference. In general, the normal flow is driven by the fluid pressure difference as well as the shear stress.

We remark that different boundary conditions across membranes and macroscopic transport equations exist in the literature. For example, an empirical boundary condition was proposed by Beavers and Joseph (1967) and later rationalized by Saffman (1971). This boundary condition was then generalized to a curved surface (Jones 1973). Recently, using multiscale homogenization and matched asymptotic expansions between the near membrane and the far region, Zampogna and Gallaire (2020) developed a macroscopic condition to simulate the interaction between an incompressible fluid flow and a permeable thin membrane. For the purpose of the present work, equation (7.19) is sufficient.

Because the vesicle is rigid, the preservation of its volume dictates that

$$\int_{S_e} \boldsymbol{u}^s \cdot \boldsymbol{n} dS = 0. \tag{7.21}$$

Henceforth, for simplicity we shall assume that the membrane is not permeable in the tangential directions ($K_{\parallel} = 0$), in which case the seepage velocity is normal to the vesicle surface.

7.2.5 Dynamics of the vesicle

The rigid-body translational and rotational velocities of the vesicle are determined by the force/torque-free conditions given by

$$\int_{S_e} \boldsymbol{\sigma}_f^e \cdot \boldsymbol{n} dS = \mathbf{0}, \quad \int_{S_e} \boldsymbol{x} \times \boldsymbol{\sigma}_f^e \cdot \boldsymbol{n} dS = \mathbf{0}. \tag{7.22}$$

We can relate the rigid-body velocities $\boldsymbol{U}$ and $\boldsymbol{\Omega}$ to the seepage velocity $\boldsymbol{u}^s$ at the exterior surface using the reciprocal theorem for Stokes flow (Masoud and Stone 2019). The formula for a general body shape is given in Elfring (2015). For the case of a spherical particle, the rigid-body translational and rotational velocities are given by, respectively,

$$\boldsymbol{U} = -\frac{1}{4\pi R^2} \int_{S_e} \boldsymbol{u}^s dS, \quad \boldsymbol{\Omega} = -\frac{3}{8\pi R^3} \int_{S_e} \boldsymbol{n} \times \boldsymbol{u}^s dS. \tag{7.23}$$

In the study of the rigid-body motion of micro-swimmers with prescribed kinematics (gaits) such as squirmers, the reciprocal theorem allows one to bypass the calculation of the unknown flow field, provided one can solve the resistance/mobility problem for the swimmer shape. For the problem considered here, the seepage velocity of the vesicle is not known *a priori*; we need to determine the rigid-body motion, the exterior/interior flow fields and the distribution of ABPs simultaneously.

7.2.6 Non-dimensional equations for a spherical vesicle

For a spherical vesicle, the angular velocity vanishes ($\boldsymbol{\Omega} = \mathbf{0}$) and the torque balance is automatically satisfied. We define a characteristic swim speed $\tilde{U}_s$ such that

$$U_s(\boldsymbol{x}) = \tilde{U}_s \hat{U}_s(\boldsymbol{x}). \tag{7.24}$$

For a spatially homogeneous swim speed, $\hat{U}_s(\boldsymbol{x}) = 1$. The average density of ABPs inside the vesicle is $\overline{n} = N/V_i$, where $V_i = 4\pi(R - \ell_m)^3/3$ is the volume of the interior. We use this average density to scale the probability density such that

$$\Psi = \overline{n} g, \tag{7.25}$$

where g is the non-dimensional probability density. To render the governing equations non-dimensional, we scale pressures and stresses by $\overline{n} k_s T_s$, length by R, and fluid/vesicle velocities by $\overline{n} k_s T_s K_{\perp}/(\eta_e \ell_m)$. Recall that the activity $k_s T_s = \zeta \tilde{U}_s^2 \tau_R / 6$.

Using the characteristic swim speed, we define the swim Péclet number

$$Pe_s = \frac{\tilde{U}_s \tau_D}{R} = \frac{\tilde{U}_s R}{D_T} \tag{7.26}$$

that compares the swim speed to the diffusive speed R/τ_D, where $\tau_D = R^2/D_T$ is a diffusive timescale. Another dimensionless parameter for ABPs is defined as

$$\gamma = \sqrt{\frac{\tau_D}{\tau_R}} = \frac{R}{\delta}, \tag{7.27}$$

where $\delta = \sqrt{D_T \tau_R}$ is a microscopic length that quantifies the distance traveled by translational diffusion on the timescale of τ_R. Alternate parameters including ℓ/δ and ℓ/R are often used in the literature. These parameters are direct comparisons between different length scales. We note that they are related to Pe_s and γ by $Pe_s = (\ell/\delta)^2(\ell/R)^{-1}$ and $\gamma = (\ell/R)^{-1}\ell/\delta$.

The non-dimensional exterior problem is given by

$$\begin{aligned} Da\nabla^2 \boldsymbol{u}^e &= \nabla p_f^e, && (7.28)\\ \nabla \cdot \boldsymbol{u}^e &= 0, && (7.29)\\ \boldsymbol{u}^e &\to \boldsymbol{0} \quad \text{and} \quad p_f^e \to 0 \quad \text{as} \quad r \to \infty, && (7.30)\\ \boldsymbol{u}^e &= \boldsymbol{U} + \boldsymbol{u}^s \quad \text{at} \quad r = 1, && (7.31) \end{aligned}$$

where

$$Da = \frac{K_\perp}{R\ell_m}, \tag{7.32}$$

is a Darcy number that compares the permeability of the membrane to its characteristic cross-sectional area.

In the interior, the rigid-body translation $\boldsymbol{U}$ has no effect on the fluid dynamics and we only need to consider the deviation $\boldsymbol{u}' = \boldsymbol{u}^i - \boldsymbol{U}$. Thus, the non-dimensional flow problem in the interior is governed by

$$\begin{aligned} \beta Da\nabla^2 \boldsymbol{u}' &= \nabla P, && (7.33)\\ \nabla \cdot \boldsymbol{u}' &= 0, && (7.34)\\ |\boldsymbol{u}'|, P &< \infty \quad \text{at} \quad r = 0, && (7.35)\\ \boldsymbol{u}' &= \boldsymbol{u}^s \quad \text{at} \quad r = \Delta. && (7.36) \end{aligned}$$

Here,

$$\beta = \frac{\eta_i}{\eta_e} \tag{7.37}$$

is the interior-to-exterior viscosity ratio and

$$\Delta = \frac{R - \ell_m}{R} \tag{7.38}$$

is the radius ratio between the interior and the exterior surfaces of the membrane. For a thin membrane, $\ell_m/R \ll 1$, Δ is $O(1)$. The non-dimensional total pressure is given by

$$P = p_f^i + \frac{k_B T}{k_s T_s} n = p_f^i + \frac{6\gamma^2}{Pe_s^2} n, \tag{7.39}$$

where we have used the relation $k_B T/k_s T_s = D_T/(\overline{U}_0^2 \tau_R/6) = 6\gamma^2/Pe_s^2$.

The non-dimensional deviatoric stress tensors in the exterior and interior are, respectively,

$$\boldsymbol{\tau}^e = Da\left[\nabla \boldsymbol{u}^e + (\nabla \boldsymbol{u}^e)^T\right], \quad \boldsymbol{\tau}^i = \beta Da\left[\nabla \boldsymbol{u}' + (\nabla \boldsymbol{u}')^T\right]. \tag{7.40}$$

The seepage velocity is given by

$$\boldsymbol{u}^s = \boldsymbol{n}\boldsymbol{n} \cdot \left(\boldsymbol{\sigma}_f^e\big|_{S_e} - \boldsymbol{\sigma}_f^i\big|_{S_i}\right) \cdot \boldsymbol{n}, \tag{7.41}$$

where $\boldsymbol{\sigma}_f^e = -p_f^e \boldsymbol{I} + \boldsymbol{\tau}^e$ and $\boldsymbol{\sigma}_f^i = -p_f^i \boldsymbol{I} + \boldsymbol{\tau}^i$. The volume conservation of the vesicle is

$$\int_{S_e} \boldsymbol{u}^s \cdot \boldsymbol{n} = 0. \tag{7.42}$$

The rigid-body translational velocity of the vesicle is then

$$\boldsymbol{U} = -\frac{1}{4\pi} \int_{S^2} \boldsymbol{u}^s d\Omega. \tag{7.43}$$

The non-dimensional Smoluchowski equation, its fluxes, boundary condition, and particle conservation are, respectively,

$$\nabla \cdot \boldsymbol{j}_T + \nabla_R \cdot \boldsymbol{j}_R = 0, \tag{7.44}$$

$$\boldsymbol{j}_T = \alpha Da \boldsymbol{u}' g + Pe_s \hat{U}_s(\boldsymbol{x}) \boldsymbol{q} g - \nabla g, \tag{7.45}$$

$$\boldsymbol{j}_R = \frac{1}{2} \alpha Da \boldsymbol{\omega}' g - \gamma^2 \nabla_R g, \tag{7.46}$$

$$\boldsymbol{n} \cdot \boldsymbol{j}_T = 0 \quad \text{at} \quad r = \Delta, \tag{7.47}$$

$$\int g d\boldsymbol{q} d\boldsymbol{x} = \frac{4\pi}{3} \Delta^3, \tag{7.48}$$

where we have introduced three non-dimensional parameters α, Pe_s and γ. The first parameter is a reduced osmotic pressure and given by

$$\alpha = \frac{\overline{n} k_s T_s \tau_D}{\eta_e}. \tag{7.49}$$

Non-dimensional parameter	Mathematical definition	Physical description
α	$\overline{n}k_sT_s\tau_D/\eta_e$	Reduced osmotic pressure
β	η_i/η_e	Viscosity ratio
γ	R/δ	Comparison of R and δ
Da	$K_\perp/(R\ell_m)$	Darcy number
Pe_s	$\tilde{U}_s\tau_D/R$	Swim Péclet number
Δ	$(R-\ell_m)/R$	Radius ratio

Table 7.1: Independent non-dimensional parameters.

Physically, this is a comparison between the active driving pressure ($\overline{n}k_sT_s$) and a viscous resistive 'pressure' (η_e/τ_D) on the timescale τ_D.

In the equations above, variables $\{\boldsymbol{u}^e, p_f^e, \boldsymbol{x}, r, \boldsymbol{U}, \boldsymbol{u}^s, P, \boldsymbol{u}'\}$ and gradient operators are non-dimensional even though the same symbols as their dimensional counterparts are used. This is to avoid inconvenience in notation and henceforth we shall work with non-dimensional quantities unless otherwise noted.

It is convenient to consider the orientational moments of the probability density function. The zeroth order moment, or the number density, is given by

$$n(\boldsymbol{x}) = \int_{S^2} g d\boldsymbol{q}, \tag{7.50}$$

where S^2 is the surface of the unit sphere in $\mathbb{R}^3$, which represents all possible orientations that $\boldsymbol{q}$ takes. Integrating the Smoluchowski equation over all orientations, we obtain a conservation equation for the number density

$$\nabla \cdot \boldsymbol{j}_n = 0, \tag{7.51a}$$

$$\boldsymbol{j}_n = \alpha Da \boldsymbol{u}' n + Pe_s \hat{U}_s(\boldsymbol{x})\boldsymbol{m} - \nabla n. \tag{7.51b}$$

This equation is coupled to the first moment, or polar order,

$$\boldsymbol{m}(\boldsymbol{x}) = \int_{S^2} \boldsymbol{q} g d\boldsymbol{q}. \tag{7.52}$$

The no-flux condition (7.14) becomes $\boldsymbol{n} \cdot \boldsymbol{j}_n = 0$ for $\boldsymbol{x} \in S_i$. Multiplying the Smoluchowski equation by $\boldsymbol{q}$ and integrating over S^2, we obtain a governing equation for the polar order,

$$\nabla \cdot \boldsymbol{j}_m - \frac{1}{2}\alpha Da \boldsymbol{\omega}^i \times \boldsymbol{m} + 2\gamma^2 \boldsymbol{m} = \boldsymbol{0}, \tag{7.53a}$$

$$\boldsymbol{j}_m = \alpha Da \boldsymbol{u}' \boldsymbol{m} + Pe_s \hat{U}_s(\boldsymbol{x}) \left(\boldsymbol{Q} + \frac{1}{3} n \boldsymbol{I} \right) - \nabla \boldsymbol{m}, \tag{7.53b}$$

where

$$\boldsymbol{Q} = \int_{S^2} \left(\boldsymbol{q}\boldsymbol{q} - \frac{1}{3} \boldsymbol{I} \right) g \, d\boldsymbol{q} \tag{7.54}$$

is the trace-free nematic order tensor and $\boldsymbol{I}$ is the identity tensor of rank two. The no-flux condition at the interior surface for the polar order becomes $\boldsymbol{n} \cdot \boldsymbol{j}_m = \boldsymbol{0}$. Different from the conservation of the total number of ABPs, the polar order is not conserved as indicated by the presence of the sink term $2\gamma^2 \boldsymbol{m}$ in equation (7.53a) even in the absence of flow. This sink term describes the randomization, due to rotary diffusion, of any polar order.

As can be inferred from the above discussion, there is an infinite hierarchical structure to the moment equations. To truncate this infinite set of equations, a closure model such as $\boldsymbol{Q} = \boldsymbol{0}$ is often considered in the literature (Saintillan and Shelley 2015; Yan and Brady 2015b). A closure leads to a set of closed equations that can be solved as an approximation to the Smoluchowski equation. We note that a closure approximation is often not uniformly accurate across different regimes of physical parameters or different spatial/time domains and care must be taken when interpreting results obtained from such methods (Dulaney and Brady 2020; Burkholder and Brady 2020; Peng and Brady 2020). A systematic approach to derive low-order closure models that are able to approximate the full solution of the Smoluchowski equation is still lacking.

The mechanism for an induced concentration gradient from a prescribed activity gradient in the absence of flow has been studied in previous works (Schnitzer 1993; Tailleur and Cates 2008; Row and Brady 2020). To illustrate this mechanism and motivate later discussions, we summarize the simple one-dimensional (1D) result here. In the absence of external linear or angular velocities, such as due to flow or orienting field, the governing equation in 1D for highly active ABPs is $\nabla \cdot (\hat{U}_s \boldsymbol{m}) = 0$, where the diffusive term is neglected. The solution in 1D is simply $\boldsymbol{m} = 0$. Then, equation (7.53a) reduces to $n\hat{U}_s = const$. Further, Row and Brady (2020) showed that this spatial variation of activity and concentration can drive a reverse osmotic flow, i.e. fluid flow from regions of high concentration to low. In this work, we exploit this spatial variation to propel a vesicle that is able to maintain an activity gradient in the swim speed of ABPs confined inside.

7.3 Vesicle motion in the limit of weak interior flow

In many situations, the advection due to the interior fluid flow is much weaker compared to the self-propulsion of the ABPs or its active swim diffusion (small Péclet number), and we may neglect the effect of the fluid velocity disturbance on the distribution of ABPs.

7.3.1 Governing equations

The behavior of the system in this small-Péclet limit can be systematically derived by considering a weakly permeable membrane, $Da \ll 1$.

If the vesicle is non-permeable ($Da = 0$), no external or internal flows can be generated, and the vesicle remains stationary despite the nonuniform density distribution and accumulation of the ABPs at the boundary. Due to the scaling of the dimensional velocities by the permeability, the leading order non-dimensional velocities are $O(1)$ as $Da \to 0$. To study the motion of the vesicle in the $Da \ll 1$ limit, we pose regular expansions for all fields:

$$\boldsymbol{u}^e = \boldsymbol{u}_0^e + Da\boldsymbol{u}_1^e + \cdots, \tag{7.55}$$

$$p_f^e = p_{f,0}^e + Dap_{f,1}^e + \cdots, \tag{7.56}$$

$$\boldsymbol{u}' = \boldsymbol{u}_0' + Da\boldsymbol{u}_1' + \cdots, \tag{7.57}$$

$$P = P_0 + DaP_1 + \cdots, \tag{7.58}$$

$$g = g_0 + Dag_1 + \cdots. \tag{7.59}$$

The dimensionless number density is given by $n = \int g d\boldsymbol{q} = n_0 + Dan_1 + \cdots$. Similarly, the expansions for the translational and the seepage velocities are, respectively,

$$\boldsymbol{U} = \boldsymbol{U}_0 + Da\boldsymbol{U}_1 + \cdots, \tag{7.60}$$

$$\boldsymbol{u}^s = \boldsymbol{u}_0^s + Da\boldsymbol{u}_1^s + \cdots. \tag{7.61}$$

From equation (7.40), we know that the leading order deviatoric stresses are $O(Da)$, which does not contribute to the $O(1)$ seepage velocity. As a result, the seepage velocity at leading order is driven by the fluid pressure difference across the membrane,

$$\boldsymbol{u}_0^s = \left(p_f^i\big|_{S_i} - p_f^e\big|_{S_e} \right) \boldsymbol{n}. \tag{7.62}$$

Inserting these expansions into the exterior Stokes equations (7.28) and (7.29) gives to leading order

$$\nabla p_{f,0}^e = 0, \quad \nabla \cdot \boldsymbol{u}_0^e = 0. \tag{7.63}$$

The kinematic boundary condition at the exterior surface is $\boldsymbol{u}_0^e(r = 1) = \boldsymbol{U}_0 + \boldsymbol{u}_0^s$. Due to the linearity of Stokes flow, we only need to solve equation (7.63) using the seepage velocity condition $[\boldsymbol{u}_0^e(r = 1) = \boldsymbol{u}_0^s]$; the rigid body translation is determined from the reciprocal theorem given by equation (7.43). Because $\boldsymbol{u}_0^s$ is in the radial direction, the exterior flow is radial and given by

$$p_{f,0}^e = 0, \quad \boldsymbol{u}_0^e = \frac{\boldsymbol{u}_0^s}{r^2}. \tag{7.64}$$

Similarly, the leading order equation governing the interior flow is given by

$$\nabla P_0 = 0, \quad \nabla \cdot \boldsymbol{u}_0' = 0. \tag{7.65}$$

At the interior surface, the flow field satisfies the condition $\boldsymbol{u}'(r = \Delta) = \boldsymbol{u}^s$. We note that the interior flow field is not analytically tractable but it is not required in order to determine the vesicle motion. The total pressure at leading order is a constant, consisting of spatially varying fluid pressure and osmotic pressure,

$$p_{f,0}^i + 6\gamma^2 n_0 / Pe_s^2 = P_0 = const. \tag{7.66}$$

Inserting the expansions into the Smoluchowski equation (7.44)–(7.48), we obtain at leading order

$$\nabla \cdot \left(Pe_s \hat{U}_s(\boldsymbol{x}) \boldsymbol{q} g_0 - \nabla g_0 \right) - \gamma^2 \nabla_R^2 g_0 = 0, \tag{7.67}$$

$$\boldsymbol{n} \cdot \left(Pe_s \hat{U}_s(\boldsymbol{x}) \boldsymbol{q} g_0 - \nabla g_0 \right) = 0 \quad \text{at} \quad r = \Delta, \tag{7.68}$$

$$\int g_0 d\boldsymbol{q} d\boldsymbol{x} = \frac{4\pi}{3}\Delta^3. \tag{7.69}$$

Using equations (7.43), (7.62) and (7.66), we obtain

$$\boldsymbol{U}_0 = \frac{3\gamma^2}{2\pi Pe_s^2} \int_{S^2} n_0(r = \Delta) \boldsymbol{n} d\Omega. \tag{7.70}$$

It is more intuitive to examine the above expression in its dimensional form

$$\boldsymbol{U}_0 = \frac{1}{4\pi} \frac{K_\perp}{\eta_e \ell_m} \int_{S^2} \Pi_0^{\text{osmo}} \boldsymbol{n} d\Omega, \tag{7.71}$$

where $\Pi_0^{\text{osmo}} = n^w k_B T$ is the dimensional osmotic pressure of ABPs in the absence of flow.

To sum up, one needs to solve equations (7.67)-(7.69) to obtain the density distribution of ABPs in the absence of flow, and then using equation (7.70) to calculate the vesicle motion. In the remainder of section 7.3, the subscript '0' (e.g., g_0, $\boldsymbol{U}_0$) will be dropped for notational convenience.

In general, one can represent the number density distribution at the spherical interior wall by the complete spherical harmonic expansion

$$n_0(\Delta,\theta,\phi) = \sum_{l=0}^{\infty}\sum_{m=-l}^{m=l} C_{l,m}Y_l^m(\theta,\phi), \tag{7.72}$$

where $Y_l^m = \sqrt{(2l+1)(l-m)!/[4\pi(l+m)!]}P_l^m(\cos\theta)\exp(im\phi)$ and P_l^m is the associated Legendre polynomial of degree l and order m. Using equation (7.70), a direct integration shows that only the $l = 1$ modes contribute to the translational velocity of the vesicle.

7.3.2 High activity

We now explore the limit of high activity, $k_sT_s/k_BT = \tilde{D}^{\mathrm{swim}}/D_T = \ell^2/(6\delta^2) \gg 1$, which is often observed in active matter systems (Takatori et al. 2016). Equivalently, we define $\epsilon = 1/\gamma^2$ (Note that $Pe_s = \gamma^2\ell/R$) and consider the limit $\epsilon \to 0$. Expanding the probability density function $g = g^{(0)} + \epsilon g^{(1)} + \cdots$, we obtain at leading order

$$\frac{\ell}{R}\nabla\cdot\left[\hat{U}_s\boldsymbol{q}g^{(0)}\right] - \frac{1}{\hat{\tau}_R}\nabla_R^2 g^{(0)} = 0, \tag{7.73}$$

where we have included the spatial variation of $\tau_R(\boldsymbol{x})$ and defined $\tau_R = \tilde{\tau}_R\hat{\tau}_R$ similar to the case of spatially varying swim speed. Integrating over the orientation space leads to an equation for the polar order

$$\nabla\cdot\left(\hat{U}_s\boldsymbol{m}^{(0)}\right) = 0. \tag{7.74}$$

Equation (7.73) is incompatible with the no-flux boundary condition and thus is only valid in the bulk of the interior. At the interior membrane surface, the swimming flux is balanced by the diffusive flux, which implies the existence of an accumulation boundary layer of thickness $O(\epsilon)$. In this high activity limit, the number of particles in the boundary layer is still finite, which suggests that the probability density is $O(1/\epsilon)$ as $\epsilon \to 0$. Therefore, the probability density in the boundary layer admits an expansion of the form $g(y,\theta,\phi,\boldsymbol{q}) = g^{(-1)}/\epsilon + g^{(0)} + \cdots$. Defining a stretched boundary-layer coordinate in the radial direction $y = (\Delta - r)/\epsilon$, the Smoluchowski equation to leading order is

$$\frac{\ell}{R}\hat{U}_s\big|_{S_i}\boldsymbol{q}\cdot\boldsymbol{e}_r\frac{\partial g^{(-1)}}{\partial y} + \frac{\partial^2 g^{(-1)}}{\partial y^2} = 0, \tag{7.75}$$

$$\frac{\ell}{R}\hat{U}_s\big|_{S_i}\boldsymbol{q}\cdot\boldsymbol{e}_r g^{(-1)} + \frac{\partial g^{(-1)}}{\partial y} = 0 \quad \text{at} \quad y = 0, \tag{7.76}$$

$$g^{(-1)} \to 0 \quad \text{as} \quad y \to +\infty. \tag{7.77}$$

Here, the Taylor expansion $\hat{U}_s(r,\theta,\phi) = \hat{U}_s\big|_{S_i} - \epsilon y \frac{d\hat{U}_s}{dr}\big|_{S_i} + \cdots$ is used. The solution is readily obtained

$$g^{(-1)} = \begin{cases} A_1(\theta,\phi,\boldsymbol{q}) \exp\left(-\frac{\ell}{R}\hat{U}_s\big|_{S_i}\boldsymbol{q}\cdot\boldsymbol{e}_r y\right), & \boldsymbol{q}\cdot\boldsymbol{e}_r > 0, \\ 0, & \text{otherwise.} \end{cases} \tag{7.78}$$

This singular accumulation only occurs for particles with orientation pointing towards the wall ($\boldsymbol{q}\cdot\boldsymbol{e}_r > 0$) because otherwise they would swim away. In equation (7.78), A_1 is an unknown function that can only be determined from the next-order solution. The boundary layer solution $g^{(0)}(y,\theta,\phi,\boldsymbol{q})$ in the limit $y \to \infty$ needs to be matched with the solution in the bulk as $r \to \Delta$.

At the interior surface of the vesicle ($y = 0$), the leading-order density is large and given by $\gamma^2 \int_{\boldsymbol{q}\cdot\boldsymbol{e}_r>0} A_1 d\boldsymbol{q}$. Just outside the boundary layer (i.e., $y \to \infty$), the density is $O(1)$ as $\gamma^2 \to \infty$. This boundary-layer structure allows us to relate the osmotic pressure at the interior surface of the vesicle to the swim pressure outside the boundary layer. To this end, we consider the ratio $n^w k_B T/\left(n^0 k_s T_s\right)$, where all quantities are dimensional. The density at the wall n^w and the density outside the boundary layer n^0 are defined locally along the interior surface and are functions of the local surface normal vector $\boldsymbol{n}$. From the above analysis, we have

$$\frac{n^w k_B T}{n^0 k_s T_s} = \frac{\gamma^2 \int_{\boldsymbol{q}\cdot\boldsymbol{e}_r>0} A_1 d\boldsymbol{q}}{\int g^{(0)}(y\to\infty,\theta,\phi,\boldsymbol{q}) d\boldsymbol{q}} \frac{k_B T}{k_s T_s} = f(\ell/R, \Delta), \tag{7.79}$$

where $\gamma^2 k_B T/k_s T_s = 6R^2/\ell^2$ is not a function of the thermal diffusivity D_T (or ℓ/δ). Because in general A_1 is not analytically tractable, the factor $f(\ell/R,\Delta)$ in the preceding equation cannot be explicitly obtained. Nevertheless, equation (7.79) reveals the important fact that at high activity

$$\Pi^{\text{osmo}} = n^w k_B T = \Pi_0^{\text{swim}} f(\ell/R,\Delta), \tag{7.80}$$

where $\Pi_0^{\text{swim}} = n^0 k_s T_s$. In other words, the osmotic pressure at the wall is equal to the swim pressure in the bulk of the interior just outside the boundary layer but modified by a scale factor that is a function of ℓ/R and Δ. We emphasize that in equation (7.80), all quantities are defined locally along the interior surface of the vesicle. This is a generalization of the result of Yan and Brady (2015b) for ABPs outside an infinite planar wall, where $n^w k_B T = n^0 k_s T_s$ in the limit $\gamma^2 \to \infty$ because of the absence of curvature of the geometry.

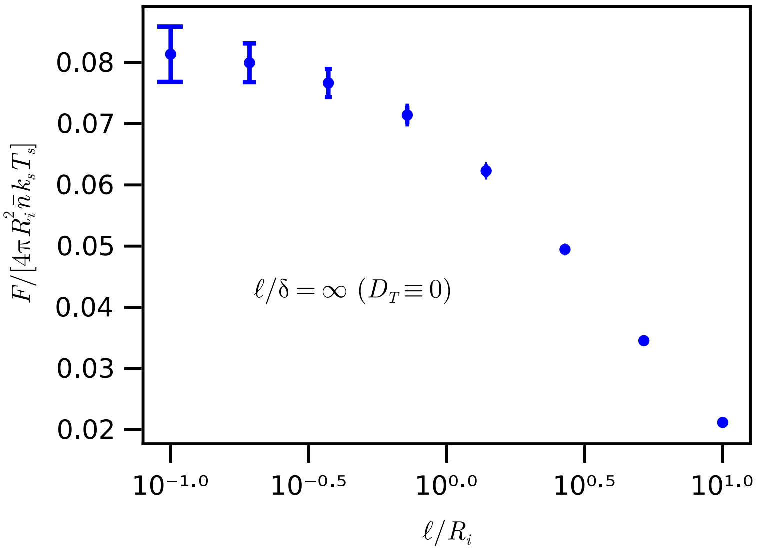

Figure 7.2: The magnitude of the dimensionless net force on the interior vesicle surface $\boldsymbol{F}^w/(4\pi R_i^2 \bar{n} k_s T_s)$ as a function of ℓ/R_i for ABPs with spatially varying swim speed. The speed profile is a step function where the swim speed in one of the hemisphere is half of that in the other. The reorientation time τ_R is a constant. The net force points towards the side with a higher swim speed.

Equation (7.80) allows us to obtain the dimensional speed of the vesicle:

$$\boldsymbol{U} = \frac{1}{4\pi} \frac{K_\perp}{\eta_e \ell_m} \int_{S^2} \Pi_0^{\text{swim}} f(\ell/R, \Delta) \boldsymbol{n} d\Omega. \tag{7.81}$$

We note that this relation holds for ABPs with spatially varying swim speed or reorientation time.

To understand the dependence of the motion of the vesicle on ℓ/R, we approach the problem from a micromechanical perspective using Brownian dynamics simulations that resolve the Langevin equations of motion governing the stochastic dynamics of an ABP in its physical and orientation space. The details of the simulation method is given in section 7.6. The ABPs are treated as point particles and their hard-particle interaction with the vesicle interior boundary is implemented using the potential-free algorithm (Heyes and Melrose 1993). In this approach, the force exerted on the wall due to the collision with ABPs is readily obtained. Consider a simulation of N ABPs that only interact with the boundary independently but not among themselves. After a time step Δt, some particles might have moved outside the interior wall. For particle i that is now outside, we add a displacement $\Delta \boldsymbol{x}_i$ to the particle such that after the move the particle is at contact with the boundary. The total force exerted on the wall is then $\boldsymbol{F}^w = -\zeta \sum_{i\in\mathcal{I}} \Delta\boldsymbol{x}_i/\Delta t$ where $\mathcal{I}$ is the set of all particles that are outside the boundary before the hard-sphere move. As seen in equation (7.71), the net speed of the vesicle is proportional to the net force $\boldsymbol{F}^w$.

In figure 7.2, we show the dimensionless net force exerted on the interior vesicle surface by the ABPs, $\boldsymbol{F}^w/(4\pi R_i^2 \bar{n} k_s T_s)$, as a function of ℓ/R_i for ABPs with no D_T (infinitely active, $\ell/\delta = \infty$) and a spatially-varying swim speed. The swim speed profile is a step function given by

$$\hat{U}_s = \begin{cases} 1 & x < 0, \\ 1/2 & x > 0. \end{cases} \tag{7.82}$$

The net force points to the side with a larger swim speed and only the force magnitude is shown in figure 7.2. As ℓ/R_i increases, the net force decreases. For large ℓ/R_i, the ABPs spend most of their time pushing against and sliding along the interior vesicle surface until rotary Brownian motion reorients them towards the bulk of the interior. In this limit, the number of particles pushing against the interior surface on the side of slow speed is comparable to the side of high speed.

As discussed earlier, in 1D the relation $nU_s = const$ holds for ABPs with spatially varying properties. In the interior of a vesicle, this relation is still useful for the qualitative understanding of the distribution of ABPs and the motion of the vesicle. Taking the step-function given by equation (7.82) as an example, $n^0 U_s = const$ means that in the bulk of the interior the density on the right side ($x > 0$) is higher than that on the left ($x < 0$), $n^0_R > n^0_L$. Because $n^w \sim n^0 k_s T_s/k_B T \sim n^0 U_s \zeta \ell/k_B T$ and $n^0 U_s = const$, we have $n^w \sim U_s$ for ABPs with constant τ_R. Therefore, the density at the interior vesicle surface on the right side is *lower* than that on the left ($n^w_R < n^w_L$), which is *opposite* to the behavior of the bulk density. Because only the ABPs at the interior surface contribute to the net force, and they can only push against the boundary, this leads to the fact that the net force is in the negative x direction (to the left). If one only had observations of the number density in the bulk, one would conclude that the vesicle moves in the direction of a lower concentration—a 'reverse' osmotic propulsion [cf. equation (7.2)].

The number density profile in the bulk and the boundary layer is sketched in figure 7.3 (red line) for a general swim-speed profile that decreases from the left to the right. The variation of the swim speed leads to a gradient in the number density in the bulk of the interior. Two thin accumulation boundary layers are established

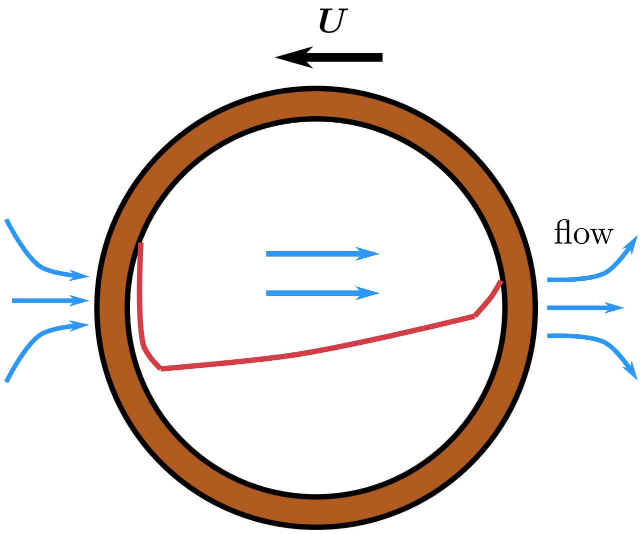

Figure 7.3: Schematic of the number density profile (red) and the flow direction (blue) in the high activity limit for a swim-speed profile that decreases from the left to the right. A weak density gradient is present in the bulk of the interior due to the variation of the swim speed. Two accumulation boundary layers are established at the left and right sides of the interior wall, with the density at the wall on the left larger than that on the right. The vesicle-ABPs system as a whole moves by way of jet propulsion.

at the left and right sides of the interior vesicle surface. Because the density at the wall on the right is smaller than that on the left, $n^w_R < n^w_L$, the dimensional version of equation (7.66) then leads to a larger fluid pressure on the low density side (right), $p^i_{f,R} > p^i_{f,L}$. Since the fluid pressure in the exterior is homogeneous, the fluid is pushed out of the vesicle from the right and drawn in from the left by conservation of mass. For the vesicle-ABPs system as a whole, it effectively moves by way of jet propulsion. This kind of noninertial jet propulsion has been proposed and studied in detail by Spagnolie and Lauga (2010) as an alternate mechanism for the locomotion of microswimmers. In their paper, the jetting velocity distribution of a microswimmer ($\boldsymbol{u}^s$) is prescribed, and then the swim speed is determined from the reciprocal theorem.

Using the approximation $n^0 U_s = const$ and the relation $\Pi_0^{\mathrm{swim}} = n^0 k_s T_s = n^0 U_s \zeta \ell / 6$, we see that it is the variation of run length $\ell(\boldsymbol{x})$ that is responsible for the net force on the vesicle interior surface and ultimately the vesicle motion. Using equation (7.81), a Taylor series expansion about the center of the vesicle leads to the scaling relation $\boldsymbol{U} \sim K_\perp R \zeta n^0 U_s \nabla \ell / (\eta_e \ell_m)$, where $\nabla \ell$ is the gradient of the run length at the center of the vesicle.

7.3.3 A large vesicle

When the vesicle is large, the confinement is weak, $\ell/R \ll 1$, ABPs exhibit a thin accumulation boundary layer at the wall and a uniform distribution in the bulk of the interior to leading order. To study this large-vesicle limit of $\ell/R \ll 1$, we first write equation (7.67) equivalently as

$$\nabla \cdot \left[\frac{\ell}{R} \hat{U}_s(\boldsymbol{x}) \boldsymbol{q} g - \left(\frac{\ell}{R}\right)^2 \left(\frac{\ell}{\delta}\right)^{-2} \nabla g \right] - \nabla_R^2 g = 0. \tag{7.83}$$

In this section, we use the definition $\epsilon = \ell/R$ and consider the limit as $\epsilon \to 0$. In the bulk of the interior, we have the expansion $g = g^{(0)} + \epsilon g^{(1)} + \cdots$ and the leading order equation $\nabla_R^2 g^{(0)} = 0$. The solution in the bulk is then $g^{(0)}(\boldsymbol{x}, \boldsymbol{q}) = n^{(0)}(\boldsymbol{x})/(4\pi)$. The boundary-layer thickness is determined by a balance between the swimming and the diffusive fluxes, which leads to the leading-order equation

$$\begin{aligned} -\frac{\partial}{\partial \rho}\left(\frac{\ell}{\delta} \hat{U}_s\big|_{S^i} \boldsymbol{q} \cdot \boldsymbol{e}_r g^{(0)} + \frac{\partial}{\partial \rho} g^{(0)} \right) - \nabla_R^2 g^{(0)} &= 0, & (7.84)\\ \frac{\ell}{\delta} \hat{U}_s\big|_{S^i} \boldsymbol{q} \cdot \boldsymbol{e}_r g^{(0)} + \frac{\partial}{\partial \rho} g^{(0)} &= 0 \quad \text{at} \quad \rho = 0. & (7.85) \end{aligned}$$

Here, we have used the stretched coordinate $\rho = (\Delta - r)/\epsilon$. Since $\ell \ll R$, curvature of the domain has no effect at $O(1)$ and the boundary-layer equation is similar to that in a planar domain. The $O(1)$ probability density in the boundary layer does not contribute to the $O(1)$ conservation because the boundary layer thickness is $O(\epsilon)$. This means that the total conservation is given by the density outside the boundary layer alone, $\int n^{(0)}(\boldsymbol{x}) d\boldsymbol{x} = 4\pi\Delta^3/3$. In the absence of curvature terms, just like the problem of ABPs on one side of an infinite planar wall (Yan and Brady 2015b), the number density at the interior wall of the vesicle at $O(1)$ can be determined analytically; the result is given by

$$\frac{n^w}{n^0} = 1 + \frac{1}{6}\left(\frac{\ell}{\delta}\right)^2 \hat{U}_0^2\big|_{S^i}. \tag{7.86}$$

In dimensional terms, this means that the osmotic pressure at the wall $\Pi_0^{\text{osmo}} = n^w k_B T = n^0 k_B T + n^0 k_s T_s \hat{U}_s^2$ where n^0 is the density outside the boundary layer. To determine n^0, one needs to solve equation (7.84) and then match the boundary-layer solution to that in the bulk.

The dimensional translational velocity in the large-vesicle limit is written as

$$\boldsymbol{U} = \frac{1}{4\pi} \frac{K_\perp}{\eta_e \ell_m} \int_{S^2} \left[n^0 k_B T + n^0 k_s T_s \hat{U}_s^2\big|_{S^i} \right] \boldsymbol{n} d\Omega. \tag{7.87}$$

For a large vesicle, the accumulation boundary layer has a similar structure to that obtained in the high-activity limit. Even for weakly active ABPs, this accumulation boundary layer exists so long as $\ell/R \ll 1$. As expected, equation (7.87) reduces to a form of (7.81) if the activity is high.

7.3.4 Vesicle motion due to an external orienting field

Another way to achieve motion is to apply an external orienting field, which affects the orientational dynamics but not the swim speed of the ABPs. Takatori and Brady (2014) showed that net directed motion of ABPs in free space can be achieved due to the fact that the external field can orient particles to move in the same direction. Instead of having ABPs with spatially varying swim speed, we consider the same orienting field as in Takatori and Brady (2014) but now with ABPs confined inside the vesicle. The only change to the orientational dynamics is that the orienting field exerts an external torque that depends on the orientation of the particle relative to the field direction; the dimensional rotary flux now becomes $\boldsymbol{j}_R = \Omega_c \boldsymbol{q} \times \hat{\boldsymbol{H}} g - D_R \nabla_R g$, where Ω_c characterizes the rate of reorientation due to the field and $\hat{\boldsymbol{H}}$ is the direction of the field. When an ABP is aligned with the field direction ($\boldsymbol{q} \parallel \hat{\boldsymbol{H}}$), the external torque vanishes. The Smoluchowski equation (7.67) for ABPs with constant properties in the presence of an orienting field is then

$$\nabla \cdot (Pe_s \boldsymbol{q} g - \nabla g) + \gamma^2 \nabla_R \cdot \left(\chi_R \boldsymbol{q} \times \hat{\boldsymbol{H}} g - \nabla_R g \right) = 0, \tag{7.88}$$

while the no-flux boundary condition (7.68) and the total conservation (7.69) remain unchanged. Here, we have defined the Langevin parameter, $\chi_R = \Omega_c \tau_R$, which measures the strength of the orienting field compared to rotary diffusion.

In the high-activity limit, an accumulation boundary layer is established at the interior wall. The boundary-layer structure is identical to that obtained for ABPs with spatially varying swim speed. At leading-order, the probability density in the bulk of the interior is governed by

$$\frac{\ell}{R} \boldsymbol{q} \cdot \nabla g^{(0)} + \nabla \cdot \left(\chi_R \boldsymbol{q} \times \hat{H} g^{(0)} - \nabla_R g^{(0)} \right) = 0. \tag{7.89}$$

Compared to (7.73) for spatial variation, the preceding equation has a constant swim speed and the orientational dynamics is affected by the orienting field. In the boundary layer, the leading-order equation is identical to (7.75) and the density at the wall is large.

Because equation (7.88) together with its no-flux boundary condition is not analytically tractable, we again make use of Brownian dynamics simulations. In figure

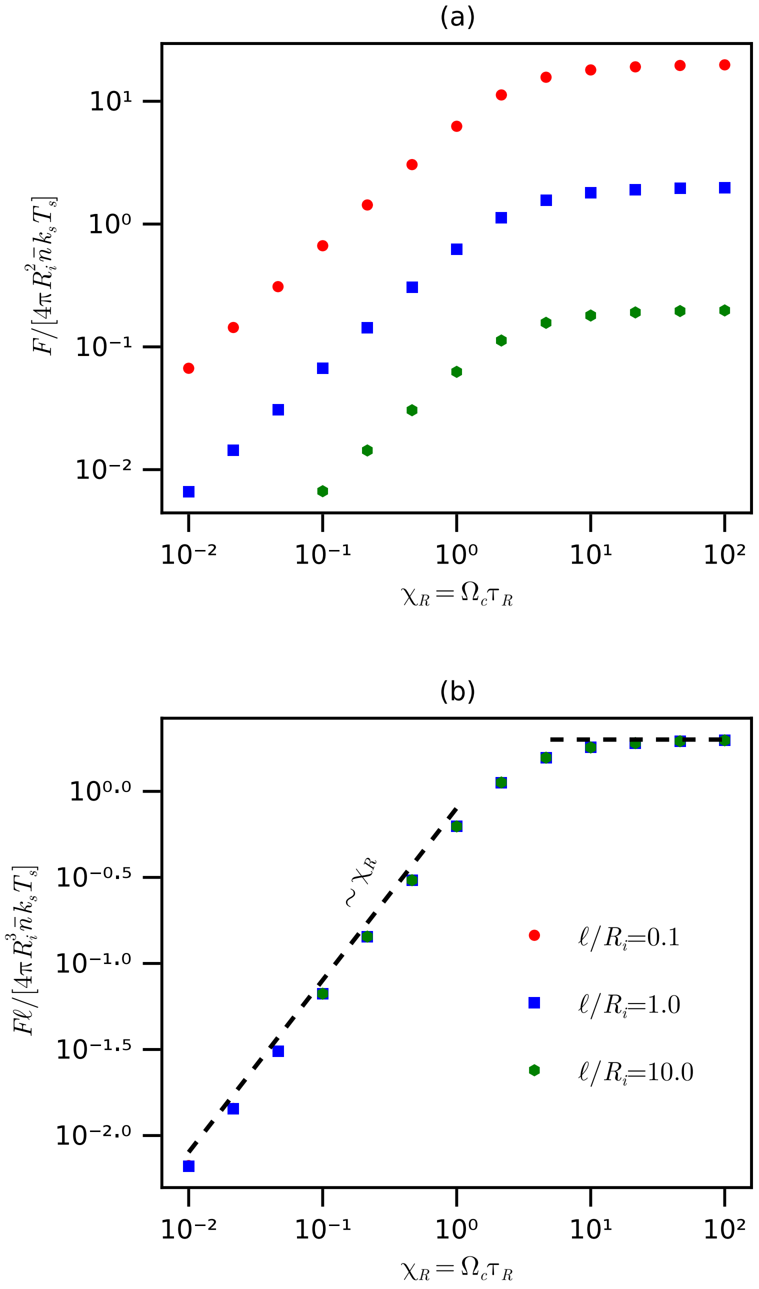

Figure 7.4: (a): The magnitude of the dimensionless net force on the interior wall $\boldsymbol{F}^w/(4\pi R_i^2 \bar{n} k_s T_s)$ as a function of the field strength χ_R for different values of ℓ/R_i. (b): The rescaled net force, $\boldsymbol{F}^w \ell/(4\pi R_i^3 \bar{n} k_s T_s)$, as a function of χ_R for different values of ℓ/R. All data collapse into one curve in panel (b). The values of ℓ/R_i in both panels are the same and are thus only shown in (b). In both panels, the translational diffusion is absent, $D_T \equiv 0$. In the weak-field limit, $\chi_R \ll 1$, the net force is linearly proportional to χ_R as shown by the dashed line.

7.4(a), we show the dimensionless net force exerted on the interior wall by the ABPs, $\boldsymbol{F}^w/(4\pi R_i^2 \overline{n} k_s T_s)$, as a function of the field strength for different values of ℓ/R. We note that the net force is in the field direction $\hat{\boldsymbol{H}}$. In figure 7.4(b), the same data is plotted but with the dimensionless net force multiplied by ℓ/R_i. This rescaling allows us to collapse all data onto a single curve. In the linear response regime, the net force is proportional to χ_R. On the other hand, the net force asymptotes to a finite value in the strong field limit. This is due to the fact that at most all N particles are aligned with $\hat{\boldsymbol{H}}$ and are pushing against the vesicle; further increasing of the field strength beyond this limit has no effect.

In 'wet' active matter systems such as the vesicle problem, the fluid mechanics is ultimately responsible for the motion of the vesicle and needs to be treated properly. Nevertheless, the perspective offered by the dry active matter force balance as discussed in section 7.1 gives the right answer for the speed of the vesicle. In particular, consider the case in which the vesicle is driven by an orienting field. The ratio N^w/N is a function of the field strength χ_R, $N^w/N = f(\chi_R)$. As a result, we have the qualitative scaling relation $F^w \sim N\zeta U_s f(\chi_R)$. Noting that $\overline{n} \sim N/R_i^3$ and $k_s T_s \sim \zeta U_s^2 \tau_R$, we have

$$\frac{F^w}{4\pi R_i^2 \overline{n} k_s T_s} \sim \frac{N\zeta U_s}{R_i^2 \overline{n} k_s T_s} f(\chi_R) \sim \frac{R_i}{\ell} f(\chi_R). \tag{7.90}$$

In the weak-field limit, $f(\chi_R) \sim \chi_R$. For large χ_R, $f(\chi_R) \sim 1$ (independent of χ_R). The above scaling argument also explains the collapse of the data as shown in figure 7.4(b). The maximum that F^w may achieve is $N\zeta U_s$, which gives the result that $F^w \ell/(4\pi R_i^3 \overline{n} k_s T_s) = 2$, this is plotted as a horizontal dashed line in figure 7.4(b).

We note that in figure 7.4, the translational diffusion is absent ($D_T \equiv 0$), which allows the system to achieve the maximum in the net force on the wall. For finite thermal diffusion, the net force is reduced and so is the speed of the vesicle.

7.4 Slow variation in activity

In the previous section, the dynamics of the vesicle is determined by the distribution of ABPs in the absence of flow. To understand the effect of interior fluid flow on the distribution of ABPs and the dynamics of the vesicle, we consider the case of slow variation in activity. When the activity gradient is small, any smooth variation of the swim speed can be approximated by a Taylor series expansion about the origin. Here, we consider the first effect of a small gradient by keeping the linear term only.

The non-dimensional swim speed can be written as

$$\hat{U}_s(\boldsymbol{x}) = 1 + \epsilon \boldsymbol{e} \cdot \boldsymbol{x}, \tag{7.91}$$

where $\epsilon = |\nabla U_s| R / U_s \ll 1$ and $\boldsymbol{e} = \nabla U_s / |\nabla U_s|$ is a constant unit vector in the direction of the gradient. If ϵ is identically zero, we have a spatially homogeneous swim speed and there is no vesicle motion due to spherical symmetry (see discussion in section 7.5). In this case of $\epsilon \equiv 0$, the solution is $\boldsymbol{u}_0' = \boldsymbol{u}_0^e = \boldsymbol{u}_0^s = \boldsymbol{U}_0 = \boldsymbol{0}$, $p_{f,0}^e = 0$ and $P_0 = const$. The distribution of ABPs is governed by equations (7.67), (7.68) and (7.69) but with $\hat{U}_s = 1$, i.e., this problem reduces to that of ABPs confined inside a fixed spherical domain. This spherical symmetry means that the number density is a function of the radial coordinate only, $n_0(\boldsymbol{x}) = n_0(r)$. As shown by Yan and Brady (2015b), the number density is a monotonically increasing function that obtains its maximum at the interior wall. Because the total pressure P_0 is a constant, this variation of number density (osmotic pressure) maintains a fluid pressure gradient with its maximum at the center of the interior domain. The fluid pressure across the membrane is constant, and no seepage velocity is generated.

To probe the first effect of a small linear gradient, we pose regular expansions for all fields and the translational velocity:

$$g = g_0 + \epsilon g_1 + \cdots, \tag{7.92}$$

$$\left(P, p_f^e, p_f^i\right) = (P_0, 0, 0) + \epsilon \left(P_1, p_1^e, p_1'\right) + \cdots, \tag{7.93}$$

$$(\boldsymbol{u}', \boldsymbol{u}^e, \boldsymbol{u}^s, \boldsymbol{U}) = \boldsymbol{0} + \epsilon \left(\boldsymbol{u}_1', \boldsymbol{u}_1^e, \boldsymbol{u}_1^s, \boldsymbol{U}_1\right) + \cdots. \tag{7.94}$$

At $O(\epsilon)$, the exterior fluid and the interior suspension are still governed by equations (7.28)–(7.31) and (7.33)–(7.36). Similarly, the seepage velocity is related to the jump in the fluid stress across the membrane given by equation (7.41). The disturbance to the distribution of ABPs at this order is governed by the inhomogeneous equation

$$\begin{aligned} \nabla \cdot (Pe_s \boldsymbol{q} g_1 - \nabla g_1) - \gamma^2 \nabla_R^2 g_1 &= -\nabla \cdot \left(\alpha Da \boldsymbol{u}_1' g_0 + Pe_s \boldsymbol{e} \cdot \boldsymbol{x} \boldsymbol{q} g_0\right) \\ &\quad - \frac{1}{2} \alpha Da \nabla_R \cdot \left(\boldsymbol{\omega}_1' g_0\right), \end{aligned} \tag{7.95}$$

with the boundary condition

$$\boldsymbol{n} \cdot (Pe_s \boldsymbol{q} g_1 - \nabla g_1) = -\alpha Da \boldsymbol{n} \cdot \boldsymbol{u}_1' g_0 - Pe_s \boldsymbol{e} \cdot \boldsymbol{x} \boldsymbol{n} \cdot \boldsymbol{q} g_0 \quad \text{at} \quad r = \Delta. \tag{7.96}$$

The net disturbance is zero, $\int g_1 d\boldsymbol{x} d\boldsymbol{q} = 0$. As can be seen from equation (7.95), the disturbance fields must be linear to the vector $\boldsymbol{e}$, which allows us to write the number density in the form

$$n_1 = \boldsymbol{e} \cdot \boldsymbol{x} h_1(r), \tag{7.97}$$

where $h_1(r)$ is a scalar function of the radial coordinate only.

Due to linearity of the Stokes equations, the interior flow problem at $O(\epsilon)$ admits a solution of the form

$$P_1 = A_1 \boldsymbol{e} \cdot \boldsymbol{x}, \tag{7.98}$$

$$\boldsymbol{u}_1' = A_2 \boldsymbol{e} + A_3 \boldsymbol{e} \cdot \left(\boldsymbol{x}\boldsymbol{x} - \frac{1}{3} r^2 \boldsymbol{I} \right) + \frac{1}{2\beta Da} P_1 \boldsymbol{x}. \tag{7.99}$$

Here, the momentum equation (7.33) is solved using a linear combination of the growing tensor harmonic functions (Leal 2007). The continuity equation (7.34) gives a constraint

$$5A_3 + \frac{3A_1}{\beta Da} = 0. \tag{7.100}$$

We can solve the external flow problem by considering two separate problems with different boundary conditions: (1) $\boldsymbol{u}_1^e = \boldsymbol{u}_1^s$ and (2) $\boldsymbol{u}_1^e = \boldsymbol{U}_1$ at $r = 1$. Instead of solving the flow field due to the second boundary condition in terms of the yet unknown velocity $\boldsymbol{U}_1$, it will be determined from the reciprocal theorem (7.43). As a result, one only needs to compute the exterior flow field due to the seepage velocity $\boldsymbol{u}_1^s$. The exterior flow problem with the first boundary condition has a solution of the form

$$p_1^e = A_4 \boldsymbol{e} \cdot \frac{\boldsymbol{x}}{r^3}, \tag{7.101}$$

$$\boldsymbol{u}_1^e = A_5 \boldsymbol{e} \frac{1}{r} + A_6 \boldsymbol{e} \cdot \left(\frac{\boldsymbol{I}}{r^3} - 3\frac{\boldsymbol{x}\boldsymbol{x}}{r^5} \right) + \frac{1}{2Da} p_1^e \boldsymbol{x}, \tag{7.102}$$

where the decaying tensor harmonic functions are used. To satisfy the continuity equation (7.29), we must have

$$A_4 = 2DaA_5. \tag{7.103}$$

The seepage velocity connects the interior and exterior flow field via

$$\boldsymbol{u}_1'(\boldsymbol{x} = \Delta \boldsymbol{e}_r) = \boldsymbol{u}_1^s = \boldsymbol{u}_1^e(\boldsymbol{x} = \boldsymbol{e}_r), \tag{7.104}$$

which reduces to

$$A_2 - \frac{1}{3}\Delta^2 A_3 = A_5 + A_6 \quad \text{and} \quad A_3\Delta^2 + \frac{A_1\Delta^2}{2\beta Da} = -3A_6 + \frac{A_4}{2Da}. \tag{7.105}$$

The volume conservation (7.42) is satisfied. The velocity of the vesicle is obtained from the reciprocal theorem, which gives

$$\boldsymbol{U}_1 = -\frac{1}{4\pi} \int_{S^2} \boldsymbol{u}_1^s d\Omega = -\left(A_2 + \frac{A_1\Delta^2}{6\beta Da} \right) \boldsymbol{e}. \tag{7.106}$$

Finally, to solve equation (7.41) at this order, we need to compute the fluid stress at the interior and the exterior wall. At the interior wall, we have

$$\begin{aligned}\boldsymbol{\sigma}^i_{f,1}\cdot\boldsymbol{e}_r = \quad & -\Delta\left(A_1 - h_1(\Delta)\frac{k_BT}{k_sT_s}\right)\boldsymbol{e}\cdot\boldsymbol{e}_r\boldsymbol{e}_r \\ & +\Delta\left(\frac{7}{3}A_3\beta Da + \frac{3}{2}A_1\right)\boldsymbol{e}\cdot\boldsymbol{e}_r\boldsymbol{e}_r + \Delta\left(\frac{1}{3}A_3\beta Da + \frac{1}{2}A_1\right)\boldsymbol{e}. \qquad (7.107)\end{aligned}$$

The traction at the exterior wall has two contributions. The first is due to the vesicle translating at a constant speed $\boldsymbol{U}_1$, which is given by (Guazzelli and Morris 2011, pp. 44)

$$\boldsymbol{\sigma}^e_{U_1}\cdot\boldsymbol{e}_r = -\frac{3}{2}Da\boldsymbol{U}_1. \qquad (7.108)$$

The second contribution is from the seepage velocity boundary condition $\boldsymbol{u}^s_1$, which is given by

$$-A_4\boldsymbol{e}\cdot\boldsymbol{e}_r\boldsymbol{e}_r + Da\left(-A_5 - 6A_6 + \frac{A_4}{2Da}\right)\boldsymbol{e} + Da\left(-A_5 + 18A_6 - \frac{3A_4}{2Da}\right)\boldsymbol{e}\cdot\boldsymbol{e}_r\boldsymbol{e}_r. \qquad (7.109)$$

Using equations (7.106)–(7.109) we can obtain the jump in the fluid stress across the membrane, which then allows us to calculate the seepage velocity using equation (7.41). Equating this result with the seepage velocity obtained from equation (7.102) by setting $r = 1$, we arrive at the following equations for the coefficients:

$$A_5 + A_6 = 0, \qquad (7.110)$$

and

$$\begin{aligned}\frac{A_4}{2Da} - 3A_6 = \quad & A_1\Delta\left(-1 + \frac{\Delta}{4\beta}\right) + \frac{3}{2}DaA_2 - \frac{8}{3}A_3\beta\Delta Da - 2A_4 \\ & -2A_5Da + 12A_6Da - \Delta h_1(\Delta)\frac{k_BT}{k_sT_s}. \qquad (7.111)\end{aligned}$$

Equation (7.110) implies that $\boldsymbol{u}^s_1$ is proportional to $\boldsymbol{e}\cdot\boldsymbol{e}_r\boldsymbol{e}_r$ and the component proportional to $\boldsymbol{e}$ is zero, which is consistent with the fact that the seepage velocity is in the normal ($\boldsymbol{e}_r$) direction. At this stage, we have obtained 6 equations for the 6 unknown coefficients A_i ($i = 1\cdots 6$), which are given by equations (7.100), (7.103), (7.105), (7.110) and (7.111). Using these equations, one could express A_i in terms of the boundary value of h_1 at the interior wall, i.e., $h_1(\Delta)$. These relations are obtained as

$$A_6 = \frac{\Delta^2}{4}\frac{k_BT}{k_sT_s}\frac{h_1(\Delta)}{\Delta + Da(6\beta + 4\Delta)}, \qquad (7.112)$$

and

$$A_1 = \frac{40Da\beta}{\Delta^2}A_6, \quad A_2 = -8A_6, \quad A_3 = -\frac{24}{\Delta^2}A_6, \tag{7.113}$$

$$A_4 = -2DaA_6, \quad A_5 = -A_6. \tag{7.114}$$

From equation (7.106), we have the net motion of the vesicle

$$\boldsymbol{U}_1 = \frac{4}{3}A_6\boldsymbol{e} = \frac{\Delta^2}{3}\frac{k_BT}{k_sT_s}\frac{h_1(\Delta)}{\Delta + Da(6\beta + 4\Delta)}\boldsymbol{e}. \tag{7.115}$$

Equation (7.115) is the main result of this section. In obtaining (7.115) the only assumption made is the small linear gradient in the swim speed; therefore, it applies generally for all ranges of the parameters α, β, Da, Pe_s, and γ. In particular, no restriction on the activity of the ABPs (e.g., ℓ/δ) is made. We note that $h_1(\Delta)$ depends parametrically on all the above parameters.

To obtain $h_1(r)$, we need to solve equation (7.95) that governs the disturbance probability density distribution of the ABPs. As an approximation, we consider the general solution using the $\boldsymbol{Q} = \boldsymbol{0}$ closure. At $O(1)$, the spherical symmetry allows us to write the number density and polar order in the form

$$n_0(\boldsymbol{x}) = n_0(r), \tag{7.116}$$

$$\boldsymbol{m}_0(\boldsymbol{x}) = \boldsymbol{x}f(r), \tag{7.117}$$

which, when inserted into equations (7.51a) and (7.53a), leads to a couple of ordinary differential equations (ODEs) for $n_0(r)$ and $f(r)$. The solutions to n_0 and $\boldsymbol{m}_0$ under this assumption are obtained by Yan and Brady (2015b).

Next, we consider the disturbance distribution of ABPs at $O(\epsilon)$. At this order, the number density distribution is governed by

$$\nabla \cdot \boldsymbol{j}_{n,1} = 0 \quad \text{and} \quad \boldsymbol{j}_{n,1} = \alpha Da\boldsymbol{u}_1' n_0 + Pe_s\boldsymbol{m}_1 + Pe_s\boldsymbol{e}\cdot\boldsymbol{x}\boldsymbol{m}_0 - \nabla n_1. \tag{7.118}$$

The no-flux boundary condition is $\boldsymbol{n}\cdot\boldsymbol{j}_{n,1} = 0$ at $r = \Delta$. Similarly, the governing equation for the polar order (assuming $\boldsymbol{Q}_1 = \boldsymbol{0}$) is

$$\nabla \cdot \boldsymbol{j}_{m,1} + 2\gamma^2\boldsymbol{m}_1 - \frac{1}{2}\alpha Da\boldsymbol{\omega}_1' \times \boldsymbol{m}_0 = 0, \tag{7.119}$$

and

$$\boldsymbol{j}_{m,1} = \alpha Da\boldsymbol{u}_1'\boldsymbol{m}_0 + \frac{1}{3}Pe_s\left(n_0\boldsymbol{e}\cdot\boldsymbol{x} + n_1\right)\boldsymbol{I} - \nabla\boldsymbol{m}_1. \tag{7.120}$$

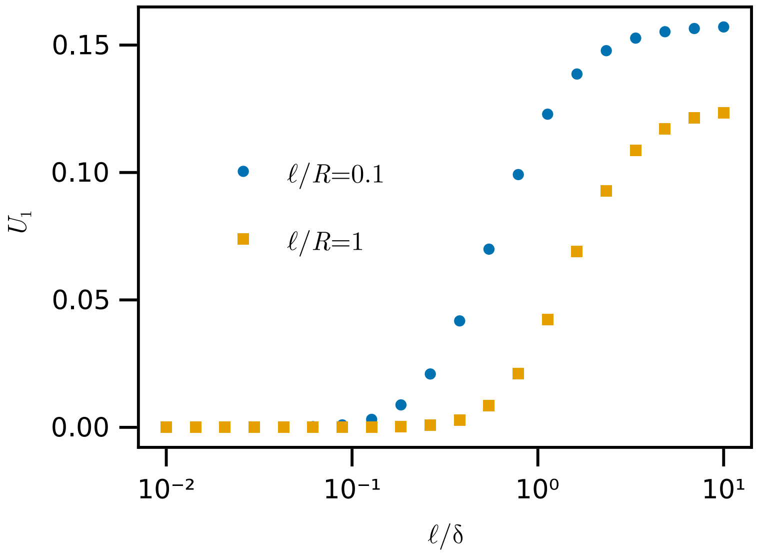

Figure 7.5: The dimensionless speed of the vesicle U_1 as a function of ℓ/δ for different fixed values of ℓ/R. All other parameters are fixed: $\Delta = 0.98, \alpha = 1, Da = 0.1$ and $\beta = 1.0$.

No-flux at $r = \Delta$ is $\boldsymbol{n} \cdot \boldsymbol{j}_{m,1} = \boldsymbol{0}$. Similar to equation (7.97), linearity and symmetry allow us to write the solution to the polar order in the form

$$\boldsymbol{m}_1 = \boldsymbol{e}h_2(r) + \boldsymbol{e} \cdot \boldsymbol{x}\boldsymbol{x}h_3(r), \tag{7.121}$$

where $h_2(r)$ and $h_3(r)$ are functions of the radial coordinate only and satisfy a coupled set of ODEs that can be found in Appendix 7.7.

In figure 7.5 we show the dimensionless speed of the vesicle (U_1) as a function of ℓ/δ for $\ell/R = \{0.1, 1\}$. With other dimensionless parameters fixed, the increase of ℓ/δ means the decrease of the translational diffusivity and thus the increase of activity. The speed of the vesicle vanishes as the activity approaches zero, $\ell/\delta \to 0$. As ℓ/δ increases, the speed of the vesicle increases and asymptotes to a finite value for large ℓ/δ. The speed is larger for a smaller ℓ/R because a thin boundary layer near the interior wall develops that enhances the front-back asymmetry of the density distribution.

7.5 Concluding remarks

In this Chapter we have proposed a composite low-Reynolds-number propulsion system made up of active Brownian particles encapsulated in a vesicle for the purpose of enhanced transport beyond that of passive Brownian diffusion. Instead of using the self-propulsion of a microswimmer directly, such as by attaching a cargo to its surface, we considered an alternate mechanism in which the vesicle is propelled by a fluid seepage velocity generated by a concentration gradient of these encapsulated particles. In the present work, we considered the cases in which the concentration gradient is generated by either a prescribed activity gradient in the swim speed of these ABPs or an external orienting field. By tuning the spatial pattern of variation in the swim speed, one could obtain a concentration profile that in turn propels the vesicle with a certain speed or in a desired direction. Alternatively, the application of an external orienting field can push the ABPs against the wall and generate net thrust for the vesicle. We provided a continuum formulation governing the dynamics of the vesicle-ABPs system and explicitly analyzed its behavior in the limits of weak interior flow and small activity gradient. For the composite system as a whole, it moves by jet propulsion at low Reynolds number, i.e., fluid is drawn in from one side of the vesicle and expels from the other. The encapsulation of ABPs only provides a mechanism to generate such a seepage flow.

We emphasize that in the present model it is the concentration gradient rather than the species of the solute particles that is ultimately responsible for vesicle locomotion. Any osmotic solute, not necessarily active, is able to propel the vesicle so long as a concentration gradient is maintained. For a passive solute, one can maintain a concentration gradient using chemical reaction, e.g., by placing a distribution of sources and sinks. In this Chapter, we analyzed how such a concentration gradient may be generated by an activity gradient or by the application of an external orienting field. For magnetotactic bacteria or synthetic active particles, an aligning magnetic field can be used to control the direction of the concentration gradient and therefore the direction of motion of the vesicle.

In obtaining the results we assumed that the ABPs can be treated as a continuum and only contribute to the suspension stress via the osmotic pressure. We note that additional constitutive models at the continuum level for the suspension stress can be readily incorporated into our model. The hydrodynamic interactions of the active particles with each other or the confining vesicle boundary is neglected. These effects can be studied using a colloidal approach by considering the detailed interactions among the active particles and with the boundary. For example, this is considered in the study of a single squirmer encapsulated in a porous container by Marshall and Brady (2021) and for the case of a collection of squirmers inside a droplet that is immersed in another fluid by Huang et al. (2020).

To achieve net motion of the spherical vesicle, a number density distribution at the vesicle interior wall that breaks the front-back symmetry is required. Instead of maintaining an asymmetric density distribution in a spherical vesicle using ABPs with spatially-varying properties or ABPs with constant properties but in an orienting field, one can also consider an asymmetric vesicle. For ABPs with constant properties confined in an asymmetric container, a symmetry-breaking density distribution will emerge because the accumulation of ABPs at the wall depends on the local curvature. The effect of vesicle shape on its net motion is left for a future study.

The enhancement of transport revealed by our study may be useful for the development of synthetic microscale propelling systems for the purpose of delivery of therapeutic payloads, penetrating complex media, or clearing clogged arteries. We hope that our proposed theoretical designs can prompt new experimental implementations.

7.6 Appendix:Brownian dynamics simulations

The dynamics of ABPs confined inside the vesicle in an external orienting field can be resolved using Brownian dynamics (BD) simulations. Each ABP follows the Langevin equations of motion given by

$$\mathbf{0} = -\zeta\left(\boldsymbol{U} - U_s\boldsymbol{q}\right) + \boldsymbol{F}^B + \boldsymbol{F}^w \quad \text{and} \quad \mathbf{0} = -\zeta_R\boldsymbol{\Omega} + \boldsymbol{L}^B + \boldsymbol{L}^e, \tag{7.122}$$

where $\boldsymbol{U}$ ($\boldsymbol{\Omega}$) is the instantaneous linear (angular) velocity, $\boldsymbol{F}^B$ is the Brownian force, $\boldsymbol{F}^w$ is the hard-sphere force due to collisions with the interior wall, ζ_R is the rotary Stokes drag coefficient, $\boldsymbol{L}^B$ is the Brownian torque, and $\boldsymbol{L}^e$ is the external torque due to the field.

The Brownian force and torque satisfy the white noise statistics: $\overline{\boldsymbol{F}^B} = \mathbf{0}$, $\overline{\boldsymbol{F}^B(0)\boldsymbol{F}^B(t)} = 2k_BT\zeta\delta(t)\boldsymbol{I}$, and $\overline{\boldsymbol{L}^B} = \mathbf{0}$, $\overline{\boldsymbol{L}^B(0)\boldsymbol{L}^B(t)} = 2\zeta_R^2\delta(t)\boldsymbol{I}/\tau_R$. Here, $\delta(t)$ is the delta function. In the BD simulations, the particle orientations are represented using unit quaternions. At each time step, the instantaneous particle velocities are computed and then used to update the positions and orientations. The kinematic equation relating the angular velocity and the rate-of-change of the quaternion is given by Delong et al. (2015).

In figure 7.4, all data points are obtained by averaging over the long-time behavior of the system. In each simulation, 10^5 noninteracting ABPs are used, and the system is evolved for a sufficiently long time such that the steady state is reached.

7.7 Appendix: Equations for h_1, h_2 and h_3

In this appendix we provide the detail on the derivation of the ODEs for h_1, h_2, and h_3. Note that the conservation

$$\int_{|\boldsymbol{x}|\le\Delta} n_1 d\boldsymbol{x} = 0 \tag{7.123}$$

is satisfied.

Note that

$$\nabla f(r) = \boldsymbol{x}\frac{1}{r}f', \tag{7.124}$$

and

$$\nabla(\boldsymbol{e}\cdot\boldsymbol{x}f) = \boldsymbol{e}f + \boldsymbol{e}\cdot\boldsymbol{x}\boldsymbol{x}\frac{1}{r}f'. \tag{7.125}$$

Using the identity

$$\nabla\cdot(\underbrace{\boldsymbol{x}\boldsymbol{x}\cdots\boldsymbol{x}}_{k}f(r)) = [(d+k-1)f + rf']\underbrace{\boldsymbol{x}\boldsymbol{x}\cdots\boldsymbol{x}}_{k-1}, \tag{7.126}$$

we can obtain

$$\begin{aligned}\nabla\cdot[\boldsymbol{e}\cdot\boldsymbol{x}\boldsymbol{x}f(r)] &= \boldsymbol{e}\cdot[\nabla\cdot(\boldsymbol{x}\boldsymbol{x}f(r))] = \boldsymbol{e}\cdot\boldsymbol{x}(4f+rf'), & (7.127)\\ \nabla\cdot[\boldsymbol{e}\cdot\boldsymbol{x}\boldsymbol{x}\boldsymbol{x}f(r)] &= \boldsymbol{e}\cdot[\nabla\cdot(\boldsymbol{x}\boldsymbol{x}\boldsymbol{x}f(r))] = \boldsymbol{e}\cdot\boldsymbol{x}\boldsymbol{x}(5f+rf'). & (7.128)\\ & & (7.129)\end{aligned}$$

Similarly, we have

$$\nabla^2 f = \frac{2}{r}f' + f'', \tag{7.130}$$

$$\nabla^2[\boldsymbol{e}\cdot\boldsymbol{x}f] = \boldsymbol{e}\cdot\boldsymbol{x}\left(\frac{4f'}{r} + f''\right), \tag{7.131}$$

$$\nabla^2(\boldsymbol{e}\cdot\boldsymbol{x}\boldsymbol{x}f(r)) = 2\boldsymbol{e}f + \boldsymbol{e}\cdot\boldsymbol{x}\boldsymbol{x}\left(\frac{6}{r}f' + f''\right). \tag{7.132}$$

The equation for h_1 is given by

$$\begin{aligned}&\alpha Da\frac{dn_0}{dr}\left(\frac{1}{r}A_2 + \frac{2}{3}rA_3 + \frac{r}{2\beta Da}A_1\right) + Pe_s\left(\frac{1}{r}\frac{dh_2}{dr} + 4h_3 + r\frac{dh_3}{dr}\right)\\ &+Pe_s\left(4f + r\frac{df}{dr}\right) - \frac{4}{r}\frac{dh_1}{dr} - \frac{d^2h_1}{dr^2} = 0.\end{aligned} \tag{7.133}$$

The no-flux condition is given by

$$Pe_s(r^2f+h_2+r^2h_3)-h_1-r\frac{dh_1}{dr}+A_2\alpha Dan_0+\frac{\alpha}{6\beta}r^2n_0(3A_1+4A_3Da\beta)=0, \tag{7.134}$$

evaluated at $r=\Delta$. The governing equation for h_2 is

$$\begin{aligned}&\alpha Da\left(A_2-\frac{1}{3}r^2A_3\right)f+\frac{1}{3}Pe_s\left(n_0+h_1\right)-\frac{2}{r}\frac{dh_2}{dr}-\frac{d^2h_2}{dr^2}-2h_3\\&+2\gamma^2h_2+\frac{1}{2}\alpha Da\left(\frac{5}{3}A_3+\frac{A_2}{2\beta Da}\right)r^2f=0.\end{aligned} \tag{7.135}$$

The no-flux condition at $r=\Delta$ is

$$\frac{dh_2}{dr}=0. \tag{7.136}$$

The governing equation for h_3 is

$$\begin{aligned}&\alpha Da\left(A_3+\frac{A_1}{2\beta Da}\right)f+\alpha Da\frac{1}{r}\frac{df}{dr}\left(A_2+\frac{2}{3}r^2A_3+\frac{A_1r^2}{2\beta Da}\right)\\&+\frac{1}{3}Pe_s\frac{1}{r}\left(\frac{dn_0}{dr}+\frac{dh_1}{dr}\right)-\frac{6}{r}\frac{dh_3}{dr}-\frac{d^2h_3}{dr^2}\\&+2\gamma^2h_3-\frac{1}{2}\alpha Da\left(\frac{5}{3}A_3+\frac{A_2}{2\beta Da}\right)f=0.\end{aligned} \tag{7.137}$$

The no-flux condition is

$$\alpha Darf\left(A_2+\frac{2}{3}r^2A_3+\frac{r^2A_1}{2\beta Da}\right)+\frac{1}{3}Pe_sr(n_0+h_1)-2rh_3-r^2\frac{dh_3}{dr}=0, \tag{7.138}$$

evaluated at $r=\Delta$. We solve these equations in MATLAB using a Chebyshev collocation method Trefethen (2000).

Chapter 8

CONCLUSIONS AND OUTLOOK

8.1 Conclusions

In this thesis, I presented a series of theoretical and computational studies on the transport and microrheology of active colloids. In free space and in the absence of external flow, active colloids exhibit enhanced diffusive transport at long times due to their swim diffusivity. To understand the transport of active colloids in Poiseuille flow, a generalized Taylor dispersion theory is developed in Chapter 2 and used to characterize the long-time transport behavior. In particular, I showed that the vorticity-induced rotation allows active colloids to swim upstream provided that their swim speed is large enough compared to the flow speed. I also showed that the interplay between the swim diffusivity and the classical Taylor dispersion gives rise to a non-monotonic dispersion behavior as a function of the flow speed. These interesting behaviors of active colloids in Poiseuille flow result from the combined effects of channel confinement and the background flow. To understand the effect of swimmer shape on the dynamics and transport, active ellipsoidal colloids are considered in Chapter 3. The steric interaction between the ellipsoidal particle and the channel walls gives rise to wall-induced rotation that tends to align the particles with the wall.

In Chapters 4-6, I considered the microrheology of active colloids by tracking the dynamics of a colloidal probe particle. In the absence of hydrodynamic interactions, I showed that active colloids exhibit a swim-thinning behavior in the low-Pe limit. For large Pe, the probe speed is much larger than the swim speed of active colloids, the microviscosity is indistinguishable from that of passive colloids. Because of a thermodynamic uncertainty relation, one cannot meaningfully quantify the fluctuations in the external force if the probe velocity is prescribed. To resolve this difficulty, a generalized microrheology model is considered in which the probe is trapped by a moving harmonic trap.

In the microrheology problem, the probe motion drives an asymmetric number density distribution around the probe, which ultimately leads to a net force on the probe. To exploit this density asymmetry, in Chapter 7 I considered a composite propulsion system in which active colloids are encapsulated inside a vesicle with a semi-permeable membrane. By immersing the vesicle system in water and allowing water to pass through the membrane, the vesicle can self-propel provided that an asymmetric number density inside the vesicle is maintained.

8.2 Outlook

This thesis constitutes a theoretical study on the dynamics of active colloids in flow and under confinement. In particular, the focus was on the transport of active colloids in channel flows and the particle-tracking microrheology of active colloids. In the majority of this thesis, the dynamics of a single particle is considered and the hydrodynamic interactions among particles or between the particle and the boundary are neglected.

In the microrheology problem, I showed that by considering the disturbance flow of the active colloids or the probe, a negative microviscosity can be obtained. This analysis suggests that hydrodynamic interactions are important in the accurate quantification of the microrheology of active colloids. For passive colloids, hydrodynamic interaction between particles gives rise to a force-thickening behavior in the large *Pe* limit (Khair and Brady 2006; Swan and Zia 2013). An important future direction is to study the microrheology of active colloids with finite volume fractions and including full hydrodynamic interactions. This problem can be studied by using a particle-based simulation technique such as Stokesian dynamics (Brady and Bossis 1988).

Another issue for future consideration is the effect of shape on the dynamics of active colloids. For example, in Chapter 3 the dynamics of an active ellipsoidal particle in Poiseuille flow is considered. Even in the absence of hydrodynamic interactions, the steric interaction between the ellipsoid and the channel walls gives rise to alignment with the walls. Many biological microswimmers have a nonspherical shape and the effect of shape anisotropy or asymmetry on their dynamics is not well understood.

Bibliography

R. Alonso-Matilla, B. Chakrabarti, and D. Saintillan. Transport and dispersion of active particles in periodic porous media. *Phys. Rev. Fluids*, 4:043101, Apr 2019. doi: 10.1103/PhysRevFluids.4.043101.

R. Aris. On the dispersion of a solute in a fluid flowing through a tube. *Proc. R. Soc. A*, 235(1200):67–77, 1956. doi: 10.1098/rspa.1956.0065.

J. Arlt, V. A. Martinez, A. Dawson, T. Pilizota, and W. C. Poon. Dynamics-dependent density distribution in active suspensions. *Nat. Commun.*, 10(1):1–7, 2019. doi: 10.1038/s41467-019-10283-0.

Y. A. Ayala, B. Pontes, D. S. Ether, L. B. Pires, G. R. Araujo, S. Frases, L. F. Romão, M. Farina, V. Moura-Neto, N. B. Viana, et al. Rheological properties of cells measured by optical tweezers. *BMC Biophys.*, 9(1):1–11, 2016. doi: 10.1186/s13628-016-0031-4.

L. Baraban, R. Streubel, D. Makarov, L. Han, D. Karnaushenko, O. G. Schmidt, and G. Cuniberti. Fuel-free locomotion of Janus motors: magnetically induced thermophoresis. *ACS Nano*, 7(2):1360–1367, 2013.

R. N. Bearon. An extension of generalized Taylor dispersion in unbounded homogeneous shear flows to run-and-tumble chemotactic bacteria. *Phys. Fluids*, 15(6): 1552–1563, 2003. doi: 10.1063/1.1569482.

R. N. Bearon, A. L. Hazel, and G. J. Thorn. The spatial distribution of gyrotactic swimming micro-organisms in laminar flow fields. *J. Fluid Mech.*, 680:602–635, 2011. doi: 10.1017/jfm.2011.198.

G. S. Beavers and D. D. Joseph. Boundary conditions at a naturally permeable wall. *J. Fluid Mech.*, 30(1):197–207, 1967. doi: 10.1017/S0022112067001375.

C. Bechinger, R. Di Leonardo, H. Löwen, C. Reichhardt, G. Volpe, and G. Volpe. Active particles in complex and crowded environments. *Rev. Mod. Phys.*, 88: 045006, Nov 2016. doi: 10.1103/RevModPhys.88.045006.

M. A. Bees and O. A. Croze. Dispersion of biased swimming micro-organisms in a fluid flowing through a tube. *Proc. R. Soc. A*, 466(2119):2057–2077, 2010. ISSN 1364-5021. doi: 10.1098/rspa.2009.0606.

H. C. Berg. *Random walks in biology*. Princeton University Press, 1993.

A. P. Berke, L. Turner, H. C. Berg, and E. Lauga. Hydrodynamic attraction of swimming microorganisms by surfaces. *Phys. Rev. Lett.*, 101:038102, Jul 2008. doi: 10.1103/PhysRevLett.101.038102.

J.-F. Berret. Local viscoelasticity of living cells measured by rotational magnetic spectroscopy. *Nat. Commun.*, 7(1):1–9, 2016. doi: 10.1038/ncomms10134.

L. Bianchi, D. Angelini, and F. Lacquaniti. Individual characteristics of human walking mechanics. *Pflügers Archiv*, 436(3):343–356, 1998.

J. R. Blake. A spherical envelope approach to ciliary propulsion. *J. Fluid Mech.*, 46(1):199–208, 1971. doi: 10.1017/S002211207100048X.

R. W. Blake. *Fish locomotion*. CUP Archive, 1983.

J. F. Brady. Brownian motion, hydrodynamics, and the osmotic pressure. *J. Chem. Phys.*, 98(4):3335–3341, 1993. doi: 10.1063/1.464105.

J. F. Brady and G. Bossis. Stokesian dynamics. *Annu. Rev. Fluid Mech.*, 20(1): 111–157, 1988.

C. Brennen and H. Winet. Fluid mechanics of propulsion by cilia and flagella. *Annu. Rev. Fluid Mech.*, 9(1):339–398, 1977. doi: 10.1146/annurev.fl.09.010177.002011.

H. Brenner. Dispersion resulting from flow through spatially periodic porous media. *Philos. Trans. Royal Soc. A*, 297(1430):81–133, 1980. doi: 10.1098/rsta.1980.0205.

H. Brenner and A. D. Edwards. *Macrotransport processes*. Elsevier, 2013.

F. P. Bretherton. The motion of rigid particles in a shear flow at low reynolds number. *J. Fluid Mech.*, 14(2):284–304, 1962. doi: 10.1017/S002211206200124X.

A.-I. Bunea and R. Taboryski. Recent advances in microswimmers for biomedical applications. *Micromachines*, 11(12), 2020. ISSN 2072-666X. doi: 10.3390/mi11121048.

E. W. Burkholder and J. F. Brady. Tracer diffusion in active suspensions. *Phys. Rev. E*, 95:052605, May 2017. doi: 10.1103/PhysRevE.95.052605.

E. W. Burkholder and J. F. Brady. Do hydrodynamic interactions affect the swim pressure? *Soft Matter*, 14:3581–3589, 2018. doi: 10.1039/C8SM00197A.

E. W. Burkholder and J. F. Brady. Fluctuation-dissipation in active matter. *J. Chem. Phys.*, 150(18):184901, 2019. doi: 10.1063/1.5081725.

E. W. Burkholder and J. F. Brady. Nonlinear microrheology of active Brownian suspensions. *Soft Matter*, 16:1034–1046, 2020. doi: 10.1039/C9SM01713E.

I. C. Carpen and J. F. Brady. Microrheology of colloidal dispersions by Brownian dynamics simulations. *J. Rheol.*, 49(6):1483–1502, 2005. doi: 10.1122/1.2085174.

M. E. Cates and J. Tailleur. When are active Brownian particles and run-and-tumble particles equivalent? consequences for motility-induced phase separation. *Europhys. Lett.*, 101(2):20010, 2013.

M. E. Cates and J. Tailleur. Motility-induced phase separation. *Annu. Rev. Condens. Matter Phys.*, 6(1):219–244, 2015.

H. Chen and J.-L. Thiffeault. Shape matters: a Brownian microswimmer in a channel. *J. Fluid Mech.*, 916, 2021.

S. Chilukuri, C. H. Collins, and P. T. Underhill. Impact of external flow on the dynamics of swimming microorganisms near surfaces. *J. Phys.: Condens. Matter*, 26(11):115101, mar 2014. doi: 10.1088/0953-8984/26/11/115101.

S. Chilukuri, C. H. Collins, and P. T. Underhill. Dispersion of flagellated swimming microorganisms in planar Poiseuille flow. *Phys. Fluids*, 27(3):031902, 2015. doi: 10.1063/1.4914129.

D. D. Chin and D. Lentink. Flapping wing aerodynamics: from insects to vertebrates. *J. Exp. Biol.*, 219(7):920–932, 04 2016. ISSN 0022-0949. doi: 10.1242/jeb.042317.

J. Y. Y. Chui, C. Douarche, H. Auradou, and R. Juanes. Rheology of bacterial superfluids in viscous environments. *Soft Matter*, 17:7004–7013, 2021. doi: 10.1039/D1SM00243K.

A. Chwang and T. Y. Wu. A note on the helical movement of micro-organisms. *Proc. R. Soc. B*, 178(1052):327–346, 1971.

P. Cicuta and A. M. Donald. Microrheology: a review of the method and applications. *Soft matter*, 3(12):1449–1455, 2007.

A. Costanzo, R. D. Leonardo, G. Ruocco, and L. Angelani. Transport of self-propelling bacteria in micro-channel flow. *J. Phys. Condens. Matter*, 24(6): 065101, jan 2012. doi: 10.1088/0953-8984/24/6/065101.

O. A. Croze, G. Sardina, M. Ahmed, M. A. Bees, and L. Brandt. Dispersion of swimming algae in laminar and turbulent channel flows: consequences for photobioreactors. *J. R. Soc. Interface*, 10(81), 2013. ISSN 1742-5689. doi: 10.1098/rsif.2012.1041.

A. Dehkharghani, N. Waisbord, J. Dunkel, and J. S. Guasto. Bacterial scattering in microfluidic crystal flows reveals giant active Taylor–Aris dispersion. *Proc. Natl. Acad. Sci. USA*, 116(23):11119–11124, 2019. ISSN 0027-8424. doi: 10.1073/pnas.1819613116.

J. D. DeLaurier. An aerodynamic model for flapping-wing flight. *Aeronaut. J.*, 97 (964):125–130, 1993.

S. Delong, F. Balboa Usabiaga, and A. Donev. Brownian dynamics of confined rigid bodies. *J. Chem. Phys.*, 143(14):144107, 2015. doi: 10.1063/1.4932062.

J. K. G. Dhont, G. W. Park, and W. J. Briels. Motility-induced inter-particle correlations and dynamics: a microscopic approach for active Brownian particles. *Soft Matter*, 17:5613–5632, 2021. doi: 10.1039/D1SM00426C.

M. Doi, S. F. Edwards, and S. F. Edwards. *The theory of polymer dynamics*, volume 73. Oxford University Press, 1988.

J. Donelan, R. Kram, and A. D. Kuo. Simultaneous positive and negative external mechanical work in human walking. *J. Biomech.*, 35(1):117–124, 2002. ISSN 0021-9290. doi: 10.1016/S0021-9290(01)00169-5.

K. D. Dorfman and H. Brenner. Generalized Taylor-Aris dispersion in discrete spatially periodic networks: Microfluidic applications. *Phys. Rev. E*, 65:021103, Jan 2002. doi: 10.1103/PhysRevE.65.021103.

R. Dreyfus, J. Baudry, M. L. Roper, M. Fermigier, H. A. Stone, and J. Bibette. Microscopic artificial swimmers. *Nature*, 437(7060):862–865, 2005.

A. R. Dulaney and J. F. Brady. Waves in active matter: The transition from ballistic to diffusive behavior. *Phys. Rev. E*, 101:052609, May 2020. doi: 10.1103/PhysRevE.101.052609.

G. J. Elfring. A note on the reciprocal theorem for the swimming of simple bodies. *Phys. Fluids*, 27(2):023101, 2015. doi: 10.1063/1.4906993.

J. Elgeti and G. Gompper. Wall accumulation of self-propelled spheres. *Europhys. Lett.*, 101(4):48003, feb 2013. doi: 10.1209/0295-5075/101/48003.

J. Elgeti, R. G. Winkler, and G. Gompper. Physics of microswimmers–single particle motion and collective behavior: a review. *Rep. Prog. Phys.*, 78(5):056601, 2015. doi: 10.1088/0034-4885/78/5/056601.

P. Erkoc, I. C. Yasa, H. Ceylan, O. Yasa, Y. Alapan, and M. Sitti. Mobile microrobots for active therapeutic delivery. *Adv. Ther.*, 2(1):1800064, 2019. doi: 10.1002/adtp.201800064.

B. Ezhilan and D. Saintillan. Transport of a dilute active suspension in pressure-driven channel flow. *J. Fluid Mech.*, 777:482–522, 2015.

O. Felfoul, M. Mohammadi, S. Taherkhani, D. De Lanauze, Y. Z. Xu, D. Loghin, S. Essa, S. Jancik, D. Houle, M. Lafleur, et al. Magneto-aerotactic bacteria deliver drug-containing nanoliposomes to tumour hypoxic regions. *Nat. Nanotechnol.*, 11(11):941–947, 2016. doi: 10.1038/nnano.2016.137.

G. Foffano, J. Lintuvuori, A. Morozov, K. Stratford, M. Cates, and D. Marenduzzo. Bulk rheology and microrheology of active fluids. *Eur. Phys. J. E.*, 35(10):1–11, 2012.

D. R. Foss and J. F. Brady. Brownian dynamics simulation of hard-sphere colloidal dispersions. *J. Rheol.*, 44(3):629–651, 2000. doi: 10.1122/1.551104.

I. Frankel and H. Brenner. On the foundations of generalized Taylor dispersion theory. *J. Fluid Mech.*, 204:97–119, 1989. doi: 10.1017/S0022112089001679.

X. Gao, L. Yang, J. A. Petros, F. F. Marshall, J. W. Simons, and S. Nie. In vivo molecular and cellular imaging with quantum dots. *Curr. Opin. Biotech.*, 16(1): 63–72, 2005. ISSN 0958-1669. doi: 10.1016/j.copbio.2004.11.003.

J. G. Gibbs and Y.-P. Zhao. Autonomously motile catalytic nanomotors by bubble propulsion. *Appl. Phys. Lett.*, 94(16):163104, 2009.

J. Gray and G. J. Hancock. The propulsion of sea-urchin spermatozoa. *J. Exp. Biol.*, 32(4):802–814, 12 1955. ISSN 0022-0949. doi: 10.1242/jeb.32.4.802.

E. Guazzelli and J. F. Morris. *A physical introduction to suspension dynamics*, volume 45. Cambridge University Press, 2011.

S. Guo, D. Samanta, Y. Peng, X. Xu, and X. Cheng. Symmetric shear banding and swarming vortices in bacterial superfluids. *Proc. Natl. Acad. Sci. USA*, 115(28): 7212–7217, 2018. ISSN 0027-8424. doi: 10.1073/pnas.1722505115.

B. M. Haines, A. Sokolov, I. S. Aranson, L. Berlyand, and D. A. Karpeev. Three-dimensional model for the effective viscosity of bacterial suspensions. *Phys. Rev. E*, 80:041922, Oct 2009. doi: 10.1103/PhysRevE.80.041922.

Y. Hatwalne, S. Ramaswamy, M. Rao, and R. A. Simha. Rheology of active-particle suspensions. *Phys. Rev. Lett.*, 92:118101, Mar 2004. doi: 10.1103/PhysRevLett.92.118101.

F. Hecht. New development in freefem++. *J. Numer. Math.*, 20(3-4):251–265, 2012. ISSN 1570-2820.

D. Heyes and J. Melrose. Brownian dynamics simulations of model hard-sphere suspensions. *J. Non-Newtonian Fluid Mech.*, 46(1):1 – 28, 1993. ISSN 0377-0257. doi: 10.1016/0377-0257(93)80001-R.

J. Higdon. The hydrodynamics of flagellar propulsion: helical waves. *J. Fluid Mech.*, 94(2):331–351, 1979.

J. Hill, O. Kalkanci, J. L. McMurry, and H. Koser. Hydrodynamic surface interactions enable Escherichia coli to seek efficient routes to swim upstream. *Phys. Rev. Lett.*, 98:068101, Feb 2007. doi: 10.1103/PhysRevLett.98.068101.

N. A. Hill and M. A. Bees. Taylor dispersion of gyrotactic swimming microorganisms in a linear flow. *Phys. Fluids*, 14(8):2598–2605, 2002. doi: 10.1063/1.1458003.

J. R. Howse, R. A. L. Jones, A. J. Ryan, T. Gough, R. Vafabakhsh, and R. Golestanian. Self-motile colloidal particles: From directed propulsion to random walk. *Phys. Rev. Lett.*, 99:048102, Jul 2007. doi: 10.1103/PhysRevLett.99.048102.

J. Hu, S. Jafari, Y. Han, A. J. Grodzinsky, S. Cai, and M. Guo. Size- and speed-dependent mechanical behavior in living mammalian cytoplasm. *Proc. Natl. Acad. Sci. USA*, 114(36):9529–9534, 2017. ISSN 0027-8424. doi: 10.1073/pnas.1702488114.

Z. Huang, T. Omori, and T. Ishikawa. Active droplet driven by a collective motion of enclosed microswimmers. *Phys. Rev. E*, 102:022603, Aug 2020. doi: 10.1103/PhysRevE.102.022603.

L. A. Jackson, E. J. Anderson, N. G. Rouphael, P. C. Roberts, M. Makhene, R. N. Coler, M. P. McCullough, J. D. Chappell, M. R. Denison, L. J. Stevens, A. J. Pruijssers, A. McDermott, B. Flach, N. A. Doria-Rose, K. S. Corbett, K. M. Morabito, S. O'Dell, S. D. Schmidt, P. A. Swanson, M. Padilla, J. R. Mascola, K. M. Neuzil, H. Bennett, W. Sun, E. Peters, M. Makowski, J. Albert, K. Cross, W. Buchanan, R. Pikaart-Tautges, J. E. Ledgerwood, B. S. Graham, and J. H. Beigel. An mRNA vaccine against SARS-CoV-2 — preliminary report. *N. Engl. J. Med.*, 383(20):1920–1931, 2020. doi: 10.1056/NEJMoa2022483.

G. B. Jeffery. The motion of ellipsoidal particles immersed in a viscous fluid. *Proc. R. Soc. A*, 102(715):161–179, 1922. doi: 10.1098/rspa.1922.0078.

A. Jepson, V. A. Martinez, J. Schwarz-Linek, A. Morozov, and W. C. K. Poon. Enhanced diffusion of nonswimmers in a three-dimensional bath of motile bacteria. *Phys. Rev. E*, 88:041002, Oct 2013. doi: 10.1103/PhysRevE.88.041002.

W. Jiang and G. Chen. Dispersion of active particles in confined unidirectional flows. *J. Fluid Mech.*, 877:1–34, 2019. doi: 10.1017/jfm.2019.562.

W. Jiang and G. Chen. Transient dispersion process of active particles. *J. Fluid Mech.*, 927:A11, 2021. doi: 10.1017/jfm.2021.747.

I. P. Jones. Low reynolds number flow past a porous spherical shell. *Proc. Camb. Phil. Soc.*, 73(1):231–238, 1973. doi: 10.1017/S0305004100047642.

G. Junot, N. Figueroa-Morales, T. Darnige, A. Lindner, R. Soto, H. Auradou, and E. Clément. Swimming bacteria in Poiseuille flow: The quest for active bretherton-jeffery trajectories. *Europhy. Lett.*, 126(4):44003, jun 2019. doi: 10.1209/0295-5075/126/44003.

A. Kaiser, A. Peshkov, A. Sokolov, B. ten Hagen, H. Löwen, and I. S. Aranson. Transport powered by bacterial turbulence. *Phys. Rev. Lett.*, 112:158101, Apr 2014. doi: 10.1103/PhysRevLett.112.158101.

V. Kantsler, J. Dunkel, M. Blayney, and R. E. Goldstein. Rheotaxis facilitates upstream navigation of mammalian sperm cells. *Elife*, 3, 2014. doi: 10.7554/eLife.02403.

C. Y. Kao, W. H. Lin, C. C. Tseng, A. B. Wu, M. C. Wang, and J. J. Wu. The complex interplay among bacterial motility and virulence factors in different escherichia coli infections. *Eur. J. Clin. Microbiol. Infect. Dis.*, 33(12):2157–2162, Dec 2014. ISSN 1435-4373. doi: 10.1007/s10096-014-2171-2.

T. Kaya and H. Koser. Characterization of hydrodynamic surface interactions of escherichia coli cell bodies in shear flow. *Phys. Rev. Lett.*, 103:138103, Sep 2009. doi: 10.1103/PhysRevLett.103.138103.

T. Kaya and H. Koser. Direct upstream motility in Escherichia coli. *Biophys. J.*, 102 (7):1514 – 1523, 2012. ISSN 0006-3495. doi: 10.1016/j.bpj.2012.03.001.

A. S. Khair and J. F. Brady. “Microviscoelasticity” of colloidal dispersions. *J. Rheol.*, 49(6):1449–1481, 2005. doi: 10.1122/1.2085173.

A. S. Khair and J. F. Brady. Single particle motion in colloidal dispersions: a simple model for active and nonlinear microrheology. *J. Fluid Mech.*, 557:73–117, 2006. doi: 10.1017/S0022112006009608.

M. K. Kim, K. Drescher, O. S. Pak, B. L. Bassler, and H. A. Stone. Filaments in curved streamlines: rapid formation of *Staphylococcus aureus* biofilm streamers. *New J. Phys.*, 16(6):065024, jun 2014. doi: 10.1088/1367-2630/16/6/065024.

S. Kim and S. J. Karrila. *Microhydrodynamics: principles and selected applications*. Butterworth-Heinemann, 1991. doi: 10.1016/C2013-0-04644-0.

C. M. Kjeldbjerg and J. F. Brady. Theory for the casimir effect and the partitioning of active matter. *Soft Matter*, 17(3):523–530, 2021.

D. L. Koch and G. Subramanian. Collective hydrodynamics of swimming microorganisms: Living fluids. *Annu. Rev. Fluid Mech.*, 43(1):637–659, 2011. doi: 10.1146/annurev-fluid-121108-145434.

A. H. Kumar, S. J. Thomson, T. R. Powers, and D. M. Harris. Taylor dispersion of elongated rods. *Phys. Rev. Fluids*, 6:094501, Sep 2021. doi: 10.1103/PhysRevFluids.6.094501.

G. V. Lauder. Fish locomotion: Recent advances and new directions. *Annu. Rev. Mar. Sci.*, 7(1):521–545, 2015. doi: 10.1146/annurev-marine-010814-015614. PMID: 25251278.

G. V. Lauder and E. D. Tytell. Hydrodynamics of undulatory propulsion. In *Fish Biomechanics*, volume 23 of *Fish Physiology*, pages 425–468. Academic Press, 2005. doi: 10.1016/S1546-5098(05)23011-X.

G. V. Lauder, E. J. Anderson, J. Tangorra, and P. G. Madden. Fish biorobotics: kinematics and hydrodynamics of self-propulsion. *J. Exp. Biol.*, 210(16):2767–2780, 2007.

E. Lauga. Bacterial hydrodynamics. *Annu. Rev. Fluid Mech.*, 48(1):105–130, 2016. doi: 10.1146/annurev-fluid-122414-034606.

E. Lauga and S. Michelin. Stresslets induced by active swimmers. *Phys. Rev. Lett.*, 117:148001, Sep 2016. doi: 10.1103/PhysRevLett.117.148001.

E. Lauga and T. R. Powers. The hydrodynamics of swimming microorganisms. *Rep. Prog. Phys.*, 72(9):096601, aug 2009. doi: 10.1088/0034-4885/72/9/096601.

L. G. Leal. *Advanced transport phenomena: fluid mechanics and convective transport processes*, volume 7. Cambridge University Press, 2007.

G. Li and J. X. Tang. Accumulation of microswimmers near a surface mediated by collision and rotational Brownian motion. *Phys. Rev. Lett.*, 103:078101, Aug 2009. doi: 10.1103/PhysRevLett.103.078101.

G. Li, J. Bensson, L. Nisimova, D. Munger, P. Mahautmr, J. X. Tang, M. R. Maxey, and Y. V. Brun. Accumulation of swimming bacteria near a solid surface. *Phys. Rev. E*, 84:041932, Oct 2011. doi: 10.1103/PhysRevE.84.041932.

J. Lighthill. Flagellar hydrodynamics. *SIAM Rev.*, 18(2):161–230, 1976.

M. Lighthill. On the squirming motion of nearly spherical deformable bodies through liquids at very small Reynolds numbers. *Commun. Pure Appl. Math.*, 5 (2):109–118, 1952. doi: 10.1002/cpa.3160050201.

A. Loisy, J. Eggers, and T. B. Liverpool. Active suspensions have nonmonotonic flow curves and multiple mechanical equilibria. *Phys. Rev. Lett.*, 121:018001, Jul 2018. doi: 10.1103/PhysRevLett.121.018001.

H. M. López, J. Gachelin, C. Douarche, H. Auradou, and E. Clément. Turning bacteria suspensions into superfluids. *Phys. Rev. Lett.*, 115:028301, Jul 2015. doi: 10.1103/PhysRevLett.115.028301.

E. Lushi, R. E. Goldstein, and M. J. Shelley. Collective chemotactic dynamics in the presence of self-generated fluid flows. *Phys. Rev. E*, 86:040902, Oct 2012. doi: 10.1103/PhysRevE.86.040902.

A. M. Maier, C. Weig, P. Oswald, E. Frey, P. Fischer, and T. Liedl. Magnetic propulsion of microswimmers with dna-based flagellar bundles. *Nano Lett.*, 16 (2):906–910, 2016.

S. A. Mallory, C. Valeriani, and A. Cacciuto. An active approach to colloidal self-assembly. *Annu. Rev. Phys. Chem.*, 69:59–79, 2018.

A. Manela and I. Frankel. Generalized Taylor dispersion in suspensions of gyrotactic swimming micro-organisms. *J. Fluid Mech.*, 490:99–127, 2003. doi: 10.1017/S0022112003005147.

M. C. Marchetti, J. F. Joanny, S. Ramaswamy, T. B. Liverpool, J. Prost, M. Rao, and R. A. Simha. Hydrodynamics of soft active matter. *Rev. Mod. Phys.*, 85: 1143–1189, Jul 2013. doi: 10.1103/RevModPhys.85.1143.

Marcos, H. C. Fu, T. R. Powers, and R. Stocker. Bacterial rheotaxis. *Proc. Natl. Acad. Sci. USA*, 109(13):4780–4785, 2012. ISSN 0027-8424. doi: 10.1073/pnas.1120955109.

K. J. Marshall and J. F. Brady. The hydrodynamics of an active squirming particle inside of a porous container. *J. Fluid Mech.*, 919:A31, 2021. doi: 10.1017/jfm.2021.276.

H. Masoud and H. A. Stone. The reciprocal theorem in fluid dynamics and transport phenomena. *J. Fluid Mech.*, 879:P1, 2019. doi: 10.1017/jfm.2019.553.

A. J. Mathijssen, N. Figueroa-Morales, G. Junot, É. Clément, A. Lindner, and A. Zöttl. Oscillatory surface rheotaxis of swimming E. coli bacteria. *Nat. Commun.*, 10(1):3434, 2019. doi: 10.1038/s41467-019-11360-0.

M. Medina-Sánchez, H. Xu, and O. G. Schmidt. Micro- and nano-motors: the new generation of drug carriers. *Ther. Deliv.*, 9(4):303–316, 2018. doi: 10.4155/tde-2017-0113.

A. Meyer, A. Marshall, B. G. Bush, and E. M. Furst. Laser tweezer microrheology of a colloidal suspension. *J. Rheol.*, 50(1):77–92, 2006. doi: 10.1122/1.2139098.

G. Miño, J. Dunstan, A. Rousselet, E. Clément, and R. Soto. Induced diffusion of tracers in a bacterial suspension: theory and experiments. *J. Fluid Mech.*, 729: 423–444, 2013. doi: 10.1017/jfm.2013.304.

A. Morozov and D. Marenduzzo. Enhanced diffusion of tracer particles in dilute bacterial suspensions. *Soft Matter*, 10:2748–2758, 2014. doi: 10.1039/C3SM52201F.

R. W. Nash, R. Adhikari, J. Tailleur, and M. E. Cates. Run-and-tumble particles with hydrodynamics: Sedimentation, trapping, and upstream swimming. *Phys. Rev. Lett.*, 104:258101, Jun 2010. doi: 10.1103/PhysRevLett.104.258101.

S. Nawaz, P. Sánchez, K. Bodensiek, S. Li, M. Simons, and I. A. T. Schaap. Cell visco-elasticity measured with afm and optical trapping at sub-micrometer deformations. *PLOS ONE*, 7(9):1–9, 09 2012. doi: 10.1371/journal.pone.0045297.

J. M. Nitsche and H. Brenner. On the formulation of boundary conditions for rigid nonspherical Brownian particles near solid walls: Applications to orientation-specific reactions with immobilized enzymes. *J. Colloid Interface Sci*, 138(1): 21–41, 1990. ISSN 0021-9797. doi: 10.1016/0021-9797(90)90177-P.

T. Omori and T. Ishikawa. Upward swimming of a sperm cell in shear flow. *Phys. Rev. E*, 93:032402, Mar 2016. doi: 10.1103/PhysRevE.93.032402.

O. S. Pak, W. Gao, J. Wang, and E. Lauga. High-speed propulsion of flexible nanowire motors: Theory and experiments. *Soft Matter*, 7:8169–8181, 2011. doi: 10.1039/C1SM05503H.

O. S. Pak, E. Lauga, C. Duprat, and H. Stone. *Theoretical models of low-Reynolds-number locomotion*. Royal Society of Chemistry, 2015.

B.-W. Park, J. Zhuang, O. Yasa, and M. Sitti. Multifunctional bacteria-driven microswimmers for targeted active drug delivery. *ACS Nano*, 11(9):8910–8923, 2017. doi: 10.1021/acsnano.7b03207.

B. S. Pattni, V. V. Chupin, and V. P. Torchilin. New developments in liposomal drug delivery. *Chem. Rev.*, 115(19):10938–10966, 2015. doi: 10.1021/acs.chemrev.5b00046.

W. F. Paxton, S. Sundararajan, T. E. Mallouk, and A. Sen. Chemical locomotion. *Angew. Chem. Int. Ed.*, 45(33):5420–5429, 2006. doi: 10.1002/anie.200600060.

T. J. Pedley and J. O. Kessler. A new continuum model for suspensions of gyrotactic micro-organisms. *J. Fluid Mech.*, 212:155–182, 1990. doi: 10.1017/S0022112090001914.

Z. Peng and J. F. Brady. Upstream swimming and Taylor dispersion of active Brownian particles. *Phys. Rev. Fluids*, 5:073102, Jul 2020. doi: 10.1103/PhysRevFluids.5.073102.

Z. Peng, T. Zhou, and J. F. Brady. Activity-induced propulsion of a vesicle. *arXiv preprint arXiv:2112.05904*, 2021.

M. F. Platzer, K. D. Jones, J. Young, and J. C. Lai. Flapping wing aerodynamics: progress and challenges. *AIAA J.*, 46(9):2136–2149, 2008.

A. Poncet, O. Bénichou, V. Démery, and D. Nishiguchi. Pair correlation of dilute active Brownian particles: From low-activity dipolar correction to high-activity algebraic depletion wings. *Phys. Rev. E*, 103:012605, Jan 2021. doi: 10.1103/PhysRevE.103.012605.

E. M. Purcell. Life at low reynolds number. *Am. J. Phys.*, 45(1):3–11, 1977.

E. M. Purcell. The efficiency of propulsion by a rotating flagellum. *Proc. Natl. Acad. Sci. USA*, 94(21):11307–11311, 1997.

S. Ramaswamy. The mechanics and statistics of active matter. *Annu. Rev. Condens. Matter Phys.*, 1(1):323–345, 2010. doi: 10.1146/annurev-conmatphys-070909-104101.

J. Rao, A. Dragulescu-Andrasi, and H. Yao. Fluorescence imaging in vivo: recent advances. *Curr. Opin. Biotech.*, 18(1):17–25, 2007. ISSN 0958-1669. doi: 10.1016/j.copbio.2007.01.003.

D. Ray, C. Reichhardt, and C. J. O. Reichhardt. Casimir effect in active matter systems. *Phys. Rev. E*, 90:013019, Jul 2014. doi: 10.1103/PhysRevE.90.013019.

B. Rodenborn, C.-H. Chen, H. L. Swinney, B. Liu, and H. Zhang. Propulsion of microorganisms by a helical flagellum. *Proc. Natl. Acad. Sci. USA*, 110(5): E338–E347, 2013.

P. Romanczuk, M. Bär, W. Ebeling, B. Lindner, and L. Schimansky-Geier. Active Brownian particles. *Eur. Phys. J. Spec. Top.*, 202(1):1–162, 2012.

L. Rothschild. Non-random distribution of bull spermatozoa in a drop of sperm suspension. *Nature*, 200(4904):381–381, 1963. ISSN 1476-4687. doi: 10.1038/200381a0.

H. Row and J. F. Brady. Reverse osmotic effect in active matter. *Phys. Rev. E*, 101: 062604, Jun 2020. doi: 10.1103/PhysRevE.101.062604.

R. Rusconi, S. Lecuyer, L. Guglielmini, and H. A. Stone. Laminar flow around corners triggers the formation of biofilm streamers. *J. R. Soc. Interface*, 7(50): 1293–1299, 2010. doi: 10.1098/rsif.2010.0096.

S. D. Ryan, B. M. Haines, L. Berlyand, F. Ziebert, and I. S. Aranson. Viscosity of bacterial suspensions: Hydrodynamic interactions and self-induced noise. *Phys. Rev. E*, 83:050904, May 2011. doi: 10.1103/PhysRevE.83.050904.

P. G. Saffman. On the boundary condition at the surface of a porous medium. *Stud. Appl. Math.*, 50(2):93–101, 1971. doi: 10.1002/sapm197150293.

D. Saintillan. The dilute rheology of swimming suspensions: A simple kinetic model. *Exp. Mech.*, 50(9):1275–1281, 2010. doi: 10.1007/s11340-009-9267-0.

D. Saintillan and M. J. Shelley. Active suspensions and their nonlinear models. *C. R. Phys.*, 14(6):497–517, 2013.

D. Saintillan and M. J. Shelley. *Theory of Active Suspensions*, pages 319–355. Springer New York, New York, NY, 2015. ISBN 978-1-4939-2065-5. doi: 10.1007/978-1-4939-2065-5_9.

M. J. Schnitzer. Theory of continuum random walks and application to chemotaxis. *Phys. Rev. E*, 48:2553–2568, Oct 1993. doi: 10.1103/PhysRevE.48.2553.

M. Shapiro and H. Brenner. Taylor dispersion of chemically reactive species: Irreversible first-order reactions in bulk and on boundaries. *Chem. Eng. Sci.*, 41 (6):1417 – 1433, 1986. ISSN 0009-2509. doi: 10.1016/0009-2509(86)85228-9.

M. Shapiro and H. Brenner. Chemically reactive generalized Taylor dispersion phenomena. *AIChE J.*, 33(7):1155–1167, 1987. doi: 10.1002/aic.690330710.

J. Shen, T. Tang, and L.-L. Wang. *Spectral methods: algorithms, analysis and applications*, volume 41. Springer Science & Business Media, 2011.

Y. Shen, A. Siryaporn, S. Lecuyer, Z. Gitai, and H. A. Stone. Flow directs surface-attached bacteria to twitch upstream. *Biophys. J.*, 103(1):146 – 151, 2012. ISSN 0006-3495. doi: 10.1016/j.bpj.2012.05.045.

W. Shyy, H. Aono, S. K. Chimakurthi, P. Trizila, C.-K. Kang, C. E. Cesnik, and H. Liu. Recent progress in flapping wing aerodynamics and aeroelasticity. *Prog. Aero. Sci.*, 46(7):284–327, 2010.

A. Siitonen and M. Nurminen. Bacterial motility is a colonization factor in experimental urinary tract infection. *Infect. Immun.*, 60(9):3918–3920, 1992. ISSN 0019-9567.

A. V. Singh, Z. Hosseinidoust, B.-W. Park, O. Yasa, and M. Sitti. Microemulsion-based soft bacteria-driven microswimmers for active cargo delivery. *ACS Nano*, 11(10):9759–9769, 2017. doi: 10.1021/acsnano.7b02082.

A. V. Singh, M. H. D. Ansari, P. Laux, and A. Luch. Micro-nanorobots: important considerations when developing novel drug delivery platforms. *Expert Opin. Drug Deliv.*, 16(11):1259–1275, 2019. doi: 10.1080/17425247.2019.1676228.

A. Sokolov, M. M. Apodaca, B. A. Grzybowski, and I. S. Aranson. Swimming bacteria power microscopic gears. *Proc. Natl. Acad. Sci. USA*, 107(3):969–974, 2010. ISSN 0027-8424. doi: 10.1073/pnas.0913015107.

A. P. Solon, M. E. Cates, and J. Tailleur. Active Brownian particles and run-and-tumble particles: A comparative study. *Eur. Phys. J. Spec. Top.*, 224(7): 1231–1262, 2015.

S. E. Spagnolie and E. Lauga. Jet propulsion without inertia. *Phys. Fluids*, 22(8): 081902, 2010. doi: 10.1063/1.3469786.

T. M. Squires and J. F. Brady. A simple paradigm for active and nonlinear microrheology. *Phys. Fluids*, 17(7):073101, 2005. doi: 10.1063/1.1960607.

H. A. Stone and A. D. T. Samuel. Propulsion of microorganisms by surface distortions. *Phys. Rev. Lett.*, 77:4102–4104, Nov 1996. doi: 10.1103/PhysRevLett.77.4102.

K. M. Stroka, H. Jiang, S.-H. Chen, Z. Tong, D. Wirtz, S. X. Sun, and K. Konstantopoulos. Water permeation drives tumor cell migration in confined microenvironments. *Cell*, 157(3):611–623, 2014. ISSN 0092-8674. doi: 10.1016/j.cell.2014.02.052.

J. W. Swan and R. N. Zia. Active microrheology: Fixed-velocity versus fixed-force. *Phys. Fluids*, 25(8):083303, 2013. doi: 10.1063/1.4818810.

J. W. Swan, R. N. Zia, and J. F. Brady. Large amplitude oscillatory microrheology. *J. Rheol.*, 58(1):1–41, 2014.

J. Tailleur and M. E. Cates. Statistical mechanics of interacting run-and-tumble bacteria. *Phys. Rev. Lett.*, 100:218103, May 2008. doi: 10.1103/PhysRevLett.100.218103.

S. C. Takatori and J. F. Brady. Towards a thermodynamics of active matter. *Phys. Rev. E*, 91:032117, Mar 2015. doi: 10.1103/PhysRevE.91.032117.

S. C. Takatori and J. F. Brady. Superfluid behavior of active suspensions from diffusive stretching. *Phys. Rev. Lett.*, 118:018003, Jan 2017. doi: 10.1103/PhysRevLett.118.018003.

S. C. Takatori, W. Yan, and J. F. Brady. Swim pressure: Stress generation in active matter. *Phys. Rev. Lett.*, 113:028103, Jul 2014. doi: 10.1103/PhysRevLett.113.028103.

S. C. Takatori and J. F. Brady. Swim stress, motion, and deformation of active matter: effect of an external field. *Soft Matter*, 10:9433–9445, 2014. doi: 10.1039/C4SM01409J.

S. C. Takatori and A. Sahu. Active contact forces drive nonequilibrium fluctuations in membrane vesicles. *Phys. Rev. Lett.*, 124:158102, Apr 2020. doi: 10.1103/PhysRevLett.124.158102.

S. C. Takatori, R. De Dier, J. Vermant, and J. F. Brady. Acoustic trapping of active matter. *Nat. Commun.*, 7(1):1–7, 2016. doi: 10.1038/ncomms10694.

A. Tasora and M. Anitescu. A matrix-free cone complementarity approach for solving large-scale, nonsmooth, rigid body dynamics. *Comput. Methods Appl. Mech. Eng.*, 200(5):439–453, 2011. ISSN 0045-7825. doi: 10.1016/j.cma.2010.06.030.

A. Tasora, D. Negrut, and M. Anitescu. Large-scale parallel multi-body dynamics with frictional contact on the graphical processing unit. *Proc. Inst. Mech. Eng., Part K: J. Multi-Body Dyn.*, 222(4):315–326, 2008. doi: 10.1243/14644193JMBD154.

G. I. Taylor. Dispersion of soluble matter in solvent flowing slowly through a tube. *Proc. R. Soc. A*, 219(1137):186–203, 1953. ISSN 0080-4630. doi: 10.1098/rspa.1953.0139.

G. I. Taylor. The dispersion of matter in turbulent flow through a pipe. *Proc. R. Soc. A*, 223(1155):446–468, 1954a. ISSN 0080-4630. doi: 10.1098/rspa.1954.0130.

G. I. Taylor. Conditions under which dispersion of a solute in a stream of solvent can be used to measure molecular diffusion. *Proc. R. Soc. A*, 225(1163):473–477, 1954b. doi: 10.1098/rspa.1954.0216.

G. I. Taylor. Analysis of the swimming of microscopic organisms. *Proc. R. Soc. A*, 209(1099):447–461, 1951.

G. I. Taylor. The action of waving cylindrical tails in propelling microscopic organisms. *Proc. R. Soc. A*, 211(1105):225–239, 1952. doi: 10.1098/rspa.1952.0035.

M. Theillard, R. Alonso-Matilla, and D. Saintillan. Geometric control of active collective motion. *Soft Matter*, 13:363–375, 2017. doi: 10.1039/C6SM01955B.

I. Theurkauff, C. Cottin-Bizonne, J. Palacci, C. Ybert, and L. Bocquet. Dynamic clustering in active colloidal suspensions with chemical signaling. *Phys. Rev. Lett.*, 108(26):268303, 2012.

V. P. Torchilin. Multifunctional nanocarriers. *Adv. Drug Deliv. Rev.*, 64:302–315, 2012. ISSN 0169-409X. doi: 10.1016/j.addr.2012.09.031.

T. Trantidou, L. Dekker, K. Polizzi, O. Ces, and Y. Elani. Functionalizing cell-mimetic giant vesicles with encapsulated bacterial biosensors. *Interface Focus*, 8 (5):20180024, 2018. doi: 10.1098/rsfs.2018.0024.

L. N. Trefethen. *Spectral Methods in MATLAB*. Society for Industrial and Applied Mathematics, 2000. doi: 10.1137/1.9780898719598.

C.-K. Tung, F. Ardon, A. Roy, D. L. Koch, S. S. Suarez, and M. Wu. Emergence of upstream swimming via a hydrodynamic transition. *Phys. Rev. Lett.*, 114:108102, Mar 2015. doi: 10.1103/PhysRevLett.114.108102.

W. E. Uspal, M. N. Popescu, S. Dietrich, and M. Tasinkevych. Self-propulsion of a catalytically active particle near a planar wall: from reflection to sliding and hovering. *Soft Matter*, 11:434–438, 2015. doi: 10.1039/C4SM02317J.

H. R. Vutukuri, M. Hoore, C. Abaurrea-Velasco, L. van Buren, A. Dutto, T. Auth, D. A. Fedosov, G. Gompper, and J. Vermant. Active particles induce large shape deformations in giant lipid vesicles. *Nature*, 586(7827):52–56, 2020. doi: 10.1038/s41586-020-2730-x.

S. Wang and N. Wu. Selecting the swimming mechanisms of colloidal particles: bubble propulsion versus self-diffusiophoresis. *Langmuir*, 30(12):3477–3486, 2014.

Z.-G. Wang. 50th anniversary perspective: Polymer conformation—a pedagogical review. *Macromolecules*, 50(23):9073–9114, 2017.

D. Weihs, T. G. Mason, and M. A. Teitell. Bio-microrheology: A frontier in microrheology. *Biophys. J.*, 91(11):4296–4305, 2006. ISSN 0006-3495. doi: 10.1529/biophysj.106.081109.

H. H. Wensink and H. Löwen. Aggregation of self-propelled colloidal rods near confining walls. *Phys. Rev. E*, 78:031409, Sep 2008. doi: 10.1103/PhysRevE.78.031409.

J. L. West and N. J. Halas. Engineered nanomaterials for biophotonics applications: Improving sensing, imaging, and therapeutics. *Annu. Rev. Biomed. Eng.*, 5(1): 285–292, 2003. doi: 10.1146/annurev.bioeng.5.011303.120723.

C. Wilhelm, F. Gazeau, and J.-C. Bacri. Rotational magnetic endosome microrheology: Viscoelastic architecture inside living cells. *Phys. Rev. E*, 67:061908, Jun 2003. doi: 10.1103/PhysRevE.67.061908.

B. J. Williams, S. V. Anand, J. Rajagopalan, and M. T. A. Saif. A self-propelled biohybrid swimmer at low reynolds number. *Nat. Commun.*, 5(1):1–8, 2014.

A. Würger. Self-diffusiophoresis of Janus particles in near-critical mixtures. *Phys. Rev. Lett.*, 115:188304, Oct 2015. doi: 10.1103/PhysRevLett.115.188304.

V. Yadav, W. Duan, P. J. Butler, and A. Sen. Anatomy of nanoscale propulsion. *Annu. Rev. Biophys.*, 44(1):77–100, 2015. doi: 10.1146/annurev-biophys-060414-034216. PMID: 26098511.

W. Yan and J. F. Brady. The swim force as a body force. *Soft Matter*, 11:6235–6244, 2015a. doi: 10.1039/C5SM01318F.

W. Yan and J. F. Brady. The force on a boundary in active matter. *J. Fluid Mech.*, 785:R1, 2015b. doi: 10.1017/jfm.2015.621.

W. Yan and J. F. Brady. The curved kinetic boundary layer of active matter. *Soft Matter*, 14:279–290, 2018. doi: 10.1039/C7SM01643C.

W. Yan, H. Zhang, and M. J. Shelley. Computing collision stress in assemblies of active spherocylinders: Applications of a fast and generic geometric method. *J. Chem. Phys*, 150(6):064109, 2019. doi: 10.1063/1.5080433.

A. Yao, M. Tassieri, M. Padgett, and J. Cooper. Microrheology with optical tweezers. *Lab Chip*, 9(17):2568–2575, 2009.

G. A. Zampogna and F. Gallaire. Effective stress jump across membranes. *J. Fluid Mech.*, 892:A9, 2020. doi: 10.1017/jfm.2020.144.

R. N. Zia. Active and passive microrheology: Theory and simulation. *Annu. Rev. Fluid Mech.*, 50(1):371–405, 2018. doi: 10.1146/annurev-fluid-122316-044514.

R. N. Zia and J. F. Brady. Single-particle motion in colloids: force-induced diffusion. *J. Fluid Mech.*, 658:188–210, 2010. doi: 10.1017/S0022112010001606.

A. Zöttl and H. Stark. Nonlinear dynamics of a microswimmer in Poiseuille flow. *Phys. Rev. Lett.*, 108:218104, May 2012. doi: 10.1103/PhysRevLett.108.218104.

A. Zöttl and H. Stark. Periodic and quasiperiodic motion of an elongated microswimmer in Poiseuille flow. *Eur. Phys. J. E*, 36(1):1–10, 2013.

Appendix A

MOMENTS OF THE SMOLUCHOWSKI EQUATION

As presented in the main text, an active Brownian particle swims with an intrinsic swim speed U_s in a direction $\boldsymbol{q}$ ($|\boldsymbol{q}| = 1$) that relaxes over time via continuous rotary diffusion characterized by the rotary diffusivity D_R. In the continuum perspective, the dynamics of an ABP can be described by the probability density function $P(\boldsymbol{x}, \boldsymbol{q}, t)$ of finding the particle at position $\boldsymbol{x}$ with orientation $\boldsymbol{q}$ at time t. As presented in the main text, the evolution of P is governed by the Smoluchowski equation:

$$\frac{\partial P}{\partial t} + \nabla \cdot \boldsymbol{j}_T + \nabla_R \cdot \boldsymbol{j}_R = 0, \tag{A.1}$$

where $\boldsymbol{j}_T$ ($\boldsymbol{j}_R$) is the translational (rotational) flux. For the simplest case in which an ABP swims freely, we have $\boldsymbol{j}_T = U_s \boldsymbol{q} P - D_T \nabla P$ and $\boldsymbol{j}_R = -D_R \nabla_R P$, where D_T is the translational diffusivity of the ABP and is assumed to be a constant.

A.1 The rotational operator

The rotational operator in equation (A.1) is defined as (Doi et al. 1988)

$$\nabla_R = \boldsymbol{q} \times \frac{\partial}{\partial \boldsymbol{q}}. \tag{A.2}$$

In 3D, one can parametrize $\boldsymbol{q}$ in a spherical coordinate system such that

$$\boldsymbol{q} = \sin\theta \cos\phi \boldsymbol{e}_x + \sin\theta \sin\phi \boldsymbol{e}_y + \cos\theta \boldsymbol{e}_z, \tag{A.3}$$

where θ is the polar angle, ϕ is the azimuthal angle, and $\{\boldsymbol{e}_x, \boldsymbol{e}_y, \boldsymbol{e}_z\}$ are the basis vectors of the reference Cartesian coordinate system. Using this parameterization, the operator $\partial/\partial\boldsymbol{q}$ is simply the gradient on the unit sphere, which is written as

$$\frac{\partial}{\partial \boldsymbol{q}} = \boldsymbol{e}_\theta \frac{\partial}{\partial \theta} + \frac{1}{\sin\theta} \boldsymbol{e}_\phi \frac{\partial}{\partial \phi}, \tag{A.4}$$

where $\boldsymbol{e}_\theta$ ($\boldsymbol{e}_\phi$) is the basis vector in θ (ϕ) direction. As a result, the rotational operator is

$$\nabla_R = \boldsymbol{e}_\phi \frac{\partial}{\partial \theta} - \frac{1}{\sin\theta} \boldsymbol{e}_\theta \frac{\partial}{\partial \phi}. \tag{A.5}$$

We note that a similar parametric form in 2D can be readily obtained. These parametric forms of the operator are useful for the numerical simulation of the Smoluchowski equation.

For smooth scalar functions $A = A(\boldsymbol{q})$ and $B = B(\boldsymbol{q})$, the rotational operator satisfies

$$\int A\nabla_R(B)d\boldsymbol{q} = -\int B\nabla_R(A)d\boldsymbol{q}, \tag{A.6}$$

which is the formula of integration by parts on the unit sphere in both 2D and 3D. With (A.6), it follows that for a vector-valued function $\boldsymbol{F} = \boldsymbol{F}(\boldsymbol{q})$,

$$\int A\nabla_R \cdot \boldsymbol{F} = -\int \boldsymbol{F} \cdot \nabla_R A d\boldsymbol{q}, \tag{A.7}$$

and

$$\int A\nabla_R^2(B)d\boldsymbol{q} = \int B\nabla_R^2(A)d\boldsymbol{q}. \tag{A.8}$$

Because an implied convention is used in the cross product in (A.2), the rotational operator is a pseudo operator. To avoid this, one can equivalently formulate the Smoluchowski equation using only the orientational gradient $\nabla_q = \partial/\partial\boldsymbol{q}$ (Saintillan and Shelley 2015). The integration-by-parts formula for ∇_q is given by

$$\int A\nabla_q \cdot \boldsymbol{B}d\boldsymbol{q} = (d-1)\int \boldsymbol{q}\cdot\boldsymbol{B}Ad\boldsymbol{q} - \int \boldsymbol{B}\cdot\nabla_q A d\boldsymbol{q}, \tag{A.9}$$

where $\boldsymbol{B} = \boldsymbol{B}(\boldsymbol{q})$ is a vector-valued function. Setting $A = const$ in the above, one obtains the divergence theorem in orientation space

$$\int \nabla_q \cdot \boldsymbol{B}d\boldsymbol{q} = (d-1)\int \boldsymbol{q}\cdot\boldsymbol{B}d\boldsymbol{q}. \tag{A.10}$$

Noting that $\boldsymbol{q}\cdot\nabla_q = 0$ and using (A.9), we have

$$\int A\nabla_q \cdot \left(\underbrace{\boldsymbol{q}\cdots\boldsymbol{q}}_{k}\right)d\boldsymbol{q} = (d-1)\int \underbrace{\boldsymbol{q}\cdots\boldsymbol{q}}_{k-1}Ad\boldsymbol{q}, \tag{A.11}$$

where k is an integer.

In manipulating orientational derivatives, the following differential identities are often useful. First, the orientational gradient of the unit swimming director is

$$\nabla_q\boldsymbol{q} = \frac{\partial\boldsymbol{q}}{\partial\boldsymbol{q}} = \boldsymbol{I} - \boldsymbol{q}\boldsymbol{q}, \tag{A.12}$$

which is simply the identity tensor on the unit sphere. The dot product $\boldsymbol{q}\cdot(\boldsymbol{I}-\boldsymbol{q}\boldsymbol{q}) = 0$ because $\boldsymbol{q}$ is perpendicular to the surface of the unit sphere representing orientations. Similarly, we have

$$\boldsymbol{q}\cdot\frac{\partial}{\partial\boldsymbol{q}} = 0. \tag{A.13}$$

The cross derivative

$$\frac{\partial}{\partial \boldsymbol{q}} \times \boldsymbol{q} = \boldsymbol{0} \tag{A.14}$$

due to symmetry. The orientational Laplacian is

$$\nabla_R^2 = \nabla_q^2. \tag{A.15}$$

One can also show that

$$\boldsymbol{q} \times \nabla_R = -\frac{\partial}{\partial \boldsymbol{q}}. \tag{A.16}$$

Several identities involving the derivatives of the polyadic products of $\boldsymbol{q}$ are useful:

$$\nabla_R \times \boldsymbol{q} = -(d-1)\boldsymbol{q}, \tag{A.17}$$

$$\nabla_q \cdot (\underbrace{\boldsymbol{q}\boldsymbol{q}\cdots\boldsymbol{q}}_{k \text{ terms}}) = (d-1)\underbrace{\boldsymbol{q}\boldsymbol{q}\cdots\boldsymbol{q}}_{k-1 \text{ terms}}, \tag{A.18}$$

$$\nabla_q^2(\boldsymbol{q}\boldsymbol{q}) = -2d\left(\boldsymbol{q}\boldsymbol{q} - \frac{1}{d}\boldsymbol{I}\right) \tag{A.19}$$

A.2 The orientational moments

Due to the polar nature of ABPs (the presence of $\boldsymbol{q}$), the mathematical dimensionality of its phase space ($\boldsymbol{x}$ and $\boldsymbol{q}$) is high. In 3D, it has a dimensionality of 5 if one parametrizes the swimming direction $\boldsymbol{q}$ using the polar and azimuthal angles of a spherical coordinate system. This poses a challenge for direct numerical simulations of the Smoluchowski equation. On the other hand, one often does not require the full distribution but rather its orientational moments. These often include the number density

$$n(\boldsymbol{x}, t) = \int P d\boldsymbol{q}, \tag{A.20}$$

the polar order

$$\boldsymbol{m}(\boldsymbol{x}, t) = \int \boldsymbol{q} P d\boldsymbol{q}, \tag{A.21}$$

and the nematic order

$$\boldsymbol{Q}(\boldsymbol{x}, t) = \int \left(\boldsymbol{q}\boldsymbol{q} - \frac{1}{d}\boldsymbol{I}\right) P d\boldsymbol{q}, \tag{A.22}$$

where $d = 2, 3$ is the dimensionality of the physical space and $\boldsymbol{I}$ is the identity tensor.

As an example, we consider the dynamics of a spheroidal ABP with length $2a$ and diameter $2b$ in simple shear flow. The Smoluchowski equation using the orientational gradient formulation can be written as

$$\frac{\partial P}{\partial t} + \nabla \cdot \boldsymbol{j}_T + \nabla_q \cdot \boldsymbol{j}_q = 0, \tag{A.23}$$

$$\boldsymbol{j}_T = \boldsymbol{u}P + U_s \boldsymbol{q}P - \boldsymbol{D}(\boldsymbol{q}) \cdot \nabla P, \tag{A.24}$$

$$\boldsymbol{j}_q = \left[\boldsymbol{q} \cdot \boldsymbol{\Omega} + \beta(\boldsymbol{I} - \boldsymbol{qq}) \cdot \boldsymbol{E} \cdot \boldsymbol{q}\right] P - D_R \nabla_q P, \tag{A.25}$$

where $\Omega_{ij} = (\partial u_j/\partial x_i - \partial u_i/\partial x_j)/2$ is the anti-symmetric part of the velocity gradient tensor, $E_{ij} = (\partial u_j/\partial x_i + \partial u_i/\partial x_j)/2$ is the symmetric part, $\boldsymbol{D}(\boldsymbol{q}) = D_{\|}\boldsymbol{qq} + D_{\perp}(\boldsymbol{I} - \boldsymbol{qq})$ is the translational diffusivity, and $\beta = (r^2 - 1)/(r^2 + 1)$ is the Bretherton parameter with $r = a/b$ being the aspect ratio. The flow field is given by

$$\boldsymbol{u} = \dot{\gamma} y \boldsymbol{e}_x, \tag{A.26}$$

where $\dot{\gamma}$ is the shear rate.

If the rotational operator is used to formulate the Smoluchowski equation as done in (A.1), one needs to define the rotary flux as

$$\boldsymbol{j}_R = \nabla_R \cdot \left[\frac{1}{2}\boldsymbol{\omega} P + \beta \boldsymbol{q} \times (\boldsymbol{E} \cdot \boldsymbol{q})\, P\right], \tag{A.27}$$

where $\boldsymbol{\omega} = \nabla \times \boldsymbol{u}$ is the vorticity vector of the flow field. To see this, using the relations $\boldsymbol{\Omega} = \frac{1}{2}\boldsymbol{\epsilon} \cdot \boldsymbol{\omega}$ and $\boldsymbol{\omega} = \boldsymbol{\epsilon} : \boldsymbol{\Omega}$ with $\boldsymbol{\epsilon}$ being the Levi-Civita tensor, one can show that

$$\nabla_R \cdot \left[\frac{1}{2}\boldsymbol{\omega} P + \beta \boldsymbol{q} \times (\boldsymbol{E} \cdot \boldsymbol{q})\, P\right] = \nabla_q \cdot \left[\boldsymbol{q} \cdot \boldsymbol{\Omega} P + \beta(\boldsymbol{I} - \boldsymbol{qq}) \cdot \boldsymbol{E} \cdot \boldsymbol{q} P\right]. \tag{A.28}$$

We emphasize again that both formulations give the same Smoluchowski equation.

To derive the governing equation for the k-th orientational moment, we multiply equation (A.23) by the k-adic product of $\boldsymbol{q}$ and integrate over the orientation space. The zeroth moment, or number density, is governed by

$$\frac{\partial n}{\partial t} + \nabla \cdot \left(\boldsymbol{u} n + U_s \boldsymbol{m} - \langle D \rangle \nabla n - \Delta D \nabla \cdot \boldsymbol{Q}\right) = 0, \tag{A.29}$$

where the translational diffusivity is written as

$$\begin{aligned} \boldsymbol{D} &= \left(\frac{2}{3}D_{\perp} + \frac{1}{3}D_{\|}\right)\boldsymbol{I} + (D_{\|} - D_{\perp})\left(\boldsymbol{qq} - \frac{1}{3}\boldsymbol{I}\right), \\ &= \langle D \rangle\, \boldsymbol{I} + \Delta D \left(\boldsymbol{qq} - \frac{1}{3}\boldsymbol{I}\right). \end{aligned} \tag{A.30}$$

The first moment is the polar order and satisfies

$$\frac{\partial \boldsymbol{m}}{\partial t} + \nabla \cdot \boldsymbol{j}_m + 2D_R \boldsymbol{m} - \boldsymbol{m} \cdot (\beta \boldsymbol{E} + \boldsymbol{\Omega}) + \beta \tilde{\boldsymbol{B}} : \boldsymbol{E} = \boldsymbol{0}, \tag{A.31}$$

where the flux for $\boldsymbol{m}$ is

$$\boldsymbol{j}_m = \boldsymbol{u}\boldsymbol{m} + U_s \left(\boldsymbol{Q} + \frac{1}{3} n \boldsymbol{I} \right) - \left(\langle D \rangle - \frac{1}{3} \Delta D \right) \nabla \boldsymbol{m} - \Delta D \nabla \cdot \tilde{\boldsymbol{B}}, \tag{A.32}$$

and

$$\tilde{B}_{ijk} = \int q_i q_j q_k P d\boldsymbol{q} \tag{A.33}$$

is the third moment. The nematic order satisfies

$$\begin{aligned} &\frac{\partial \boldsymbol{Q}}{\partial t} + \nabla \cdot \boldsymbol{j}_Q + \boldsymbol{\Omega} \cdot \boldsymbol{Q} - \boldsymbol{Q} \cdot \boldsymbol{\Omega} - \beta (\boldsymbol{E} \cdot \boldsymbol{Q} + \boldsymbol{Q} \cdot \boldsymbol{E}) \\ &- \frac{2}{3} \beta n \boldsymbol{E} + 2\beta \tilde{\boldsymbol{C}} : \boldsymbol{E} + 6 D_R \boldsymbol{Q} = 0, \end{aligned} \tag{A.34}$$

where the flux for $\boldsymbol{Q}$ is

$$\begin{aligned} \boldsymbol{j}_Q = \boldsymbol{u}\boldsymbol{Q} + U_s \left(\tilde{\boldsymbol{B}} - \frac{1}{3} \boldsymbol{m} \boldsymbol{I} \right) - \left(\langle D \rangle - \frac{1}{3} \Delta D \right) \nabla \boldsymbol{Q} \\ - \Delta D \nabla \cdot \tilde{\boldsymbol{C}} + \frac{1}{3} \Delta D (\nabla \cdot \boldsymbol{Q}) \boldsymbol{I} + \frac{1}{9} \Delta D \nabla n \boldsymbol{I}, \end{aligned} \tag{A.35}$$

and

$$\tilde{C}_{ijkl} = \int q_i q_j q_k q_l P d\boldsymbol{q} \tag{A.36}$$

is the fourth moment. In deriving the equations for orientational moments, the differential and integral identities in the previous section are used.

It is clear that there are an infinite sequence of equations governing the orientational moments. The equation governing the k-th moment depends on the $k+1$ or higher order moments. It is common to consider only the equations governing the first few moments and use a closure approximation for higher order moments. For example, in the absence of flow ($\boldsymbol{u} = \boldsymbol{0}$) for isotropic ABPs ($\Delta D = 0$), the $\boldsymbol{Q} = \boldsymbol{0}$ closure is often used (Saintillan and Shelley 2015; Yan and Brady 2015b); this leads to a set of closed equations for the number density and polar order.

As one might expect, this $\boldsymbol{Q} = \boldsymbol{0}$ closure does not offer a universal approximation for the dynamics of ABPs, particularly in the presence of external orienting or flow fields. Taking the equations for ABPs in simple shear as an example, one way to obtain a closure at the $\boldsymbol{Q}$ level is to examine equation (A.34). If we neglect the gradient terms $\nabla \cdot \boldsymbol{j}_Q$ and higher order moments completely, one arrives at steady state the algebraic equation

$$\boldsymbol{\Omega} \cdot \boldsymbol{Q} - \boldsymbol{Q} \cdot \boldsymbol{\Omega} - \beta(\boldsymbol{E} \cdot \boldsymbol{Q} + \boldsymbol{Q} \cdot \boldsymbol{E}) - \frac{2}{3}\beta n \boldsymbol{E} + 6D_R \boldsymbol{Q} = 0. \tag{A.37}$$

For a spherical ABP, $\beta = 0$, we obtain the closure $\boldsymbol{Q} = \mathbf{0}$. If the particle is non-spherical, $\boldsymbol{Q}$ does not vanish but instead is related to the rate-of-strain tensor, which can be obtained by inverting the above equation.

Another approach to close the moment equations is to consider a tensor harmonics expansion of the probability density (Saintillan and Shelley 2013):

$$P(\boldsymbol{x}, \boldsymbol{q}, t) = \frac{1}{4\pi}\left[n(\boldsymbol{x}, t) + 3\boldsymbol{q} \cdot \boldsymbol{m}(\boldsymbol{x}, t) + \frac{15}{2}\boldsymbol{q}\boldsymbol{q} : \boldsymbol{Q}(\boldsymbol{x}, t) + \cdots\right]. \tag{A.38}$$

Mathematically, this represents a severely truncated spherical harmonics expansion (or Fourier series in 2D), which is expected to be a good approximation if the probability density is locally close to the uniform orientational distribution. Truncating at the $\boldsymbol{Q}$ level, one can then derive closures for higher order moments by integration. For example, the third moment can be shown to be

$$\tilde{B}_{ijk} = \frac{1}{5}(m_i \delta_{jk} + m_j \delta_{ik} + m_k \delta_{ij}), \tag{A.39}$$

where δ_{ij} is the Kronecker delta.

One can see that the above equation does not reflect the effects of external orienting or flow fields, therefore the truncated probability density does not work when the orientational distribution is highly distorted due to external flow as shown in Peng and Brady (2020).

A.3 The spatial moments

In free space, one can also consider the spatial moments of the Smoluchowski equation. The k-th polyadic spatial moment is defined as

$$\boldsymbol{P}_k(\boldsymbol{q}, t) = \int \underbrace{\boldsymbol{x} \cdots \boldsymbol{x}}_{k \text{ times}} P(\boldsymbol{x}, \boldsymbol{q}, t) d\boldsymbol{x}. \tag{A.40}$$

The zeroth spatial moment,

$$P_0(\boldsymbol{q}, t) = \int P d\boldsymbol{x}, \tag{A.41}$$

is the net orientational distribution.

As an example, we again consider the problem of an ABP in simple shear. The equation governing the zeroth moment is given by

$$\frac{\partial P_0}{\partial t} + \nabla_q \cdot (\boldsymbol{H} P_0) - D_R \nabla_q^2 P_0 = 0, \tag{A.42}$$

where $\boldsymbol{H} = \boldsymbol{q} \cdot \boldsymbol{\Omega} + \beta(\boldsymbol{I} - \boldsymbol{qq}) \cdot \boldsymbol{E} \cdot \boldsymbol{q}$. The first moment satisfies

$$\frac{\partial \boldsymbol{P}_1}{\partial t} + \nabla_q \cdot (\boldsymbol{H} \boldsymbol{P}_1) - D_R \nabla_q^2 \boldsymbol{P}_1 = \boldsymbol{P}_1 \cdot \dot{\boldsymbol{\Gamma}} + U_s \boldsymbol{q} P_0, \tag{A.43}$$

where $\dot{\boldsymbol{\Gamma}} = \boldsymbol{E} + \boldsymbol{\Omega}$ is the velocity gradient tensor. For the case of an ABP in simple shear, the spatial moment equation at order k is coupled only to lower order moments. As a result, the set of moment equations up to order k is closed. We note that, in general, the spatial moment equations can also have an infinite hierarchical structure similar to that of the orientational moments.

For ABPs, the hydrodynamic stresslet is proportional to the nematic order. The spatially averaged nematic filed $\langle \boldsymbol{Q} \rangle (t) = \int (\boldsymbol{qq} - \boldsymbol{I}/3) P d\boldsymbol{q} d\boldsymbol{x}$ in simple shear satisfies a closed equation given by

$$\begin{aligned} &\frac{\partial}{\partial t} \langle \boldsymbol{Q} \rangle + \boldsymbol{\Omega} \cdot \langle \boldsymbol{Q} \rangle - \langle \boldsymbol{Q} \rangle \cdot \boldsymbol{\Omega} + 6 D_R \langle \boldsymbol{Q} \rangle = 0, \\ &\langle \boldsymbol{Q} \rangle (t=0) = \int \left(\boldsymbol{qq} - \frac{1}{3} \boldsymbol{I} \right) P_0(\boldsymbol{q}, 0) d\boldsymbol{q}. \end{aligned} \tag{A.44}$$

We note that the net nematic order can be obtained by using either $\langle \boldsymbol{Q} \rangle = \int \boldsymbol{Q} d\boldsymbol{x}$ or $\langle \boldsymbol{Q} \rangle = \int (\boldsymbol{qq} - \boldsymbol{I}/3) P_0(\boldsymbol{q}, t) d\boldsymbol{q}$. By defining

$$\hat{\boldsymbol{Q}} = \left(\langle Q_{xx} \rangle, \langle Q_{xy} \rangle, \langle Q_{xz} \rangle, \langle Q_{yy} \rangle, \langle Q_{yz} \rangle \right)^T, \tag{A.45}$$

we can write

$$\frac{\partial}{\partial t} \hat{\boldsymbol{Q}} = \boldsymbol{A}_1 \cdot \hat{\boldsymbol{Q}}, \tag{A.46}$$

where

$$\boldsymbol{A}_1(t) = - \begin{pmatrix} 6D_R & -\dot{\gamma} & 0 & 0 & 0 \\ \frac{1}{2}\dot{\gamma} & 6D_R & 0 & -\frac{1}{2}\dot{\gamma} & 0 \\ 0 & 0 & 6D_R & 0 & -\frac{1}{2}\dot{\gamma} \\ 0 & \dot{\gamma} & 0 & 6D_R & 0 \\ 0 & 0 & \frac{1}{2}\dot{\gamma} & 0 & 6D_R \end{pmatrix} \tag{A.47}$$

We can further generalize the flow to be oscillatory, $\dot{\gamma}(t) = \dot{\gamma}_0 \cos(\omega t)$, in which case $\boldsymbol{A}$ has one real and two pairs of complex eigenvalues, which indicates that we have damped oscillation in the solution. The solution can be readily obtained via the matrix exponential

$$\hat{\boldsymbol{Q}}(t) = \exp\left(\int_0^t \boldsymbol{A}_1(s)ds\right) \cdot \hat{\boldsymbol{Q}}(0). \tag{A.48}$$